



University of
Nottingham
UK | CHINA | MALAYSIA

Investigation of Novel Analytical Tools and Experimental Methods for the Development of Intermediate Temperature Heat Pipes

Submitted March 2021 in partial fulfilment of the condition for the award of
the degree of **Engineering Doctorate**.

Thomas C. Werner
Student ID: 4289404

Engineering Doctorate Centre for Carbon Capture and Storage and
Cleaner Fossil Energy
Fluids and Thermal Research Group
Faculty of Engineering
University of Nottingham

Dedicated to Nilda Werner and Abraham Rosenberg.

Abstract

Heat pipes have been a large part of the thermal management market for the past four decades and have contributed to the development and optimisation of countless components in the design of satellites, spaceships, formula racing cars, power plants and electronics cooling. These thermal management systems span a wide range of temperatures, which in turn, requires the heat pipe fluid to be specially selected to meet the application requirements. Recently, there has been an increasing demand for heat pipes which can operate in the 300°C to 600°C temperature range – a range which is still severely underdeveloped in the heat pipe marketplace due to the lack of conventional fluids which can adequately operate at these temperatures. This range is dubbed the ‘medium’ or ‘intermediate’ temperature range.

Though there has been some development in this temperature range with the aim of testing particular fluids and metals which may be suitable, there appears to currently be a severe lack of continuity in the work with little progression towards a definitive solution and little effort to catalogue successful and unsuccessful tests. The author has identified from literature review of the topic that the lack of a framework to follow which would aid the researcher to advance more rapidly in identification, modelling and experimentation of potential fluids may be a contributing factor. Previous works on the topic tends to follow a ‘patchwork’ process, often with overlaps in testing and with a focus only on long term compatibility tests without a well-rounded scientific process beforehand which often lead

to incompatible results. This in some ways has ‘stalled’ the assessment of new potential fluids due to the long-winded nature of the approach.

The following work intends to progress the research capabilities in this temperature range and set the foundations for rapid directed research effort in this area by developing the necessary equipment, techniques, databases and modelling tools. While the means to develop novel fluids themselves is beyond the scope of this work, the intention of this work is to advance the capabilities of the participating organisations to reach a point in which they are able to focus solely on novel fluids following the framework laid out in this thesis. The work also provides a comprehensive analysis of all currently available fluids and, through the developed ‘fluid selection process’, has identified a range of fluids which have the best potential for further development. The most cost-effective solutions were found to be Bismuth Trichloride and Antimony Trichloride, while other fluids such as Ruthenium Pentafluoride, Rhenium Heptoxide and Rhenium Heptafluoride have excellent thermal transport capability in the intermediate temperature range but are substantially more expensive. The fluid selection process has also proven to work universally in any temperature range through application in commercial projects. This has led to the identification of alternative fluids in what was previously thought as well-established temperature ranges which could provide better cost-benefit while maintaining high thermal conduction capabilities.

The focal fluid selected to prove the processes was Antimony Trichloride due to the low cost and greater ease of handling. Theoretical analysis concluded that refractory

metals such as Tungsten, Molybdenum, Zirconium and Tantalum are most likely to be compatible with halides in general. Preliminary contact angle results showed a Molybdenum has a superior wetting ability than the conventionally used Stainless Steel and the Molybdenum/Zirconium alloy TZM when testing with Antimony Trichloride. The wetting ability of Antimony Trichloride is also superior to that of water on the same surfaces. Compatibility tests were in agreement with predictions that refractory metals have the highest resistance to reaction with Halides. Molybdenum was shown to have the greatest resistance to reaction from analysing surface changes through SEM and EDX techniques. Molybdenum is selected to be focus of the future work due to its superior corrosion resistance, reasonable cost and wide application in targeted industries such as nuclear and aerospace.

Water heat pipe tests were conducted to prove the testing ability of medium temperature heat pipe test rig. The study focused on the upper limitation of mesh wick heat pipes in the horizontal position. Experimental results show good agreement with numerical predictions of power handling capacity surrounding the boiling limit of the heat pipe, but they underestimated the temperature drop experienced across the heat pipe possibly due to there being a higher thermal resistance across multiple mesh layer than expected. The attempted fabrication of Molybdenum/Antimony Trichloride heat pipes was unsuccessful using conventional joining methods, future work will aim to create heat pipe structures using Electron Beam or Laser welding.

This work has developed numerous novel concepts and analyses including: (1) Comprehensive fluid property, metal property and fluid/metal compatibility databases (2) Development of a heat pipe modelling tool incorporating these databases (3) Construction of a test rig able to test heat pipes in the medium temperature range (4) Development of short term compatibility and wettability tests for air sensitive fluids (5) Analysis of the performance of water heat pipes around their boiling limit, within the ‘intermediate’ temperature range.

Acknowledgements

This work would not have been possible without the generous funding from Boyd Corp (formally Aavid Thermacore Ltd.), the EPSRC and the University of Nottingham. I thank all those involved from each institution in bringing this project to its initial fruition.

A very special thanks to my supervisors Prof. Yuying Yan, Mr. David Mullen and Dr. Elvedin Halimic for guiding me through the project and providing me with support and encouragement. To all my friends at Boyd, Mr. Steven Cochrane, Mr. Kevin Lynn and Dr. Xiao Yang, your support has been invaluable.

I will forever have a deep gratitude for all the emotional and intellectual support from my other half Dr. Deborah Anne Cornell. To all my family who have stood by me in the best and worst of times and given me the strength to overcome the toughest of challenges - my father Dr. Carlos Werner, my mother Mrs. Gillian Werner, my sister Dr. Alexandra Werner, my grandparents Mr. James Oswin Hall and Mrs. Margaret Hall without whom the completion of this thesis would not have been possible.

To Prof. Hao Liu and Dr Shenyi Wu for their support, and to all my friends at Nottingham University, Mr. Richard Seeley, Mr. Lewis Tuck, Mr. Matteo Spanu, Dr. Kuo Huang, Mr. Wei Gong, Dr. Yiyi Chen, Mr. Zeyu Liu, Mr. Xin Wang and Mr. Edward Wright. I can't thank you enough for all the good times and making this phase of my life unforgettable.

Table of Contents

Abstract	iii
Acknowledgements	vii
List of Figures	xviii
List of Tables	xxvi
Nomenclature	xxix
Publications	xxxiv
Chapter I Introduction	1
1.1 Outline and Background of research	2
1.2 Aims and Outcomes	4
1.3 Thesis structure	7
Chapter II Literature review	9
2.1 Introduction	10
2.2 Concept and history of heat pipe	12
2.2.1 Classification of heat pipes	14
2.3 Heat pipe theory and modelling	16
2.3.1 Fluid Flow	19
2.3.2 Pressure Distribution	20
2.3.3 Wick structure	25
2.3.3.1 Liquid/vapour interface	27
2.3.3.2 Conductivity of wicks	27
2.3.4 Thermal network	31

2.3.5	Working limitations of heat pipes.....	34
2.3.5.1	Capillary limit	34
2.3.5.2	Boiling limit	36
2.3.5.3	Sonic limit	43
2.3.5.4	Entrainment limit.....	44
2.3.5.5	Viscous limit	46
2.3.6	Other mechanisms.....	47
2.3.7	Heat pipe heat flux in medium temperature range.....	48
2.4	Heat pipe working fluid	50
2.4.1	Organic Fluids.....	51
2.4.1.1	Thermal degradation	52
2.4.1.2	Rate equations	53
2.4.1.3	Stability prediction	56
2.4.1.4	Halogenated Alkanes.....	58
2.4.1.5	Halogenated aromatic compounds	58
2.4.1.6	Previously tested organic fluids in medium temperature range	60
2.4.2	Inorganic fluids	61
2.4.2.1	Stability prediction model for inorganic fluids	62
2.4.2.2	Compatibility of metal/fluid envelopes.....	63
2.4.2.3	Liquid metals.....	66
2.4.2.4	Previously tested inorganic fluids in medium temperature range	68

2.5	Current experimental studies in medium and high temperature heat pipes	70
2.5.1	Experimental techniques.....	71
2.5.2	Heat pipe life tests.....	72
2.5.3	Heat pipe thermal performance tests.....	74
2.6	Chapter Summary	77
Chapter III Methodology - Analysis and application of experimental and		
	numerical methods	78
3.1	Experimental methods	79
3.2	Wettability and Compatibility Testing.....	81
3.2.1	Wettability testing (using measure of contact angle).....	81
3.2.2	Contact angle measuring techniques.....	83
3.2.2.1	General apparatus.....	84
3.2.2.2	Procedure: Sample preparation	85
3.2.2.3	Procedure: Liquid contact angle.....	90
3.2.2.4	Procedure: Solid-to-liquid contact angle.....	91
3.2.2.5	Software	92
3.2.3	Compatibility tests	94
3.2.3.1	General apparatus.....	95
3.2.3.2	Procedure: Compatibility tests	97
3.2.3.3	Procedure: Roughness tests.....	98
3.2.3.4	Procedure: Microscope Imaging	99
3.2.3.5	Procedure: SEM/EDX Imaging.....	99

3.3	Medium temperature thermal performance test rig	100
3.3.1	Flow meter calibration	101
3.3.1.1	Procedure: Flow meter calibration	102
3.3.2	Thermocouple calibration	104
3.3.2.1	Procedure: Thermocouple calibration	104
3.3.3	Condenser heat loss.....	106
3.3.3.1	Procedure: Condenser heat loss test.....	107
3.3.4	Heater heat loss	109
3.3.4.1	Procedure: Heater heat loss test	109
3.4	Error analysis	112
3.4.1	Overview of instrumentation used and accuracies.....	112
3.4.2	Thermocouple calibration and derivation of thermocouple error analysis.....	113
3.4.3	Statistical analysis of temperature measurements.....	116
3.4.4	Temperature difference error analysis	117
3.4.5	Error in reported circulator oil fluid properties.....	118
3.4.6	Error analysis of experimental equations.....	118
3.4.7	Sessile drop error analysis	121
3.5	Chapter Summary	123
	Chapter IV Investigation and modelling of medium temperature fluids	124
4.1	Introduction.....	125
4.1.1	Aims.....	126
4.2	Fluid selection process	128

4.2.1	Methodology	129
4.2.1.1	Initial selection – Database search	130
4.2.1.2	Fluid analysis.....	131
4.2.1.3	Fluid selection	136
4.2.2	Database creation	139
4.2.2.1	Fluid property database	141
4.2.2.2	Compatibility database.....	142
4.2.2.3	Metal property database	142
4.2.3	Selection criteria	142
4.2.3.1	Surface Tension.....	143
4.2.3.2	Thermal Degradation and compatibility	143
4.2.3.3	Toxicity	144
4.2.3.4	Cost.....	145
4.2.3.5	Handling.....	145
4.2.4	Conclusions.....	146
4.3	Fluid selection & analysis.....	148
4.3.1	Phase 1: Initial selection	149
4.3.2	Phase 2: Fluid analysis.....	151
4.3.2.1	Property data analysis.....	151
4.3.2.2	Merit analysis	153
4.3.2.3	Vapour pressure analysis.....	155
4.3.2.4	Thermal transport analysis	157
4.3.2.5	Stability and toxicity analysis	159

4.3.3	Phase 3: Fluid selection	161
4.3.3.1	Weighted analysis	162
4.3.4	Conclusions.....	163
4.4	Heat pipe modelling using chosen fluids	164
4.4.1	Horizontal model	165
4.4.2	Mesh wick 45° gravity aided model	166
4.4.3	Final fluid models	167
4.4.4	Results and discussion of fluid modelling	169
4.5	Chapter Summary	171
	Chapter V Calculation, design and construction of a high temperature test rig for novel heat pipes.....	173
5.1	Introduction.....	174
5.2	Engineering Design Assessment.....	176
5.2.1	General layout.....	177
5.2.2	Component assessment	180
5.2.3	Test approach and strategy.....	184
5.3	Heater block design.....	185
5.3.1	Performance assessment	186
5.3.2	Final design.....	187
5.4	Calorimeter unit design.....	190
5.4.1	Calorimeter performance qualification	192
5.4.1.1	Calorimeter heat transfer performance.....	197
5.4.2	Final calorimeter design.....	200

5.5	Final test rig design.....	202
5.5.1	Heat loss calculation	202
5.5.2	Data acquisition and Methodology	205
5.5.2.1	Thermocouples.....	206
5.5.2.2	Flow meter programming & control	207
5.5.2.3	Pico logger settings & automated calculations	207
5.6	Test rig CFD analysis.....	209
5.6.1	CFD boundary conditions	209
5.6.2	Full assembly performance	212
5.6.3	Heater block analysis	214
5.7	Qualification testing.....	216
5.7.1	Dry-out tests.....	217
5.7.2	Angle test	217
5.7.3	Heat loss tests.....	217
5.7.4	Baseline Testing.....	218
5.8	Life test rig	219
5.8.1	Accelerated life test theory and approach.....	219
5.8.2	Life test rig design assessment.....	220
5.8.3	Life test strategy.....	220
5.8.4	Final test rig model	221
5.9	Chapter Summary	223
	Chapter VI Experimental analysis of fluid/metal compatibility and wettability	224
6.1	Introduction.....	225

6.2	Material selection for Heat Pipe	227
6.2.1	Compatibility model	231
6.3	Wettability study of chosen fluids on metals	233
6.3.1	Test samples.....	235
6.3.2	Water test results.....	237
6.3.3	Antimony Trichloride test results	244
6.4	Compatibility study of fluid with selected metals	249
6.4.1	Compatibility test.....	250
6.4.2	Results and Analysis.....	252
6.4.2.1	Stainless Steel 304 compatibility with Antimony Trichloride.....	258
6.4.2.2	Niobium compatibility with Antimony Trichloride	261
6.4.2.3	Molybdenum compatibility with Antimony Trichloride 264	
6.5	Chapter Summary	267
Chapter VII Experimental analysis of water heat pipe thermal transport limitations		
269		
7.1	Water Heat Pipe thermal performance analysis.....	270
7.1.1	Heat Pipe Design.....	273
7.1.2	Material analysis	276
7.1.3	Aim and setup	277
7.1.3.1	Test rig.....	278
7.1.3.2	Test structure: Preliminary tests and optimisation	279

7.1.4	Heat pipe testing approach and methodology	280
7.1.5	Test matrix	282
7.2	Thermal transport performance testing on Water Heat pipes	284
7.2.1	Test plan.....	284
7.2.1.1	Procedure.....	285
7.2.2	Theory	286
7.2.2.1	Predicted heat pipe performance	287
7.3	Results and Discussion	291
7.3.1	Heat pipe heat transport limit analysis.....	291
7.3.2	Heat pipe temperature difference analysis	295
7.3.3	Heat pipe thermal resistance analysis	299
7.3.4	Effective conductivity quantification and analysis	302
7.3.5	Boiling point identification, quantification and analysis	304
7.3.6	Error analysis	305
7.3.7	Discussion.....	306
7.4	Summary and Conclusions	309
	Chapter VIII Heat Pipe fabrication and industrial case study.....	310
8.1	Introduction.....	311
8.2	Fabrication methods.....	312
8.2.1	General manufacturing process.....	312
8.2.2	Joining methods	315
8.2.3	Wick Structure design.....	316
8.3	Filling methods	317

8.3.1	Conventional fill method	319
8.3.2	Push-pot fill method.....	319
8.3.3	Inert atmosphere/vacuum fill method	321
8.3.4	Crimping	321
8.4	Fabrication attempts.....	323
8.5	Fluid selection analysis case study	325
8.5.1	Application example	326
8.5.2	Fluid analysis	327
8.6	Chapter Summary	329
	Chapter IX Conclusions and Recommendations	330
9.1	Conclusions.....	331
9.1.1	Summary of thesis.....	331
9.1.2	Originality and contributions	333
9.2	Recommendations and future work	336
	References.....	339

List of Figures

Figure 2-1 Variations of types of heat pipe developed over the years.....	13
Figure 2-2 Principal working fluids for heat pipes spanning all working temperature ranges	14
Figure 2-3 The internal liquid/vapour interface of a heat pipe. Source: [9]	16
Figure 2-4 Heat transport operating limits for standard capillary driven heat pipes. Source: [10].....	17
Figure 2-5 Heat pipe theory topic structure overview	19
Figure 2-6 Axial pressure variation at a) low vapour flow rates b) moderate vapour flow rates c) high vapour flow rates. Source: Faghri (2012) [9].....	21
Figure 2-7 Radial Reynolds number vs heat input p / length of heat pipe. Source: [13]...	23
Figure 2-8 Graphs of (A) The temperature profile of a Sodium heat pipe and (B) The pressure profile across a converging/diverging nozzle. Source: [15]	24
Figure 2-9 Common wick sections. Source: [1]	26
Figure 2-10 Thermal resistance network model for a Heat Pipe	33
Figure 2-11 Effects of increase in heat flux and saturation temperature on the maximum nucleation radius	43
Figure 2-12 Wave disturbance pattern in stratified flow containing a mesh wick structure where entrained droplets are formed. Two different entrainments modes are shown: A) Roll-wave entrainment and B) Stripping entrainment. Source: [40]	46

Figure 2-13 (1) Various intermediate species in the decomposition reaction and their relative internal energies (2) Unimolecular decomposition of species D to A + B. Source: [49].....	53
Figure 2-14 Pressure at which the unimolecular rate constants fall by a factor of two. Source: Benson and Sidney (1960).....	55
Figure 2-15 Bond dissociation energies for various vapours. Source: [47].....	57
Figure 2-16 Corrosion of Iron by film of molten Bismuth Trichloride (hypothetical reaction cells). Source: [47]	64
Figure 2-17 Decomposition potential of various inorganic chlorides. Source: [47].....	66
Figure 2-18 Apparatus set up for high temperature water heat pipe life test by Anderson et al. [10]	73
Figure 2-19 Apparatus setup for Lithium and Silver heat pipe testing Source: [85].....	75
Figure 2-20 Typical schematic diagram for a heat pipe thermal performance rig (top) and a picture of a test rig using a variable conductance calorimeter (bottom) from recent literature. Sources: [86] and [82]	76
Figure 3-1 Umbrella view of the overall thesis	79
Figure 3-2 Contact angle example diagram	82
Figure 3-3 Kruss contact angle measuring apparatus	84
Figure 3-4 Polishing Apparatus	86
Figure 3-5 Polishing process.....	86
Figure 3-6 Inert atmosphere sample	89
Figure 3-7 MBraun Glovebox.....	89
Figure 3-8 Solid-to-liquid contact angle test apparatus	91

Figure 3-9 Kruss apparatus software	93
Figure 3-10 pyDSA software	93
Figure 3-11 Compatibility sample pre and post-test prep sequence	95
Figure 3-12 Starting image of compatibility test	98
Figure 3-13 Experimental layout	101
Figure 3-14 Thermocouple isothermal oven temperature data	105
Figure 3-15 Individual thermocouple temperature difference trend with polynomial expression	106
Figure 3-16 Condenser heat loss trend against average condenser fluid temperature ...	108
Figure 3-17 Heater thermocouple temperature reading over time	110
Figure 3-18 Average thermocouple temperature difference from benchmark	114
Figure 3-19 Chapter summary overview	123
Figure 4-1 Selection Criteria subsection breakdown	128
Figure 4-2 Process flow chart for fluid selection and modelling	130
Figure 4-3 Fluid property database fluid selection filters	131
Figure 4-4 Figure of merit comparison example	134
Figure 4-5 Vapour pressure comparison example	135
Figure 4-6 Process flow chart for each potential fluid	137
Figure 4-7 Weighted selection table example	139
Figure 4-8 Figure of merit curves for fluids 1 to 18	153
Figure 4-9 Figure of merit curve for fluids 19 to 37	154
Figure 4-10 Vapour pressure analysis for fluids 1 to 18	155
Figure 4-11 Vapour pressure analysis for fluids 19 to 37	156

Figure 4-12 Capillary limit analysis for fluids 1 to 18.....	158
Figure 4-13 Capillary limit analysis for fluids 19 to 37.....	158
Figure 4-14 Weighted selection table for shortlisted fluids.....	162
Figure 4-15 Heat pipe thermal limitations in the horizontal orientation for primary shortlisted fluids and previously studied fluids	165
Figure 4-16 Heat pipe thermal limitations at a 45° gravity aided orientation for primary shortlisted fluids and previously studied fluids	167
Figure 4-17 Heat pipe operating domains for previously studied fluids (TiCl ₄ and AlBr ₃) and current shortlisted fluids (BiCl ₃ and SbCl ₃)	168
Figure 4-18 Heat pipe operating domains for a Water/Mo heat pipe	169
Figure 5-1 Test rig schematic	177
Figure 5-2 Calorimeter loop layout.....	178
Figure 5-3 Full test rig diagram	179
Figure 5-4 Figure of apparatus setup	179
Figure 5-5 Thermocouple types	183
Figure 5-6 Cartridge heater concept model	186
Figure 5-7 Final heater design engineering drawing	188
Figure 5-8 Final heater design exploded view	189
Figure 5-9 Initial calorimeter concept design	194
Figure 5-10 Reynolds number of Dibenzyltoluene for a rage of flow rates over expected operating temperature range	195
Figure 5-11 Final calorimeter design.....	196

Figure 5-12 Dibenzyltoluene Nusselt and Prandtl number throughout operating temperature range.....	198
Figure 5-13 Convective heat transfer coefficient of Dibnzyltoluene through calorimeter channels over expected temperature range	199
Figure 5-14 Calculated temperature difference at designated flow rate	199
Figure 5-15 Final Calorimeter design engineering drawing	200
Figure 5-16 Final Calorimeter design drawing.....	201
Figure 5-17 Final Calorimeter design exploded view.....	201
Figure 5-18 Cross section view of heat pipe test rig.....	202
Figure 5-19 Thermocouple types used.....	206
Figure 5-20 Thermocouple types used.....	210
Figure 5-21 CFD model and cabinet in Ansys Icepak.....	211
Figure 5-22 Dibenzyltoluene property data in Ansys Icepak and convergence criteria	211
Figure 5-23 CFD heat pipe temperature profile at various input powers. The calorimeter temperature input is of 200°C and flow rate is 0.0167 Kg/s.....	212
Figure 5-24 Heat input vs heat output from calorimeter.....	213
Figure 5-25 Heater block modelling results at 220W	214
Figure 5-26 Heat Pipe production flow chart	216
Figure 5-27 Life test rig exploded view.....	222
Figure 6-1 Tensile strength vs thermal conductivity metal search filter	228
Figure 6-2 Hardness vs Price metal search filter	229
Figure 6-3 Final metal output from filter search.....	230
Figure 6-4 Contact angle test example.....	233

Figure 6-5 Metal sample example.....	236
Figure 6-6 Average sample roughness chart.....	239
Figure 6-7 Static contact angle results chart.....	241
Figure 6-8 Advancing contact angle results chart.....	242
Figure 6-9 Comparison of static and advancing contact angle results.....	243
Figure 6-10 Time-lapse image of SbCl ₃ melting on Molybdenum surface	244
Figure 6-11 Contact angle measurement over time for SbCl ₃ on Molybdenum surface	246
Figure 6-12 Contact angle measurement over time for SbCl ₃ on TZM surface	246
Figure 6-13 Contact angle measurement over time for SbCl ₃ on Stainless Steel 304 surface.....	247
Figure 6-14 SEM image of Stainless Steel 304 surface.....	258
Figure 6-15 EDX line scan of Stainless Steel 304 sample.....	259
Figure 6-16 EDX Point analysis on Stainless Steel 304 sample.....	260
Figure 6-17 SEM image of Niobium surface.....	261
Figure 6-18 EDX line scan of Niobium sample.....	262
Figure 6-19 EDX Point analysis on Niobium sample.....	263
Figure 6-20 SEM image of Molybdenum surface and roughness test results	264
Figure 6-21 EDX lines can on Molybdenum sample.....	265
Figure 6-22 EDX Point analysis on Molybdenum sample	266
Figure 7-1 Component testing diagram	279
Figure 7-2 Test process flow chart.....	280
Figure 7-3 All limitations for horizontal water heat pipe	289

Figure 7-4 Evaporator and Condenser heat fluxes associated with maximum thermal power capacity form Figure 7-3.....	290
Figure 7-5 Experimental and numerical thermal heat transport prediction results. Values next to experimental data points indicate the input power for the steady state condition. The points correlating with the range of calculated boiling limit curves are proposed as the ‘transition’ zone. The error bars are calculated from instrument error propagation theory.	292
Figure 7-6 Graph of experimental steady state values correlating with a nucleation radius of 1.2E-7	293
Figure 7-7 Graph of experimental steady state values correlating with a nucleation radius of 0.6E-7	294
Figure 7-8 Graph of experimental steady state values correlating with a nucleation radius of 0.47E-7	294
Figure 7-9 Average temperature difference against the input power for experimental steady state results.....	297
Figure 7-10 Experimental average temperature difference values at estimated boiling limit against the heat flux input compared to numerical predictions.....	298
Figure 7-11 Experimental average temperature difference values at estimated boiling limit against the calculated vapour temperature for each steady state value compared to predicted trend	299
Figure 7-12 Thermal resistance at each experimental steady state against the input thermal load for thermal resistance calculated from the output thermal load (measure by calorimeter). Highlighted points show an alternative indication for the ‘transition’ zone.	

Here the transition point for 270°C and 300°C circulator temperature differs from those indicated in Figure 7-5.....	300
Figure 7-13 Thermal resistance of transition zone points against heat flux input	301
Figure 7-14 Scatter plot of all the calculated effective conductivities of steady state values within the ‘transition zone’	303
Figure 7-15 Multi variable scatter plot of steady state conditions. Line represents the maximum thermal conductivity path which can be used as the transition point.	305
Figure 8-1 Manufacturing process for sodium/stainless steel heat pipe	314
Figure 8-2 Charging processes.....	318
Figure 8-3 Schematic Diagram Showing the Main Elements of a High Temperature Heat Pipe Charging Facility	320
Figure 8-4 Standard crimping process	322
Figure 8-5 Custom built argon purged welding chamber	323
Figure 8-6 Argon purged welding attempt.....	324
Figure 8-7 Argon purged welding results	324

List of Tables

Table 2-1 Liquid pressure drop expressions for various wick types. Source: [1].....	26
Table 2-2 Alternative conductivity equations for other mesh types. Source: [19]	29
Table 2-3 Empirical boiling correlations	37
Table 2-4 Maximum achieved heat fluxes for previous testing on medium temperature fluids by Saaski et. al. [47].....	49
Table 2-5 Various halogenated aromatic fluids and their properties	59
Table 2-6 Decomposition temperatures for halocarbon refrigerants in presence of steel and the influence of metals on decomposition of R-11 at 249°C. Source: [54]	60
Table 2-7 Summary of organic fluids tested in the medium temperature range.....	60
Table 2-8 Common heat pipe liquid metals	67
Table 2-9 Liquid metals tested in the medium temperature range.....	67
Table 2-10 Most recent compatible results for novel inorganic fluids	69
Table 2-11 Papers outlining medium and high temperature heat pipe testing.....	71
Table 3-1 Sample list and end polish specifications	87
Table 3-2 Compatibility test apparatus list	96
Table 3-3 Test rig apparatus list.....	100
Table 3-4 Flow rate calibration results example.....	103
Table 3-5 Condenser heat loss results table	108
Table 3-6 Heater heat loss results table	111
Table 3-7 Table of experimental instruments and their associated error.....	113
Table 3-8 Error analysis of thermocouple calibration data.....	116

Table 3-9 Static and advancing contact angle results table	122
Table 4-1 Property data sources.....	140
Table 4-2 Phase 1 fluid shortlist	150
Table 4-3 Property data analysis of shortlisted fluids.....	152
Table 4-4 Phase 2 fluid shortlist analysis	160
Table 4-5 Phase 3 shortlisted fluids	161
Table 4-6 Ranked fluid selection results.....	162
Table 4-7 Heat pipe modelling parameters	164
Table 4-8 Fluid output data from 45° gravity aided model	170
Table 5-1 Components list.....	182
Table 5-2 Types of heater used in heat pipe test rigs.....	185
Table 5-3 Calorimeter design table.....	192
Table 5-4 Heat loss calculations for 200°C circulator temperature.....	204
Table 5-5 Heat loss calculations for 250°C circulator temperature.....	204
Table 5-6 Heat loss calculations for 270°C circulator temperature.....	205
Table 5-7 Heat loss calculations for 300°C circulator temperature.....	205
Table 5-8 Comparison of CFD and analytical heat loss predictions	214
Table 6-1 Electromotive Force Difference potential of Antimony Trichloride and Bismuth Trichloride with various metals. Property data source: [119].....	232
Table 6-2 Sample log extract. See full log in Appendix A.....	237
Table 6-3 Roughness test results, average peak length, Ra (µm).....	238
Table 6-4 Static contact angle test results.....	240
Table 6-5 Advancing contact angle test results	240

Table 6-6 Contact angle of Antimony Trichloride on various metal surfaces.....	247
Table 6-7 List of metal samples.....	249
Table 6-8 Compatibility test progression timeline for each sample. Images show the a snapshot of the molten SbCl ₃ exposed sample at each time step.	251
Table 6-9 Compatibility results	253
Table 6-10 Microscope images of top and bottom of metal samples before and after compatibility testing.....	254
Table 7-1 Heat pipe design considerations	273
Table 7-2 Heat pipe design summary	274
Table 7-3 Final heat pipe dimensions	274
Table 7-4 Heat pipe list summary	275
Table 7-5 Water heat pipe metal envelope alloys.....	276
Table 7-6 Test component list.....	279
Table 7-7 Latin square example with test parameters	283
Table 7-8 Test parameters.....	285
Table 7-9 Various experimental temperature difference definitions. The ‘E’ and ‘C’ variables are temperature readings in the positions indicated in	287
Table 7-10 Heat pipe performance at transition point indicated in Figure 7-15.....	304
Table 7-11 Repeatability of 200°C circulator temperature tests.....	306
Table 8-1 Potential Tungsten Joining Technique Analysis:	315

Nomenclature

Symbol	Definition	Units
A	Area OR Bond vibration frequency constant	m^2 -
A_p	Area of surface pores	m^2
b	Dimensionless constant	-
C	Compressibility parameter OR Total concentration	- -
C_o	Sonic velocity	ms^{-1}
c_p	Specific heat capacity at constant pressure	JK^{-1}
D	Diameter OR Chemical species	m -
d_h	Hydraulic diameter	m
d	Diameter	m
E	Electromotive force OR Energy	JC^{-1} J
E^+	Activation Energy	J
E^0	Base Electromotive force	V
E_t	Entrainment parameter $\left(\frac{\sigma}{\rho L \delta}\right)$	-
F	Friction parameter OR Faraday constant	- $Cmol^{-1}$
f	Friction factor	-
G^0	Base Gibbs free energy	$Jmol^{-1}$
g	Gravitational acceleration	ms^{-2}
h_{fg}, L	Enthalpy of vaporisation/Latent heat of vaporisation	JKg^{-1}
K	Permeability OR Pyrolysis rate constants	m^{-1} -

K'	Pressure loss coefficient	-
l	Length	m
k, λ	Thermal conductivity	$Wm^{-1}K^{-1}$
M	Merit Number $\left(\frac{\rho L \sigma}{\mu}\right)$	Wm^{-2}
M_a	Representative pure metal	-
M_b	Representative halide metal	-
\dot{m}	Mass flow rate	Kgs^{-1}
m	Mass	Kg
N	Number of samples OR Number of mesh layers OR Number of groves	- - -
Nu	Nusselt number $\left(\frac{\alpha L}{k}\right)$	-
n	Number of electrons	-
P	Pressure	Nm^{-2}
P'	Wetted perimeter of surface pores	m
Pr	Prandtl Number $\left(\frac{c_p \mu}{k}\right)$	-
\dot{Q}	Heat transfer rate	W
q	Heat flux	Wm^{-2}
R	Gas constant OR Thermal Resistance	$Jmol^{-1}K^{-1}$ KW^{-1}
Re_r	Radial Reynolds number $\left(\frac{\rho u D}{\mu}\right)$	-
Re	Reynolds number $\left(\frac{\rho u D}{\mu}\right)$	-
R_1	First order rate constant	s^{-1}
R_{Cr}	Critical decomposition rate	h^{-1}
R_a	Rayleigh Number $\left(\frac{\rho \beta \Delta T l^3 g}{\mu \alpha}\right)$	-
$R_{f,h}$	Rate of pyrolysis at high pressure	$molm^{-3}s^{-1}$

$R_{f,l}$	Rate of pyrolysis at low pressure	$molm^{-3}s^{-1}$
R_f	Rate of pyrolysis	$molm^{-3}s^{-1}$
R_g	Gas Constant	$JKg^{-1}K^{-1}$
r_h	Hydraulic radius	m
r_n	Nucleation radius	m
r	Radius	m
T	Temperature	K
u, v	Velocity	ms^{-1}
\bar{v}	Average velocity	ms^{-1}
We	Weber Number $\left(\frac{\rho v^2 l}{\sigma}\right)$	-
X_c	Representative halogen reactant	-
X_{cp}	Representative halogen product	-
x_i	Current Value	-
\bar{x}	Mean	-
z	Axial coordinate	m
α_v	Velocity profile correction factor	-
α_t	Thermal expansion correction factor	-
α	Convective heat transfer coefficient	$Wm^{-2}K^{-1}$
β	Thermal Expansion Coefficient	K^{-1}
T	Viscosity ratio	-
δ^*	Reference surface depth	m
γ	Ratio of specific heats (cp/cv)	-
δ	Unit length OR Surface depth	m m
ε	Void Fraction	-
θ	Angle	Deg
μ	Viscosity	$kgm^{-1}s^{-1}$

π	Pi	-
ρ	Density	Kgm^{-2}
σ	Surface tension	Nm^{-2}
$\sigma_{\bar{x}}$	Standard deviation of the mean	-
σ_x	Standard deviation	-
ϵ	Stephan-Boltzmann constant	$Wm^{-2}K^{-4}$

Subscripts

Symbol	Definition
∞	Ambient
h	Hot surface
hot	Hot side
hp	Heat pipe
a	Adiabatic
av	Average
b	Boiling
c	Capillary
cap, max	Max Capillary limit
co	Condenser
$cold$	Cold Side
cr	Critical
cw	Calorimeter Wall
e	Evaporator
ent	Entrainment
f	Fluid
g	Gravity
l	Liquid
min	Minimum

<i>o</i>	Outer
<i>pw</i>	Pipe-wick interface
<i>r</i>	Radial
<i>s</i>	Solid
<i>sat</i>	Saturation
<i>sl</i>	Solid-liquid interface
<i>v</i>	Vapour
<i>w</i>	Wick
<i>wv</i>	Wick-vapour interface
<i>xs</i>	Cross-section
δ	Phase change

Publications

Thomas C. Werner, Yuying Yan, David Mullen, Elvedin Halimic, “Experimental analysis of a high temperature water heat pipe for thermal storage applications” Thermal Science and Engineering Progress, 2020

Thomas C. Werner, Yuying Yan, David Mullen, Elvedin Halimic, “Heat pipe for applications above 280°C” UK Heat Transfer Conference, 2019

Costa, S, Mahkamov, K, Kenisarin, M, Ismail, M, Halimic, E, Mullen, D, Lynn, K, & Werner, T. “Experimental and Numerical Study on Melting of Solar Salt in a Finned Metallic Container”, SME International Mechanical Engineering Conference, 2018

Publications in progress

Thomas C. Werner, Yuying Yan “A review of medium temperature heat pipe applications, challenges and future direction with an approach to fluid selection” Target journal: Applied Thermal Engineering or Case Studies in Thermal Engineering

Thomas C. Werner, Yuying Yan “Compatibility study of Antimony Trichloride with various refractory metals” Target journal: Journal of Material Science

Chapter I

Introduction

1.1 Outline and Background of research

Thermal management forms a fundamental part of most engineering products and industries. In modern day, heat regulation is a vital component to any high-power technology industry, including industries such as consumer/high power electronics, motor vehicle, aerospace, defence, power generation and medical devices. To advance, enhance, optimize and innovate new component designs in all these fields, the ability to conduct heat at high rates is vital. In this respect, the heat pipe has had a high interest in many applications requiring heat regulation due to its superior heat transfer qualities with ability to transfer heat at conductivity rates far beyond any conventional solid material. The heat pipe can be so effective, in fact, that it can even completely replace actively pumped cooling systems diminishing the system complexity and potential for failure while maintaining an equivalent rate of cooling.

Since the conception of the heat pipe in the 60s, their use has been abundant, particularly in space and electronics applications. From this, heat pipes were developed for use in every temperature range spanning cryogenic to exceptionally high temperature applications. Over this time, however, the development of heat pipes in a particular temperature range has proven exceptionally challenging due to the lack of conventional fluids which are able to operate in it. This is the ‘medium temperature range’, loosely spanning 300°C to 600°C. This range is dictated though the maximum working temperature of water heat pipes to the minimum working temperature of liquid metals such

as Lithium and Potassium. Within this range, there is a limited choice of fluids which can be used to cover this gap, and the fluids which are theoretically able, such as Mercury for example, is met with extreme production difficulties relating to wick wetting, compatibility with wall metals and worker safety in the filling process.

While some fluids are able to cover the upper or lower limits of the gap, their heat transfer capacity tends to be magnitudes lower than that of water or any liquid metal, reducing the effectiveness of the heat pipe and many present compatibility challenges with conventional metals. This study is aimed at analysing fluids which may be capable of operating over either a larger portion or all of the medium temperature range compared to currently studied fluids and develop the necessary equipment to be able to study these fluids in the medium temperature range. The outcome of this work intends to be a foundation by which novel fluids can be developed and tested for use in the medium temperature range using the framework and techniques proposed in this thesis.

1.2 Aims and Outcomes

This thesis has the aim of advancing research in the medium temperature range by creating analytical and experimental tools to identify and validate the most likely currently available fluids and metals to take forward into prototyping. In addition to this, the end results of this thesis are to provide a structure by which to rapidly identify and assess the viability of new experimental fluids which may be unveiled in future work.

The main objectives of the project are defined as follows:

1. Develop a new, more accessible and more extensive databases of fluid properties, metal properties and fluid/metal compatibilities.

During the initial phase of the project, it was noticed that there are no comprehensive databases available (at least publicly) which provide a meaningful overview of compatibility tests which have already been published and extensive and accessible fluid and metal properties which can be used for heat pipe modelling. This became the first project objective.

2. Develop a new heat pipe modelling code which can easily incorporate the databases.

To be able to predict the performance of a heat pipe containing any of the fluids and metals in the previously created databases, a heat pipe modelling program was created in MATLAB. This is the source of all predictive modelling graphs in this work.

3. Develop a framework by which fluids can be rapidly identified and selected for testing.

Heat pipe fluid selection for a specific application is very subjective. Each application (in any temperature range) may have different weightings and prioritisations which could see a benefit in identifying a selection of fluids and weighing their merits. This work proposes such a framework and outlines a process by which large databases of fluids can be scanned to find a handful of potential fluids for a specific application. This was developed initially to scan the large databases and identify the most suitable available fluid for the medium temperature range, but its benefits to industry were quickly realised and the process was adapted to cater for a wide range of temperatures and applications.

4. Perform extensive metal search and compatibility modelling to select likely compatible metals.

The next phase in creating a heat pipe after selecting a fluid is to select an adequate metal. In this work a few key metals were initially identified using the Citrix database of metals and alloys using key filters. From these metals, a compatibility model based on electromotive force potential is used to predict the compatibility of the shortlisted metals and fluids.

5. Develop methods and test rigs to perform compatibility tests and wettability tests on the selected fluids and metals.

Once a key fluid and metals were shortlisted, custom rigs were developed in order to assess short term compatibility and compare the wettability of the fluid on various

metal surfaces. The development of these rigs was unique due to the high reactivity nature of the selected fluid.

6. Develop a test rig which can support heat pipe testing in the medium temperature range.

In all partnering institutions, there was no test rig identified which could test heat pipe prototypes within the medium temperature range (300°C to 600°C). Hence a major part of this project was to conceive, design and construct a test rig which would be capable of this.

7. Validate the test rig at the lower end of the medium temperature range using water heat pipes.

To validate the constructed test rig, water heat pipes were used in the 300°C temperature range. The results from these experiments analysed the performance of water heat pipes around its boiling limit, something which there are limited studies covering.

1.3 Thesis structure

The thesis is arranged into nine chapters. Chapters 4 to 7 detail the original contributions to the field and contain published works. A brief description of each chapter follows:

Chapter 1 – Introduces the need for this research and the relevance to industry

Chapter 2 – A literature review of various aspects of heat pipe modelling and the previous work that has been done on medium temperature heat pipe development

Chapter 3 – Outlines all the experimental and numerical procedures and processes which were used throughout the thesis.

Chapter 4 – Details the creation of fluid, metal and compatibility databases. Outlines the processes developed to interact with the database and create the ‘fluid assessment framework’. Undertakes an extensive review of 350 inorganic fluids to select the optimal fluid to take forward for further testing. Models each shortlisted fluid to predict their heat transport capability in the horizontal orientation.

Chapter 5 – Outlines the major work undertaken in developing a custom medium temperature heat pipe test rig which is capable of testing heat pipe in the medium temperature range.

Chapter 6 – Details the compatibility and wettability tests undertaken on custom test rigs and presents the attained results.

Chapter 7 – Outlines testing with water heat pipes using the medium temperature test rig to analyse the performance of water heat pipes over its Boiling limit up to 320°C.

Chapter 8 – Details the suggested manufacturing strategies for developing a medium temperature heat pipe prototype using the identified fluids and metals. It also outlines attempts which were made at Thermacore to manufacture a first pass prototype and the difficulties that were met as well as how to overcome these in future.

Chapter 9 – A summary of the main conclusions and suggestions for future work.

Chapter II

Literature review

2.1 Introduction

Heat pipes can be described as structures of very high thermal conductance. Often referred to as super thermal conductors, they are used as means to distribute and/or dissipate heat within a physical system. They provide an excellent alternative to active cooling systems through their ability to conduct large heat fluxes from source to sink using only solid heat pipe structures. The distinct advantage of these is their light weight, reliability, minimal maintenance requirements and an extensive working life.

Currently heat pipes are used in a wide range of commercial applications such as aviation part cooling, communication systems heat management, CPU cooling, high power electronics cooling, power station heat exchange, satellite and spaceship thermal management, formula racing cooling systems, etc. The temperatures in which the heat pipes operate are generally categorized into three ranges; low (0 to 450 K), intermediate (450 to 725 K) and high (725 to 2500 K) [1]. The primary focus of this investigation is geared towards heat pipes in the intermediate range. There is currently very little option of effective working fluids for heat pipes in the 573 to 873 K temperature range (falling within the intermediate category). Various fluids which could theoretically work within the temperature range have been identified in prior research and some life tests have been performed. A review of current work which has been done in the intermediate temperature range and identification of areas which could be further explored in terms of working fluid analysis and testing will be highlighted.

The focus of the research will be evaluating the thermo-fluid properties, limitations and compatibilities of alternative fluids which can theoretically operate within the required temperature range. The initial stages are to determine which fluids are of interest to be further explored. This is determined through analysis of previous research done in the area together with a thermal transport assessment of each fluid. Later stages then analyse and compare application specific properties, such as the wettability, compatibility, thermal decomposition and reactivity of each shortlisted fluid.

The interest in pursuing the optimisation of heat pipes within the medium temperature range stems from the increased need for thermal management for applications operating at these temperatures. These include applications such as geothermal power harvesting, waste heat recovery, electronics cooling, fuel cell thermal management and nuclear power radiators. Hence, the development of effective heat pipes within the medium temperature range is of great interest to companies currently working in the thermal management field.

2.2 Concept and history of heat pipe

The first instance of the idea behind the modern Heat Pipe occurring was in 1942 when Gaugler, while assigned to General Motors Corporation, first filed for a patent outlining a 'heat transfer device' consisting of an evacuated tube and wick structure with working fluid inside proposed to be either ammonia, water or methyl/ethyl alcohols [2]. The invention, however, did not fully come into fruition until 1963 when Grover [3] independently developed what he refers to as a 'structure of very high thermal conductance' composed of a Niobium1% Zirconium evacuated tube with Lithium as the working fluid. Thus, the popularised modern heat pipe was born. The principal mechanisms and concepts behind this particular heat pipe are further detailed in the report by Cotter [4] in 1965.

Throughout the 1960's, various similar conceptions, using the same principals of passive heat transfer and heat pipe theory, began to emerge particularly within the Aerospace industry. This solidified its place as an industry standard means for highly effective heat transfer and management. As such, heat pipes started to become an area of interest for researchers and industry. This gave a rise to a rapid advancement in its capabilities by investigation and development into pipe hydrodynamics, fluid/metal compatibilities, capillary structures, manufacturing methods, shape design, etc. Since the operational requirements of a heat pipe tends to be application specific (for example different operating temperature ranges, different orientations relative to gravity/no gravity, minimum power conduction requirements, geometrical constraints, etc.) research and

development into design optimisation for numerous applications began to emerge. Nowadays, heat pipes have spread into a wide range of applications and numerous variations of this technology have spawned as a result. Some common types of heat pipe are highlighted in Figure 2-1.

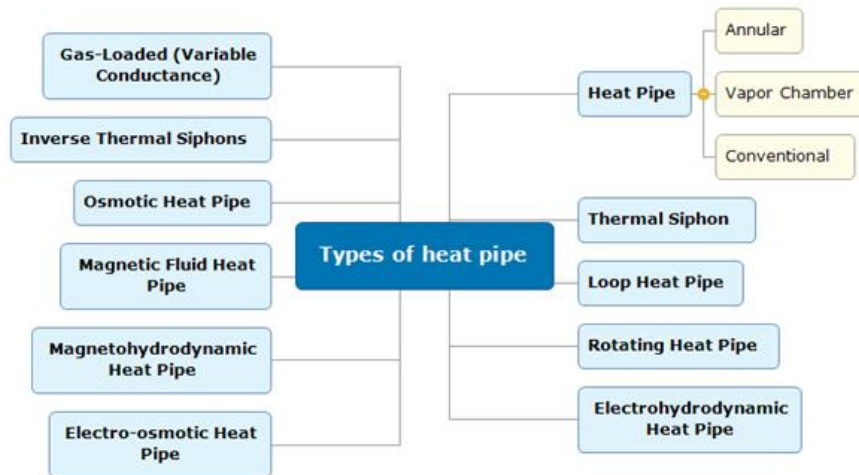


Figure 2-1 Variations of types of heat pipe developed over the years

In 1989 the 6th International Heat Pipe Convention took place, whereby three papers were published highlighting the developments of heat pipe technologies in the America's, Eastern Europe and Western Europe [5]–[7]. In these it was possible to analyse the research focus and direction each part of the world was heading in relating to heat pipe usage and development. Since then the technological landscape has vastly changed, but the general purpose of heat pipes in each industrial sector has maintained relatively stable. Adaptations to cater for new designs and technologies as well as more thorough and accurate modelling due to increased computational power have been the main advancements in the field since this period.

2.2.1 Classification of heat pipes

Generally, heat pipes can be classified into three main categories: low, medium and high temperatures. The low temperature category these include heat pipes spanning from cryogenic applications to most common applications using heat pipes at room temperature upwards to around 300°C. The medium temperature range as define by Anderson (2007) is a small window between where low temperature heat pipes reach their maximum capacity and high temperature heat pipes begin their minimum capacity temperature. This spans from around 300°C to 500°C. High temperature heat pipes are those which operate at temperatures above 500°C and generally consist of liquid metal working fluids. Figure 2-2 shows some of the principal working fluids currently in use and their useful temperature ranges. While heat pipes operating in the low and high temperature ranges are well established and are currently being produced for a huge range of applications spanning from satellite thermal management to nuclear waste heat recovery.

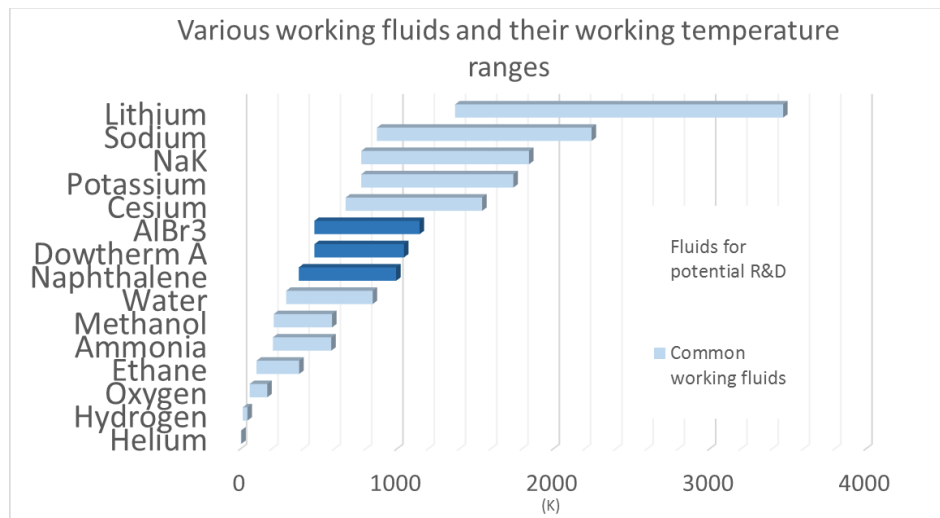


Figure 2-2 Principal working fluids for heat pipes spanning all working temperature ranges

High temperature heat pipes using liquid metal working fluids have long been established in applications such as nuclear heat exchangers, thermionic generators, industrial ovens, etc. These applications usually involve heat transfer at temperatures above 700 K. Metals such as Sodium, Potassium, Silver, Lithium and Caesium have all been well established in this temperature range. Their high surface tension and latent heat make them ideal heat pipe working fluids, capable of transmitting large heat fluxes and reaching effective thermal conductivities of up to 10^8 W/mK [8]. The main potential difficulty for such heat pipes lies in the start-up dynamics where the metal often must transition from solid to liquid first, requiring some level of pre-heating.

The medium temperature range spans from the highest effective temperature of water heat pipes and the lowest effective temperature of metal heat pipes, this is roughly 550 to 700 K. Thus far there are no thoroughly tested fluids which can definitively operate within this temperature range. Numerous studies have been conducted on potential fluids which could theoretically work within this range including fluid categories such as Halides, Elemental fluids and Organic fluids, but none have conclusively determined a viable fluid to take forward as standard.

2.3 Heat pipe theory and modelling

Although many different types of heat pipe exist with varying shapes, structures, functionality and design, the general principal behind the heat pipe remains the same throughout. All heat pipes are composed of an outer metal structure (the heat pipe wall) with a two-phase working fluid within. When a temperature difference is applied across the structure, the fluid circulates by evaporation and condensation at each end of the pipe. The vapour phase flows through the void within the pipe (also referred to as a vapour chamber) from the evaporator region to the condenser region and the condensed liquid phase is pumped back through various means depending on the type of heat pipe at hand.

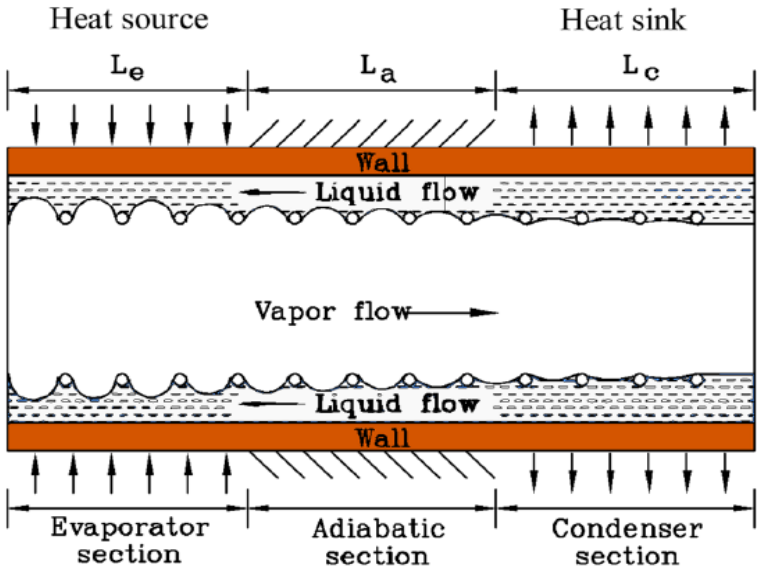


Figure 2-3 The internal liquid/vapour interface of a heat pipe. Source: [9]

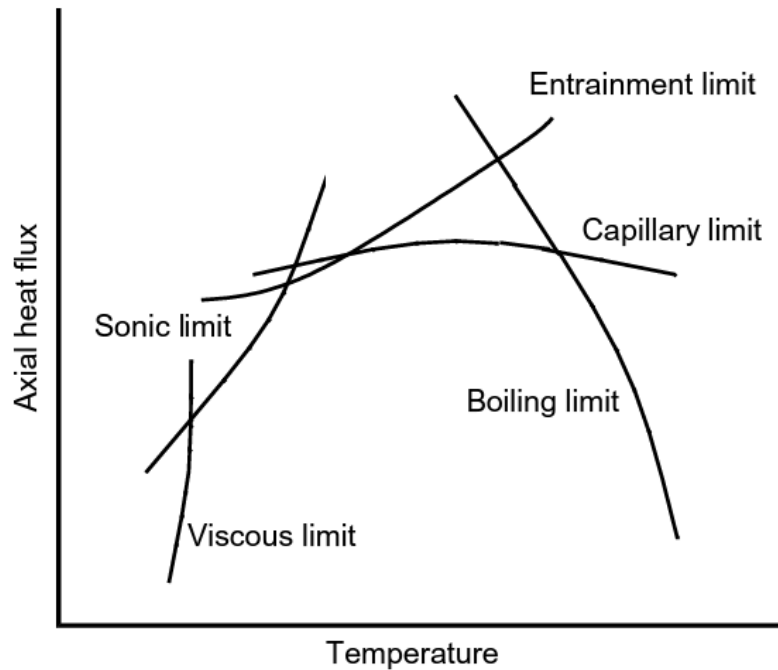


Figure 2-4 Heat transport operating limits for standard capillary driven heat pipes. Source: [10]

The principal method of liquid phase delivery is through capillary action in the wick structure of the heat pipe. Other methods used to pump the liquid phase back include; osmosis, electro-hydrodynamics, electro-osmosis and magneto-hydrodynamics [9]. The focus of this study is on conventional heat pipes as first described by Grover [3].

The heat pipe is divided into three sections: the evaporator section, the adiabatic (transport) section and the condenser section. External heat applied to the evaporator region is conducted through the wall and wick structure causing the liquid within the wick to vaporise. The vapour then travels through the adiabatic region to the condenser driven by the pressure differential caused by the vapour influx. The vapour then transfers its energy in the form of latent heat to the heat sink causing condensation.

The condensed liquid seeps into the porous wick structure and is driven back to the evaporator region through capillary action. Throughout the spread of liquid in the wick, the meniscus of the liquid at the liquid-vapour interface tends to recede into the pores as it travels from the condenser back to the evaporator as demonstrated in Figure 2-3. This difference in curvature is caused by the capillary pressure change across the heat pipe.

The heat transport capacity of the heat pipe is determined through the fluid properties. The functionality of the fluid is determined by a set of limitations as described in Figure 2-3. These set the boundary for the maximum heat flux which can be applied to the heat pipe at a given temperature before it loses its heat transportation capabilities. These form the principal operational assessment of the working fluid to predict its heat transport capacity before conducting compatibility and life tests on the heat pipe. Each of these limitations can be quantified as demonstrated by Reay and Kew (2006) [1] and Faghri (1995) [11]. These will be further explored in this chapter.

Overall, there are many factors contributing to the functionality of the heat pipe. Many of these different aspects are phenomena which have been analysed and studied extensively on their own, such as flow in porous media, multiphase flow, thermo-fluid heat transport, pool boiling on porous surfaces, evaporation/condensation modelling and solid-state heat conduction. In order to make a prediction of the performance of new working fluids based on their property data, a combination of these theories should be used. In the following sections, the basic concepts and theories for each aspect of the heat pipe is

outlined in order to gain a complete understanding of the system. The subject areas to be explored are divided up as seen in Figure 2-5.

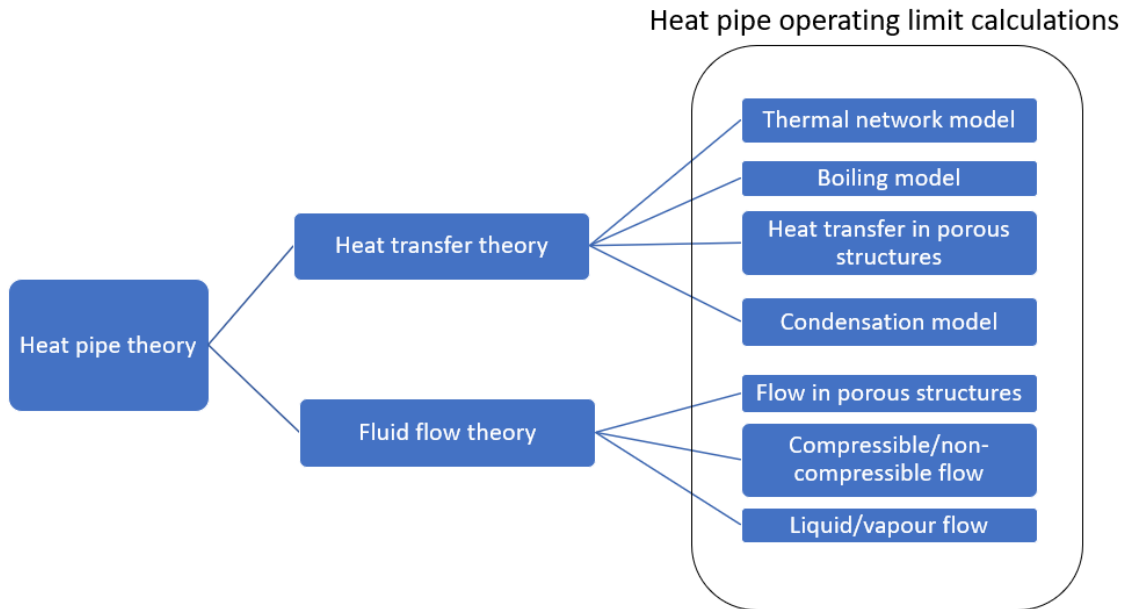


Figure 2-5 Heat pipe theory topic structure overview

2.3.1 Fluid Flow

The fluid flow within a heat pipe has two components: the vapour flow and the liquid flow. The vapour phase is modelled as a gas flow in a pipe or channel. The walls tend to have a high roughness due to the coarse nature of the wick structure. This can contribute to higher vapour pressure drops across the pipe. The liquid phase is reliant on its surface tension and ability to wet the wick structure in order to successfully flow. The study of fluid flow through porous media is utilised to characterise the capillary action and pressure losses in the liquid flow. The liquid/vapour interface is also a subject of great

interest. The interaction at this boundary is a key element to determining the nature of the flow and pressure drops within each of the phases.

It is clear that modelling of such devices includes studies such as two-phase flow in a pipe, flow through porous media and liquid/vapour interface modelling. The following section will highlight the main flow theory describing both the vapour and liquid flows showing how to characterise and quantify key operational parameters and describe the typical flow behaviours.

2.3.2 Pressure Distribution

The internal pressure changes during the heat pipe start-up and operation are of vital importance to its functionality. Faghri (1995) [11] states that the vapour pressure change across the heat pipe can be associated to friction, inertia/blowing from evaporation and suction from condensation. The liquid pressure along the pipe changes mainly as a result of friction. The axial variation of both the liquid and vapour pressures are outlined in Figure 2-6. These figures represent the variation in vapour and liquid pressure throughout the heat pipe under 3 main operating modes: low, moderate and high evaporator heat flux which in turn equate to low, moderate and high vapour flow rates respectively. As can be seen, at low vapour flow rates the vapour pressure tends to plateau along the condenser region, whereas at higher flow rates there is some pressure recovery present along the condenser region due to the reduction in mass flow rate from condensation and hence, the inertial term of the flow would be negative. The liquid pressure drop is proportional to the permeability and area of the wick following Darcy's law. The total

capillary pressure required to overcome the liquid and vapour losses is therefore the sum of the two pressure drops. As can also be observed in Figure 2-6, gravitational forces directly affect the liquid pressure drop, hence in a gravitational field, the capillary pressure must be larger in order to overcome the additional liquid pressure drop.

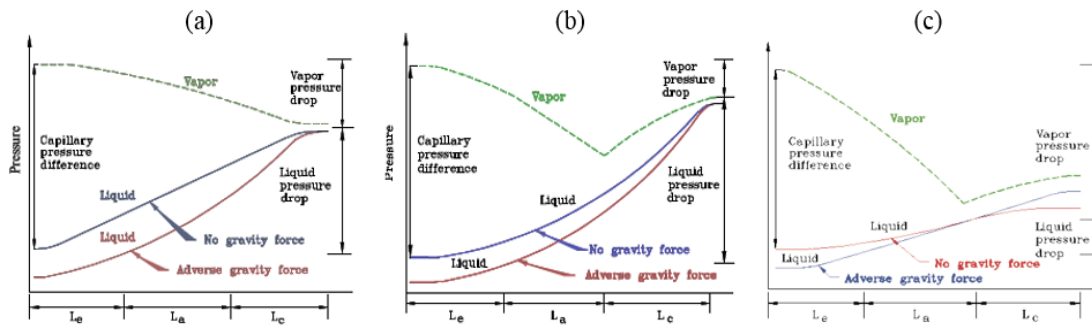


Figure 2-6 Axial pressure variation at a) low vapour flow rates b) moderate vapour flow rates c) high vapour flow rates. Source: Faghri (2012) [9]

For the heat pipe to function, the capillary pressure must be equal or greater than the sum of the losses incurred in the vapour and liquid phases as well as any gravitational potential work done. As demonstrated in Figure 2-6 (b), during moderate vapour flows, the dynamic effects cause a vapour pressure recovery across the condenser. Grover et. al. (1966) [3] successfully demonstrated this heat recovery using a sodium heat pipe and achieving up to 60% pressure recovery. When considering the pressure drop in the condenser region, however, it is usual to assume there is no net pressure drop or gain should the vapour pressure change greatly exceed the liquid pressure change in the condenser [10].

Since there is a clear variation in temperature and pressure across the pipe while in operation, it is reasonable to assume that a two-dimensional analysis would be required to accurately describe the mechanisms in play. Indeed Bankston et al. [12] and [13] were early researcher to use numerical methods to solve the associated Navier-Stokes equations. The work shows that at high evaporation and condensation rates, a reversal of axial flow can occur at $Re > 2.3$. Despite this, it was shown that a one-dimensional analysis yields good results for $Re < 10$ [12].

There are three main types of pressure drops in the vapour phase; the evaporator drop (ΔP_{ve}), the adiabatic drop (ΔP_{va}) and the condenser drop (ΔP_{vc}). In the evaporator and condenser regions, the pressure drops are a direct result of evaporation and condensation respectively, hence, there is a direct relation to the radial flow of the fluid. Assuming the vapour is modelled as an incompressible flow (i.e. the flow velocity is small compared to the speed of sound, $Ma < 0.3$), the relation between the radial Reynolds number, Re_r , and the heat input per unit length was described by Busse (1967) [14] as seen in Figure 2-7, where the radial Reynolds number is defined as ratio of inertial to viscous forces in the radial direction of the wick structure:

$$Re_r = \frac{\rho_v v_r r_r}{\mu_r} \quad 1$$

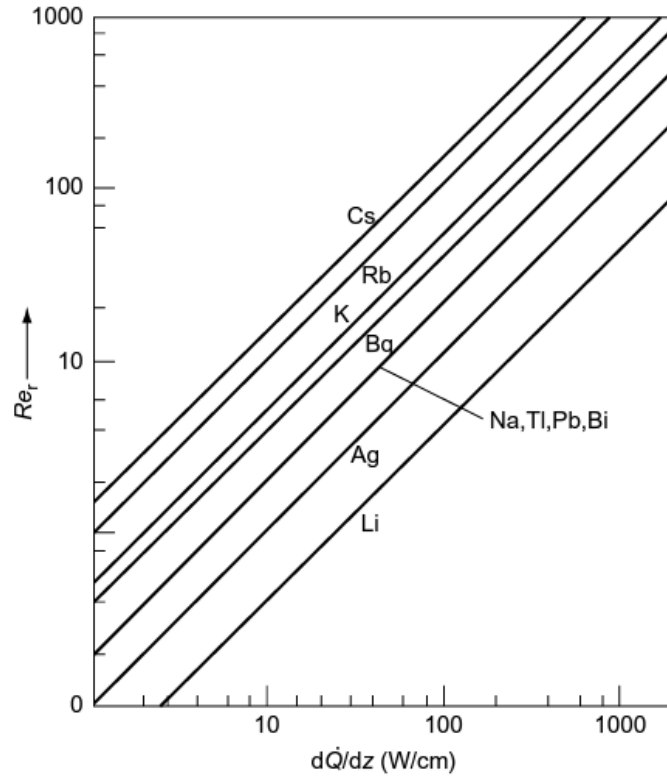


Figure 2-7 Radial Reynolds number vs heat input p / length of heat pipe. Source: [13]

Through a one-dimensional numerical analysis of all three pressure drops, Busse[14] reached the flowing expression to describe the total vapour pressure drop across the pipe:

$$\Delta P_v = \left(1 - \frac{4}{\pi^2}\right) \frac{\dot{m}}{8\rho_v r_v^4} + \frac{8\mu_v \dot{m} l_a}{\pi\rho_v r_v^4} \quad 2$$

The assumptions made may be considered invalid at start-up and in the case of high temperature liquid metal pipes.

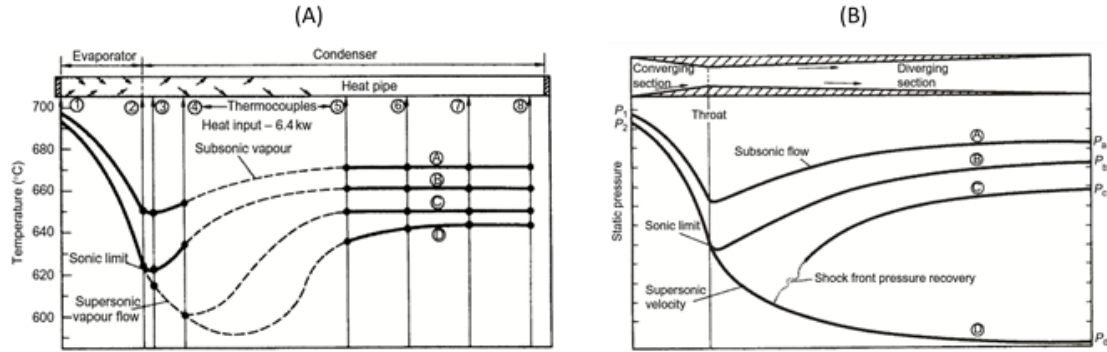


Figure 2-8 Graphs of (A) The temperature profile of a Sodium heat pipe and (B) The pressure profile across a converging/diverging nozzle. Source: [15]

In the cases where the vapour must be modelled as a compressible flow, Deverall et al. [15] pointed out that the vapour flow resembles that of a gas flowing through a converging-diverging nozzle. The axial mass flow increases along the evaporator region up to a maximum value. The vapour velocity then decreases along the adiabatic and condenser sections. A graphical representation of this observation is demonstrated in where Kemme (1968) [16] used a sodium heat pipe transmitting 6.4 kW of energy and using varying argon-helium ratios to alter the thermal resistance.

The curves represented in Figure 2-8 (A) are as follows:

- A: Subsonic flow with pressure recovery
- B: Sonic flow at end of evaporator, choked flow
- C: Further reduction of condenser pressure (by cooling), choked flow
- D: Further reduction of condenser pressure (by cooling), choked flow

Deverall (1970) [15] conducted a one dimensional analysis on this study and found that it provided a good description of the fluid behaviour. It was found that the heat flow through the heat pipe is expressed as:

$$\dot{Q} = \frac{\rho_v A C_o L C}{\sqrt{2(\gamma + 1)}} \quad 3$$

Where C_o is the sonic velocity of the vapour corresponding to its stagnation temperature, T_o and C is the compressibility parameter (choked flow at $M = 1$).

2.3.3 Wick structure

The flow through wicks tends to be a laminar flow in most cases. A modified version of the Hagen-Poiseuille equation, considering small interconnected channels, is used to model the flow. In general, there are three main types of wick capillary geometry:

- i. Interconnecting homogenous porous structures (gauzes, felts, sintered wicks, etc.)
- ii. Open groves
- iii. Composite wicks (a combination of groves and fine mesh)

Each wick type uses a unique variation of the Hagen-Poiseuille to account for the different geometrical structures and in some cases with the presence of correction factors.

Figure 2-9 demonstrates some common wick sections used. The relevant equations for pressure loss through each wick type can be seen in Table 2-1.

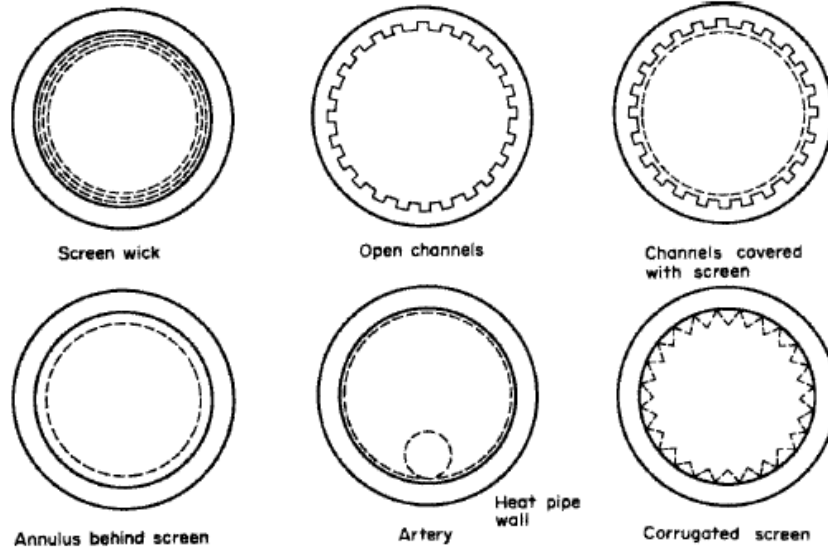


Figure 2-9 Common wick sections. Source: [1]

Table 2-1 Liquid pressure drop expressions for various wick types. Source: [1]

Flow type	Equation	Reference
Homogenous wicks	$\Delta P_l = \frac{b\mu_l \dot{Q} l_{eff}}{\pi(r_w^2 - r_v^2)\epsilon r_c^2 \rho_l L}$	Derived from the Heigan-Poiseuille equation [1]
	OR	
	$\Delta P_l = \frac{\mu_l \dot{m} l_{eff}}{\rho_l k A}$	Derived from Darcy's law [1]
	OR	
	$\Delta P_l = \frac{150\mu_l(1 - \epsilon')^2 l_{eff} u_l}{D^2 \epsilon'^3}$ (for laminar flow only)	Derived from the Heigan-Poiseuille equation with correction factors by Blake & Kosenev [1], [17]
Longitudinal wicks	groove $\Delta P_l = \frac{8\mu_l \dot{Q} l}{\pi \left(\frac{1}{2} D_e\right)^4 N \rho_l L}$	Derived from the Heigan-Poiseuille equation [1]
Composite wicks	$\Delta P_l = \frac{6\mu_l \dot{Q} l}{\pi r_v \delta_{an}^3 \rho_l L}$	Derived from the Heigan-Poiseuille equation [1]

2.3.3.1 Liquid/vapour interface

The focal point of studies involving the liquid/vapour interface in a heat pipe is surrounding the entrainment limitation. Grover [18] points out that the physical characteristics of the wick (pore size, spacing and weave) tend to impose a periodic pattern on the interface. It is known that for Weber numbers greater than one, waves tend to grow exponentially, causing high probability of entrainment occurring. A studies by Kemme et al. shows that very fine screen meshes tend to suppress entrainment [16]. It is uncommon, however, that a heat pipe would need to be operated close to its entrainment limit. The Weber number is defined as the ratio of drag to cohesion forces:

$$We = \frac{\rho v^2 l}{\sigma} \quad 4$$

2.3.3.2 Conductivity of wicks

When in operation, wick structures consist of a porous media with a fluid occupying the pores. For this reason, the conductivity of the wick is a function of the pore and fluid properties in accordance with its void fraction. The void fraction is a ratio between the volume occupied by the fluid and the total volume of the wick. Chisholm [19] describes that when the fluid and wick are modelled in parallel, the effective thermal conductivity of the structure becomes

$$\lambda_{eff} = \varepsilon \lambda_l + (1 - \varepsilon) \lambda_w \quad 5$$

If the fluid and wick are modelled perpendicular to each other, then the effective conductivity becomes

$$\frac{1}{\lambda_{eff}} = \frac{\varepsilon}{\lambda_l} + \frac{(1 - \varepsilon)}{\lambda_w} \quad 6$$

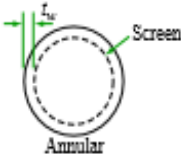
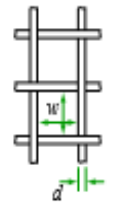
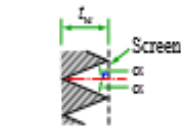
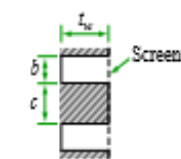
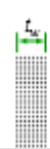
If modelled in series. While these equations are useful to provide upper and lower limitations of the wick conductivity, often they do not represent the true conductivity of the structure. This is particularly true when the conductivities of the wick and the fluid are vastly different from one another. Table 2-2 shows improved equations for different mesh types which have been developed over various journal papers.

For further analysis of wick structures, Chisholm [19] also various properties are used to describe the structure such as the minimum capillary radius and the permeability. The minimum capillary radius helps to describe the pore structure of complex wicks. This is given as:

$$r_c = \frac{2\sigma \cos \theta}{\Delta P_c} \quad 7$$

This quality can also be measured experimentally using the ‘rising column’, ‘falling column’ or ‘bubble test’ methods. These all use the maximum capillary difference Δp_c to determine the minimum capillary radius and often presume a contact angle of zero.

Table 2-2 Alternative conductivity equations for other mesh types. Source: [19]

Wick Type*		Thermal conductivity		Porosity
		Equation†	Derivation Numbers (see Section 6)	
Single-layer wire mesh screens (heat-pipe axis in plane of paper in this sketch)		$\lambda_w = \lambda_f$	—	$z = 1$
 $\frac{1}{N} = d + w$ N = number of apertures per unit (m) of screen	 Screen-covered grooves (isosceles triangle)	$\lambda_w \approx 0.85\lambda_s [\lambda_f / (\lambda_s \sin \alpha)]^{0.63}$	18, 31	$z = 0.5$
	 Screen-covered grooves (rectangle)	$\lambda_w \approx z\lambda_f + (1-z)\lambda_s$	26, 28	$z = \frac{b}{b+c}$
	Multiple wire mesh screens‡, plain or sintered (screen dimensions as for single layers illustrated above)	$\lambda_w \approx \frac{\lambda_f[\lambda_f + \lambda_s - (1-z)(\lambda_f - \lambda_s)]}{\lambda_f + \lambda_s + (1-z)(\lambda_f - \lambda_s)}$	19, 21, 25, 26	Best obtained experimentally, but can be estimated from the equation for single screens $z \approx 1 - \frac{\pi Nd}{4}$
	Unconsolidated packed spherical particles (d = average particle diameter)	Plain	$\lambda_w \approx \frac{\lambda_f[2\lambda_f + \lambda_s - 2(1-z)(\lambda_f - \lambda_s)]}{2\lambda_f + \lambda_s + (1-z)(\lambda_f - \lambda_s)}$	4, 26
		Sintered	$\lambda_w \approx \frac{\lambda_s[2\lambda_s + \lambda_f - 2z(\lambda_s - \lambda_f)]}{2\lambda_s + \lambda_f + z(\lambda_s - \lambda_f)}$	19, 21, 28
	Sintered felted metal fibres‡ (d = fibre diameter)	$\lambda_w \approx z^2\lambda_f + (1-z)^2\lambda_s + \frac{4z(1-z)\lambda_f\lambda_s}{\lambda_f + \lambda_s}$	11, 19, 22, 30, 33	Obtain z experimentally or use manufacturer's data

* In the sketches the axis of the heat pipe and therefore the direction of fluid flows are normal to the plane of the paper unless stated otherwise.

† Figures in brackets refer to notes in Section 7.2.

‡ These wicks are positioned so that the layers follow the contour of the inner surface of the heat-pipe wall.

The permeability of the wick is a direct function of the size and shape of the porous channels. By assuming a laminar flow (and therefore negligible inertial effects) the permeability of an object is independent of flow rate and the nature of the liquid. The permeability of wicks is usually anisotropic when comparing the axial to radial permeabilities. When assessing the pressure drop in the liquid phase, only the axial permeability is considered [1], [19] and is measured through:

$$K = \frac{l\dot{m}\mu_l}{A_w\Delta P_l\rho_l} \quad 8$$

More accurate permeability values for specific wick structures can be determined experimentally. These usually are measure through a constant mass flow whereas heat pipes in operation tend to experience a varied mass flow along its length with maximum mass flow occurring at the adiabatic section. This maximum mass flow rate together with effective evaporator and condenser lengths are usually used to determine the Reynolds number and pressure drops along the pipe. It is approximated that the maximum flow rate is equal to the overall rate of heat transfer divided by the latent heat of vaporisation [20], [21] (assuming no or negligible heat losses).

$$\dot{m} = \frac{\dot{Q}}{h_{fg}} \quad 9$$

Where the Reynolds number is defined as the ratio of inertial to viscous forces in a flow:

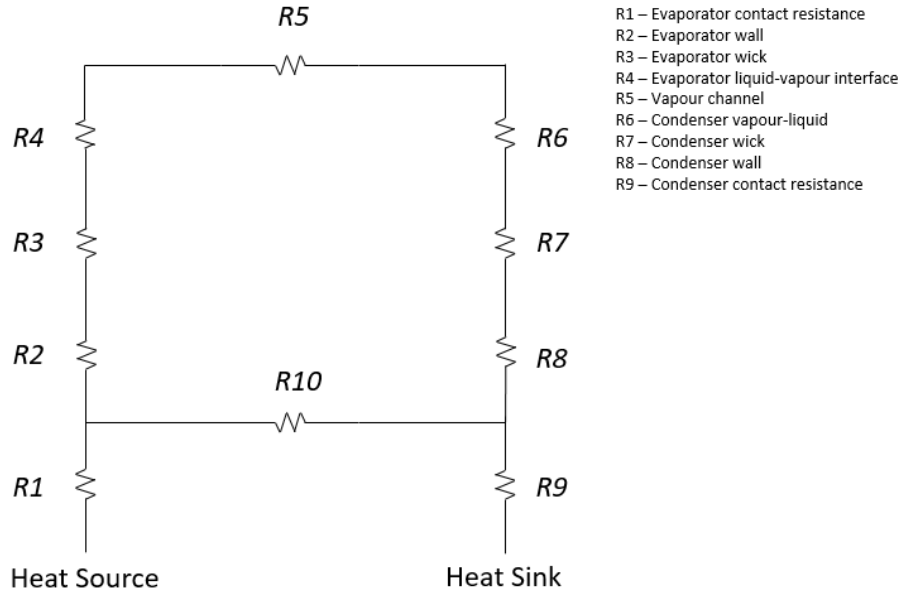
$$Re = \frac{\rho u D}{\mu} \quad 10$$

2.3.4 Thermal network

The heat transfer modelling of a heat pipe can be divided into two categories: 1D/2D heat conduction modelling (by modelling the pipe as a solid material with an equivalent conduction coefficient) and 3D two-phase thermo-fluid modelling (by modelling the two-phase fluid within the pipe hence the behaviour of the heat transfer fluid). The modelling of two phase fluids in simple thermosiphon systems (with no wick structures) have been explored by Fadhl (2013, 2015) using a Volume of Fluid (VOF) Ansys Model with user-defined code functions for modelling of the phase change [22], [23]. Arab and Abbas (2014) [24] propose a reduced order model to predict the impact of changing the working fluid in trapezoidal micro-grooved heat pipes. These more complex modelling methods may be explored in future to enable a prediction of the heat pipe performance using various previously untested fluids. The basic heat transfer principals, however, can still be applied to these devices where the pipes are modelled as one-dimensional solid objects with equivalent conductivities. Hence, the overall thermal resistance of the heat pipe can be defined through equation 11.

$$R = \frac{T_{hot} - T_{cold}}{\dot{Q}} \quad 11$$

Additionally, the total conductivity of the system can be broken down into its various components for a fuller understanding of the thermal resistance throughout the system. details the individual resistive components involved in the thermal resistance network.



Thermal Resistance	Expression
R_1	$\frac{1}{h_e S_e}$
R_2	$\frac{\log_e \left(\frac{r_o}{r_i} \right)}{2\pi l_e \lambda_x}$
R_3	$\frac{\log_e \left(\frac{r_i}{r_v} \right)}{2\pi l_e \lambda_w}$
R_4	$\frac{\sqrt{RT_{eff}^3 / 2\pi}}{L^2 l_e r_i \rho_v}$
R_5	$\frac{T_{eff} \Delta P_v}{LQ \rho_v}$

R_6	$\frac{\sqrt{RT_{eff}^3/2\pi}}{L^2 l_c r_i \rho_v}$
R_7	$\frac{\log_e \left(\frac{r_i}{r_v} \right)}{2\pi l_c \lambda_w}$
R_8	$\frac{\log_e \left(\frac{r_o}{r_i} \right)}{2\pi l_c \lambda_x}$
R_9	$\frac{1}{h_c S_c}$
R_{10}	$\frac{l_e + l_a + l_c}{A_x \lambda_x + A_w \lambda_w}$

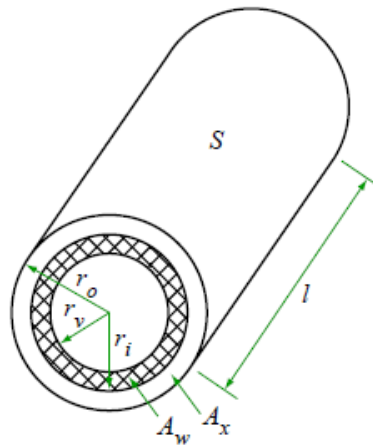


Figure 2-10 Thermal resistance network model for a Heat Pipe. Source: [19]

Zuo et. al. (1998) [25] uses this thermal resistance network model to predict the transient behaviour of the heat pipe using first-order linear ordinary differentials. Using this resistance model, it is possible to calculate the individual resistive expressions at each point.

2.3.5 Working limitations of heat pipes

The operating limitations of a heat pipe are the primary numerical analysis methods used to determine its suitability for operation. They also serve to predict the performance of a given heat pipe when making any fundamental changes to the structure (e.g. shape, dimensions, porosity, working fluid, etc.). These are the starting points to designing and building any heat pipe structure necessary for an application. Here each of these limitations will be described and numerically evaluated through one dimensional empirical equation.

2.3.5.1 Capillary limit

The capillary limit is the minimum capillary force required to ensure the full wetting of the wick. This acts as the returning mechanism for the liquid phase from the condenser to the evaporator. The capillary pressure must be greater than or equal to the sum of pressure losses along the vapour-liquid path [1], [11], [20], [21].

$$\Delta P_c \geq \Delta P_l + \Delta P_v + (\Delta P_{e,\delta} + \Delta P_{co,\delta}) + \Delta P_g \quad 12$$

The maximum capillary pressure attainable is dependent on the physical properties of both the wick and the fluid. Faghri et. al. [11] derives that for a cylindrical heat pipe where the vapour flow can be approximated to a laminar and incompressible flow and the wet point is located at the beginning of the condenser section (also neglecting the pressure

drops due to evaporation and condensation due to negligible pressure differences) the equality shown in equation 12 can be expressed as

$$\frac{2\sigma}{r_c} \geq \frac{\mu_l(\dot{Q}l)_{cap,max}}{\rho_l A_w K h_{fg}} + \frac{4\mu_v \dot{Q}_e}{\pi \rho_v r_v^4 h_{fg}} \left[L_e \left(1 + \frac{FRe_r}{2\pi \mu_v l_e h_{fg}} \right) + 2L_a \right] + \rho_l g (l_e + l_a) \sin \theta \quad 13$$

Assuming there is an equal heat distribution along the heat pipe and the evaporation and condensation rates are in equilibrium (i.e. $\dot{m}_l = \dot{m}_v = \frac{Q(z)}{h_{fg}}$), where $(QL)_{cap,max}$ is the ‘heat transport factor’ as described by Faghri et al. [11]. For a laminar incompressible flow where the wet point is near the condenser end cap the equation is expressed as

$$\frac{2\sigma}{r_c} \geq \left(\frac{\mu_l}{\rho_l A_w K h_{fg}} + \frac{16\mu_v}{2\rho_v r_v^2 h_{fg} A_v} \right) (\dot{Q}L)_{cap,max} + \rho_l g L_t \sin \theta \quad 14$$

In cases where vapour compressibility is contributing factor or the liquid permeability/flow area are not constant, an alternative numerical evaluation is used

$$\frac{2\sigma}{r_c} - \int_0^{l_{min}} \rho_l g \sin \theta dz \geq \int_0^{l_{min}} \frac{\mu_l \dot{m}_l(l)}{\rho_l h_{fg}} A_w K dz + \Delta p_v \quad 15$$

Where l_{min} is the location of the wet point (usually can be assumed to be at the end cap).

2.3.5.2 Boiling limit

When referring to the upper temperature limitation of heat pipes, it is largely driven by the boiling phenomenon and is derived by calculation of the critical heat flux of the fluid on a particular surface. While the terminology ‘Boiling limit’ is often used in literature to match the terminology used in all other heat pipe limitations, this can generally be used interchangeably with ‘critical heat flux’. The term ‘Boiling limit’ therefore acts as a general term covering all variation of mechanisms which can cause the critical heat flux to be reached over a wide range of wick and heat pipe types.

Various empirical correlations have been defined to describe the boiling phenomenon within different types of wick structures. In general, it was found that boiling a liquid from a porous surface required much lower wall superheating due to the excess of nucleate sites. A study by Marto et al. [26] analysed this phenomenon by observing pool boiling from various metallic porous surfaces. Experiments conducted by [8] using a sodium compound wicked heat pipes showed that the heat fluxes reached at the evaporator wall were three times higher than the critical heat fluxes under pool boiling conditions. The actual boiling limit was not determined as the experiment was limited by the melting temperature of components in the apparatus.

The boiling limit has been widely studied for a variety of surface conditions and wick types [27], however, it remains a notoriously difficult limit to predict with certainty due to the ‘random’ nature of the boiling phenomena and the number of factors which can

affect it (porosity, permeability, surface finish, capillary potential, etc.). Various empirical correlations have been defined to describe the boiling phenomenon within different types of wick structures, surface conditions and geometries. In general it was found that boiling a liquid from a porous surface required much lower wall superheating due to the excess of nucleate boiling sites [28]. A study by Marto et. al. [26] analysed this phenomenon by observing pool boiling from various metallic porous surfaces. Experiments conducted by Ivanovskii et. al. [8] using sodium compound wicked heat pipes showed that the heat fluxes reached at the evaporator wall were three times higher than the critical heat fluxes under pool boiling conditions. Several authors have proposed relationships to predict the critical heat flux under approximate conditions found inside a heat pipe [1], a summary of the principal correlations considered for this study is presented in Table 2-3.

Table 2-3 Empirical boiling correlations

Author	Correlation
Rohsenow and Griffith [29]	$q_{cr} = 0.012L\rho_v \left(\frac{\rho_l - \rho_v}{\rho_v} \right)^{0.6}$
Caswell and Balzhieser [30]	$q_{cr} = 1.02 \times 10^{-6} \frac{L^2 \rho_v k_l}{c_p^y} \left(\frac{\rho_l - \rho_v}{\rho_v} \right)^{0.6} Pr^{0.71}$
Ferrell et. al. [31]	$q_{cr} = \frac{g \left(h_{co} \rho_l \left(\frac{\sigma_l}{\sigma_{lo}} \right) - \rho_l l \sin \theta \right)}{\frac{l_e \mu_l}{h_{fg} \rho_l k d} \left(\frac{l_e}{2} + l_a \right)}$
Ferrell et. al. [31]	$q_{cr} = \frac{g \left(h_{co} \rho_l \left(\frac{\sigma_l}{\sigma_{lo}} \right) - \rho_l l \sin \theta (1 + \alpha_t \Delta T) \right)}{\frac{l_e \mu_l}{h_{fg} \rho_l k d (1 + \alpha_t \Delta T)} \left(\frac{l_e}{2} + l_a \right)}$
Ivanovskii et al [8]	$q_{cr} = \frac{4\pi l_e \lambda_e T_v \sigma_l}{h_{fg} \rho_v \ln \frac{r_i}{r_v}} \left(\frac{1}{r_n} - \frac{1}{r_{eff}} \right)$

The boiling limit chosen for the study in Chapter 7 is that by Ivanovskii et. al. [8] as this is most commonly used for mesh type wicks [1]. The equation is a derivation of the critical heat flux for an equivalent planar mesh surface is commonly used in the heat pipe field by numerous authors including Chi [32] and Faghri [11]. The re-arrangement of the equation to determine the maximum heat transfer rate is presented in Equation .

$$Q_b = \frac{2\pi l_e k_e T_v}{h_{fg} \rho_v \ln\left(\frac{r_i}{r_v}\right)} \left(\frac{2\sigma}{r_n} - P_c \right) \quad 16$$

Where ‘ r_n ’ indicates the maximum nucleation radius (i.e. the maximum bubble radius which can be released from the wick structure pores). This equation is a representation of the heat transfer rate required to maintain equilibrium vapour bubbles of radius ‘ r_b ’ within the wick. Depending on surface conditions and presence of dissolved gas, the nucleation radius has a finite value, ‘ r_n ’, to which bubbles will begin to grow within the wick structure and form film boiling conditions. The nucleation radius largely relies on empirical data to be determined and have a large variance from wick to wick. One estimation method would be to use the pore size of the wick as the maximum nucleation value, depending on the homogeneity of the wick, however, this could present a large error. As mesh wick is used in this study, the porosity can indeed have a lot of variance. The approach in this case was to match a range of ‘ r_n ’ values to the acquired data. Using this approach, the average value of the range can be used for future predictions using the

designated wick structure or a maximum and minimum range value can be determined depending on the application.

Boiling limit derivation and the nucleation radius

The boiling limit equation is highly dependent on two processes: the formation of bubble (nucleation) and the subsequent growth and motion of those bubbles. The maximum nucleation radius presented in equation denotes the finite radius at which the vapour bubbles will begin to collapse within the wick structure [32]. This equation is derived from the equation of a bubble at equilibrium, where the one-dimensional analysis of the forces present at the bubble boundary can be resolves as:

$$\pi r_b^2 (P_{sat} - P_l) = 2\pi r_b \sigma \quad 17$$

Where ‘ r_b ’ is the bubble radius, ‘ σ ’ is the surface tension, ‘ P_{sat} ’ is the saturation vapour pressure at the pipe-wick interface and ‘ P_l ’ is the liquid pressure. Assuming that the capillary pressure at any point along the heat pipe is equal to the sum of the liquid pressure and vapour pressure at that point, this equation can be rearranged to:

$$\pi r_b^2 (P_{sat} - P_v + P_c) = 2\pi r_b \sigma \quad 18$$

The Clausius-Clapeyron equation relating temperature and pressure along a saturation line states that:

$$\frac{dP}{dT} = \frac{L\rho_v}{T_v} \quad 19$$

Where ‘ L ’ is the latent heat capacity, ‘ ρ_v ’ is the vapour density and ‘ T_v ’ is the vapour temperature. Using this equality, the term $(P_{sat} - P_v)$ in equation can be converted to represent the temperature change across the wick structure.

$$T_{pw} - T_{wv} = \frac{T_v}{L\rho_v} \left(\frac{2\sigma}{r_b} - P_c \right) \quad 20$$

Where ‘ T_{pw} ’ is the temperature at the pipe-wick interface and ‘ T_{wv} ’ is the temperature at the wick-vapour interface. The term ‘ $T_{pw} - T_{wv}$ ’ therefore denoted the temperature difference across the wick structure. Using conduction theory for heat transfer across cylindrical structures (assuming there is a uniform heat flux across the evaporator section) the temperature difference across the wick can also be defined as:

$$T_{pw} - T_{wv} = \frac{Q \ln \left(\frac{r_i}{r_v} \right)}{2\pi l_{eff} k_{eff}} \quad 21$$

Hence by combining equation with equation , the maximum heat transfer at the evaporator can be represented as:

$$\dot{Q} = \frac{2\pi l_{eff} k_{eff} T_v}{L \rho_v \ln\left(\frac{r_i}{r_b}\right)} \left(\frac{2\sigma}{r_b} - P_c\right) \quad 22$$

This equation therefore represents the heat transfer rate required to maintain vapour bubbles at radius ‘ r_b ’ in equilibrium in the heat pipe wick structure [32]. The term ‘ r_b ’ can then be replaced by ‘ r_n ’, the initial bubble radius at its formation in order to assign a finite value. Hence, if the thermal load exceeds the calculated value, bubble will begin to form and grow in the wick structure. Griffith and Wallis [33] used water immersed copper sheets to estimate the r_n values on plane surfaces with the presence of non-condensable gasses. The experiments concluded that for those conditions the nucleation radius can vary from 10E-4 to 10E-3 inches. The presence of non-condensable gasses, however, greatly affect this value and may differ significantly in degassed systems (such as conventional heat pipes). Marcus [34] has observed ‘ r_n ’ values between 10E-5 and 10E-6 when analysing conventional degassed heat pipes but states that “The consequences of wick boiling depends on the nature of the wick used”. Surface features which may influence the maximum nucleation radius include:

- Surface finish and uniformity
- Wick pore size and uniformity
- Surface to wick interface
- Wick to wick layer interface (if using meshed wick)

Griffith et al. [33] observes that the surface conditions generally affects the boiling process in two ways; through altering the bubble shape, size and frequency and affecting the amount of superheat needed to initiate bubble growth. The latter tends to be the main focus of studies which analyse the effect of varying surface conditions. An approximate solution to the estimated nucleation radius assuming ideal surface conditions can be calculated from the fluid properties using the nucleation theory [34].

$$r_n = \sqrt{\frac{2\sigma T_v k_l \left(\frac{1}{\rho_l} - \frac{1}{\rho_g} \right)}{Lq_r}} \quad 23$$

Where ‘ q_r ’ is the radial heat flux into the evaporator. Using this approximation, it is possible to determine the effect that both the saturation temperature and heat flux will have on the nucleation radius value. presents a series of constant heat flux lines at increasing saturation temperature of water.

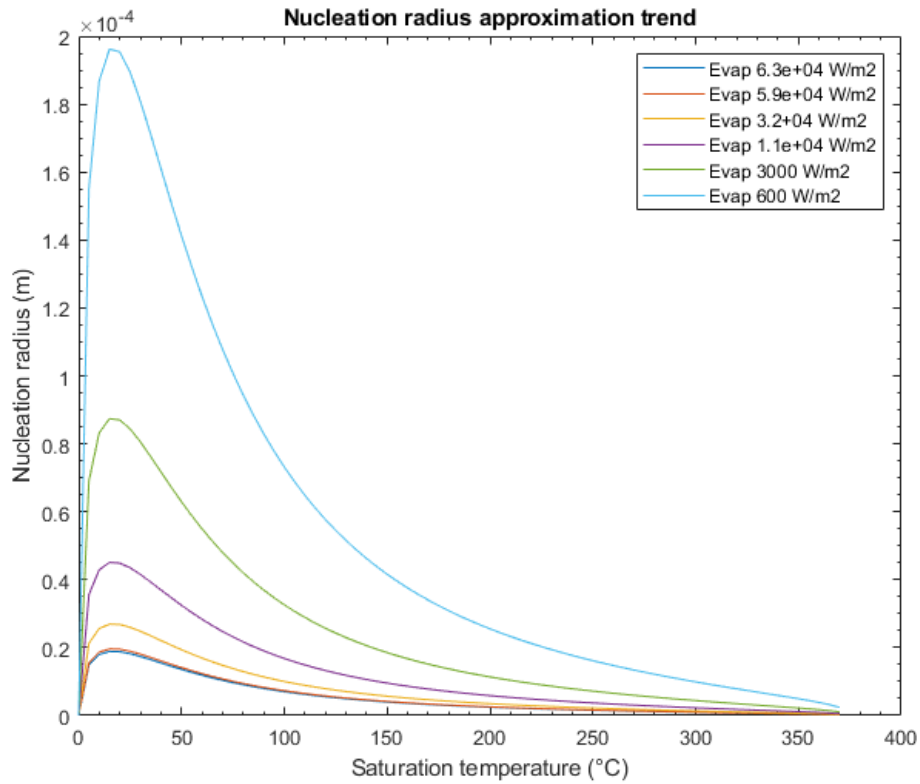


Figure 2-11 Effects of increase in heat flux and saturation temperature on the maximum nucleation radius

2.3.5.3 Sonic limit

Once reaching temperature capable of overcoming the viscous forces in play, the increase in heat flux into the system can cause the evaporated vapour to reach sonic velocities and cause ‘choking’ of the evaporator. This has a direct impact on thermal load handling capabilities of the heat pipe. Levy et al. [35] derived a closed-form relation of the sonic limit reaching the relation for heat input needed to reach sonic velocities.

$$\dot{Q}_s = \frac{\rho_v c_v h_{fg} A_v}{\sqrt{2(K' + 1)}} = A_v \rho_v h_{fg} \left[\frac{K' R_g T_v}{2(K' + 1)} \right]^{\frac{1}{2}} \quad 24$$

Where ‘ K' ’ is the ration of specific heats and ‘ R_g ’ is the gas constant. Additionally, Busse (1973) [36] derives another equation which shows good agreement with empirical data.

$$q = 0.474 h_{fg} (\rho_v P_v)^{0.5} \quad 25$$

2.3.5.4 Entrainment limit

When observing the liquid/vapour interface within the heat pipe, the shearing effect of the vapour flow against the liquid boundary causes small turbulences at the boundaries. Once the magnitude of the shear force reaches a maximum limit, the liquid flow will begin to entrain into the vapour flow. This can ultimately lead to dry out in the evaporator. As the vapour flow velocity is much greater than the liquid flow, the shear stress at the interface can mainly be attributed to the vapour flow. Kemme (1967) [15] defines the axial heat flow entrainment limit as

$$\dot{Q}_{ent} = A_v h_{fg} \left(\frac{\sigma \rho_v}{2r_h} \right)^{\frac{1}{2}} \quad 26$$

Or

$$q = \sqrt{\frac{2\pi\rho_v h_{fg}^2 \sigma_1}{z}} \quad 27$$

Where

$$r_h = \frac{2A_l}{P'} \quad 28$$

Where ‘ P' ’ is the wetted perimeter of the individual surface pores and ‘ A_l ’ is the area of the individual surface pores. Additionally, Prenger et al. [37] derived a relation based on a physical model and the critical Weber number.

$$\dot{Q} = \sqrt{\frac{2\pi E_t}{\alpha_v}} \frac{\delta}{\delta^*} \quad 29$$

Where E_t is a dimensionless entrainment parameter ($\frac{\sigma_l}{\rho_l L \delta}$), ‘ α_v ’ is the velocity profile correction factor, ‘ δ ’ is the surface depth and ‘ δ^* ’ is the reference surface depth.

Though many entrainment models have been developed and tested over the years Faghri et al. [11] observes that in general the studies fail to observe entrainment occurring in conventional capillary-driven heat pipes, possibly due to the dampening effects of the capillary structure on boundary turbulences. The entrainment phenomenon itself has been studied in finer detail by authors such Ishii et. al [38] and Kataoka et. al. [39] who applied various visualisation techniques in stratified flows with high velocity gasses. Kim et. al. [40] then incorporated these findings into a study which analysed stratified flows in mesh

wicked heat pipes. Here the wave disturbance patterns such as those in Figure 2-12 were observed by Kim.

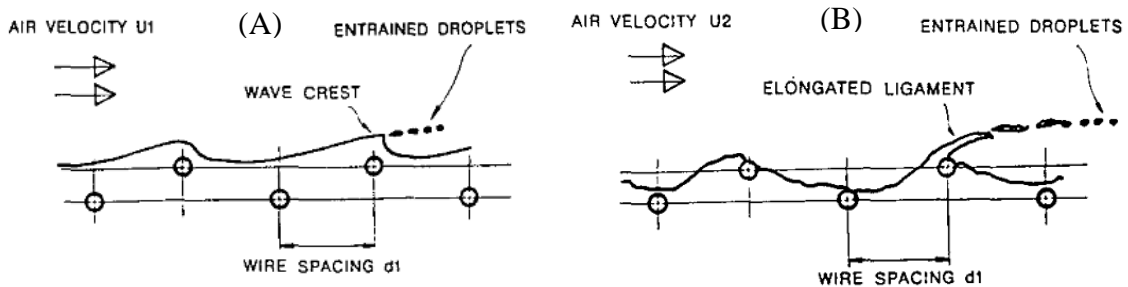


Figure 2-12 Wave disturbance pattern in stratified flow containing a mesh wick structure where entrained droplets are formed. Two different entrainment modes are shown: A) Roll-wave entrainment and B) Stripping entrainment. Source: [40]

The study by Kim et al. [40] agreed with predictions by Faghri et al. [11] concluded that the presence of a capillary structure may act as a dampener to the liquid/vapour surface oscillations. The main conclusion of this study found that “the critical (vapour) velocity for a given heat pipe mesh wick is strongly influenced by the mesh dimensions and that the previously developed criteria for estimating the critical velocity results in significant underestimations of the upper critical velocity for all but very small pore sizes” [40].

2.3.5.5 Viscous limit

This is the minimum temperature at which the pressure difference caused by the vapour pressure due to boiling exceeds the viscous forces, allowing for fluid circulation. Busse et al. [36] derives the limitation by manipulation of conservation equations and equations of state reaching the relation

$$\dot{q} = \frac{r_v L \rho_v P_v}{16 \mu_v l_{eff}} \quad 30$$

Where the effective length, ' l_{eff} ', is calculated as:

$$l_{eff} = \frac{l_{ev}}{2} + l_a + \frac{l_c}{2} \quad 31$$

Or it can be defined as a function of the heat input and output distribution as follows

$$l_{eff} = \frac{1}{q_{max}} \int_0^{l_t} q(z) dz \quad 32$$

The temperature dependency of viscous effects is demonstrated by the term $\rho_v P_v$, which is directly proportional to temperature. At low temperatures the viscous effects tend to be the limiting factor in heat transportation, whereas at high temperatures, the sonic limitations tend to be the primary limiting factor due to the choking phenomenon.

2.3.6 Other mechanisms

When in steady state, the output heat in the condenser is equal to the input heat at the evaporator. When dealing with high temperature heat pipes, heat transfer through

radiation can become the main transfer mechanism from the condenser [11]. The total heat input into the evaporator becomes

$$\dot{Q}_e = \iint_{A_{co}} \epsilon \sigma (T^4 - T_\infty^4) dA_{co} = 2\pi r_o l_c \epsilon (T^4 - T_\infty^4) \quad 33$$

Where ‘ r_o ’ is the outer pipe radius and ‘ l_c ’ is the length of the condenser and ‘ A_{co} ’ is the surface area of the condenser. Here it can be seen that the physical heat transport capacity of the system is dependent on the heat retransfer surface area and the operating temperature. This indicated that the test rig design constraints (such as operating environment, maximum allowable temperatures of the apparatus, etc) may be a major limiting factor during heat pipes capacity tests at high temperatures.

2.3.7 Heat pipe heat flux in medium temperature range

Heat pipes which have been previously produced for use in the ‘medium’ temperature range include; various organic fluid heat pipe by Kenney et al. [41], Ti/water and Monel/water heat pipe by Sarraf et al. [42], further Ti/water and Monel/water testing and testing on Halides by Anderson et al [43], Ti/water heat pipes for space radiators by Hay et al. [44], Sulphur heat pipes by Rosenfeld et al. [45] and life tests using naphthalene, quinoline, biphenyl, o-terphenyl, decafluorobiphenyl, and perfluoro-1,3,5-triphenylbenzene performed by Grzyll et. al. [46] and Saaski et al. [47]. In these cases, some were developed for specific applications and other only for the purpose of research.

The maximum heat flux that a heat pipe is able to achieve is generally determined by the specific properties of the heat pipe which is being studied. This includes the physical geometry such as wick type, pipe length, pipe diameter, surface conditions and operation angle, however the most important determinant is of course the particular fluid which is being used. To better understand the heat fluxes which are to be expected from medium temperature fluids which have been previously tested, Table 2-5 shows a summary of fluids that were tested by Saaski et. al. [47] which fall within the medium temperature range.

Table 2-4 Maximum achieved heat fluxes for previous testing on medium temperature fluids by Saaski et. al. [47]

<i>Fluid</i>	<i>Wick type</i>	<i>Heat pipe diameter (cm)</i>	<i>Heat pipe length (cm)</i>	<i>Maximum heat flux tested (W/cm²)</i>	<i>Orientation</i>	<i>Author</i>
O-Terphenyl	Screen	1.26	44.5	5.1	Vertical	Saaski
Antimony Trichloride	Screen	1.26	44.5	2.7	Vertical	Saaski
Naphthalene	Screen	1.26	44.5	4.3	Vertical	Saaski
Biphenyl	Screen	1.26	44.5	5.9	Vertical	Saaski
Titanium tetrachloride	Screen	1.26	44.5	2.5	Vertical	Saaski
1-Fluoronaphthalene	Screen	1.26	44.5	4.9	Vertical	Saaski

2.4 Heat pipe working fluid

As discussed previously, the working fluid in the heat pipe plays a vital role in the functionality of the device. The usefulness of the fluid is defined by its key properties such as its viscosity, surface tension, vapour pressure and heat capacity. All these qualities combined determine the heat transport capabilities of the fluid and its limitations. A general assessment of the heat transport capacity of the fluid with respect to temperature can be determined through its 'Merit Number' [1], [11]. This provides a preliminary judgement of the effectiveness of the fluid at transporting heat and an indication of the effectiveness of the fluids against others over a certain temperature range. Once a selection of fluids is made from this analysis there is several further criteria to be assessed to make a weighted comparative study on each fluid. These comprise of two categories: the numerical assessment and the industrial assessment. The various criteria for each of these categories are detailed below in order of importance.

Numerical assessment criteria:

- Melting point/boiling point/critical temperature
- Merit number
- Vapour pressure
- Fluid stability/thermal decomposition
- Fluid Compatibility with metals

Environmental criteria:

- Toxicity and handling analysis
- Economic analysis
- Compatibility with commonly used materials

The following chapter will address each of these criteria and detail the fluid categories which will be taken into consideration as well as the work which has already been done in each fluid category. The numerical modelling of each assessment criteria and the methodology behind the industrial assessment will be outlined. Previous studies for of fluids used in the medium temperature range will also be outlined. To categorise the fluid analysis, there are two distinguishable fluid groups which all fluids can be subdivided into Organic and Inorganic compounds. These are defined as follows:

Organic compound: Any compound which contains carbon bonds

Inorganic compound: Two or more elements combined in definite proportions with no carbon bonds

2.4.1 Organic Fluids

Interest in organic fluids for use in heat pipes has a long history dating back to work by Saaski et al at the NASA Lewis Research centre [47]–[49], Grzyll et al. at the Mainstream Engineering Corporation [46], [50] and Kenney et al at the University of New Mexico [41]. Much of this work investigates the use of organic fluids up to 400°C using

the theory of thermal stability developed by Johns et al. [51]. A review of key concepts involved in the stability theory as well as a summary of lifetime testing done on organic fluids in the context of heat pipe applications is presented.

2.4.1.1 Thermal degradation

Thermal degradation is mainly related to organic chemicals to assess their stability at high temperatures. The principal behind it is to determine the rate of pyrolysis based on the activation energy of the various bonds within the molecule to break the molecule into its constituents. In the Rice, Ramsper and Kassel (RRK) model [52], the first order rate of bond breakage is given as

$$R_1 = Ae^{\frac{E^+}{RT}} \quad 34$$

Where ' E^+ ' is the activation energy and ' A ' is a constant in the same magnitude as the bond vibration frequency. When dealing with a complex molecule, however, the many intermediary reactions and activated species may occur. This causes the decomposition rate to lose its linearity with the bond breakage rate due to collisions occurring with many lower energy molecule impacts retarding the decomposition process. The particles denoted with a '+' symbolise an energised state greater than their critical energy. In this state the molecule will either decompose or return to its original state by colliding with a lower energy particle. Sources of complexity and error in the modelling of these reactions come from intermediate stage reaction complexity, reaction with impurities or decomposed products and the heterogeneous nature of the container should residual air still be present

[41]. Saaski et al. [49] propose a simple reaction model in Figure 2-13 by showing all the possible intermediate species in the hypothetical reaction of species D to decomposition products A and B.

As seen in Figure 2-13 this reaction would possess a total of 16 rate constants. The vapour can also exist in a variety of conditions, all of which would affect the rate of decomposition in different ways. Some of the main cases will be highlighted.

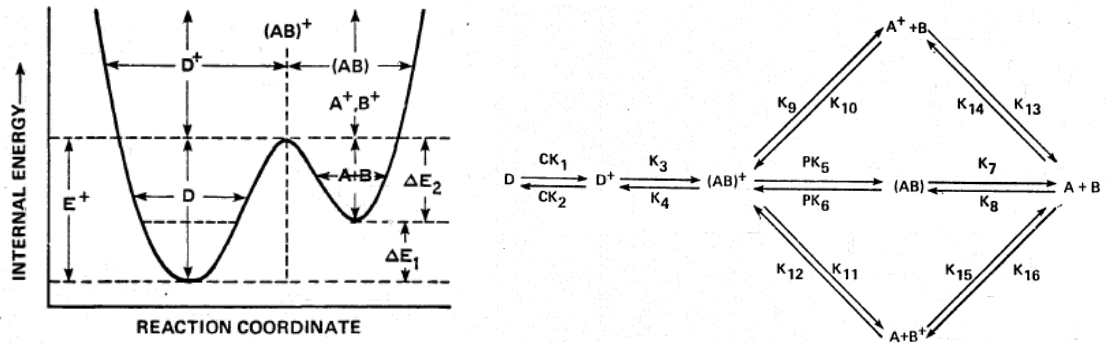


Figure 2-13 (1) Various intermediate species in the decomposition reaction and their relative internal energies (2) Unimolecular decomposition of species D to A + B. Source: [49]

2.4.1.2 Rate equations

The general form of the equation giving the rate of pyrolysis for any given species is

$$R_f = \frac{[D] \left(\frac{K_1}{K_2} \right) K_3}{1 + \frac{K_3}{cK_2}} \quad 35$$

Where C is the total concentration. The assumption made in this case are:

- $\Delta E_2 > 0$ (energy needed to form $(AB)^+$ and (AB))
- $K_7 \gg PK_6$
- The concentration of D is much greater than A or B

The intermediate species concentrations do not have an influence on decomposition rate; however, the decomposition rate is directly related to the system pressure. At low pressure the decomposition rate becomes:

$$R_{f,l} \cong C[D]K_1 \quad 36$$

Since A and B are in such small quantities, the concentration is proportional to $[D]$ hence the pyrolysis increases at a rate of $[D]^2$. At high pressure the rate equation takes the form

$$R_{f,h} \cong C[D] \left(\frac{K_1}{K_2} \right) K_3 \quad 37$$

In the instance where $\Delta E_2 \rightarrow 0$ (where A and B become free radicals) the high-pressure rate becomes

$$R_{f,h} \cong \frac{[D]}{2} \left(\frac{K_1}{K_2} \right) K_3 \quad 38$$

Benson and Sidney (1960) [52] shows in Figure 2-14 the pressure limitation where the decomposition rate reduces by a factor of two for a given number of atoms and degrees of freedom possessed by the molecule. The pressure limit reduction is caused by the energy absorbing effects of multiple bonds.

Number of Atoms in Molecule	Degrees of Freedom	Characteristic Pressure (atm, STP)
2	1	4000.
2	2	225.
3	3	25.
3	4	4.
3	5	1.
4	6	0.3
4	7	0.09
4	8	0.03
5	9	0.01
5	10	0.005
5	11	0.003
6	12	1.2E-3

Figure 2-14 Pressure at which the unimolecular rate constants fall by a factor of two. Source: Benson and Sidney (1960)

Ingold et. al. [53] explores this pressure dependency by studying the thermal decomposition of several paraffin hydrocarbons. This gave the rate equations of the form

$$R_{f,l} \cong AP + BP^2 \quad 39$$

For low pressure pyrolysis (0 – 0.66 atm) and

$$R_{f,l} \cong A'P \quad 40$$

For high pressure pyrolysis (>0.66 atm). Where A' , A and B are curve-fitting rate constants. In general, the thermal decomposition of a vapour is characterised by 3 factors:

1. An Arrhenius-type rate equation with a pre-exponential factor of approximately 10^{13} s^{-2}
2. Concentration dependant rate constant at low pressure
3. A relatively concentration-independent rate constant at high pressure

2.4.1.3 Stability prediction

The stability of a molecule is determined by its bond stability. When analysing a compound, acquiring data on its bond strength is of great interest to determine its stability. Since the dissociation energy of covalent bonds are generally consistent independent of molecular structure, this data can also be used to make predictions on stability of compound with limited data available.

One particular characteristic of stable compound is described by Saaski and Owzarski [47] where they analyse the structure of electron orbitals around certain types of bonds. It was found that the stability of a molecule can be determined by the bond strengths of localised hybrid orbitals (σ bonds) and delocalised hybrid orbitals (π bonds). Hence organic compound stability can be described through containing carbon rings tend to have high levels of stability due to their π bond structure. Naphthalene is one such structure which stands out due to its high boiling point and heat transport capabilities. Some common dissociation energies are presented in Figure 2-15.

1. Characterising the bond dissociation energies of various σ bonds (particularly C-H bonds)
2. Defining classes of compound with π orbital bonding
3. Correlating points 1 and 2 with available data

	H	CH ₃	C ₂ H ₅	CHO	OH	F	Cl	Br	I	NH ₂	CN	C ₂ H
H	104	104	98	-79	119	136	103	88	71	104	120	
CH ₃	104	88	85	71-75	88	108	84	70	56	79	105-110	
C ₂ H	<121	-110	-109									
C ₂ H ₃	104	92	-90	-84			84		-55		-121	
CH ₃ CO	89	81	83	-59	110	119	79	-67	-51	-98		
C ₂ H ₅	98	85	85	-71	90		81	69	53	78		
C ₂ H ₅ O	102	80	82		42	-	-	-	-			
n-C ₃ H ₇	98	85	79	-71			82	69	50	77		~106
i-C ₃ H ₇	95	84	-75		92	106	81	68	53	85		~103
n-C ₄ H ₉	94	78	78									
t-C ₄ H ₉	91	80			91		79	63	50	84		
C ₆ H ₅	112	93	94	-83	96	125	86	70-72	61	-94	-124	-119
C ₆ H ₅ CH ₂	85	70	68		77		68	51	38	59	-95	
C ₁₀ H ₇								70				
C ₁₀ H ₇ -CH ₂	-76											

Figure 2-15 Bond dissociation energies for various vapours. Source: [47]

The critical decomposition rate for a fluid is relative to the application at hand. Saaski and Owzarski (1977) give a hypothetical maximum allowable decomposition rate of 0.1% volume decomposition per year, this gives

$$R_{Cr} = 1.14 \times 10^{-7} \text{ hr}^{-1} \quad 41$$

The works of Siefert et. al. and Miller (1972) both run pyrolysis experiments on different compounds at temperature between 343 and 412°C. It was found that aromatic ethers presented high stability, alkylated aromatic ethers varied in stability and saturated alkyl compound demonstrated very poor stability. It was also noted that molecular symmetry tends to be beneficial to its stability.

2.4.1.4 Halogenated Alkanes

Due to low dissociation energies and susceptibility to catalytic decomposition, long chain halogenated compound tends to have relatively low decomposition temperatures. Studies conducted on coolants R12, R22, R114 and R216 found that the maximum operating temperatures would be in the region of 200 to 250°C without the presence of oxides and 100 to 125°C in the presence of oxides. The catalytic effects of various metals were also determined as follows (in order of high to low decomposition effect):

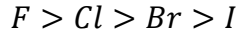
*Silver > Aluminium > Steel > Nickel > Copper > Stainless Steel > Inconel
> Platinum*

It was also noted that catalytic effects are related to factors such as temperature, pressure, relative strength of chemical bonds, type of molecule hybridization and intermediate species. Hence, the catalytic effects for other chemical groups may differ significantly. The conclusion of the studies show that halogenated hydrocarbon would be unable to perform as working fluids.

2.4.1.5 Halogenated aromatic compounds

The σ bond strength of an aromatic compound with a halogen attached is what give the fluid it's resilience to decomposition. The magnitude of the σ bond strength varies with

the halogen attached. Saaski and Owzarski (1978) [47] determined that the strongest to weakest the halogen order is



This indicated that fluorinated species are expected to be the most stable. Some examples of fluids in this category are detailed in Table 2-5.

Table 2-5 Various halogenated aromatic fluids and their properties

Fluid	Melting Point (°C)	Boiling Point (°C)
Dowtherm E	-	177.8
Naphthalene	80.1	218
Monochloronaphthalene	-25	250
Dichloronaphthalene	60	-
Octofluronaphthalene	88	-
Octachloronaphthalene	185	-
1-Fluronaphthalene	-9	216

Extensive work has been done by Miller (1972) [54] on halogenated aromatic fluids and their decomposition during gas phase pyrolysis with surface activated catalytic effects. The survival time are in agreement with the relative bond strengths of each halogen. It is important to note, however, that the results do not reflect the formation of NGS's and sludge/tar, both of which would cause adverse effects as a heat pipe working fluid. The fluids are also in complete vapour states and in the presence of air.

Table 2-6 Decomposition temperatures for halocarbon refrigerants in presence of steel and the influence of metals on decomposition of R-11 at 249°C. Source: [54]

Fluid	Decomposition Rate Percent Per Year		Metal	Decomposition Rate Percent Per Year
	0.1	1.0		
R-11	89°C	129°C	Silver	1500
R-12	100	145	Steel	120
R-113	91	137	Nickel	110
R-114	97	146	18-8 Stainless	20
			Inconel	3
			Platinum	1

2.4.1.6 Previously tested organic fluids in medium temperature range

The most recent research directed towards identifying and testing organic fluids for the intermediate temperature range have origin in various institutions in the USA. Various works by Anderson et al. [10], [43], [55]–[57] Devarakonda et al. [58], Rosenfeld et al. [45], Groll et al. [6] and Vasil'ev et al. [59]. Table 2-7 shows a summary of all results falling within the medium temperature range, the highest tested temperature for organic fluids is 400°C.

Table 2-7 Summary of organic fluids tested in the medium temperature range

<i>Fluid</i>	<i>Working Temperature range (°C)</i>	<i>Author(s)</i>	<i>Summary</i>
Dowtherm A	150-450	Anderson 2007 [43] Groll 1989 [46] Kenney 1978 [41]	Highest tested temperature: 400°C Tested compatible metals: 304 SS, 321 SS, St35, Ti 99.4
Naphthalene	135-350	Vasil'ev 1988 [59] Gryzl 1994 [46]	Highest tested temperature: 320°C Tested compatible metals: Al 6061, A-178 Steel, 13CrMo44, St35, CuNi10Fe, 316L, Ti 99.4, 316 SS, Alloy 20 SS

Diphenyl	250-400	Groll 1989c Saaki 1980 [49]	Highest tested temperature: 400°C Tested compatible metals: 304 SS, Carbon Steel, Black Iron, 316 SS, Mild Steel
		Gryzll 1994 [46] Groll 1989 [6] Saaki 1980 [49] Kenney 1978 [41]	
O-Terphenyl	250-400	Gryzll 1994 [46] Saaski 1980 [49]	Highest tested temperature: 380°C Tested compatible metals: Al 6061, A-178 Steel, 316 SS

From extensive literature surveying, it is concluded that most organic compounds suffer from decomposition at temperature above 400°C. In addition to the tests presented in Table 2-7, there have been numerous more recent tests on these and other organic fluids at temperatures reaching up to 450°C (Dowtherm A [43], [60], P-Terphenyl [61], Diphenyl [55]), all current studies, however, are yet to present a successful result above 400°C. From this it can be concluded that the vast majority of viable organic medium temperature fluids have been empirically proven to only have a functioning capacity of no more than 400°C. While this does give some overlap into the medium temperature range, it is unlikely that an organic fluid would be able to reliably cover all of the temperature range, and thus, has limited scope for use as a mass-produced medium temperature solution.

2.4.2 Inorganic fluids

Inorganic fluids have been analysed and tested largely alongside organics in studies by Saaski et al at the NASA Lewis Research centre [47]–[49], Grzyll et al. at the Mainstream Engineering Corporation [46], [50] and Kenney et al at the University of New

Mexico [41]. In the study by Saaski and Owzarski [47] the analysis of two particular fluid groups within the 'inorganic' category is carried forward. These are halogenated alkanes and halogenated aromatic compounds.

2.4.2.1 Stability prediction model for inorganic fluids

Inorganic fluids are characterised as being either molecular or ionic liquids. Molecular and ionic behaviours differ from one another, molecular fluids do not lose their structure in the liquid/vapour transition whereas with Ionic compound the structure tends to be destroyed. Most inorganic fluids which fall into the medium temperature working fluid range tend to be in the metal halide category. The physical properties of these inorganic compounds can be generally characterised as:

- The vapour pressure characteristics are similar to water or somewhere in-between water and liquid metals
- The thermal conductivities and surface tension are similar to organic fluids
- Liquid densities are high compared to organic fluids (this is good as Nussle film tends to be thinner)
- Limited amount of data tends to be available
- They tend to vary in toxicity from non-toxic to extremely toxic
- Latent heat of vaporisation (for metal halides) varies between 30000 to 100000 Kcal/g-mole

The stability of inorganic compounds tends to be very good (usually around -100kcal/g-mole free energy at 25°C), with the distinct advantage of no NCG formation on decomposition. The decomposition of metal halides in the presence of water results in the halogen's acid with a metal oxide. The main factor to determine the suitability of the inorganic fluids as working fluids is their reactions with the metal envelope. The main methods to determine the fluid/envelope stability are discussed below.

2.4.2.2 Compatibility of metal/fluid envelopes

The reactivity of a metal halide in contact with a metal container is characterised by their relative stabilities. The general reaction can be expressed as



Where M_bX_c is the metal halide and M_a is the wall metal. The free energy change during this reaction is given by

$$\Delta G = \Delta G^0 RT + \ln \left[\left(\frac{(M_aX_{cp})^f (M_b)^g}{(M_a)^f (M_bX_c)^g} \right) \right] \quad 43$$

Where ' ΔG ' is the Gibbs free energy (J/molK). The electromotive force can be calculated as

$$\Delta E = \Delta E^0 - \frac{RT}{nF} \ln \left[\frac{(M_a X_{cp})^f (M_b)^g}{(M_a)^f (M_b X_c)^g} \right]$$

Where n is the number of electrons transferred in the balance equation and F is the Faraday constant (96485C/mol). If the reaction has a large negative energy formation, the left to right reaction will be spontaneous. However, a film of the shell metal halide may form over the surface due to the low solubility of a metal in a dissimilar metal halide. An example of this is given in the reaction between Bismuth Trichloride and Iron as seen in Figure 2-16.

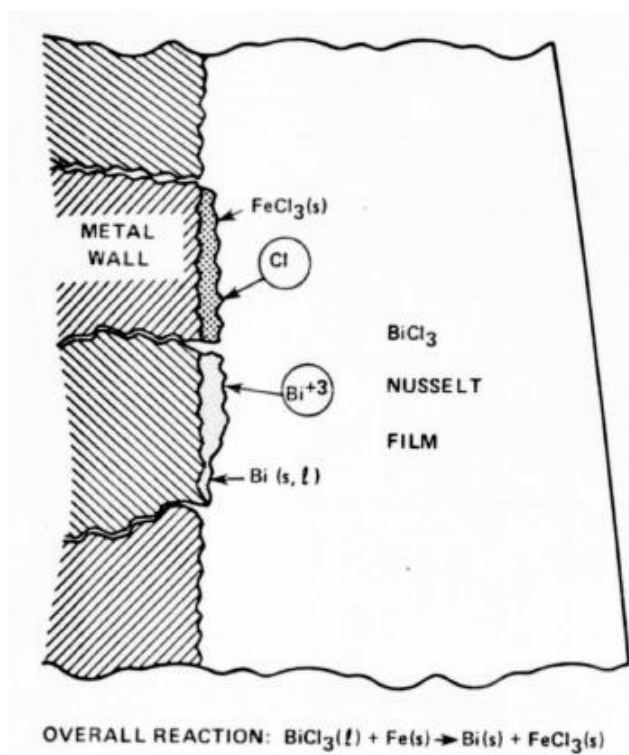


Figure 2-16 Corrosion of Iron by film of molten Bismuth Trichloride (hypothetical reaction cells). Source: [47]

The FeCl₃ and Bi ‘cells’ that can be seen in Figure 2-16 form over the metal surface and act as electrodes coupled by Ionic conduction in the liquid Bismuth Chloride. By neglecting the solubility of Fe in BiCl₃ and of BiCl₃ in FeCl₃, the activities of the various constituents can be approximated to unity. The model also neglects the changes in mutual solubilities and diffusivities during phase change. To determine the EMF of the reaction the decomposition potentials of the fluid and metal wall halides must be determined. These can be found from existing data tables as shown in Figure 2-16. The total EMF for a given reaction is then calculated as:

$$\Delta E^0 = E_p(\textit{product halide}) - E_p(\textit{initial halide})$$

If the result returns a positive value, then spontaneous reaction will occur between the wall and the fluid. If the EMF is strongly negative the reaction between the fluid and the wall is insignificant. From this it can be inferred that the ideal combination would be to have fluids with high decomposition potentials and walls with low decomposition potentials. Figure 2-17 shows a visual aid developed by [47] to more easily identify which chloride fluids would be compatible with standard metals. From analysis of , the chloride compounds which stand out are those of groups 4b, 5b, 3a, 4a and 5a on the periodic chart.

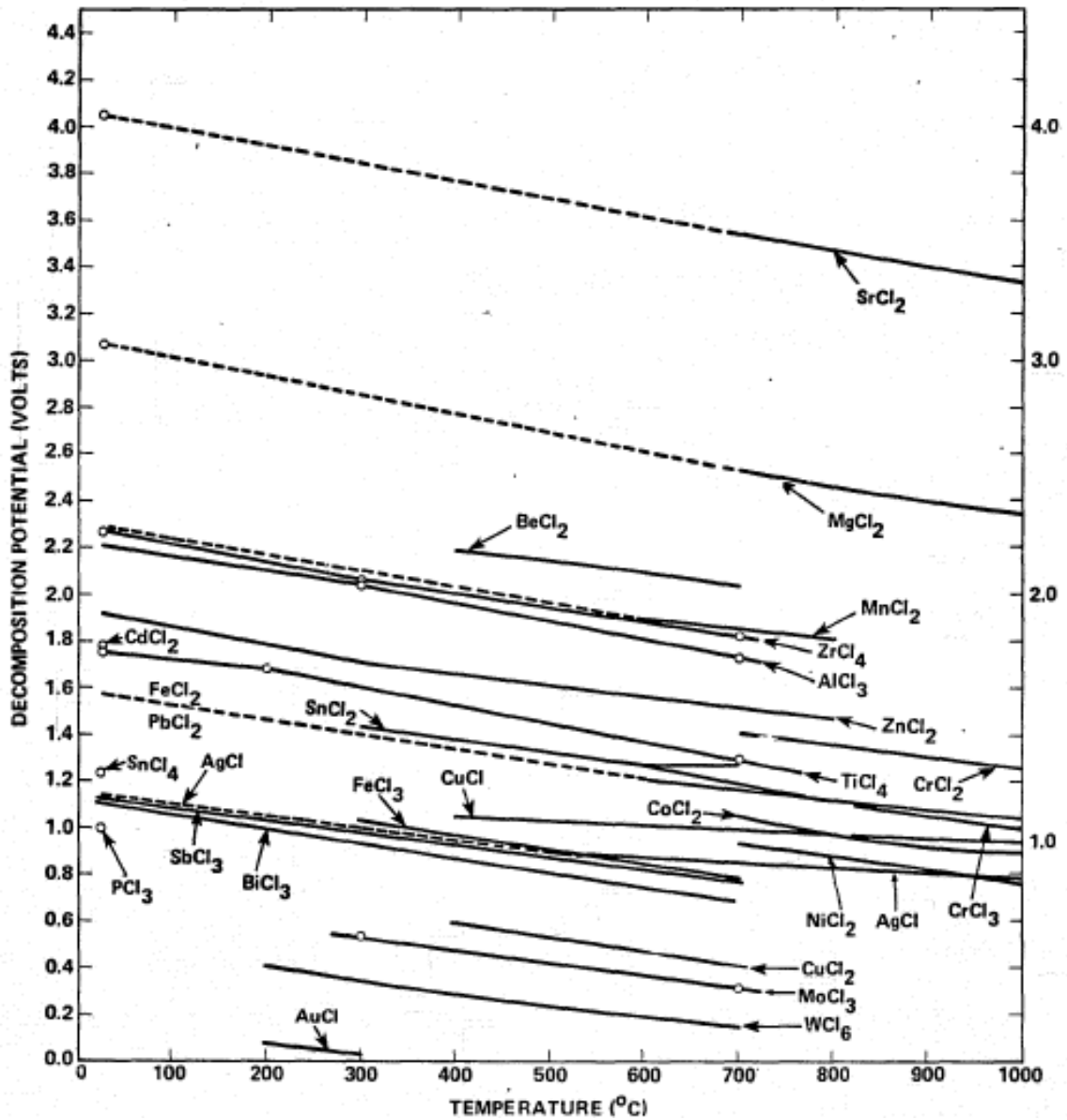


Figure 2-17 Decomposition potential of various inorganic chlorides. Source: [47]

2.4.2.3 Liquid metals

In general, liquid metals have a start-up temperature much higher than 600°C, hence the gap in the medium temperature range. Table 2-8 shows some common liquid metal elements and their working range.

Table 2-8 Common heat pipe liquid metals

<i>Fluid</i>	<i>Melting point</i>	<i>Boiling point</i>	<i>Working range (°C)</i>
Mercury	234.2	630.1	250-650
Sulphur	386	718	257-674
Caesium	302	943	350-900
Rubidium	313	959	400-1600
Potassium	336	1032	400-1800
Sodium	371	1151	600-1200
Lithium	454	1615	1000-1800
Calcium	1112	1762	1127-1827
Lead	601	2013	1397-1927
Indium	430	2353	1727-2727
Silver	1234	2485	1800-2300

Observing Table 2-8, there are distinctly five metals which can theoretically operate within the medium temperature range, these are: Mercury, Sulphur, Caesium, Rubidium and Potassium. The most obvious contenders from initial observation would be Mercury and Sulphur as these fluids span the entire working range. Naturally, these metals have indeed been the subject of many trials as heat pipe fluids, unfortunately, each of these come with their own set of drawbacks which is detailed in Table 2-9.

Table 2-9 Liquid metals tested in the medium temperature range

<i>Fluid</i>	<i>Author(s)</i>	<i>Summary</i>	<i>Primary fluid issues</i>
Mercury	Yamamoto 1994 [62]	Lowest tested temperature: 350°C Tested compatible metals: No compatible metals proven, high corrosion	Low wetting ability Highly toxic High density
Sulphur	Anderson 2007 [63]	The major factor contribution to its inadequate use in heat pipes is the incredibly high liquid	Highly toxic Low vapour pressures

Caesium	Dussinger 2005 [64]	viscosity over almost all the working temperature range A Caesium heat pipe was tested at 350°C for 48 hours with no sign of degradation	High liquid viscosity Highly corrosive Highly flammable Unstable in air Expensive to manufacture
Rubidium	El-Genk 2011 [65]	A theoretical analysis of rubidium heat pipes is conducted but no experimental validation as of yet not proof of compatible long-term metals for use with Rubidium.	Highly toxic Corrosive
Potassium	Dussinger 2005 [64]	A Potassium heat pipe was tested at 430°C for 48 hours with no sign of degradation	Highly corrosive Highly flammable Unstable in air Expensive to manufacture

Within the medium temperature range, there are Reports by Sena et al. [66], [67] show successful operation of a Potassium heat with Niobium and Tantalum wall materials at temperatures down to 522°C.

2.4.2.4 Previously tested inorganic fluids in medium temperature range

The most recent tests conducted on novel inorganic fluids are those undertaken by Anderson et al. [63]. In this work, a large range of fluids were selected for lifetime testing, mostly resulting in incompatible matches at high temperatures. The most promising results from Anderson as well as previous studies which have tested at or near the medium temperature range can be found in Table 2-10. Here it can be seen that a series of halides have shown good compatibility with Hastelloy within the medium temperature range. As far as the author is aware, there have been no further advancements from these to date.

Table 2-10 Most recent compatible results for novel inorganic fluids

<i>Fluid</i>	<i>Working Temperature range (°C)</i>	<i>Author(s)</i>	<i>Summary</i>
Sulfur/Iodoine10	350 - 700	Anderson 2004 [63] Reid 1991 [68]	Highest successful tested temperature: 350°C Tested compatible metals: Al 6061, A-178 Steel, 316 SS
AlBr3	120 - 420	Anderson 2007 [43] Locci 2005 [69] Tarau 2007 [57]	Highest successful tested temperature: 400°C Tested compatible metals: HastC22, HastC2000, HastB3
SbCl3	100 - 500	Saaski 1980 [49]	Highest successful tested temperature: 203°C Tested compatible metals: A-178 Steel
TiCl4	100 - 300	Anderson 2007 [43]	Highest successful tested temperature: 300°C Tested compatible metals: HastC22, HastC2000, HastB3

2.5 Current experimental studies in medium and high temperature heat pipes

As seen in previous sections, many studies have directed research specifically into the medium temperature range for heat pipes. The vast majority of research in the field comes from a handful of research centres mostly based in the USA. Early work can be dated back to at Los Alamos Scientific Laboratory, Lewis Research Centre (NASA). More recent work can be attributed to Thermacore Ltd. and Advanced Cooling Technologies Ltd dating up to 2013. Since then, there have unfortunately been limited resources invested into perusing the research, possibly due to identification of alternative solutions for the specific projects the research in the institutions were aimed towards. From 2013 to the current year (2020), the main interest of researchers has directed towards the optimisation of applications using current heat pipes or the use of nanofluids to enhance heat transfer in established heat pipe fluids [28], [70]–[74]. This, however, is of course still limited to the working temperature of that particular fluid and does little to advance the research into novel heat pipe fluids for use in the medium temperature range. As it currently stands, this work appears to be the only recent attempt at reviving investigations into medium temperature heat pipes, and the author is hopeful that the tools provided here will promote researchers to continue investigations into the field. The following chapter will review some of the major contributions and explore some of the primary techniques used in heat pipe fabrication and testing.

2.5.1 Experimental techniques

Many papers have explored a variety of experimental techniques used to evaluate the performance of heat pipes. This section will explore the main techniques used and how they are applied.

Table 2-11 Papers outlining medium and high temperature heat pipe testing

<i>Author(s)</i>	<i>Test type</i>	<i>Summary</i>
Jang [75]	Performance test	Experimental study highlighting the start-up characteristics of a potassium heat pipe. Heat pipe was tested in a vacuum chamber using radiation heat transfer mode.
Reid et al. [76]	Performance and compatibility (life) tests	Various experimental studies of water and gas-loaded sodium heat pipes.
Wits et al. [77]	Performance test	Undefined fluid operating from 0 to 100°C. Heat pipe tested at multiple angles with gravity. Air cooled condenser section with varying heat input configurations.
Tu et al. [78]	Compatibility (life) tests	Study of corrosion failures occurring with alkali metal heat pipes with a variety of steels.
Meng [79]	Compatibility (life) tests	Study of corrosion behaviour of Mo, W and SS with lithium.
Rosenfeld et al. [80]	Compatibility (life) tests	Long term life test conducted on Ti and Monel with Water at temperatures from 200°C to 300°C.
Basilus et al. [81]	Compatibility (life) tests	Compatibility tests were performed on a variety of organic fluids with Copper, Aluminium, Stainless Steel, Nickel and Refrasil.

Ghanbarpour et al. [82]	Performance test	The thermal performance of water heat pipes with nanoparticles present is assessed.
Khandekar et al. [28]	Performance test	Thermal performance of thermosyphon using water with suspended nanoparticles.
Anderson et al. [83]	Performance test	Performance of Ti/Water heat pipes for space applications.
Anderson et al. [43]	Compatibility (life) tests	Life tests conducted with water, and a variety of halides with Titanium and Monel pipe structures.
Rosenfeld et al. [84]	Compatibility (life) tests	Sodium/Inconel vapour chamber test with stainless steel mesh wick.
Anderson et al. [10]	Compatibility (life) tests	High temperature water heat pipes tests with Titanium and Monel heat pipes.
Deverall et al. [85]	Performance tests	Pioneering work on Lithium and Silver heat pipes at over 1200°C. Concept development of early heat pipes.
Min et al. [60]	Performance tests	Tests on Stainless steel/Dowtherm A heat pipes to quantify thermal performance at 250°C

2.5.2 Heat pipe life tests

Life tests are a standard testing procedure usually carried out as part of the Technology Readiness Level (TRL) advancement process. Any new metal and/or fluid must be subject to life tests which are at least equivalent to the lifetime of the application. The aim of life tests is to identify any failure modes associated with continuous long-term operation and have a bank of data proving the reliability of a specific fluid/metal combination. In the life testing process, there are three main failure modes to consider:

1. Corrosion of the metal envelope or wick structure
2. Generation of non-condensable gasses (NCG's)

3. Leakage from welded joints or damage to wick structure from the internal pressure

To monitor the heat pipe over the testing process, only temperature measurements of the outer structure is necessary. Should any of the failure methods occur, this will be detectable in temperature measurements (generally through raising heat pipe temperatures) as the heat transport capabilities of the heat pipe are compromised. The test continues until either there is total failure, or the necessary duration has been completed. In either case, the heat pipes are usually then examined using both destructive (SEM/EDX analysis of sectioned heat pipe) and non-destructive methods (CT scan).

In Table 2-11 there are a variety of experimental papers outlining life testing directed towards medium and high temperature heat pipes. Figure 2-7 shows the life test apparatus used by Anderson et al. [10] in investigating high temperature water heat pipes with a variety of wall materials.

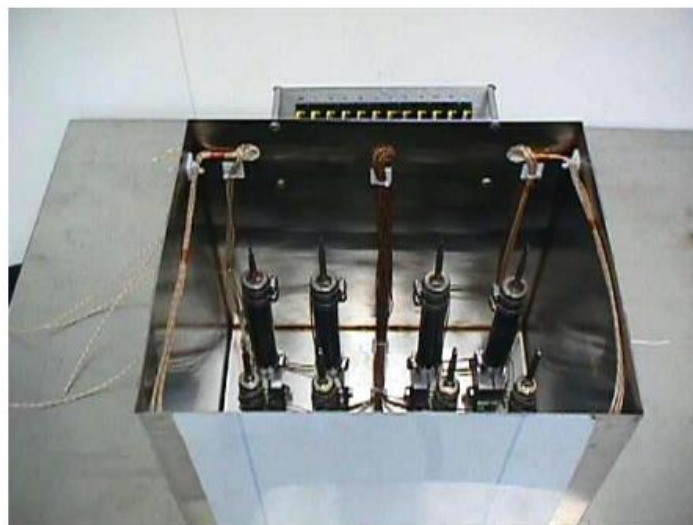


Figure 2-18 Apparatus set up for high temperature water heat pipe life test by Anderson et al. [10]

As seen in Figure 2-18, the general setup for a lifetime test rig can be fairly simple. The heat pipes are connected to a frame with heater blocks at the bottom and an aluminium box surrounds the heat pipes to contain insulation material. A PID controller is generally used to control the temperature of the heat pipes so they are kept stable at the desired test temperature. The heat pipes are then fitted with a series of thermocouples along their length to monitor the temperature at desired points.

2.5.3 Heat pipe thermal performance tests

Thermal performance tests differ from life tests in many ways, one critical differentiating factor though is the use of a calorimeter at the condenser side of the heat pipe. The addition of a calorimeter (by either convection or radiation) allows for the measurement of the heat being transferred through the heat pipe, this give a much wider picture of the heat pipe functionality. As seen in Table 2-11, thermal performance tests are widely conducted to quantify the effectiveness of a specific fluid and compare this against a baseline. Deverall and Kemme [85] pioneered this work in 1965 by testing Lithium and Silver heat pipes in the vertical orientation using both induction and electron beam heating methods in vacuum while using thermal imaging and emissivity calculations to quantify the heat transfer rate. Figure 2-19 shows the apparatus setup for the Lithium and Silver heat pipe tests.

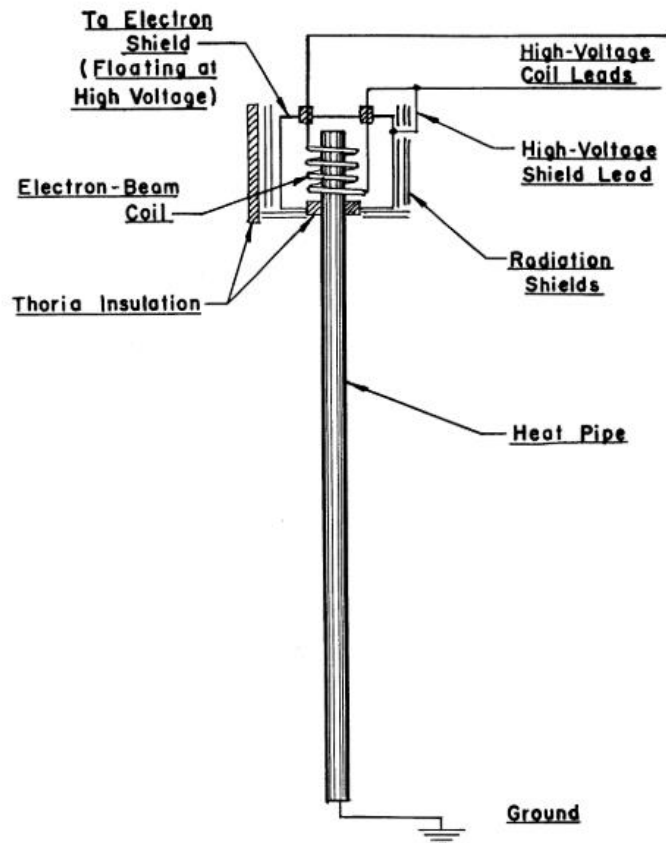


Figure 2-19 Apparatus setup for Lithium and Silver heat pipe testing Source: [85]

More recently, authors such as Ghanbarpour et al. [82], Min et al. [60] and Anderson et al. [83] have explored more precise calorimetry methods allowing the ability to quantify key features of the heat pipe such as the overall thermal conductivity and thermal resistance. In some cases, these qualities were attempted to be improved by the use of nanofluids - a more recent development in the heat pipe field. Figure 2-20 shows a typical schematic layout for heat pipe performance tests in all most recent cases. The figure also shows an advanced calorimeter developed by Anderson et al. which is able to adjust its thermal resistance using a small gas gap. This provides a means to regulate the thermal

output of the pipe allowing for various thermal load conditions to be met at a single vapour temperature.

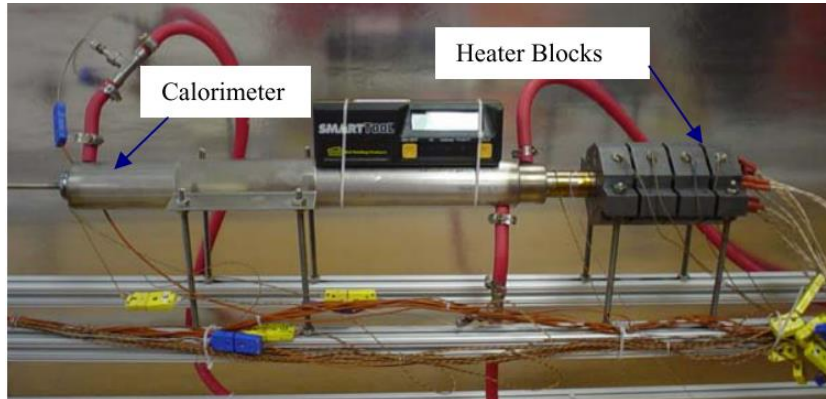
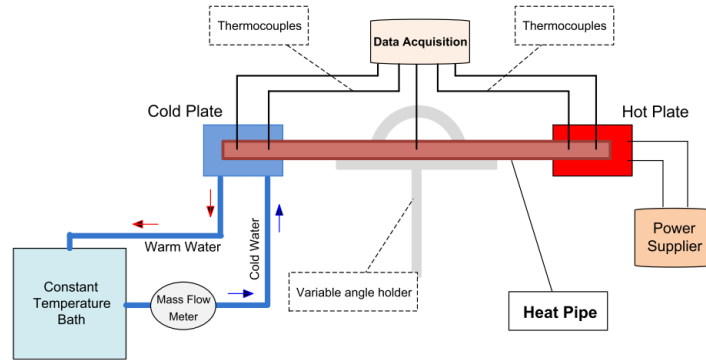


Figure 2-20 Typical schematic diagram for a heat pipe thermal performance rig (top) and a picture of a test rig using a variable conductance calorimeter (bottom) from recent literature. Sources: [86] and [82]

2.6 Chapter Summary

Heat pipes clearly have had a meteoric rise in the last 50 years and have expanded its use throughout a range of industries. Despite this, there has been a severely neglected temperature range for the development of heat pipes due to the lack of obvious/safe fluids which can work in this range. The literature review has pointed out the growing need for heat pipes in this range and has outlined the research that has been conducted in this area which thus far has not surpassed feasibility studies and individual fluid evaluations. While there has been some headway in directed investigations of medium temperature heat pipes, mostly authored by Anderson, Devarankonda and Tarau in the latest investigations, there has been no conclusive results for intermediate temperature fluids taken forward into thermal management applications.

The advantages of developing heat pipes for the intermediate temperature range are to aid the expansion of applications which heat pipes could be used for. Many industries such as renewable energy, nuclear power, high power electronics and aerospace are currently developing next generation technology which operate in the intermediate temperature range and have a great need for high level thermal management. This chapter has highlighted all the main theory surrounding the mechanisms by which the heat pipe operates and has made a comprehensive review of medium and high temperature fluids that have been identified and studied so far as well as their shortfalls. It is clear that much more work need to be done in this field to identify and quantify new potential fluids.

Chapter III

Methodology - Analysis and application of experimental and numerical methods

3.1 Experimental methods

The various testing methods and full overview of the test plans, approaches used, equipment and procedures are described in this section. Figure 3-1 shows an umbrella view of the experimental work done towards the final goal of producing a viable medium temperature heat pipe. One of the goals of this thesis is to provide a blueprint of the procedures necessary to explore new chemicals in heat pipes, this section provides an overview of all the equipment and methodology necessary to achieve this. Of course, these can be further refined and modified to suit different chemicals and metals in future work, but the general structure should follow a similar process.

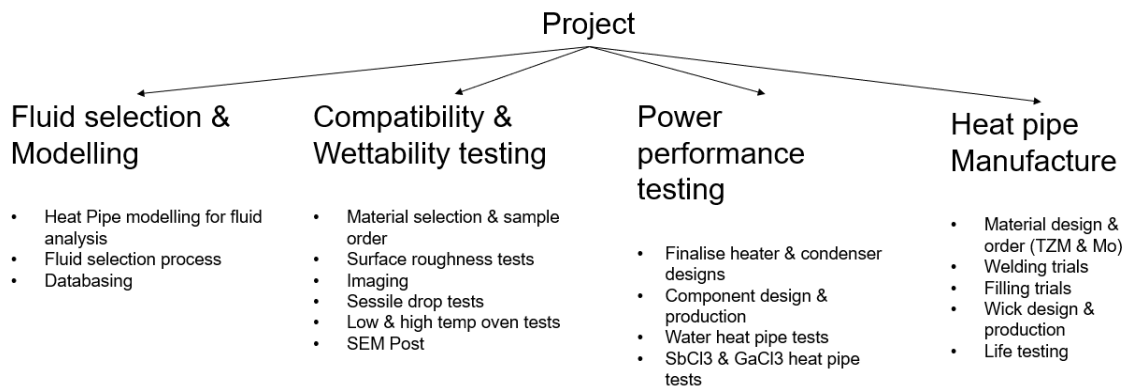


Figure 3-1 Umbrella view of the overall thesis

The experimental work is concentrated in parts 2 and 3 of the project studying the compatibility and wettability of various fluids and metals and in the development of a thermal performance test rig for medium temperature heat pipes. The designed structure of

these tests builds on the testing done by Rosenfeld et al. [87], Sarraf et al. [42], Devarakonda et al. [58] and Hay et al. [44] on high temperature water heat pipes, Jaworske et al. [88] on water/Titanium thermocycphons and Martin et al. [89] on Sodium heat pipes with reference also to the work by Yang [90], Tarau et al. [57] and Sena et al. [67]. The following chapter will detail the theory, techniques, apparatus, procedures and error analysis for all experimental methods.

3.2 Wettability and Compatibility Testing

The wettability and compatibility testing of the selected fluids on various metal samples is an essential part to selecting the best potential fluid for prototyping. Wettability tests show the relative ‘spreading’ ability of the fluid on each surface, which in turn indicates which metal may have the best capillary action associated with its wick structure. The compatibility tests indicate whether any reaction is likely to occur between the fluid and the metal resulting in undesirable by products or corrosion of the metal surfaces.

3.2.1 Wettability testing (using measure of contact angle)

A ‘wetting’ phenomenon takes place between solid/liquid substance interfaces, usually also with the presence of non-condensable gases (i.e. air). It is observed that any liquid on a solid surface forms a hemispherical shape due to the surface tension of the liquid acting against gravitational forces. The degree of wetting is dictated by the angle formed between the edges of the liquid hemisphere and the solid surface. This is measured by taking a two-dimensional side image of the droplet on the surface and measuring the angle at the left and right contact locations. The wetting angle is directly related to capillary force of the liquid in a porous surface, dictating the amount of lift that can be experienced.

In the liquid/solid droplet scenario, the interaction between the liquid and solid is dictated by the amount of surface energy – that is, the degree of intermolecular forces experienced on that surface. This creates the ‘attractive’ or ‘repulsive’ effect experienced

by the liquid. From this it can be ascertained that if the surface energy of the solid is stronger than the surface tension of the liquid, this would create a 'wetted' surface, whereas if the opposite was true this would create a 'non-wetted' surface. In the case of a heat pipe, the wick structure would benefit from the 'attractiveness' of its material to the liquid in the heat pipe as this would promote spreading through the wick structure and ultimately lead to higher capillary action. For this reason, the degree of wettability of the surface is a great measure of suitability of the metal as a heat pipe wall and wick material.

All contact angle experimentation is performed in accordance with BS EN 828:2013. The contact angle is the angle formed at the interface between liquid/vapour and solid surface as shown in Figure 3-2.

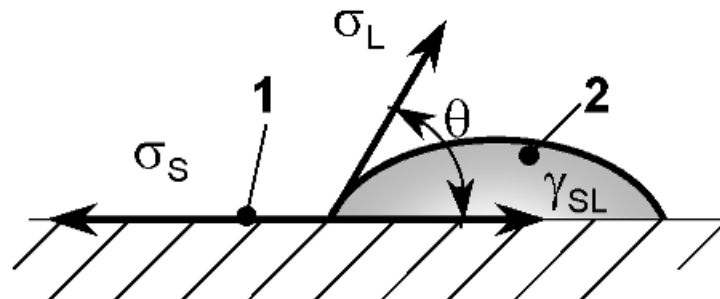


Figure 3-2 Contact angle example diagram

Where 1 is the substrate, 2 is the liquid drop, σ_L is the surface tension, σ_S is the surface free energy of the substrate, γ_{SL} is the interfacial energy of the substrate in contact with the liquid and θ is the contact angle.

This experiment aims to determine the contact angle of each chemical on each potential metal surface. The contact angle is used to calculate the capillary lift height of the liquid. The contact angle will be measured by direct inspection goniometry and a profile image of the drop will be taken and appropriate software will be used to measure the angle. For water tests standard conditions (temperature and pressure) will be maintained throughout the experiment to ensure results accuracy. For tests with halides, the temperature of the sample and surroundings is slowly elevated until melting point of the fluid is reached, and the contact angle can be measured. For health and safety reasons this experiment will be performed in a ventilated chamber. The drop volume needed will be determined so that gravitational effects on the contact angle are minimal. Measurements shall be carried out on different areas of the substrate. The microscope that will be used for the contact angle experiment can be seen in Figure 3-3.

3.2.2 Contact angle measuring techniques

In general, there are two classifications of contact angle: static and dynamic. The dynamic contact angle refers to the advancing and receding angles formed when the mass of the droplet is steadily increased and decreased, respectively. The static contact angle is the angle formed when a static droplet of the fluid is placed on the surface. For this study, both the static and advancing contact angles will be considered.

As the tests involve both liquid and solid chemicals at room temperature, two different testing techniques were employed. The first is the traditional technique where the fluid is dropped on to the metal surface through a syringe and the contact angle is measured

by a horizontally placed microscope. The second technique involves pre-placing the solid chemical on the metal surface within sealed container with an inert environment and heating the container with a heat gun until the melting point of the chemical is reached.

3.2.2.1 General apparatus

Figure 3-3 shows the apparatus used in each technique to measure the contact angle. This is the principal equipment used to image the droplet on the surface. This can be done in either still image or video form. The main test setup consists of:

- A long-range microscope
- An adjustable sample platform with monochromatic back light
- A programmable syringe
- Laptop with PyDSA and microscope software installed



Figure 3-3 Krüss contact angle measuring apparatus

Measurements using Antimony trichloride and Gallium trichloride are taken within a fume hood for safety and require a heat source to melt the chemical, in this case a variable temperature heat gun was used. Each metal sample that was used was pre-prepared by polishing the surface down to a 6um finish. The chemicals also required preparation in a low water inert atmosphere. There are three main procedures undertaken throughout testing; sample preparation, liquid contact angle testing and solids contact angle testing.

3.2.2.2 Procedure: Sample preparation

Various studies [91][92][93] have shown that the surface roughness can influence the degree of wetting between the liquid and solid. These studies show that the surface topography can have a major impact on the degree of wetting. For this reason, the sample preparation is a key process by which any meaningful comparison would only be possible if the surface topographies are be similar in roughness and structure.

Similarly, during compatibility testing, the surface roughness can be a measure of reactivity between the chemical and metal as deposits and corrosion can be indicated through roughening of the surface [94]. For these reasons, each of the samples flat surfaces is prepared beforehand using standard metal polishing process.



Figure 3-4 Polishing Apparatus

Figure 3-4 shows the apparatus used to polish the samples. These consist of rotating platforms on which the gritted paper is placed and rotated where the sample faces are then pressed against to effectively ‘sand down’ the surface to a finish. The general process requires the sample to be taken from the largest grit size to the smallest grit size in order. The grit sizes used in order of largest to smallest are P240, P400, P800, P1200 and 6um.

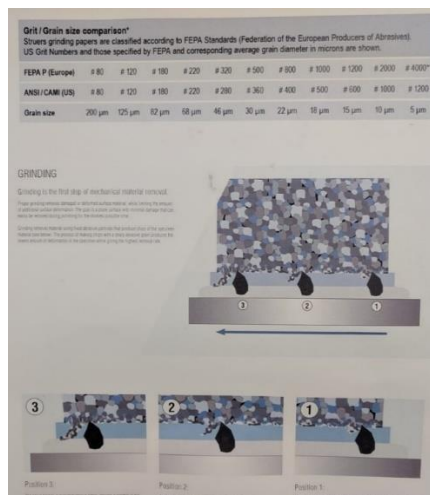


Figure 3-5 Polishing process

Figure 3-5 demonstrates how the polishing process works. The grit size determines the depth of the surface features as these are what removes the surface layer of metal. The grit must be used in the designated order as otherwise the surface features would be too large to be removed by the smaller grit sizes (which would drastically increase polishing time).

Table 3-1 shows the polish finish used for the top face of each sample. The coarse samples are used for compatibility testing as the tests aim to promote any reaction which may occur by increasing surface area while still maintaining a comparable surface finish. The smooth samples are the ones used for contact angle tests to take away any uncertainty of the contact angle with regards to a rough surface finish.

Table 3-1 Sample list and end polish specifications

Name	Date received/Produced	Size	Polished?	Weight (after polish)
Mo1	01-Jan	15x15	P240	26.6100
Mo2	01-Jan	15x15	P240	26.6900
Mo3	01-Jan	15x15	P1200	26.7300
Mo4	01-Jan	15x15	P1200	26.7400
TZM1	01-Jan	15x15	P240	26.7700
TZM2	01-Jan	15x15	P240	26.7100
TZM3	01-Jan	15x15	P1200	26.6000
TZM4	01-Jan	15x15	P1200	26.8100
W1	27-Feb	15x15	P240	50.8800
W2	27-Feb	15x15	P240	50.8100
W3	27-Feb	15x15	P1200	50.7200
W4	27-Feb	15x15	P1200	50.8300
W4	27-Feb	15x15	P1200	-
CuNi1	07-Jun	12.7x15	P240	16.6800
CuNi2	07-Jun	12.7x15	P240	16.6900
CuNi3	07-Jun	12.7x15	P1200	16.8000

CuNi4	07-Jun	12.7x15	P1200	16.3600
316SS1	24-Jul	15.875x15	P240	23.4400
316SS2	24-Jul	15.875x15	P240	23.2600
316SS3	24-Jul	15.875x15	P1200	23.6400
316SS4	24-Jul	15.875x15	P1200	23.4900
316SS4	24-Jul	15.875x15	P1200	-
304SS1	24-Jul	15x15	P240	20.9400
304SS2	24-Jul	15x15	P240	20.9600
304SS3	24-Jul	15x15	P1200	20.9800
304SS4	24-Jul	15x15	P1200	20.8700
304SS4	24-Jul	15x15	P1200	-
Ta1	27-Feb	15x15	P240	43.3300
Ta2	27-Feb	15x15	P240	43.9600
Ta3	27-Feb	15x15	P1200	44.3700
Ta4	27-Feb	15x15	P1200	44.4800
Ta4	27-Feb	15x15	P1200	-
Zr1	27-Feb	15x15	P240	17.1700
Zr2	27-Feb	15x15	P240	17.3300
Zr3	27-Feb	15x15	P1200	17.3900
Zr4	27-Feb	15x15	P1200	17.3200
Zr4	27-Feb	15x15	P1200	-
Nb1	27-Feb	15x15	P240	22.5200
Nb2	27-Feb	15x15	P240	22.6300
Nb3	27-Feb	15x15	P1200	22.4800
Nb4	27-Feb	15x15	P1200	22.9000
Nb4	27-Feb	15x15	P1200	-

In addition to polishing, the samples which will be used for the SbCl₃ and GaCl₃ contact angle tests require pre-preparation of a sealed sample within an inert atmosphere glovebox (to ensure there is no reaction with water once melted). The metal sample is lowered into a test tube and the equivalent of 4-6ul of the chemical is placed on the surface in solid form. The test tube is then sealed with a rubber septa to maintain the inert atmosphere as seen in Figure 3-6. For the inert atmosphere sample preparation process, a helium glovebox with water count of less than 6ppm is used.



Figure 3-6 Inert atmosphere sample



Figure 3-7 MBraun Glovebox

3.2.2.3 Procedure: Liquid contact angle

The first set of contact angle tests are undertaken with DI water. This will be used as a baseline to compare the wettability of the chosen metals against each other and compare the wettability of the chosen chemicals to that of water. Figure 3-3 shows the main apparatus used to conduct these tests and the equipment and procedure is described below.

Equipment:

- Sample
- 5ml syringe
- DI Water
- Kruss CA measuring system

Procedure:

- Prepare the syringe and mount on the Kruss syringe dispenser
- Set the delivery options to 4ul and 300ul/min
- Set backlight to 40%
- Position sample in focus of camera and dispense one droplet, adjust focus position accordingly
- For each sample, photograph 10 separate droplets and store the CA data
- Tests can be done on both sides of the sample for different roughness conditions comparison

3.2.2.4 Procedure: Solid-to-liquid contact angle

The second set of contact angle tests uses the selected fluids on the same (or very similar) metal surfaces. This test uses the samples prepared in inert atmosphere where the solid chemical is placed on the metal surface and films the heating process of the sample until the solid becomes fully liquid and the contact angle of the liquid chemical can be determined.

Once the video files are completed, the open access CA software pyDSA [95] is used to analyse the contact angle in each frame. A graph of contact angle over time is then plotted and the average contact angle of the point at which the chemical is liquefied to the end of the video is taken. Figure 3-8 shows the apparatus used for this procedure.

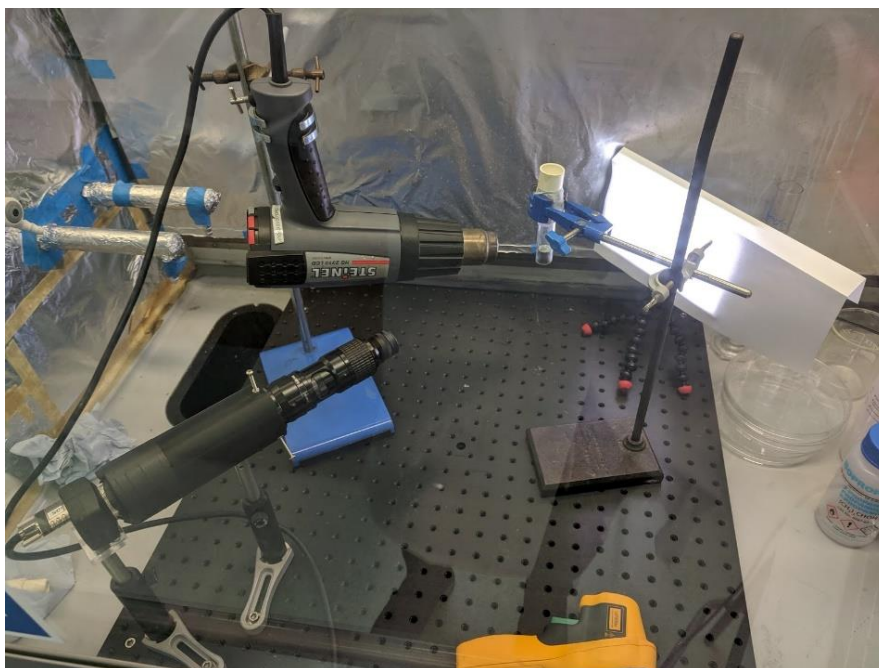


Figure 3-8 Solid-to-liquid contact angle test apparatus

Equipment:

- Microscope
- Stand and backlight
- Heat gun
- Laptop

Procedure:

- Prepare the equipment in a fume hood as present in Figure 3-7
- Ensure camera and sample are set so that the solid chemical is in focus
- Switch on the heat gun at 300°C and wait for the sample to start melting
- Once melting begins to occur, start recording on the microscope
- Stop recording a few seconds after the chemical is fully melted
- Save the video file
- Use pyDSA to calculate the contact angle over time

3.2.2.5 Software

There are two main software used for the contact angle testing, the inbuilt Kruss DSA software specific to the instrument and the open source pyDSA software [95] which is an open source python program for measuring contact angle with video files.

The Kruss software main window can be seen in Figure 3-9 where the syringe, lighting and imaging is controlled. The pyDSA software can measure the contact angle using a variety of best fit options, these can be adjusted according to the image quality and expected angle. Figure 3-10 shows the pyDSA software interface.

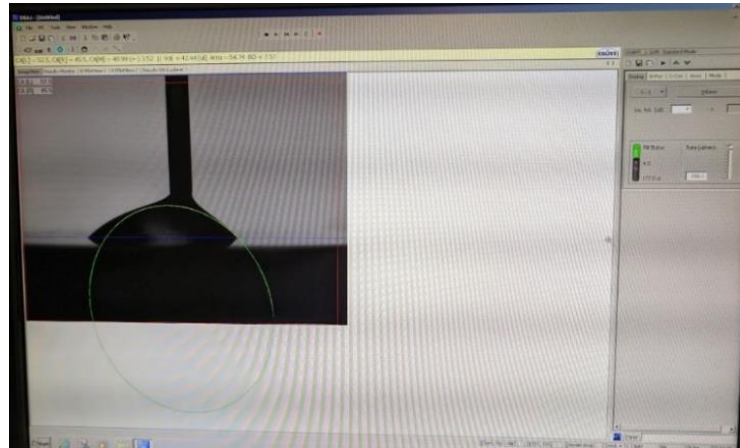


Figure 3-9 Kruss apparatus software

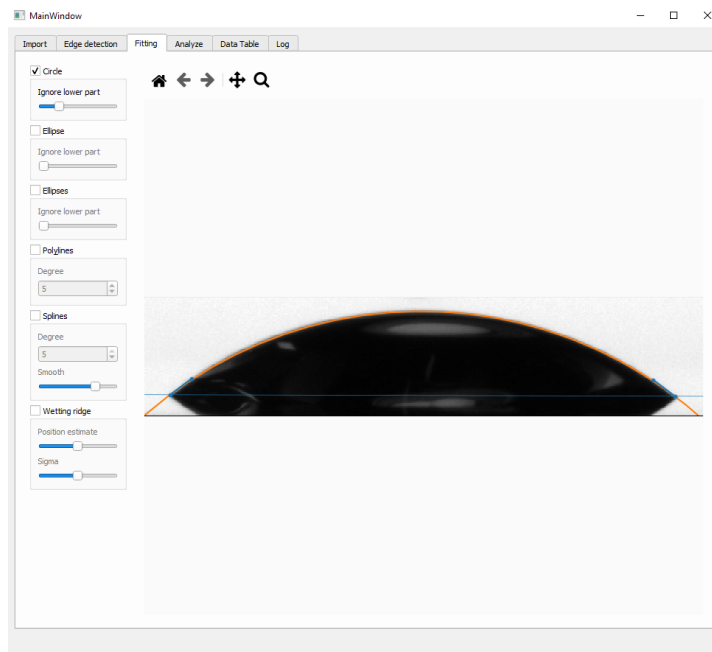


Figure 3-10 pyDSA software

3.2.3 Compatibility tests

The compatibility test aim to determine the extent of compatibility of each metal sample with the chosen chemicals at their melting point. To simulate internal heat pipe conditions and prevent any reaction of the chemical with water vapor, all samples were tested in vacuum. The metal samples were prepared according to the specification given in section 3.2.2.2. After polishing the surfaces of each sample with P240 grit, the roughness of the surfaces was tested using the Mitutoyo Surftest SJ-310 and the samples were prepared in vacuum resistant glass vials.

The main aim of the compatibility tests is to identify any reaction which may occur between the chemical and the metal by analysing the following features:

- Any changes in topography of the metal sample
- Any deposits on the metal surface
- Changes in the chemical colour in liquid form
- Deposits appearing in the chemical in liquid form
- Changes in chemistry of the liquid

These changes are tracked mainly through imaging techniques. The samples are photographed under a microscope before and after testing to identify changes on a macro scale and identify areas of interest. This then identifies section to be analysed under SEM and EDX. The surface roughness changes are identified by measuring the surface

roughness before and after the tests using the Mitutoyo Surftest mechanical surface analyser. The full sequence of testing can be seen in Figure 3-11.

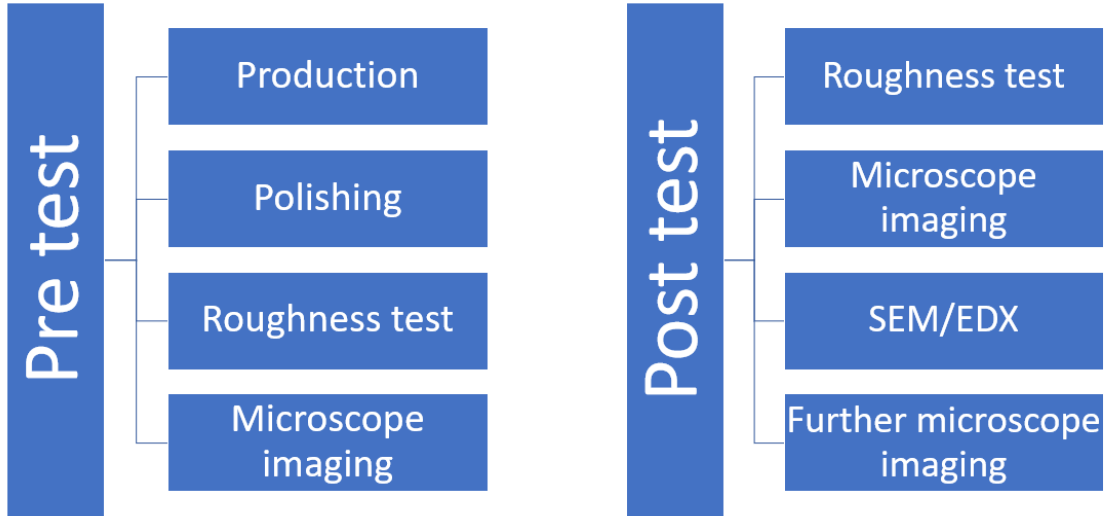


Figure 3-11 Compatibility sample pre and post-test prep sequence

The testing process simply consists of heating the vacuum sealed metal and fluid samples on a hot plate at the designated melting temperature of the fluid. A heat gun is also used to melt any condensation of the fluid occurring on the glass vial walls.

3.2.3.1 General apparatus

Table 3-2 shows a list of all apparatus used for the low and high temperature compatibility testing.

Table 3-2 Compatibility test apparatus list

Name	Image	Function
Glovebox		<p>To handle chemicals safely and prepare each compatibility sample</p>
Glass vial		<p>Vacuum resistant glass vials with a glass valve is used to keep samples under vacuum conditions</p>
Vacuum pump		<p>Pfeiffer vacuum pump is used to pull a vacuum in the glass vials</p>

<p>Hot plate</p>		<p>Hot plate used to maintain the chemicals above melting point</p>
<p>Vacuum Oven</p>		<p>Vacuum oven used to test the samples at higher temperatures</p>

3.2.3.2 Procedure: Compatibility tests

- Label the samples and prepare using the process described in section 3.2.2.2
- Photograph each sample using both a microscope and normal camera
- Insert sample into glass vial
- Insert 10g of chosen chemical into glass vial
- Seal the joints using vacuum seal grease
- Pull vacuum in glass vial to as low as is possible and close the valve
- Place sample on hotplate set to 100°C
- Photograph sample at each designated time interval
- Remove sample form hot plate and wait to cool, observe if re-solidification happens



Figure 3-12 Starting image of compatibility test

Figure 3-12 shows an image of the start of the compatibility test using Antimony Trichloride on a variety of samples.

3.2.3.3 Procedure: Roughness tests

- Program the device to desired sensitivity according to smoothness of surface being tested
- Place sample on testing platform
- Lower the testing pin manually until it touches the surface and registers as ‘mid-level’ (i.e. when the pointer on the screen is mid-range)
- Press ‘Start’

- Wait until process is finished
- Register the results for 'ra' in a results spreadsheet
- Repeat process 10 times for each sample, changing the sample orientation on the platform each time

3.2.3.4 Procedure: Microscope Imaging

- Place the sample on the microscope platform
- Manually adjust the focus
- Use the 'brightness settings' on the microscope to adjust brightness as necessary
- Click 'Save image' in the Leica software settings

3.2.3.5 Procedure: SEM/EDX Imaging

A short summary of the SEM and EDX imaging process can be found in Appendix

C.

3.3 Medium temperature thermal performance test rig

The heat pipe thermal performance test rig was developed with the aim to identify experimentally the maximum working limitation of the designed heat pipes. This section explores the validation and performance of each of the final component designs for the test rig detailed in Chapter 5. A full list of the apparatus used can be seen in Table 3-3.

Table 3-3 Test rig apparatus list

Component	Function
Julabo High Temperature Circulator	To cool and circulate the condenser fluid
Badger Pneumatic valve	Accurately control the flow rate of the cooling oil and feedback to flow meter
RHEONIC RHM 04 Flow meter	To measure the flow rate and control the valve
Heater	To provide input heat flux to heat pipe
Condenser	To provide a sink for the heat flux
Thermocouples	To measure the temperature across the heat pipe and the inlet/outlet temperature of the condenser oil
PICO temperature logger equipment	To record the temperature readings from each thermocouple over time

The test procedures and results are presented in this section. The main outputs are to define the following:

- Condenser temperature vs heat loss trend
- Heater temperature vs heat loss trend
- Condenser heat loss vs flow rate trend
- Thermocouple reading offset vs temperature

This section will summarise the procedures and results for the component part test. In each case, the outcomes will be presented and an explanation of how this was used to optimise component parts and increase precision is described.

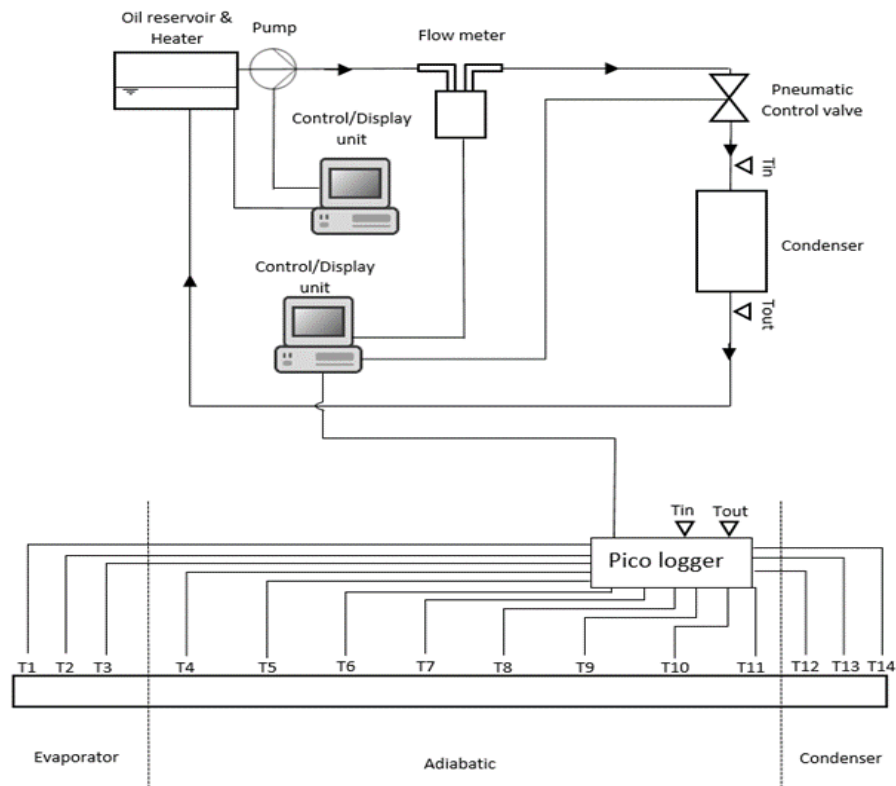


Figure 3-13 Experimental layout

3.3.1 Flow meter calibration

While the software offers a ‘calibration’ option, the flow meter has been used with various signal receivers and display software, hence the absolute accuracy of the readings are unidentified and systematic errors were prone from the receiver change. The calibration

utilises both mass and volume measurements over time to compare the displayed reading from actual values.

Nominal flow rates of 0.01, 0.02, 0.03 and 0.04 Kg/s were chosen as the reference points as these provide a low enough flow rate to more accurately determine the time at which the volume increments are reached. All tests were carried out at 80°C flow temperature. A slow-motion camera is used to record the scales as the test progresses, this allows the fluid weight data for each interval to be collected via picture, eliminating human error in the measurement. The volumetric data is measured by timer which does incur high likelihood of human error.

Equipment:

- Oil circulator and flow meter
- Scale
- 1l volumetric flask
- Camera
- Timer

3.3.1.1 Procedure: Flow meter calibration

- Set the circulator temperature to 80°C and flow meter reading to 0.01Kg/s
- Begin camera recording
- Begin timer

- Change oil outlet to volumetric flask
- Lap timer at every 50ml interval
- Stop when 1l has been reached
- Re-connect oil to circulator loop
- Increase flow rate reading by 0.01Kg/s
- Repeat steps 1 to 8 until 0.04Kg/s is reached

Table 3-4 shows an extract of the first test at 0.01Kg/s. The variables which are extracted from the tests are the time at which each volume interval was reached and the weight of the oil per time interval. The time is then corrected to account for transferal time of the oil line to the measuring vessel. From this, the mass flow rate and volume flow rates can be calculated at each interval and an average of these is taken. The ‘correction ratio’ is then calculated by dividing the set flow rate by the measured flow rate. This is done for both the mass flow rate and volume flow rate measurements, after which these two results are averaged. This process is then repeated for all four of the flow rates chosen. The final correction ratio is the total average of all the final mass and volume averages from each test; this was calculated to be 4.5.

Table 3-4 Flow rate calibration results example

Flow rate = 0.01 Kg/s								
ml	l	g	Kg	time	time	Kg/s	l/s	l/min
100	0.1	92.484	0.0925	47.66	42.86	0.002158	0.002333	0.139991
150	0.15	142.979	0.1430	71.72	66.92	0.002137	0.002241	0.134489
200	0.2	196.597	0.1966	97.34	92.54	0.002124	0.002161	0.129674
250	0.25	248.027	0.2480	121.17	116.37	0.002131	0.002148	0.128899

300	0.3	298.723	0.2987	143.94	139.14	0.002147	0.002156	0.129366
350	0.35	349.150	0.3492	166.25	161.45	0.002163	0.002168	0.130071
400	0.4	399.924	0.3999	189.17	184.37	0.002169	0.00217	0.130173
450	0.45	450.573	0.4506	211.36	206.56	0.002181	0.002179	0.130713
500	0.5	500.000	0.5000	233.7	228.9	0.002184	0.002184	0.131062
					Average	0.002155	0.002193	0.131604
		Correction ratio		4.64	kg/s			
				4.56	l/min			
				4.60	av			

3.3.2 Thermocouple calibration

To calibrate the thermocouples for accurate readings. The test aims to determine the level of variance in each thermocouple over the operating temperature range relative to both the oven temperature and a reference thermocouple temperature.

3.3.2.1 Procedure: Thermocouple calibration

The test consists of heating a calibration block with thermocouples attached in a highly thermally stable oven. To comply with national calibration standards [96] the block is heated in steps of 100°C varying from 100°C to 500°C.

Figure 3-14 shows the temperature data results for the calibration test in an isothermal oven. A time average of the last 10 minutes of each test was taken to determine each steady state thermocouple reading. From this, each thermocouple had a temperature reading difference against the oven set point was plotted as seen in Figure 3-15, where a

polynomial expression was the extracted to determine the correction factor for each thermocouple. The calibration was conducted after the testing was finished to gain a general sense of systematic error which may be present in the data. In this case it is observed that as the temperature increases, the temperature reading error tends increase with temperature from 100 to 300°C and then steadily decline again. This trend was the same for all thermocouples tested. The variation tends to reach up to 6°C at 300°C in all cases. Due to the quantity of data and the fact that the key qualities observed are dependent on temperature differences and not absolute temperature (e.g. the effective thermal conductivity), the calibration was performed by analysing the relative error of each thermocouple against each other.

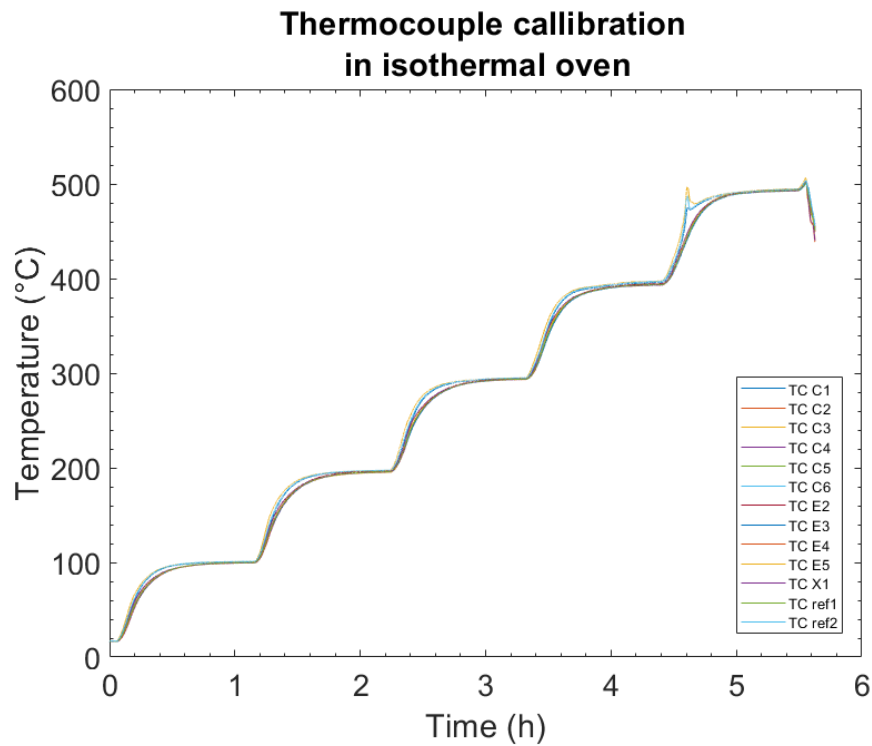


Figure 3-14 Thermocouple isothermal oven temperature data

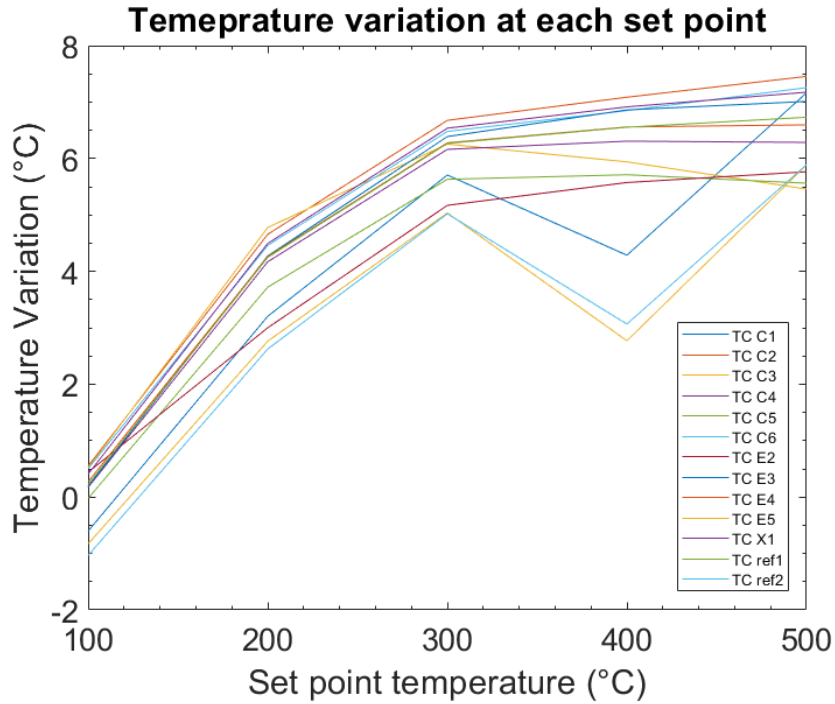


Figure 3-15 Individual thermocouple temperature difference trend with polynomial expression

3.3.3 Condenser heat loss

To define the amount of heat loss experienced by the condenser at various temperatures. At moderate temperatures, the test rig can achieve flow rates between 0.0056 kg/s and 0.0167 kg/s. To quantify the heat loss, a nominal flow rate of 0.0111 kg/s (the average flow rate of the minimum and maximum achievable) was determined to be most suitable.

The test methodology is to simply elevate the condenser temperature in steps of 50°C and record the inlet and outlet fluid temperatures from the condenser. The

temperature difference between these two values will then determine the amount of heat loss experienced over the condenser block through the heat equation, equation 45.

$$Q = \dot{m}c_p\Delta T \quad 45$$

3.3.3.1 Procedure: Condenser heat loss test

- Set the oil flow rate to 0.0111 kg/s
- Start recording the inlet and outlet fluid temperatures
- Set the circulator temperature at 50°C
- Wait until steady state is reached (approx. 1.5h)
- Increase the circulator temperature by 50°C
- Repeat steps 3 and 4 until 350°
- Stop recording data
- Cool circulator back to 50°
- Switch off

The recorded temperature data was analysed and the last 15min interval of each steady state was selected to determine the heat loss at each condenser temperature. From this, the inlet and outlet temperature data were averaged over the nominated time.

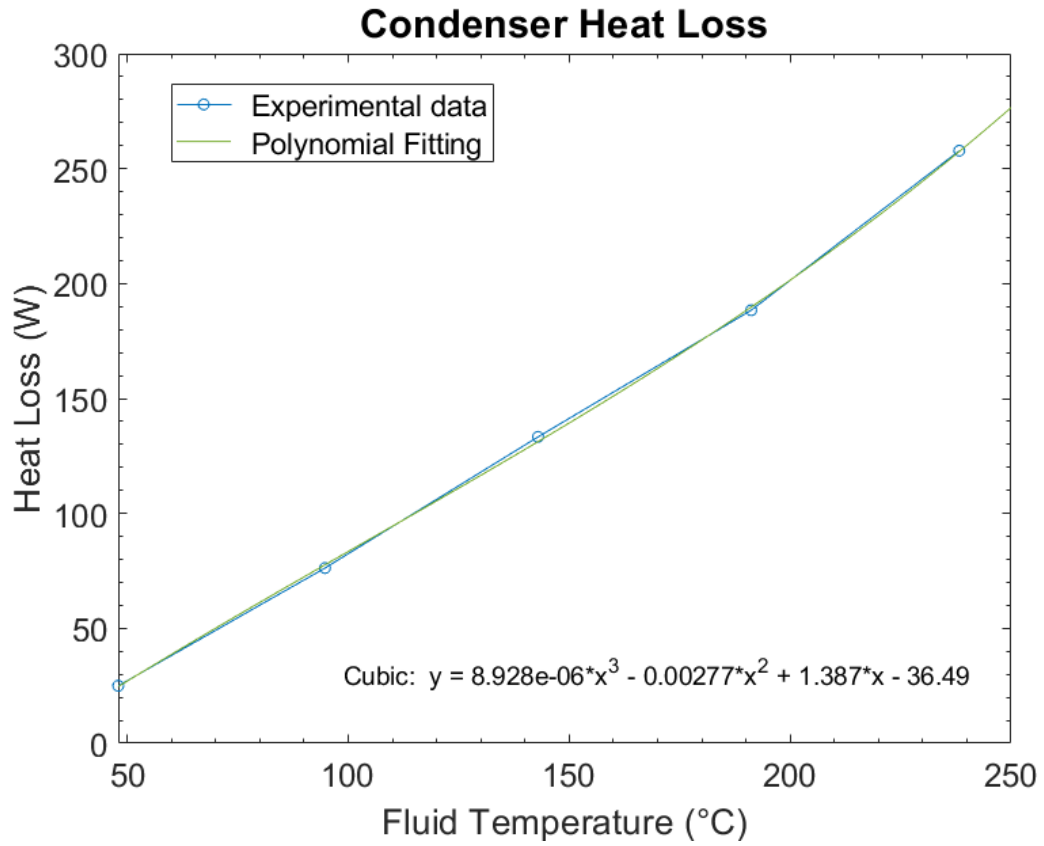


Figure 3-16 Condenser heat loss trend against average condenser fluid temperature

Figure 3-16 shows the results achieved from these tests, where the average trend line was then determined to provide a line equation and Table 3-5 shows each data point extracted from the tests.

Table 3-5 Condenser heat loss results table

Heat loss (W)	AV Fluid Temp (°C)
25.00	47.98
76.25	94.77
133.30	142.97
188.41	191.20
257.80	238.27

3.3.4 Heater heat loss

To define the amount of heat loss experience by the heater block at a given temperature. The test aims to increase the thermal load in designated intervals and record the temperature at which the heater stabilises at. This determines the thermal load required to maintain the block at a given temperature which, in turn, equates to the amount of heat loss experienced by the block.

3.3.4.1 Procedure: Heater heat loss test

- Place thermocouples at the designated locations on the heater block
- Begin recording temperature data
- Increase the power through the heater cartridges to 10W
- Leave until steady state is reached (approx. 10h)
- Increase the power input by 10W
- Repeat steps 4 and 5 until 50W is reached
- Switch off heater
- Stop recording data

The heater block temperature was averaged over a period of the last 3 hours recorded once steady state was reached. The ambient temperature was also recorded at each

steady state. Figure 3-17 shows the results of these tests and the averaged line of best fit giving the relation between the temperature and heat loss.

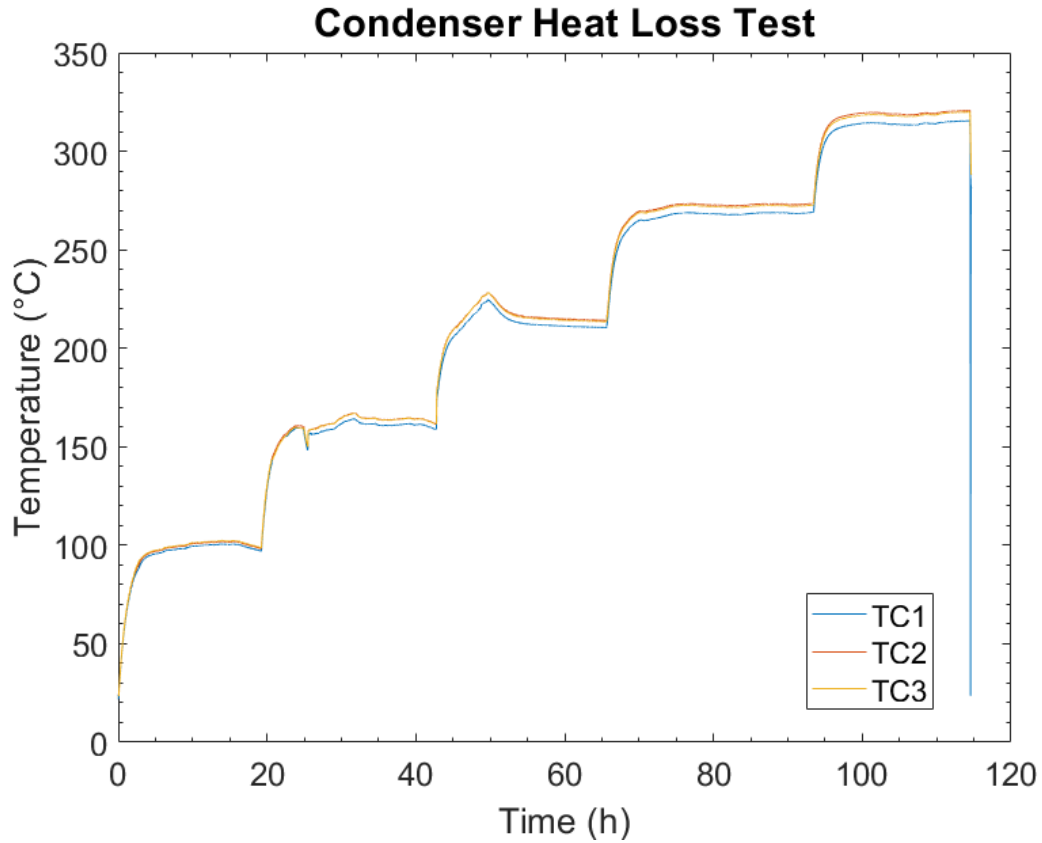


Figure 3-17 Heater thermocouple temperature reading over time

Table 3-6 shows the average results achieved for each power input over the last hour of the 3-hour heating period. As can be seen, the ambient temperature also experiences a slight increase over time, giving origin to a ‘nuisance’ factor for the heater heat loss prediction as this cannot be controlled. As the ambient temperature is expected to follow a similar trend throughout all testing, it was determined that this can still be used as an accurate representation of the heat loss to be expected.

Table 3-6 Heater heat loss results table

Power (W)	Heater temp (°C)	Ambient temp (°C)
10	100.67	17.37
20	162.00	19.24
30	215.10	19.64
40	270.54	22.31
50	317.38	23.09

3.4 Error analysis

In order to quantify the level of uncertainty in the results obtained in this study, an error analysis was carried on the calculated values which were obtained via experimentation or reliance on any equipment or method with intrinsic error. This of course is an essential part of any experimentation to gather a realistic view of how accurately the presented data represents the reality. The data presented further in the report will represent the error in the standard error bar format. This section will outline how the methodologies used behind the quantification of these error bars.

3.4.1 Overview of instrumentation used and accuracies

To first assess the source error from the instruments used to collect all the data which will be presented in this thesis, the manufacturer sourced measurement error of all equipment is presented in

Table 3-7. The manufacturer error gives a good indication of the accuracy at which the measurements can be taken and can be the basis error analysis of the reported values. The statistical error then gives an interpretation of the resultant data taken from these instruments and gives an indication of the precision at which the measurement can be taken assuming systematic errors are minimised. A comparison will be made between the instrument and statistical accuracy to determine which has the highest reported error. Though both values are important to ensure a full picture of the data, only the highest of

the two will be reported in the form of error bars. This is also true since most of the acquired data does not come from ‘population sampling’ and only from repeated measurements.

Table 3-7 Table of experimental instruments and their associated error

Form of measurement	Function	Operating range	Accuracy
K-Type Jubilee clip thermocouple	To measure the surface temperature of the adiabatic section of the heat pipe	-200°C to 1300°C	±0.75% ¹
K-Type Spring loaded M8 thermocouple	To measure the surface temperature of the Heater and Condenser sections of the heat pipe	-200°C to 1300°C	±0.75%
K-Type 150mm Stainless Steel sheathed thermocouple	To measure the temperature of the condenser circulator oil inlet and outlet	-200°C to 1300°C	±0.75%
TC-08	Thermocouple signal processing	Measurement: -270°C to 1820°C Conversion time: 1/10s Resolution: 0.025°C ²	Thermocouple dependent
Rheonik RHM 04 Coriolis flow meter	To measure the flow rate of the circulator oil	Flow rate: 0.05 Kg/min to 10 Kg/min Pressure: Up to 900 Bar Temp: -196 to +350°C ³	0.1% of flow rate
Mitutoyo Surftest SJ 400 Surface roughness tester	To measure the surface roughness of the metal samples	0 to 800um	±0.05um
Py-DSA contact angle measurement	To measure the contact angle of the fluid on metal surface using image processing	N/A	N/A
Power meter	To measure the power input to the heater cartridges	0 to 1kW	±2W
Vernier Calliper	Measure the wall thickness and inner/outer pipe diameter	0 to 100mm	±0.02mm

3.4.2 Thermocouple calibration and derivation of thermocouple error analysis

Appendix D shows the full test results for the thermocouple calibration. There you can see firstly the raw outputted value of each thermocouple for each set point (i.e.

¹ Information sourced from supplier website: <https://www.picotech.com/library/application-note/improving-the-accuracy-of-temperature-measurements>

² Information sourced from supplier website: <https://www.picotech.com/data-logger/tc-08/thermocouple-data-logger>

³ Information sourced from supplier website: <https://www.rheonik.com/products/small-size-sensors/rhm-04/>

reference temperature). The results show the temperature difference between the reading and the setpoint for each datapoint. For each given setpoint, the mean temperature difference was then calculated and the standard deviation for each dataset was also calculated. In this case the mean of each dataset represents the average systematic error which is present over all thermocouples with respect to temperature. Although this can be used to adjust the data, this would have little effect on the calculated values and would not have much benefit or change to the data analysis. The standard deviation shows the degree of variance between all the thermocouples relative to themselves. This serves as a much better indicator of the degree of error present in the overall measurements without the need for temperature adjustment of the raw data.

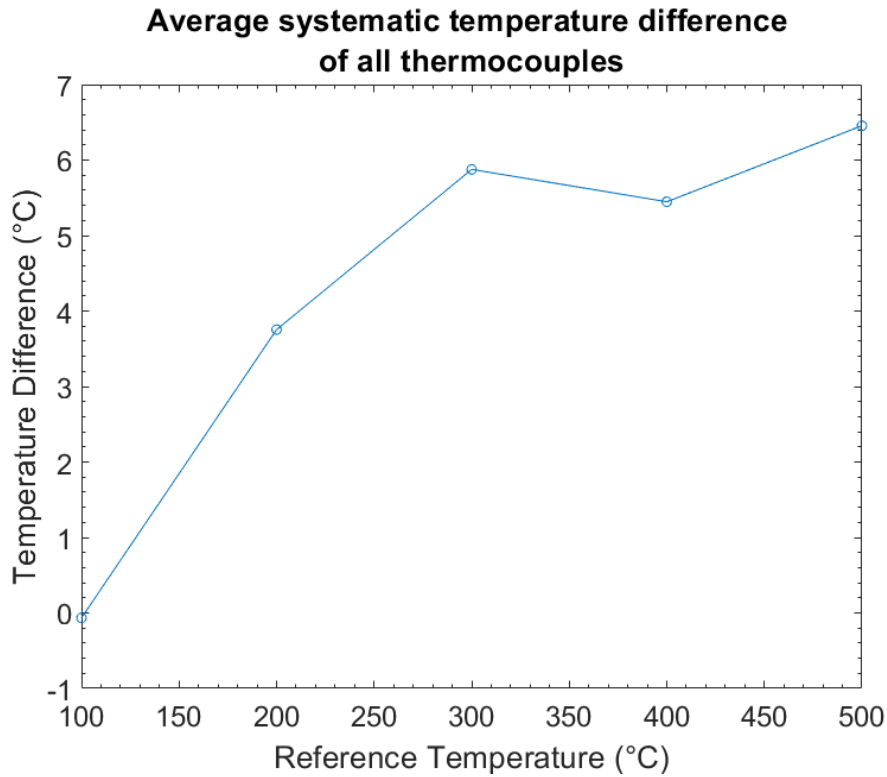


Figure 3-18 Average thermocouple temperature difference from benchmark

To calculate the error found for the mean temperature recorded of all thermocouples in the isothermal oven, the error can be estimated as the ‘Standard deviation of the mean’ as described by Taylor [97]. The standard deviation is defined as:

$$\sigma_x = \sqrt{\frac{1}{N-1} \sum_{i=1}^N (x_i - \bar{x})^2} \quad 46$$

Where ‘ σ_x ’ is the standard deviation, ‘ x_i ’ is the obtained value, ‘ \bar{x} ’ is the mean and ‘ N ’ is the number of measurements. From this parameter, the best estimation of the error is by calculating the ‘standard deviation of the mean’. This is represented as:

$$\sigma_{\bar{x}} = \frac{\sigma_x}{\sqrt{N}} \quad 47$$

Where ‘ $\sigma_{\bar{x}}$ ’ is the standard deviation of the mean, ‘ σ_x ’ is the standard deviation of the dataset and ‘ N ’ is the number of datapoints.

Table 3-8 shows the results for the mean, standard deviation (SD) and standard deviation of the mean (SDOM) for all thermocouples at each reference temperature. As seen in Table 3-8 SDOM varies between 0.15°C and 0.39°C. The largest SDOM is found at 400°C, indicating that results surrounding this temperature would present the lowest accuracy, whereas all other reference temperature has closer SODM’s indicating a higher accuracy. As the majority of the data will lie between 200°C and 300°C, it is safe to assume

that the data would remain in the higher accuracy range, nevertheless, the average SDOM of all reference temperatures was taken as the best estimated error of the thermocouples, this is $\pm 0.22^{\circ}\text{C}$.

Table 3-8 Error analysis of thermocouple calibration data

Reference temp	Mean difference	SD	SDOM
100	-0.06611	0.597055	0.154159
200	3.753779	0.788321	0.203544
300	5.87643	0.59762	0.154305
400	5.447529	1.54028	0.397699
500	6.454664	0.65767	0.16981
		Average SDOM	0.22

3.4.3 Statistical analysis of temperature measurements

In all cases where an experimental temperature value is reported, the resultant values is from a series of temperature measurements over a period of time where the experiment has remained in steady state. In most cases the number of measurements (N) will exceed $N = 500$. The reported value is the average measurement in this time period. Often two or more separate steady state conditions have been tested and the average of these results are reported. In all cases, the results were taken from data which had a standard deviation of $\leq 1^{\circ}\text{C}$, hence this value can be used as the maximum standard deviation of any data point.

For each reported temperature value, there was at least two averaged steady state values used. Considering maximum standard deviation of 1°C and the minimum number of samples used, the overall data error can be calculated using equation 46.

$$\sigma_{\bar{x}} = \frac{\sigma_x}{\sqrt{N}} = \frac{1}{\sqrt{2}} = \pm 0.71^\circ\text{C} \quad 48$$

3.4.4 Temperature difference error analysis

For any cases which use a temperature difference or temperature gradient, the uncertainty propagation theory can be applied to the temperature according to Taylor [97] where these measurements are assumed to be independent and random. The rule states that “The uncertainty in [the resultant value] is the quadratic sum”. Consider two temperature measurements as follows:

$$dT = T_1 - T_2 \quad 49$$

Where ‘ T_1 ’ and ‘ T_2 ’ are the product of repeatable experiments using the assigned thermocouples with accuracies of $\pm 0.75\%$. In this case the error presented in Equation 49 can be approximated to the sum of the intrinsic errors.

$$\partial T = \sqrt{\left(\frac{\partial T_1}{|T_1|}\right)^2 + \left(\frac{\partial T_2}{|T_2|}\right)^2} \quad 50$$

Hence, any temperature difference stated in the experimental results analysis will use this method of error analysis.

3.4.5 Error in reported circulator oil fluid properties

All circulator oil fluid properties are taken from supplier oil property data and a polynomial fit is used to estimate the fluid property that lies in intermediary values. All fluid property data can be found in Appendix E. Assuming that the error present in the values provided by the supplier is negligible⁴ the error in these measurements will be derived from the polynomial fitting to the provided datapoints. The R-square value of a polynomial serves as an indicator of ‘goodness of fit’ for the particular dataset – this will be used to assess the error in the reported data. The lowest reported R-square value was 99.67%, which indicates that that dataset will have a 0.33% error. This worst-case scenario error value will now be taken forward in any propagation calculations.

3.4.6 Error analysis of experimental equations

Using the same propagation theory, Taylor [97] states that “The fractional uncertainty in [the resultant value] is the sum in the quadrature of the original fractional uncertainties”. This of course bares a weighting on the reported values of each measured quantity as this will directly impact the fractional uncertainty. This section will outline the

⁴ This assumption is made due to necessity as the suppliers were unable to report the accuracy of these measurements

error present in all the key reported heat pipe thermal qualities taking into account the instrumentation error reported in

Table 3-7 and the oil fluid property error estimated in section 3. The thermal output of the heat pipe is measured using the following equation:

$$\dot{Q} = \dot{m}c_p\Delta T \quad 51$$

Where ‘ Q ’ is the output thermal load (W), ‘ \dot{m} ’ is the mass flow rate (Kg/s), ‘ c_p ’ is the specific heat capacity of the circulator oil at the average of inlet and outlet temperatures (J/KgK) and ‘ ΔT ’ is the inlet and outlet temperature difference (°C). Using the estimated error in the measurement of each of these quantities, the maximum expected error in the thermal load measurements can be calculated as:

$$\frac{\partial \dot{Q}}{|\dot{Q}|} = \sqrt{\left(\frac{\partial \dot{m}}{|\dot{m}|}\right)^2 + \left(\frac{\partial c_p}{|c_p|}\right)^2 + \left(\frac{\partial \Delta T}{|\Delta T|}\right)^2} \quad 52$$

The thermal resistance can then be determined by taking the temperature difference across the heat pipe and dividing it by the thermal load output.

$$R = \frac{T_e - T_c}{Q} \quad 53$$

Where ‘ R ’ is the thermal resistance, ‘ T_e ’ is the average temperature of the evaporator section, ‘ T_c ’ is the average temperature of the condenser section and ‘ Q ’ is the thermal load output measure by the calorimeter. In this case the error present in this calculation can be

$$\frac{\partial R}{|R|} = \sqrt{\frac{\partial dT^2}{|dT|} + \frac{\partial \dot{Q}^2}{|\dot{Q}|}} \quad 54$$

Equally, the effective conductivity error can then be determined through the same methodology.

$$K_{eff} = \frac{l_{eff}}{A_{xs}R} \quad 55$$

Where ‘ K_{eff} ’ is the effective thermal conductivity, ‘ l_{eff} ’ is the effective length of the heat pipe, ‘ A_{xs} ’ is the cross-sectional area of the heat pipe and ‘ R ’ is the thermal resistance of the heat pipe. The error is then calculated as:

$$\frac{\partial K_{eff}}{|K_{eff}|} = \sqrt{\frac{\partial l_{eff}^2}{|l_{eff}|} + \frac{\partial A_{xs}^2}{|A_{xs}|} + \frac{\partial R^2}{|R|}} \quad 56$$

The heat flux at the evaporator end of the heat pipe is defined through:

$$q = \frac{\dot{Q}}{A} \quad 57$$

Where ‘ \dot{q} ’ is the heat flux input, ‘ Q_{in} ’ is the measured thermal load input to the evaporator and ‘ A ’ is the surface area of the heat pipe evaporator section. The error can then be defined as:

$$\frac{\partial q}{|q|} = \sqrt{\frac{\partial \dot{Q}^2}{|\dot{Q}|} + \frac{\partial A^2}{|A|}} \quad 58$$

All equations are analysed individually for each steady state condition as the fractional uncertainties are dependent on the reported values.

3.4.7 Sessile drop error analysis

To determine the error present in the contact angle tests, the same standard deviation and standard deviation of the mean as represented by equations 46 and 47. Table 3-9 presents all the collected data for both the static and advancing water contact angle measurements for a variety of metal substrates. Both the standard deviation and standard deviation of the mean (SDM) are calculated for each value. The SDM is then subsequently used as the estimation of the error for each result. As expected, the static contact angle method presented the highest uncertainty in the results due to the variety factors which could affect the measurement (e.g. surface condition, ambient conditions, microscopic foreign bodies, etc.). The Advancing contact angle method presented a much higher

accuracy as this type of measurement suffers less from the randomised error presented in the static method.

Table 3-9 Static and advancing contact angle results table

Test type	Sample	Test 1	Test 2	Test 3	Mean	SD	SDM	
Static	Mo	50.72	66.73	63.84	60.43	8.534982	4.927674	
	TZM	60.20	75.18	73.12	69.50	8.119631	4.687871	
	Zr	51.44	72.11	68.97	64.17	11.13859	6.430869	
	304SS	76.93	75.10	74.14	75.39	1.417427	0.818352	
	Nb	47.39	52.66	58.30	52.78	5.456046	3.150049	
	316SS	53.50	79.09	70.04	67.54	12.97605	7.491728	
	Ta	52.20	75.18	51.97	59.78	13.33582	7.699441	
	CuNi	88.84	92.89	81.38	87.70	5.838581	3.370907	
W	50.64	84.44	72.04	69.04	17.10049	9.872975		
Test type	Sample	Test 1	Test 2	Test 3	Test 4	Mean	SD	SDM
Advancing	Mo	39.44	44.90	42.74	56.04	45.78	7.199171	3.599585
	TZM	56.67	49.41	64.84	68.35	59.82	8.490983	4.245492
	Zr	49.71	50.72	62.05	55.51	54.49	5.634872	2.817436
	304SS	60.87	66.83	67.29	64.23	64.81	2.947742	1.473871
	Nb	50.28	48.19	42.49	46.74	46.93	3.292213	1.646107
	316SS	64.43	62.60	54.53	54.64	59.05	5.208838	2.604419
	Ta	49.48	57.21	50.31	45.28	50.57	4.942826	2.471413
	CuNi	90.93	88.59	82.15	80.50	85.54	5.007623	2.503812
	W	51.87	56.47	64.51	58.36	57.80	5.2383	2.61915

3.5 Chapter Summary

This chapter has outlined all experimental techniques, instrumentation, procedures, methodologies and calculation of error for the experimental results which will use the described instruments thought the project. This chapter may serve as reference when analysing the experimental results presented in the following chapters to clarify any queries relating to quantitative and qualitative results analysis from the detailed equipment. A summary of the key topics covered is listed below.

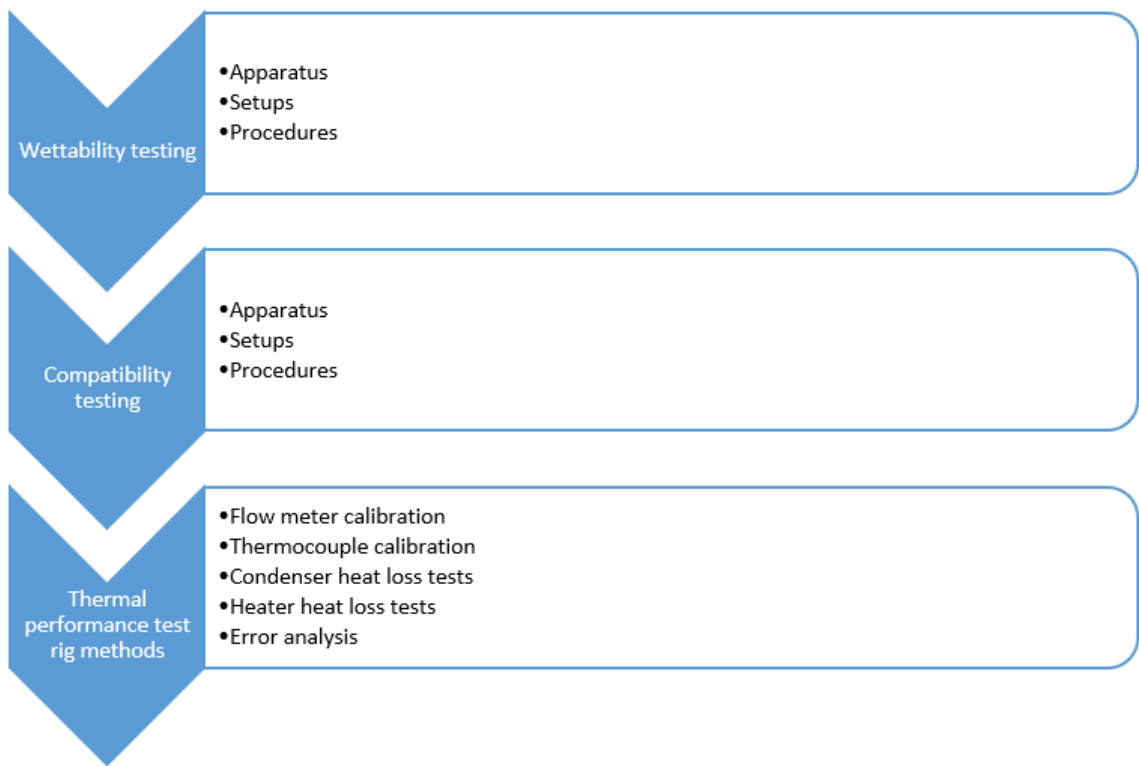


Figure 3-19 Chapter summary overview

Chapter IV

Investigation and modelling of medium temperature fluids

4.1 Introduction

This chapter will highlight the methodologies used in the fluid selection process and show the resultant analysis of a vast catalogue of potential fluids as well as the application of a heat pipe modelling programme on the shortlisted fluids. The creation of various databases which can be referenced and embedded within the heat pipe modelling for ease of fluid cross examination will also be highlighted. Working from the theory and methodologies behind the empirical based modelling highlighted in Chapters 2 and 3, this section shows the application of these in both the fluid selection process and heat pipe performance prediction modelling.

Previously, in Chapters 1 and 2, the importance of the fluid selection and why this has been a challenge in the medium temperature range for heat pipes was discussed. Due to the importance of determining an adequate fluid for the development of a medium temperature heat pipe, the fluid selection and modelling are the focal point of this study. The identification of one or more fluids to carry forward which meet the operational criteria, safety criteria and provide a cost-effective, marketable solution is the principal aim of this thesis. This is done through a combination extensive databasing and application of empirically based numerical modelling. The end goal is to develop a framework by which any new or novel fluid can be easily assessed for its potential as a heat pipe fill.

Heat pipe modelling is also of vital importance in assessing and comparing the performance of the selected fluids. The modelling in large uses established empirical

formulae to predict the thermal performance of the heat pipe, small adaptations of these formulae are assessed Chapter 7 when comparing the numerical results to experimental data. These are fed back into the model for improved accuracy. The model also offers the comparison between various equations or the selection of a specific equation to match the specific heat pipe conditions.

The fluid selection process, together with the fluid modelling program created the ‘fluid assessment framework’ by which all potential fluids can be rapidly assessed for viability. The framework aims to provide a faster pathway from conception to testing, able to iterate and compare large quantities of potential fluids to accelerate the selection process in any temperature range. In this case the framework aid in identifying potential fluids for the medium temperature range and taking forward the most viable options. Also, to quickly assess any new fluids which may be presented over the duration of the study and added to the database. The framework can also be applied in industry where the identification of the best possible fluid for a specific applications’ operating condition can be made. An example of a real case study industrial application utilising this framework is presented in Chapter 8.

4.1.1 Aims

The primary aims of the fluid analysis and modelling is to determine the optimal fluids to take forward into compatibility and wettability testing and ultimately be taken forward to prototyping. The modelling also offers numerical trend lines to compare against

experimental data for water-based heat pipes during the medium temperature heat pipe rig construction. Hence, the main aims are summarised as follows:

- Create a fluid assessment framework for rapid fluid selection from extensive databases
- Create custom fluid property and compatibility databases for ease of numerical modelling and to collate various sources
- Create a numerical model using empirical heat pipe performance calculations to determine the heat transfer limitation curves for each selected fluid
- Perform a weighted analysis to determine the most viable medium temperature fluid to take forward
- Present performance prediction graphs for all shortlisted fluids

4.2 Fluid selection process

The fluid criterion considers numerous factors from thermal performance to compatibility and toxicity. The methods of determining each criterion is detailed and subsequent quantitative analysis of available fluid data is made. The selection criterion identifies three main areas to be considered in heat pipe design: Fluid Properties, Application Requirements and Practical Requirements. These areas are subdivided into the various aspects linked to each principal condition as seen in Figure 4-1.

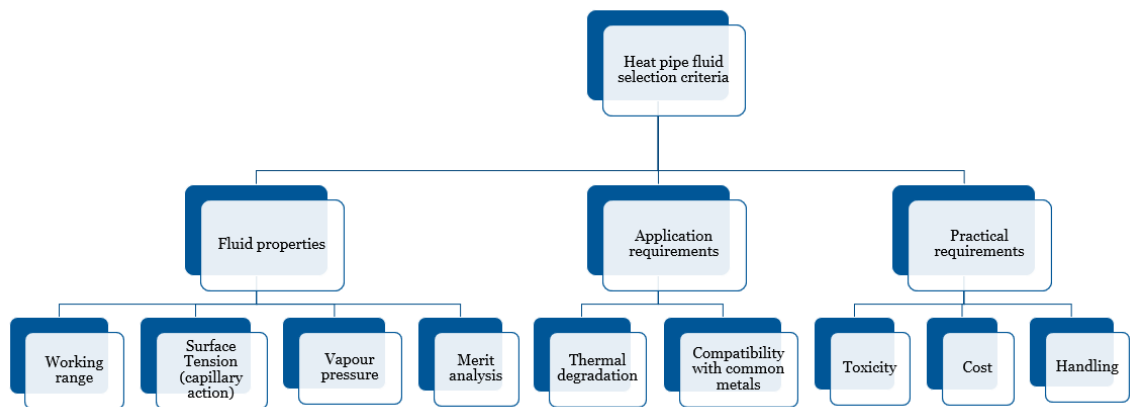


Figure 4-1 Selection Criteria subsection breakdown

Each sub-section will be fully characterised in this section of the report. Each category is then included in a weighted selection table to shortlist the top choice of fluids to be carried forward. The quantitative and qualitative methods used for each criterion is detailed.

The primary working fluid criteria is derived from each of the fluids' properties within the working temperature range. In order to determine most of the following criteria, the fluid property data must be known. The property data for each fluid is collected from various sources and collated in the 'fluid property database' detailed in section 4.2.2.1.

The desired properties in this range are those which promote heat transfer, allow for adequate levels of capillary action and remain at moderate pressures. These qualities are reflected in the merit curve, surface tension and vapour pressure respectively. Hence, these are used as comparative measures to assess the potential performance of each fluid. Limitation to handling and testing equipment available then determine the handling viability of the fluid according to its Material Safety Datasheet (MSD) outlining its toxicity, flammability and corrosiveness.

4.2.1 Methodology

The fluid selection process made use of a variety of analytical techniques to select and compare potential fluids within the required operating temperature range. In order to initially narrow the fluids to ones which function in some or all the temperature range, the property data must be analysed to determine whether key fluid properties are within range. The selection methodology follows a step process by which the potential fluids for analysis in any database is reduced to only a handful of fluids. The key process steps are detailed in Figure 4-2.

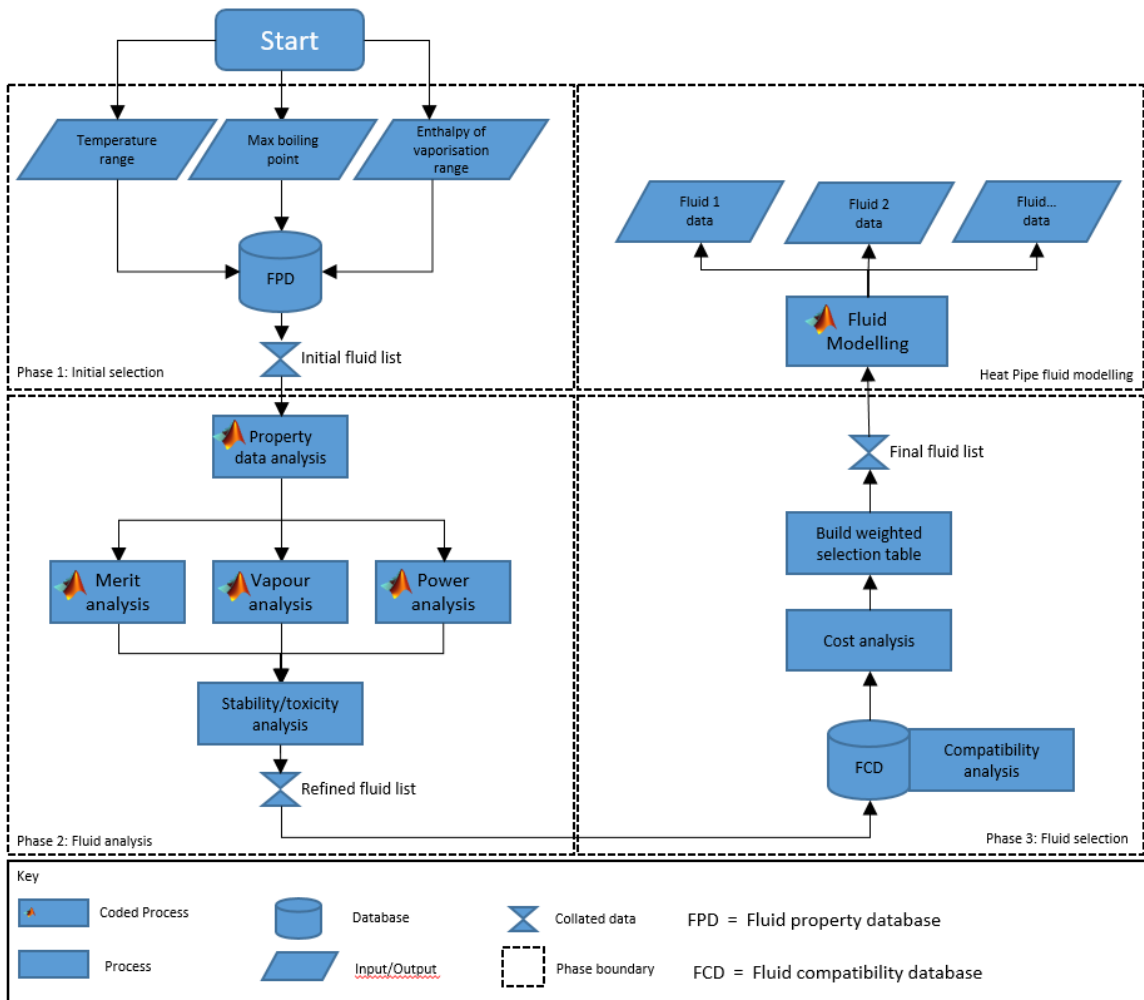


Figure 4-2 Process flow chart for fluid selection and modelling

4.2.1.1 Initial selection – Database search

To begin, an extensive search in designated databases on temperature range of heat transport capacity data with the aim to select all fluids within required range is conducted.

The general parameters to be applied are:

- Melting point must be lower than minimum operating temperature
- Boiling point (at 1atm) is usually higher than minimum operating temperature but must be within a 400°C range generally

- The maximum data range for enthalpy of vaporisation must be above maximum operating temperature
- The minimum data range for enthalpy of vaporisation must be below minimum operating temperature



Filters:

1 – Temperature range (melting point to critical temperature)

2- Boiling point

3 -Enthalpy of vaporisation data range

Figure 4-3 Fluid property database fluid selection filters

4.2.1.2 Fluid analysis

The ‘Merit Curves’ and Vapour pressure of the shortlisted fluids are then plotted against each other to compare the most viable options. The ‘Merit number’ is a commonly used measure of the heat transport capacity of the fluid given as a ratio of the heat transport enabling to heat transport retarding fluid properties. The Vapour pressure is also a key element to consider, this must be above a minimum threshold to overcome the viscous forces present in the wick and begin effective heat transportation in the pipe. It also must remain below a maximum threshold which would compromise the structural integrity of the heat pipe. The merit number, vapour pressure and weighting analysis analytical process will be discussed further.

The required property data for this process is the liquid density, liquid viscosity, thermal conductivity and latent heat capacity for each fluid. From this, stand-out fluids are selected and taken forward. At this point, a list of further criteria to perform a detailed comparative analysis is determined in accordance with the final application. In this case, the criteria chosen is:

- Thermal stability
- Stability in air
- Ease of handling
- Compatibility with conventional metals
- Completeness of property data

A deep search of these parameters is made by analysing their respective Material Safety Datasheets (MSD) and these are plotted in tabular format. From this, the fluids can be further shortlisted.

Merit analysis

The figure of merit of a fluid with respect to temperature determines the maximum heat transfer potential of a fluid by comparing its fluid flow and heat transport enabling qualities to its flow retarding quality. The result determines the maximum thermal transportation potential for a capillary limited system. The derivation of the figure of merit

can be seen in the equation relating to the maximum heat flux derived from the liquid pressure drop only in equation 59 [1].

$$\dot{Q} = \left[\frac{\rho_l \sigma_l h_{fg}}{\mu_l} \right] \left[\frac{KA}{l} \right] \left[\frac{2}{r_e} - \frac{\rho_l g l}{\sigma_l} \sin \theta \right] \quad 59$$

Where the if all geometric dependencies are removed and only the fluid properties are used to describe the maximum flux, the figure of merit emerges as

$$M = \frac{\rho_l \sigma_l h_{fg}}{\mu_l} \quad 60$$

The Merit analysis looks at the figure of merit curves of each chemical over the desired temperature range and serves as a direct comparison between the heat transport capabilities of each fluid. The higher the merit number at a given temperature, the higher the heat transport capability of that fluid. In order to undertake this analysis, key property data of each fluid must be given within the required temperature range, these are the vapour pressure, density, surface tension and liquid viscosity.

In order to conduct this analysis, an extensive database was developed where the fluid properties of each potential fluid were inputted in the desired temperature range. Some fluids, with limited property data available, were estimated based on fluids containing similar molecular structures or compared only by the available data. An example of a comparison study between the figures of merit of six different fluids is

presented in Figure 4-4. In this example Mercury, Iodine and Indium stand out as fluids which have a high potential for heat transportation in the 300°C to 600°C temperature range. As will be demonstrated though, a complete picture must be built before selecting any one fluid to take forward. Other examples of analysis conducted on the merit analysis of these and other fluids can be found widely used in literature [58], [98]–[100].

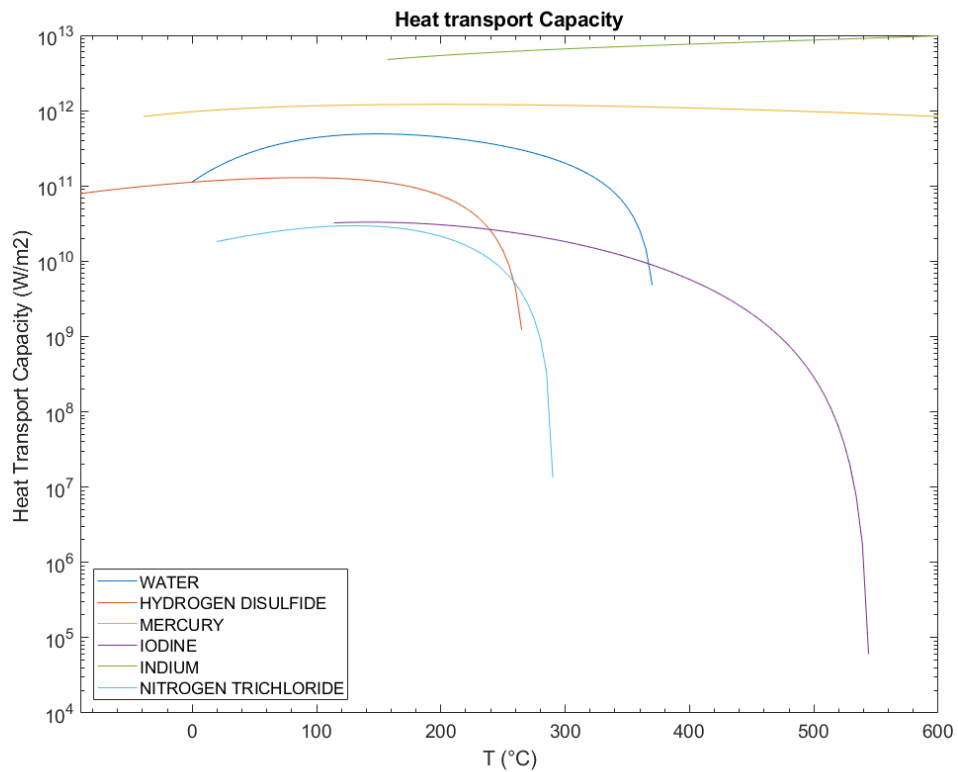


Figure 4-4 Figure of merit comparison example

Vapour pressure analysis

The vapour pressure of a fluid is a key feature to be analysed as this must be large enough to overcome frictional forces but not too large to require excessive wall thickness to cope with the internal pressure. This is the primary factor which determines the wall

thickness of the heat pipe, hence in order to decrease thermal resistance, moderate vapour pressures are desired to which minimal wall thickness is required. Due to these factors, this property forms an essential assessment criteria and comparative value between the selected fluids.

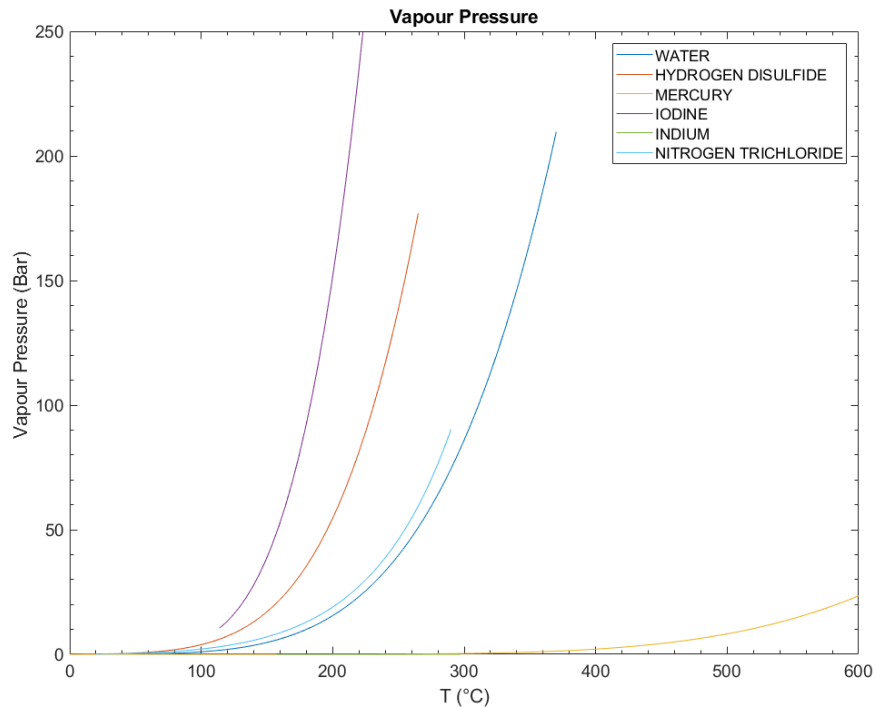


Figure 4-5 Vapour pressure comparison example

Figure 4-5 demonstrates a vapour pressure analysis on the same fluids used in the figure of merit analysis. Here it can be observed that although Mercury, Iodine and Indium stood out in the figure of merit analysis, the vapour pressure of Indium is excessively low in the desired temperature and that of Iodine is excessively high. Mercury is the most viable fluid in this case for operation above 350°C, hence this fluid could be taken forward from this analysis, however, the next process steps looks at the handling and toxicity. Due to the nature of Mercury, it can be assumed that it will have a relatively low score in these categories.

Thermal transport analysis (capillary limit)

Although the Merit analysis gives a good indication of potential performance of the fluid, a better indication when given a specific geometry is the Capillary limit curve. In most cases, the Capillary limit tends to dominate the limitation point through the majority of the fluids' working range. Hence, when given a specific geometry, the Capillary limit gives a very good indication of the maximum thermal transportation the fluid can achieve. This can then be used as another comparative tool to shortlist the most suitable fluids for a particular application. Details on the Capillary limit calculation can be found in Chapters 2 and 3.

4.2.1.3 Fluid selection

Lastly, a weighted analysis of the final shortlisted fluids is performed. The criteria for the weighted analysis table are the following:

- Stability in air
- Thermal stability at high temperature
- Toxicity/handling
- Merit curve
- Vapour pressure
- Cost

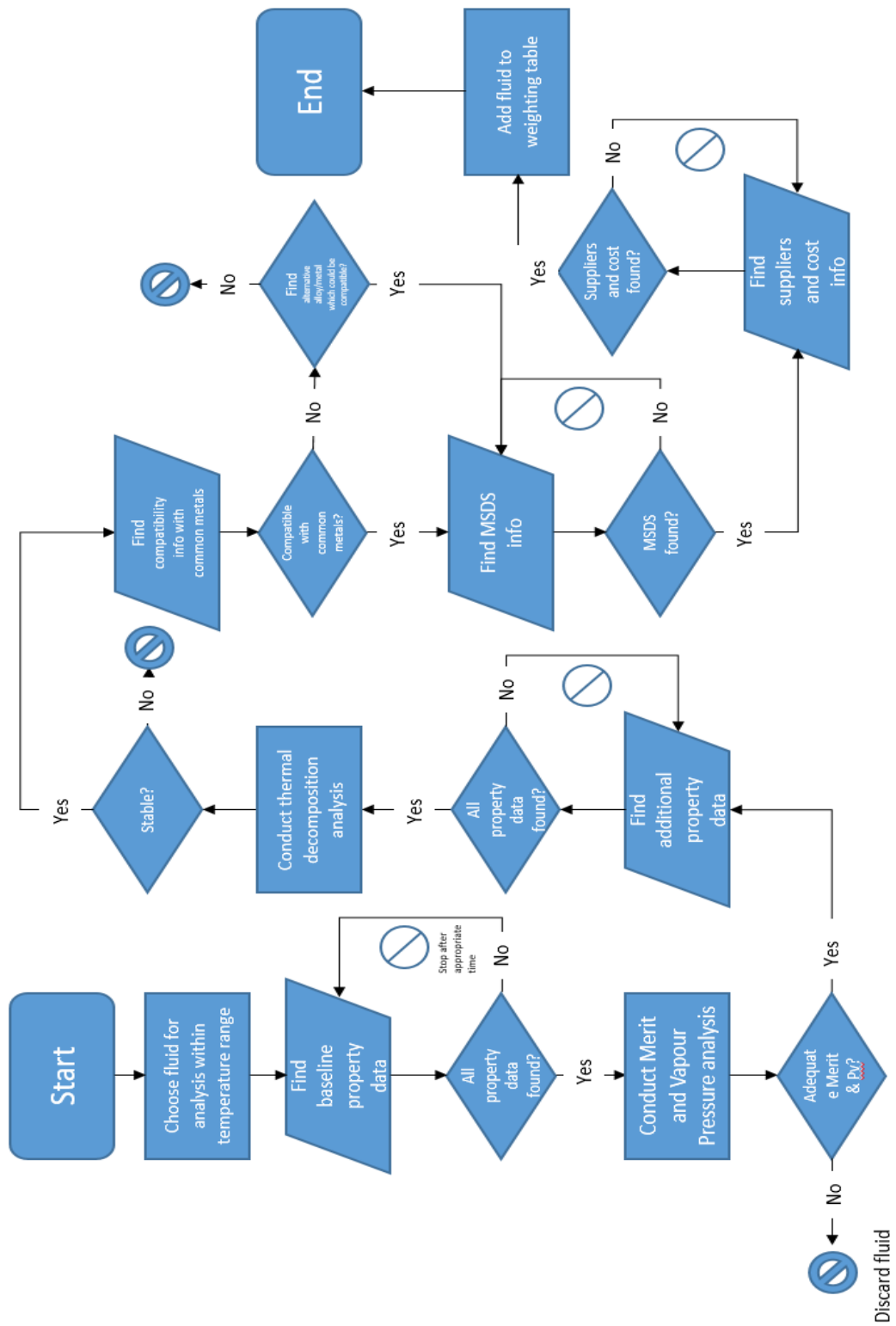


Figure 4-6 Process flow chart for each potential fluid

Figure 4-6 details a summarized process flow chart incorporating steps 2 and 3 described in Figure 4-2. The flow chart begins once the list of fluids able to operate in the temperature range is outputted from process step 1 (Database Search). This is used to streamline the analysis process for each fluid as there are often many fluids which fall within the first search criteria. The process then rapidly discards fluids which are unsuitable for any of the further criteria or have limited property data available. The shortlisted fluids are then put forward in the weighted selection table where a score is determined for each criterion and a weighted calculation determines the fluids' final score.

Weighted analysis

The final stage of the process is the weighted analysis. This considers all the determined criteria and assigns a scale of importance for each one by incorporating a 'weighting' system. Figure 4-7 shows an example of a weighted selection table where each category is weighted between 1 and 3 and the fluids are scored between 1 and 3 within the desired category. The sum of each category score multiplied by the category weighting is then divided by the sum of weightings to give the final score of the fluid as follows:

$$Final\ score = \frac{2 \times [ST] + 3 \times [TOX] + [PD] + 2 \times [MN] + 2 \times [VP] + 3 \times [C]}{13}$$

This will output a number between 1 and 3 indicating 'bad' to 'excellent' respectively. This final value can then be used to compare each of the selected fluids and identify the most suitable candidate.

The fluid scores are determined by comparing all fluids together within each category and coring them relative to each other. From this, each fluid is then assigned the 1 to 3 ranking according to their position in the category. Water is used as a reference fluid to determine the category boundaries (e.g. water would have a ranking of 3 for toxicity as it is non-toxic, if all other fluids have some level of toxicity none will be ranked as ‘3’).

	Weight	Water	Hydrogen Disulfide	Mercury	Iodine	Indium	Nitrogen Trichloride
		Inorganics					
Stability in air	2	3	3	3	3	2	2
Toxicity/ Handling	3	3	2	1	3	2	3
Property data	1	3	3	3	3	3	3
Merit Curve	2	3	2	3	2	2	2
Vapour Pressure	2	3	2	3	3	2	3
Cost	3	3	1	2	2	1	1
Score		3.00	2.00	2.31	2.62	1.85	2.23

Figure 4-7 Weighted selection table example

4.2.2 Database creation

The need for custom databases emerged as no property data source was found which contained all the required fluid properties for an extensive list of fluids. For this

reason, it became more practical to collate all data found into one source which could then be combined with the modelling code. This gives the advantage of having only a singular source for the baseline property data needed to be incorporated into the modelling process. As the modelling used incorporates such extensive property data (8 individual property data sets needed per fluid) it is imperative to create an efficient and accessible database system which can be easily updated when new fluids are to be analysed. The method chosen combines both excel and MATLAB databasing systems. The main sources of property data are detailed in Table 4-1.

Table 4-1 Property data sources

<i>Source</i>	<i>Types of property data found</i>
Chemical Property Handbook, Carl L. Yaws [101]	Polynomial
Dechema, Detherm [102]	Tabular
REFPROP, NIST [103]	Tabular
CoolProp, Ian H. Bel [104]	Tabular
National Chemical Database Service [105]	Tabular

There are three databases created: the fluid property database, the fluid compatibility database and the metal property database. The fluid property database lists all the required property data for each fluid and stores them in the form of curve fitting polynomials. This is then saved as .mat files and accessed through MATLAB which

automatically derives the property data curves and stores them as matrices. The fluid compatibility database is a log of every published fluid/metal compatibility test which is reported in any papers found. This provides a source of experimentally verified fluid/metal combination list which can be accessed during the fluid selection stage to identify viable metal envelopes for each chosen fluid. The metal property database presents polynomial equations for the tensile strength and conductivity variance over the operating temperature range where possible. If data over the temperature range is not found, fixed values are used for data at the closest temperature.

4.2.2.1 Fluid property database

The fluid property database is initially created in excel. The data primarily originated from Carl L. Yaws [1] as this was the most complete database. Data derived from other databases was translated into the polynomial function trend line determined by Yaws for each specific fluid property. shows the fluid property database structure in Excel.

Once the excel file is constructed, each fluid property tab can be converted to a .mat file via the process described in Chapter 3. These '.mat' files can then be directly loaded into the modelling code to access the property data for any of the fluids listed in the database.

4.2.2.2 Compatibility database

The compatibility database makes use of macros coding to perform internal searches for compatibility data. A dropdown list allows the selection of the fluid and the ‘Go’ button forwards the user to the published compatibility data.

Once a fluid is selected, the user will be forwarded to the compatibility data log. The database is constantly being updated as new studies are found which contain any compatibility results. The studies are referenced within the database under the ‘source’ heading.

4.2.2.3 Metal property database

The metal property database contains polynomial data for the Young’s Modulus, Tensile Strength and Thermal Conductivity where possible. Where polynomial data is not yet available, the values will defer to room temperature data. As of writing, polynomial data has been sourced only for four metal types. This database is also converted to ‘.mat’ file type to be used within the MATLAB coding.

4.2.3 Selection criteria

Section 4.2.1 detailed the various selection criterial which are used in the analysis process. This section will describe in more detail each criteria and give a deeper

explanation of how these are applied in the fluid selection process. Both quantitative and qualitative analyses are used depending on the nature of the criteria – the main objective, however, is to have a definitive ranking by which to categorise any fluid within each criteria.

4.2.3.1 Surface Tension

The surface tension of the fluid determines the extent of the capillary action possible in the wick structure. This is also a critical factor in the operation of the heat pipe as this determines the extent to which the heat pipe can operate against gravity and also the maximum length to which capillary action is possible. This has a strong bearing on the capillary limit of the heat pipe. The physics behind this quality is highlighted in Chapter 6, for purposes of fluid selection, this quality is intrinsically linked to the Merit Analysis and Thermal transport Analysis of the fluid.

4.2.3.2 Thermal Degradation and compatibility

For applications which require long term use, often they require a measure of the performance reduction over its lifetime and set the maximum allowable limit for this. The performance reduction of a heat pipe is caused by three main factors:

- Degradation of the fluid over time (thermal degradation)
- The compatibility of the fluid and metal envelope

- Reaction of the fluid with any other impurity which may be present

All these factors lead to the formation of non-condensable gasses (NCGs) within the pipe causing a reduction in performance. The fluid assessment criterion looks at both the compatibility of each fluid with commonly used metals for heat pipe production and the thermal degradation of the fluid at the maximum operating temperature.

The thermal degradation of a fluid is usually measured through its rate of pyrolysis. This determines the temperature at which the gas phase of the fluid begins to break down into its constituent atoms or molecules. This is particularly prone in long chained molecules such as organic compounds.

The compatibility is simply the affinity of reaction of the chemical at high temperatures with the wall material metals. Though some models have demonstrated some level of predictability of reaction [49] the principal method of analysis generally is experimental. The compatibility is assessed through 'life test' on each fluid/metal combination where the functionality of the heat pipe is measured over a long period of time where the heat pipe properties must remain within a threshold value. The compatibility database was developed to log the testing done by previous researchers and their main findings.

4.2.3.3 Toxicity

The toxicity of the fluid is a very important quality to be aware of. Lack of information on the correct handling of a fluid can lead to serious injury and even death. Any fluids which are toxic to humans tend to have strict handling criteria which must be adhered to by law. A thorough analysis is made on each shortlisted fluid as to the handling dangers and precautions necessary. A low score would signify that the fluid is extremely dangerous to handle and presents too high a risk should accidental exposure occur. Alternatively, a high score would indicate that the fluid is safe to handle and very few specialist equipment is needed. The use of bespoke PPE and need for gloveboxes is also factored in as this would direct impact on the time and cost of testing the fluid.

4.2.3.4 Cost

This is simply the raw cost of the material. This is conducted via a search on various chemical supply company websites and the cheapest result for small batches is selected. This is simply ranked from most expensive (low score) to least expensive (high score).

4.2.3.5 Handling

This mainly consists of identifying any use of specialist equipment or ‘controlled environments’ to handle the fluids in. Cost of new equipment needed, and safety of storage is factored into this category.

4.2.4 Conclusions

This section has presented a complete framework in which to identify, analyse, compare and select optimal heat pipe working fluids for any application. The process makes use of databases which were developed over the entirety of this project and which will aim to be continually updated. The various criteria chosen to distinguish wanted fluid characteristics is detailed and the framework in which the analysis takes place is outlined. An overview of all the processes taking place to filter the fluids down to the best viable options has been presented. The application of this framework and identification of key fluids relevant to this study is presented in Section 4.3. The framework has selected 9 key criteria by which to analyse any heat pipe fluid, these are; Merit Analysis, Vapour Pressure Analysis, Thermal Transport Analysis, Surface Tension, Compatibility/Thermal Degradation, Toxicity, Cost and Handling. The theory and application of these criteria as well as a selection process is formulated to quantitatively and qualitatively compare the performance of any selection of fluids.

In this study, the framework is aimed solely at the exploration of fluids in the ‘medium’ temperature range with aim to identify novel fluids which can be taken forward for testing. The methodology can however be applied universally and span any desired application temperature range; hence the framework can be used as a powerful industrial research and development tool. Chapter 8 outlines a real case study for an industrial application which successfully used this framework to explore potential novel fluids in the 1000°C to 1500°C temperature range proving the methodology to be successful in a

commercial setting as well as academic. Section 4.3 will present the application of this framework and outline the full identification and selection process for novel medium temperature fluids.

4.3 Fluid selection & analysis

The following section outlines the full fluid analysis on potential heat pipe fluids for the medium temperature range using the methodology described in Section 4.2. Code was developed in MATLAB to extract and plot the data from the fluid property database and compare the performance of the selected fluids. The code developed for this analysis can be found in Appendix F

By applying the methodology described in Chapter 2 and using developed code to assess multiple fluids at once, the process flow chart described in Figure 4-6 could be applied to all shortlisted fluids simultaneously. The process steps are divided into three phases, where at the end of each phase signifies a narrowing of the fluid selection. Figure 4-2 describes the processes assigned to each phase.

Work on the selection process, coding, data collection and data analysis was a continual process throughout the entire duration of the study. The results presented in this section represent the latest available data and developed code. This does not reflect the data which was available when commencing experimental analysis of compatibility and wettability tests, hence, the conclusion of this study is aimed at future work on potential fluids using the techniques developed with the available metals and fluids at the time.

4.3.1 Phase 1: Initial selection

The initial fluid selection consists mainly of the fluid property database search. The chosen filters for the medium temperature fluid selection are:

- Melting point must be $< 300^{\circ}\text{C}$
- Boiling point must be $< 700^{\circ}\text{C}$
- Hfg max data $> 400^{\circ}\text{C}$
- Hfg min data $0 < x < 300^{\circ}\text{C}$

The fluids are selected only if all the filter conditions are satisfied. This narrowed the field to 36 potential fluids from the initial 343 fluids present in the database. The shortlisted fluids are displayed in Table 4-2.

Table 4-2 Phase 1 fluid shortlist

Fluid Code	Formula	Name
6	AlBr3	ALUMINIUM BROMIDE
9	AlI3	ALUMINIUM IODIDE
14	AsBr3	ARSENIC TRIBROMIDE
19	AsI3	ARSENIC TRIIODIDE
36	B10H14	DECABORANE
45	BiBr3	BISMUTH TRIBROMIDE
46	BiCl3	BISMUTH TRICHLORIDE
52	CH4N2O	UREA
53	CH4N2S	THIOUREA
67	CbF5	COLUMBIUM FLUORIDE
87	CrC6O6	CHROMIUM CARBONYL
89	Cs	CESIUM
109	Fr	FRANCIUM
111	GaCl3	GALLIUM TRICHLORIDE
114	GeBr4	GERMANIUM BROMIDE
139	HgBr2	MERCURIC BROMIDE
140	HgCl2	MERCURIC CHLORIDE
141	HgI2	MERCURIC IODIDE
143	I2	IODINE
212	P	PHOSPHORUS - WHITE
222	PSBr3	PHOSPHORUS THIOBROMIDE
224	P4O6	PHOSPHORUS TRIOXIDE
226	P4S10	PHOSPHORUS PENTASULFIDE
244	Re2O7	RHENIUM HEPTOXIDE
248	RuF5	RUTHENIUM PENTAFLUORIDE
249	S	SULFUR
260	SbBr3	ANTIMONY TRIBROMIDE
261	SbCl3	ANTIMONY TRICHLORIDE
264	SbI3	ANTIMONY TRIIODIDE
267	Se	SELENIUM
268	SeCl4	SELENIUM TETRACHLORIDE
270	SeOCl2	SELENIUM OXYCHLORIDE
301	Si3Cl8	OCTACHLOROTRISILANE
307	SnBr4	STANNIC BROMIDE
308	SnCl2	STANNOUS CHLORIDE
311	SnI4	STANNIC IODIDE
317	TeCl4	TELLURIUM TETRACHLORIDE

4.3.2 Phase 2: Fluid analysis

The second phase makes use of the various analytical techniques presented in Chapter 3. The process follows the flow chart presented in Figure 4-2. The results of each analysis are presented in this section.

4.3.2.1 Property data analysis

The first analysis to be undertaken is an assessment of the available property data of the selected fluids. This is a crucial starting point as although some fluids may seem viable for an initial Merit and Vapour analysis, a lack of complete data would impede any heat pipe modelling to be done.

From an assessment of time and resources, it was concluded that fundamental property experiments on individual fluids to acquire any missing data would not be possible in the time frame, and would not provide a sufficient cost-benefit to the project, hence any fluids with lacking property data from the available sources was initially eliminated from the study. These were, however, kept in an archive should further research find any missing data on these fluids.

Table 4-3 summarises the latest data analysis of the shortlisted fluids. Here it can be observed that only 14 fluids possessed complete property data. Fluids highlighted in yellow signify that some property data was ‘deduced’ by taking the property data from a

similar compound. In some cases, no data on the fluid or any similar fluids was found, these are highlighted in red and discarded form further analysis.

Table 4-3 Property data analysis of shortlisted fluids

NO	FORMULA	NAME	Property data Complete?
6	AlBr3	ALUMINIUM BROMIDE	Yes, st deduced
9	A113	ALUMINIUM IODIDE	Yes, Kl deduced
14	AsBr3	ARSENIC TRIBROMIDE	Yes
19	AsI3	ARSENIC TRIIODIDE	Yes, st deduced
36	B10H14	DECABORANE	Yes, st & Kl deduced
45	BiBr3	BISMUTH TRIBROMIDE	Yes, Kl and Kv deduced
46	BiCl3	BISMUTH TRICHLORIDE	Yes, Kl deduced
52	CH4N2O	UREA	No - st missing
53	CH4N2S	THIOUREA	No - st missing
67	CbF5	COLUMBIUM FLUORIDE	No - st missing
87	CrC606	CHROMIUM CARBONYL	Yes, Kv & st deduced
89	Cs	CESIUM	Yes
109	Fr	FRANCIUM	No - rhol, st, vl, missing
111	GaCl3	GALLIUM TRICHLORIDE	Yes
114	GeBr4	GERMANIUM BROMIDE	Yes
139	HgBr2	MERCURIC BROMIDE	Yes, Kl deduced
140	HgCl2	MERCURIC CHLORIDE	Yes, Kl deduced
141	HgI2	MERCURIC IODIDE	Yes, Kl deduced
143	I	IODINE	Yes
212	P	PHOSPHORUS - WHITE	Yes
222	PSBr3	PHOSPHORUS THIOBROMIDE	Yes
224	P4O6	PHOSPHORUS TRIOXIDE	Yes
226	P4S10	PHOSPHORUS PENTASULFIDE	Yes
244	Re2O7	RHENIUM HEPTOXIDE	Yes, st deduced
248	RuF5	RUTHENIUM PENTAFLUORIDE	Yes, st deduced
249	S	SULFUR	Yes, but not for whole range
260	SbBr3	ANTIMONY TRIBROMIDE	Yes, st deduced
261	SbCl3	ANTIMONY TRICHLORIDE	Yes
264	SbI3	ANTIMONY TRIIODIDE	Yes, st deduced
267	Se	SELENIUM	
268	SeCl4	SELENIUM TETRACHLORIDE	Yes, st deduced
270	SeOCl2	SELENIUM OXYCHLORIDE	Yes
301	Si3C18	OCTACHLOROTRISILANE	Yes
307	SnBr4	STANNIC BROMIDE	Yes
308	SnCl2	STANNOUS CHLORIDE	Yes
311	SnI4	STANNIC IODIDE	Yes, st deduced
317	TeCl4	TELLURIUM TETRACHLORIDE	Yes, st deduced

4.3.2.2 Merit analysis

A merit analysis was undertaken on each of the fluids according to the process described in Section 4.2.1.2. As a means of comparison, water was included in the analysis to provide a reference point. To aid the analysis, the fluid list was split into two as shown in Figure 4-8 and Figure 4-9. These graphs give various indications; the functional limit of each fluid, which fluids have the best heat transport capability, how each fluid compares to each other and which fluids can operate over the entire temperature range.

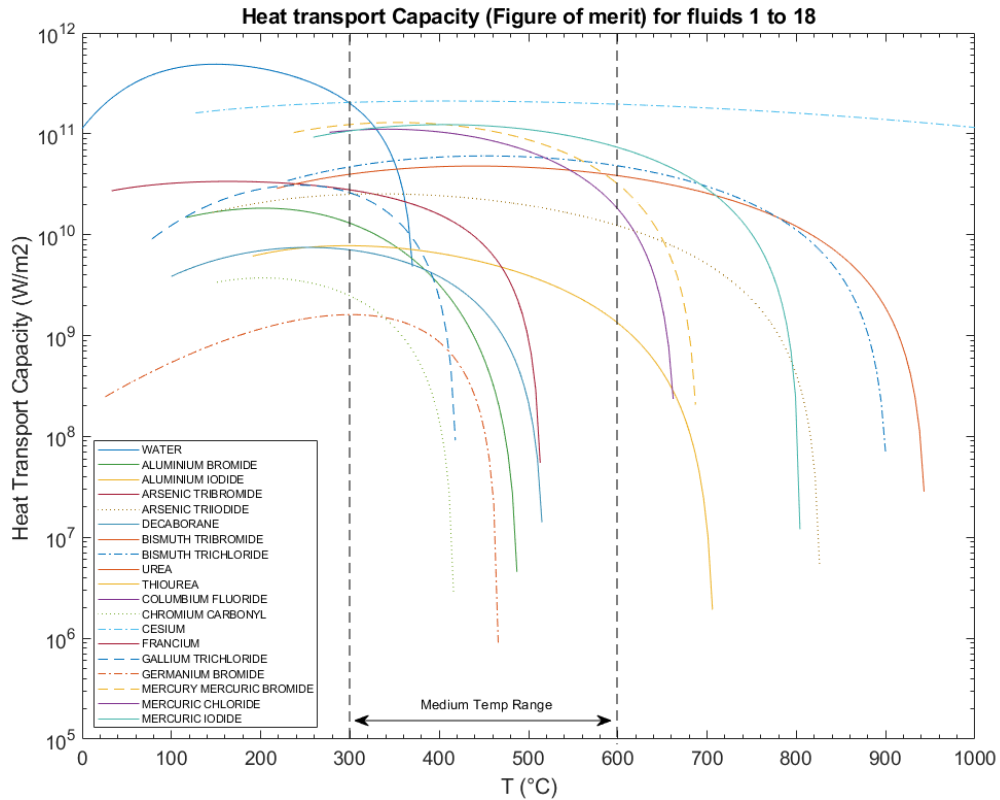


Figure 4-8 Figure of merit curves for fluids 1 to 18

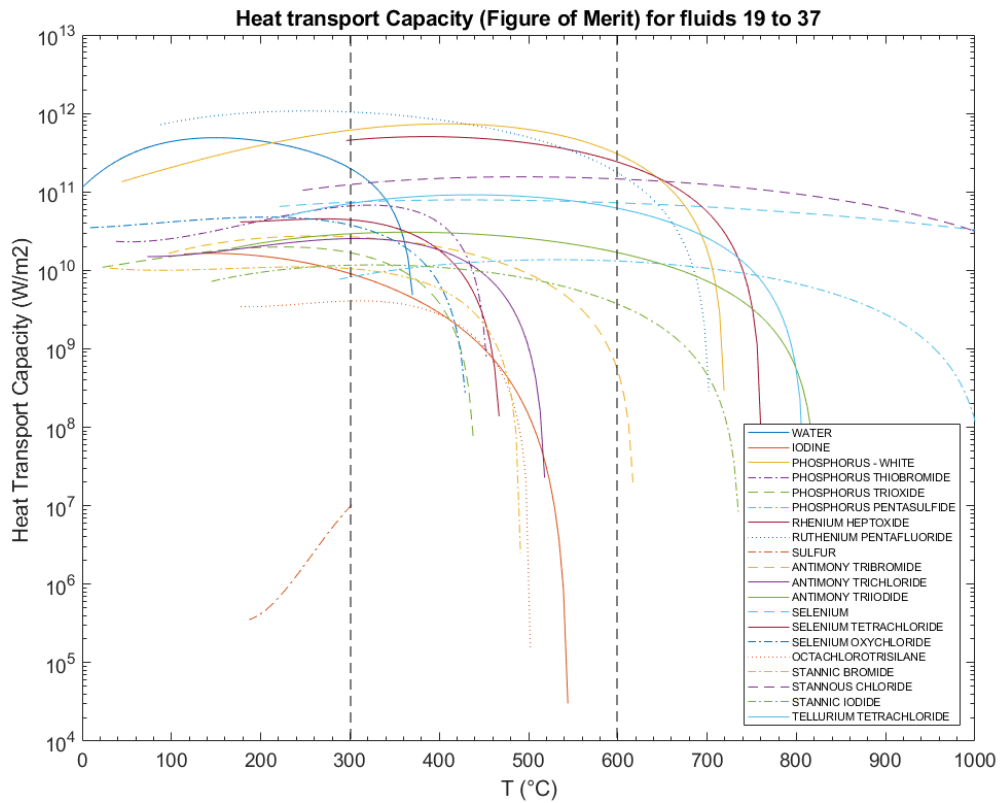


Figure 4-9 Figure of merit curve for fluids 19 to 37

Some principal observations which can be drawn from these graphs are:

- The highest performing fluids are Ruthenium based compounds, Phosphorus, Stannous Chloride, Selenium, Tellurium Tetrachloride, Caesium, Mercury based halides and Bismuth based halides
- Selenium, Antimony based halides and Phosphorus Thiobromide are viable candidates which cover the lower end of the temperature range (up to 500°C mostly).

- Most other candidates present lower merit curves, but all shortlisted fluids are viable options up to 400°C based on their figure of merit

4.3.2.3 Vapour pressure analysis

The vapour analysis simply looks at the vapour pressure of each fluid in the required operating range as detailed in Section 4.2.1.2.

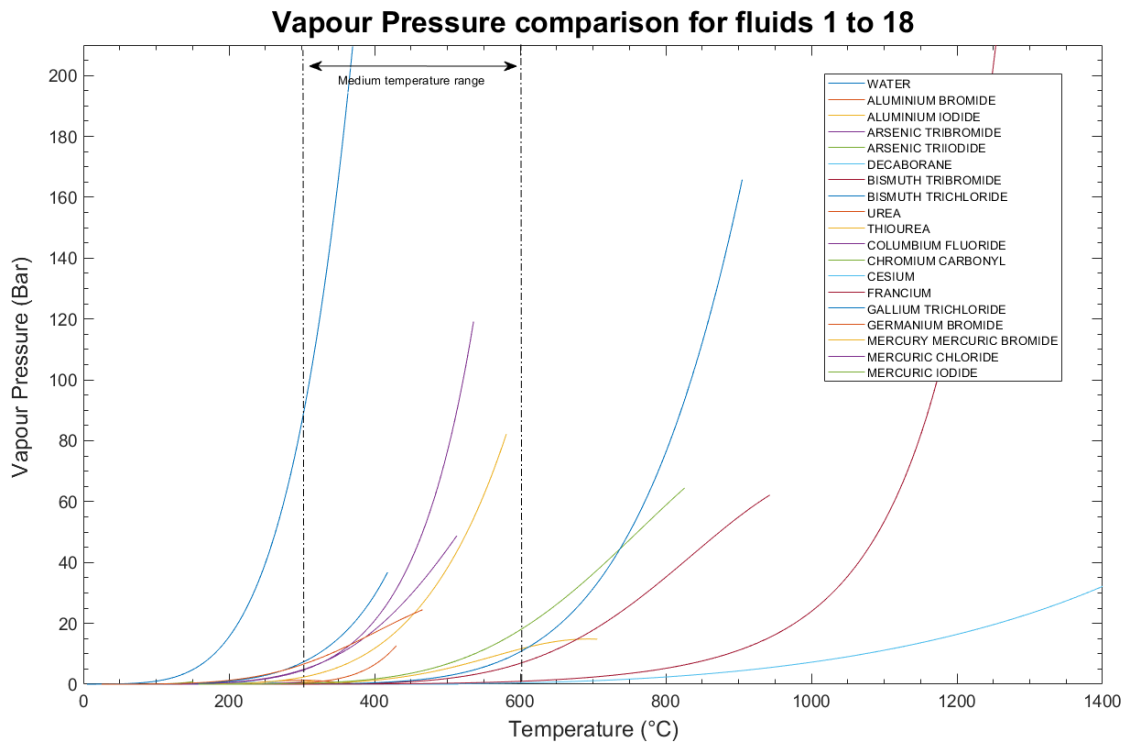


Figure 4-10 Vapour pressure analysis for fluids 1 to 18

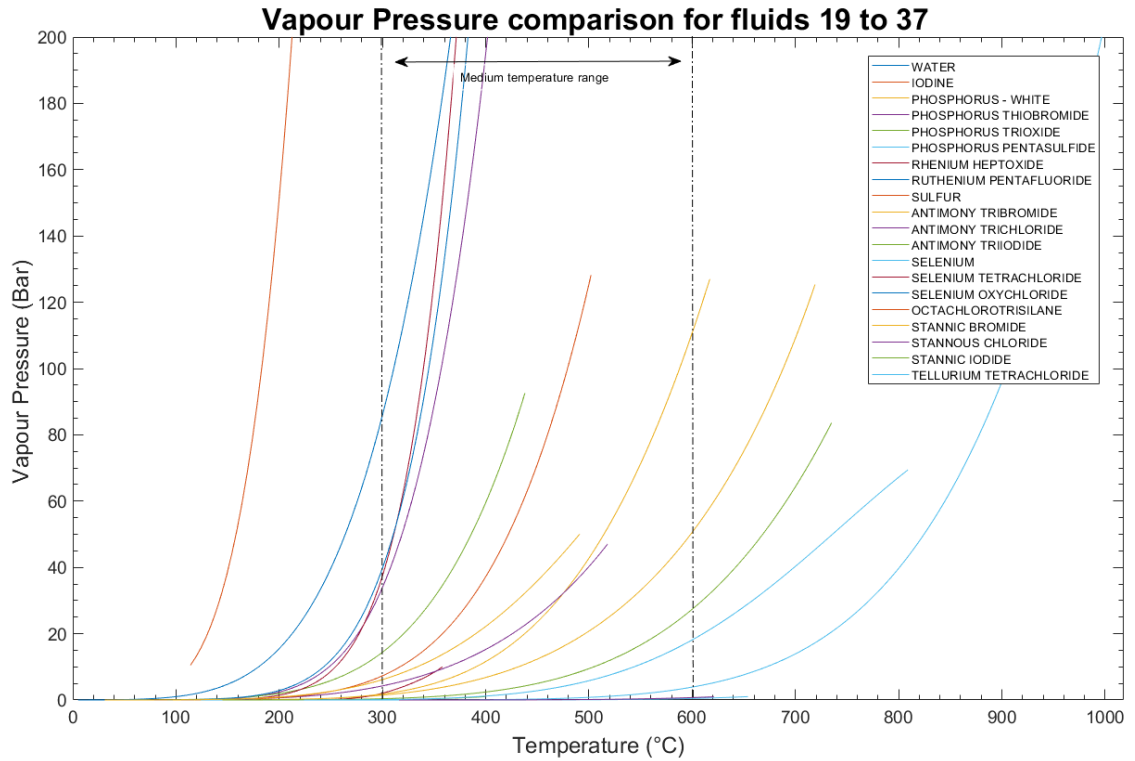


Figure 4-11 Vapour pressure analysis for fluids 19 to 37

Some principal observations which can be drawn from these graphs are:

- The highest performing fluids are Ruthenium based compounds, Phosphorus, Stannous Chloride, Selenium, Tellurium Tetrachloride, Caesium, Mercury based halides and Bismuth based halides
- Mercury based halides, Selenium, present extremely low vapour pressures – these are not visible in the scale of the current graphs
- Caesium presents a good vapour pressure at higher temperatures; in the medium temperature range it remains very low compared to other fluids

- Bismuth halides and Antimony halides have an ideal vapour pressure which cover the entire temperature range
- Phosphorus Thiobromide Presents a very high vapour pressure above 400°C which could lead to high wall thickness requirements at high temperatures

4.3.2.4 Thermal transport analysis

The thermal transport analysis looks at the Capillary limit curves of each fluid. The heat pipe geometry used to model the heat pipe limit curve was the same used in the water tests presented in 4.2.1.2. The thermal transport curve represents that of a horizontal heat pipe (i.e. no gravitational effects) with a meshed wick structure.

Figure 4-12 and Figure 4-13 show the capillary limit curves for all shortlisted fluids. Some fluids were limited by availability of data over the entire working temperature range, hence the Mercuric halides in Figure 4-12 and Rhenium Heptoxide and Stannous Chloride and Ruthenium Pentafluoride in Figure 4-13 present forward extrapolations of the thermal transport curve.

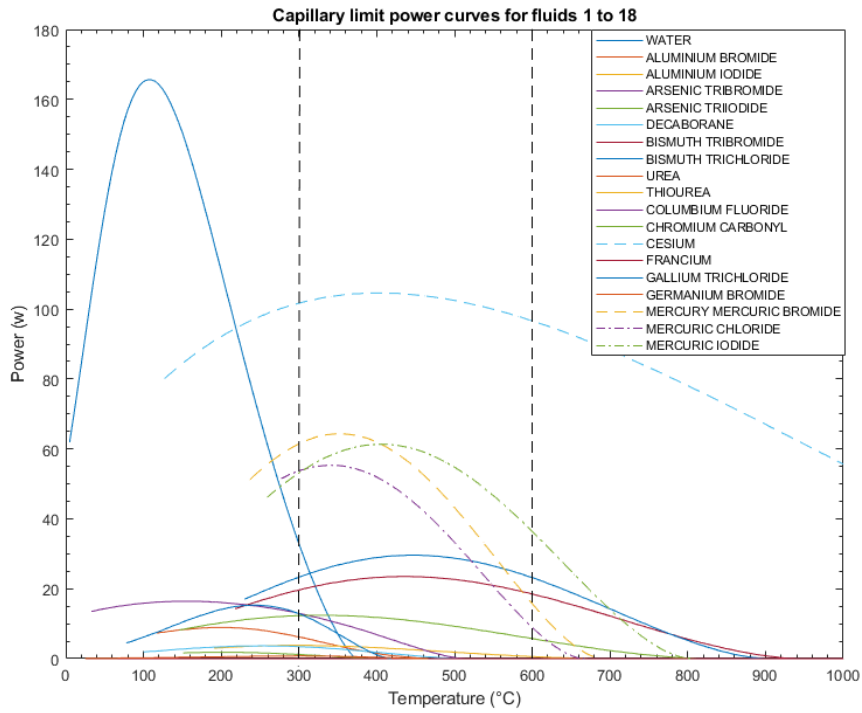


Figure 4-12 Capillary limit analysis for fluids 1 to 18

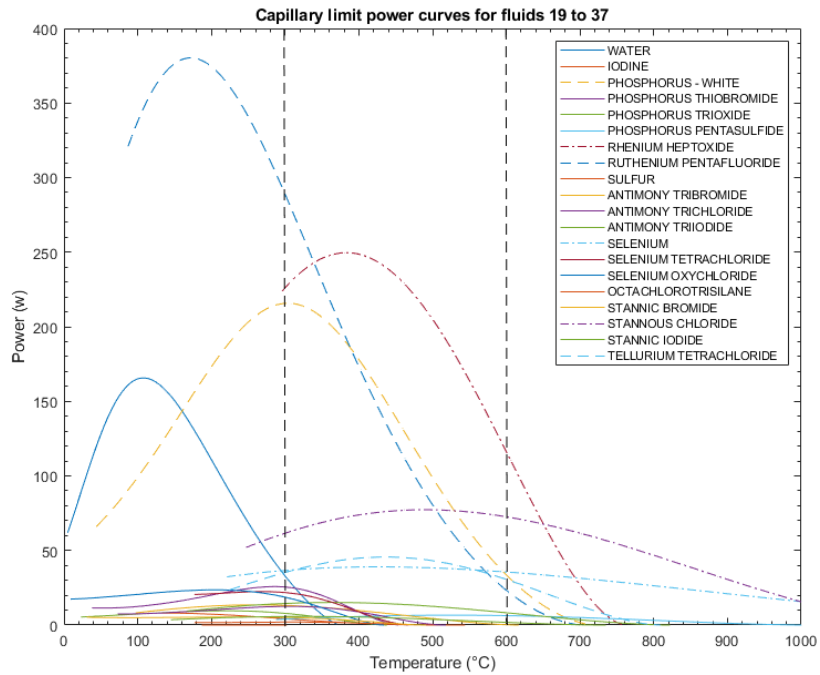


Figure 4-13 Capillary limit analysis for fluids 19 to 37

4.3.2.5 Stability and toxicity analysis

The general stability and toxicity are determined through the Material Safety Datasheets (MSD) for each fluid. The key criteria considers:

1. The fluids stability in air
 - Will it react with air under normal conditions?
 - Are there special handling requirements?

2. Toxicity
 - How toxic is the fluid on the LD50 European scale?
 - Can it be handled with local ventilation only?
 - Is a fume hood necessary?
 - Is a glovebox necessary?
 - Does the handler need any special qualifications/training?

Table 4-4 summarizes the stability and handling outcomes of each fluid and highlights the individual fluid results for the property data, vapour pressure, merit and thermal transport curve analysis. Fluids highlighted in red in the ‘formula’ column are discarded from the study. All other fluids are taken forward to the next phase of analysis.

Table 4-4 Phase 2 fluid shortlist analysis

NO	FORMULA	NAME	Stability in air	Toxicity/Handling	Property data Complete?	Vapour pressure OK?	Merit analysis	~Thermal transport curve
6	AlBr3	ALUMINIUM BROMIDE	Fumes strongly in air	Emits toxic fumes when heated	Yes, st deduced	No	Good up to 460°C	Bad
9	AlI3	ALUMINIUM IODIDE	Reacts with moisture and light	Fume hood needed	Yes, KI deduced	Yes	Good	Bad
14	AsBr3	ARSENIC TRIBROMIDE	Absorbs moisture from the air	Fume hood needed	Yes	Up to 510°C	Good up to 500°C	Low
19	AsI3	ARSENIC TRIIODIDE	Reacts slowly with oxygen in air	Glovebox needed, emits very toxic fumes when heated	Yes, st deduced	Yes	Good	Low
36	B10H14	DECABORANE	Ignites in oxygen at 100°C	Glovebox needed	Yes, st & KI deduced	No	Good up to 490°C	Bad
45	BiBr3	BISMUTH TRIBROMIDE	Reacts slowly with oxygen in air	Corrosive only	Yes, KI and Kv deduced	Yes	Good	Low
46	BiCl3	BISMUTH TRICHLORIDE	Reacts with oxygen when heated	May not need fume hood (just local ventilation)	Yes	Yes	Good	Good
52	CH4N2O	UREA	Reacts with moisture	Fume hood needed, emits toxic fumes when heated	No - st missing	Up to 420°C	Bad	Bad
53	CH4N2S	THIOUREA	Stable? Possible reaction with moisture	Fume hood needed, emits very toxic fumes when heated	No - st missing	Yes	Bad	Bad
67	CbF5	COLUMBIUM FLUORIDE	Reacts with moisture	Glovebox preferable, fume hood possible	No - st missing	Up to 500°C	Bad	Bad
87	CrC606	CHROMIUM CARBONYL	Risk of explosion when heated in confinement	Fume hood needed	Yes, Kv & st deduced	No	Low	Low
89	Cs	CAESIUM	Explosive hazard	Containers handled by qualified people only	Yes	Low at temperature range	V. Good	OK
109	Fr	FRANCIUM	Explosive hazard	Fume hood needed	No - rhol, st, vl, missing	Low at temperature range	Bad	Bad
111	GaCl3	GALLIUM TRICHLORIDE	Reaction with moisture	Glovebox needed	Yes	Up to 410°C	Ok up to 410°C	Good
114	GeBr4	GERMANIUM BROMIDE	Reacts with moisture	Fume hood needed	Yes	Up to 450°C	Low up to 450°C	Bad
139	HgBr2	MERCURIC BROMIDE	Sensitive to light, sublimates above 237°C	Glovebox needed	Yes, KI deduced	OK	OK	Low
140	HgCl2	MERCURIC CHLORIDE	Slightly volatile, sensitive to light	Glovebox needed	Yes, KI deduced	OK	OK	Low
141	HgI2	MERCURIC IODIDE	Sensitive to light, sublimates above 350°C	Glovebox needed	Yes, KI deduced	OK	OK	Low
143	I	IODINE	Readily sublimates at room temperature in air	Fume hood needed	Yes	No	Bad	Bad
212	P	PHOSPHORUS - WHITE	Dangerous reaction in air	V. poisonous, needs to be kept under water	Yes	Yes	OK	V. Good
222	PSBr3	PHOSPHORUS THIOBROMIDE	Reacts strongly to moisture	Fume hood needed	Yes	Ok up to 400°C	Ok up to 440°C	Bad
224	P4O6	PHOSPHORUS TRIOXIDE	Reacts with moisture	May not need fume hood	Yes	up to 400°C	Ok up to 430°C	Bad
226	P4S10	PHOSPHORUS PENTASULFIDE	Reacts with moisture	May not need fume hood	Yes	Beyond 450°C	Ok	Bad
244	Re2O7	RHENIUM HEPTOXIDE	Store in nitrogen	May not need fume hood	Yes, st deduced	OK	Good	V. Good
248	RuF5	RUTHENIUM PENTAFLUORIDE	Stable? Possible reaction with moisture	May not need fume hood	Yes, st deduced	Up to 510°C	V. Good	Excellent
249	S	SULFUR	Stable? Possible reaction with moisture	Fume hood needed, burns to form toxic gases	Yes, but not for whole range	Only above 450°C	Good	Bad
260	SbBr3	ANTIMONY TRIBROMIDE	Reacts with moisture in air	Fume hood needed	Yes, st deduced	Yes	Good	Low
261	SbCl3	ANTIMONY TRICHLORIDE	Reacts slowly with moisture in air	Fume hood needed	Yes	Up to 510°C	Good up to 500°C	Good
264	SbI3	ANTIMONY TRIIODIDE	Decomposes in air, store in inert gas	Glovebox needed	Yes, st deduced	Up to 520°C	Good	Low
267	Se	SELENIUM	Store in inert gas	Glovebox needed	Yes	Yes	V. Good	Good
268	SeCl4	SELENIUM TETRACHLORIDE	Reacts with moisture	Glovebox needed	Yes, st deduced	No	Ok up to 450°C	Low
270	SeOCl2	SELENIUM OXYCHLORIDE	Reacts with moisture	Glovebox needed	Yes	V. high at temperature range	Ok up to 420°C	Low
301	Si3C18	OCTACHLOROTRISILANE	Reacts with moisture	Fume hood needed	Yes	Yes	Good up to 490°C	Bad
307	SnBr4	STANNIC BROMIDE	Reacts with moisture	Glovebox needed	Yes	Yes, up to 500°C	Good up to 480°C	Bad
308	SnCl2	STANNOUS CHLORIDE	Reacts with moisture	Fume hood needed	Yes	Low at temperature range	V. Good	Excellent
311	SnI4	STANNIC IODIDE	Keep in cool, dry container	Fume hood needed	Yes, st deduced	Yes	Ok	Bad
317	TeCl4	TELLURIUM TETRACHLORIDE	Keep in cool, dry container	Glovebox needed	Yes, st deduced	Yes	Good	Low

4.3.3 Phase 3: Fluid selection

The final phase of the fluid analysis takes a closer look at the shortlisted fluids from phase 2. As well as the previously determined categories the addition of a ‘cost’ was included as seen in Table 4-5. From this, a weighting for each category and scoring for each fluid was determined as detailed in Section 4.2.1.3.

Table 4-5 Phase 3 shortlisted fluids

NO	FORMULA	NAME	Stability in air	Toxicity/Handling	Property data Complete?	Vapour pressure OK?	Merit analysis	Thermal transport curve	Cost (£/g)
14	AsBr3	ARSENIC TRIBROMIDE	Absorbs moisture from the air	Fume hood needed	Yes	Up to 510°C	Good up to 500°C	Low	-
19	AsI3	ARSENIC TRIIODIDE	Reacts slowly with oxygen in air	Glovebox needed, emits very toxic fumes when heated	Yes, st deduced	Yes	Good	Low	14.84
45	BiBr3	BISMUTH TRIBROMIDE	Reacts slowly with oxygen in air	Corrosive only	Yes, Kl and Kv deduced	Yes	Good	Low	2.14
46	BiCl3	BISMUTH TRICHLORIDE	Reacts with oxygen when heated	May not need fume hood (just local ventilation)	Yes	Yes	Good	Good	1.7
111	GaCl3	GALLIUM TRICHLORIDE	Reaction with moisture	Glovebox needed	Yes	Up to 410°C	Ok up to 410°C	Good	4.59
244	Re2O7	RHENIUM HEPTOXIDE	Store in nitrogen Stable?	May not need fume hood	Yes, st deduced	OK	Good	V. Good	43.3
248	RuF5	RUTHENIUM PENTAFLUORIDE	Possible reaction with moisture	May not need fume hood	Yes, st deduced	Up to 510°C	V. Good	Excellent	>205
260	SbBr3	ANTIMONY TRIBROMIDE	Reacts with moisture in air	Fume hood needed	Yes, st deduced	Yes	Good	Low	1.24
261	SbCl3	ANTIMONY TRICHLORIDE	Reacts slowly with moisture in air	Fume hood needed	Yes	Up to 510°C	Good up to 500°C	Good	0.42
308	SnCl2	STANNOUS CHLORIDE	Reacts with moisture	Fume hood needed	Yes	Low at temperature range	V. Good	Excellent	65.4
317	TeCl4	TELLURIUM TETRACHLORIDE	Keep in cool, dry container	Glovebox needed	Yes, st deduced	Yes	Good	Low	12.32

4.3.3.1 Weighted analysis

	Weight	Arsonic Tribromide	Arsenic Triiodide	Bismuth Tribromide	Bismuth Trichloride	Gallium Trichloride	Rhenium Heptoxide	Ruthenium Pentafluoride	Antimony Tribromide	Antimony Trichloride	Stannous Chloride	Tellurium Tetrachloride
		Inorganics										
Stability in air	2	2	3	3	3	2	3	3	2	3	2	3
Toxicity/ Handling	3	2	2	3	3	2	3	3	2	2	2	1
Property data	1	3	2	2	3	3	2	2	2	3	3	2
Merit Curve	2	3	3	3	3	2	3	3	3	3	3	3
Vapour Pressure	2	3	3	3	3	2	3	3	3	3	2	3
Cost	3	1	1	2	2	1	1	1	3	3	1	1
Score		2.15	2.23	2.69	2.77	1.85	2.46	2.46	2.54	2.77	2.00	2.00

Figure 4-14 Weighted selection table for shortlisted fluids

Table 4-6 Ranked fluid selection results

Fluid	Score
Antimony Trichloride	2.77
Bismuth Trichloride	2.77
Bismuth Tribromide	2.69
Antimony Tribromide	2.54
Rhenium Heptoxide	2.46
Ruthenium Pentafluoride	2.46
Arsenic Triiodide	2.23
Arsenic Tribromide	2.15
Stannous Chloride	2.00
Tellurium Tetrachloride	2.00
Gallium Trichloride	1.85

4.3.4 Conclusions

From this study, it can be concluded that Antimony Trichloride and Bismuth Trichloride both scored the highest total score in the weighted selection process. Bismuth Tribromide and Antimony Tribromide also subsequently scored second and third highest scored respectively. These four chemicals can be conclusively determined to be the most viable medium temperature fluids out of the 343 inorganic chemicals present in the current database which have complete, or semi-complete property data available⁵.

Antimony Trichloride and/or Bismuth Trichloride should be the focal chemicals for compatibility and wettability studies. This study will further the techniques and approaches to compatibility and wettability studies using Antimony Trichloride only. Future work should be aimed towards Bismuth Trichloride initially, then move to other shortlisted fluids which displayed very high thermal handling potential but scored low on availability and pricing such as Rhenium Heptoxide and Ruthenium Pentafluoride. It is also important to continually expand the catalogue of fluids available particularly to begin exploration of azeotropic fluids. Using the procedures developed throughout this study, experimental analysis can be fast tracked as new fluids are identified.

⁵ The analysis presented in this section was a product of the continual development of the fluid assessment framework over the entire duration of the project. The databases, code and framework structure were continually updated and developed to include better methodology and more fluid property data – all of which occurred in parallel to testing. For this reason, the conclusions presented here may differ from the fluid selection completed before experimental testing commenced, although the fluid taken forward still scored among the highest ranking. The conclusions presented here are aimed towards future work and does not reflect the knowledge and data available at the point at which compatibility and wettability testing commenced

4.4 Heat pipe modelling using chosen fluids

The following section presents the resultant numerical modelling of the top two shortlisted fluids from the fluid selection analysis: Antimony Trichloride and Bismuth Trichloride. Other fluids which were identified in the most recent medium temperature heat pipe study by Anderson et al. [106] are also modelled to compare their performance. All models include a Molybdenum shell as this showed the highest likelihood of compatibility following the metal compatibility analysis conducted in Chapter 6. All modelling uses the theory outlined in Chapter 2, Section 2.3. An outline of the model itself, which was developed in Matlab, can be found in Appendix F. To make a meaningful comparison of each of the shortlisted fluids, each fluid was modelled using identical pipe geometries listed in Table 4-7.

Table 4-7 Heat pipe modelling parameters

Measurement	Value
Heat Pipe Length (mm)	460
Evaporator Length (mm)	100
Condenser Length (mm)	150
Adiabatic Length (mm)	210
Effective Length (mm)	230
Diameter (mm)	12
Wall Thickness (mm)	0.8
Orientation	Variable
Wall Material	Molybdenum
Wick type	Mesh
Mesh count (/inch)	200
Number of wraps	3
Material	Molybdenum

4.4.1 Horizontal model

When observing the thermal handling performance of the various shortlisted inorganic fluids as well as other halide fluids studied in the most recent publications on the topic by Anderson et al. [106] such as Titanium Tetrachloride (TiCl_4) and Aluminium Tribromide (AlBr_3) in Figure 4-15, it is clear that Bismuth Trichloride (BiCl_3) shows a vastly superior performance, both in the power handling capacity and in the total temperature range it is able to operate in.

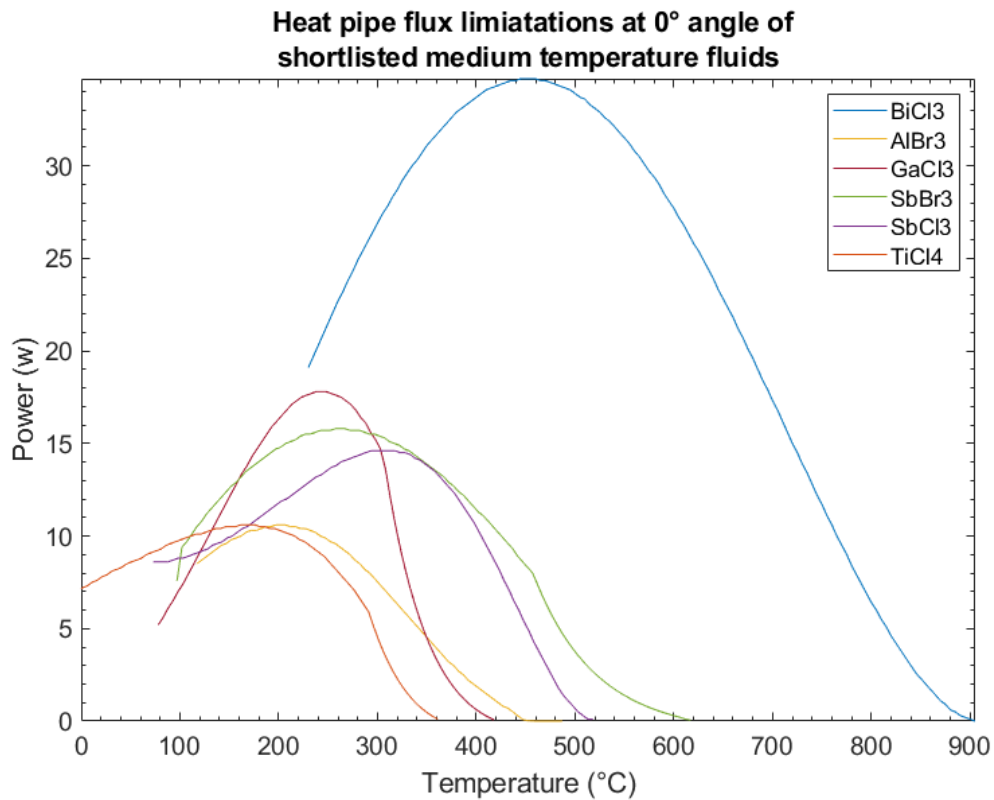


Figure 4-15 Heat pipe thermal limitations in the horizontal orientation for primary shortlisted fluids and previously studied fluids

The second fluid highlighted from the selection process is Antimony Trichloride (SbCl_3). In Figure 4-15 it can be seen that its close relative Antimony Tribromide (SbBr_3) actually has a marginally greater power handling capacity than SbCl_3 and also is able to operate at slightly higher temperatures, though it is important to note that some of the property data used for SbBr_3 was estimated by comparison with similar fluids. Ultimately though, the disadvantage of the use of SbBr_3 is that it has a lower stability in air compared to SbCl_3 , which makes the handling of the chemical unjustifiably more difficult compared to the performance benefit.

4.4.2 Mesh wick 45° gravity aided model

To observe the further potential of these fluids, they were also modelled in a gravity aided position at 45° inclination in Figure 4-16. Here it can be observed that BiCl_3 has an outstanding performance compared to all other fluids. In most cases the other fluids still have an adequate performance, but it can be seen that the boiling limit is predicted to have a large effect on all fluids at the higher end of their operating temperature except in the case of BiCl_3 . It can also be seen that in the gravity aided position BiCl_3 is the only fluid which is able to cover the entire 'medium' temperature range (i.e. 300°C to 600°C) and is even able to extend beyond into what is typically the operating temperature of liquid metals.

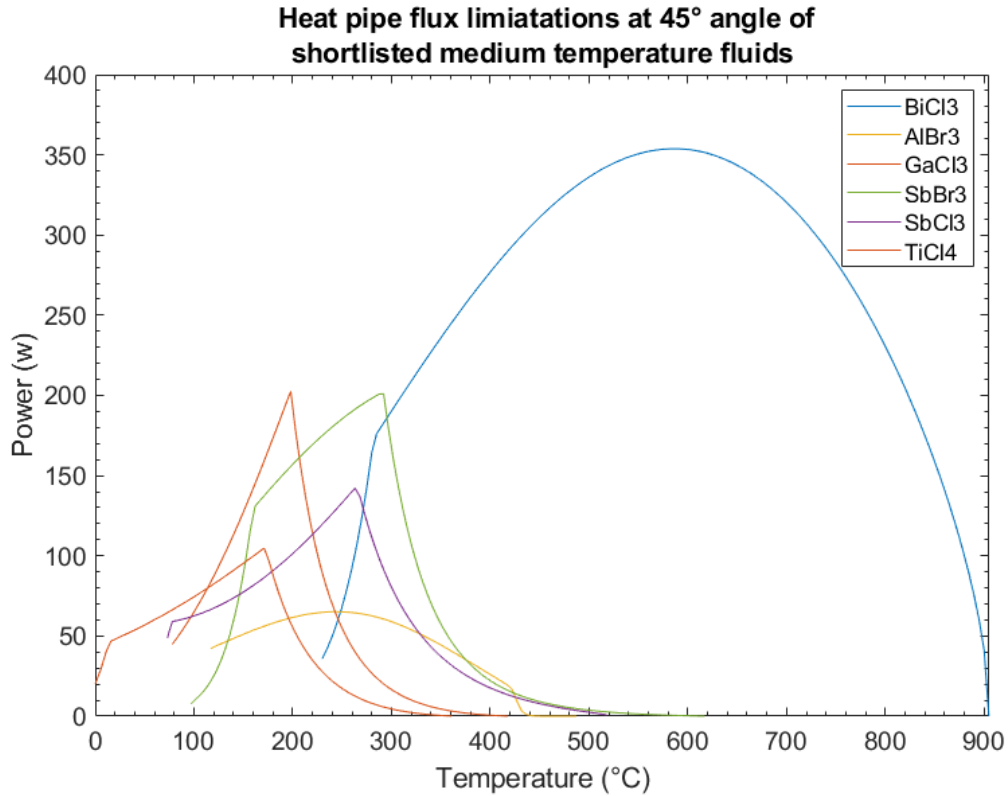


Figure 4-16 Heat pipe thermal limitations at a 45° gravity aided orientation for primary shortlisted fluids and previously studied fluids

4.4.3 Final fluid models

The full heat pipe operating domain of the fluids investigated by Anderson et al. [106], TiCl₄ and AlBr₃, as well the fluids identified in this study as having the best potential for use in the medium temperature range, BiCl₃ and SbCl₃, are shown in Figure 4-17. Overall, it can be seen that BiCl₃ and SbCl₃ both have a favourable performance compared to TiCl₄ and AlBr₃ in terms of maximum thermal capacity and temperature range. One disadvantage seen in SbCl₃, however, is the effect of the boiling limit beyond 200°C which is predicted to have a large impact on its thermal performance, though it is

important to note that this can certainly be mitigated when performing wick optimisation studies in future work.

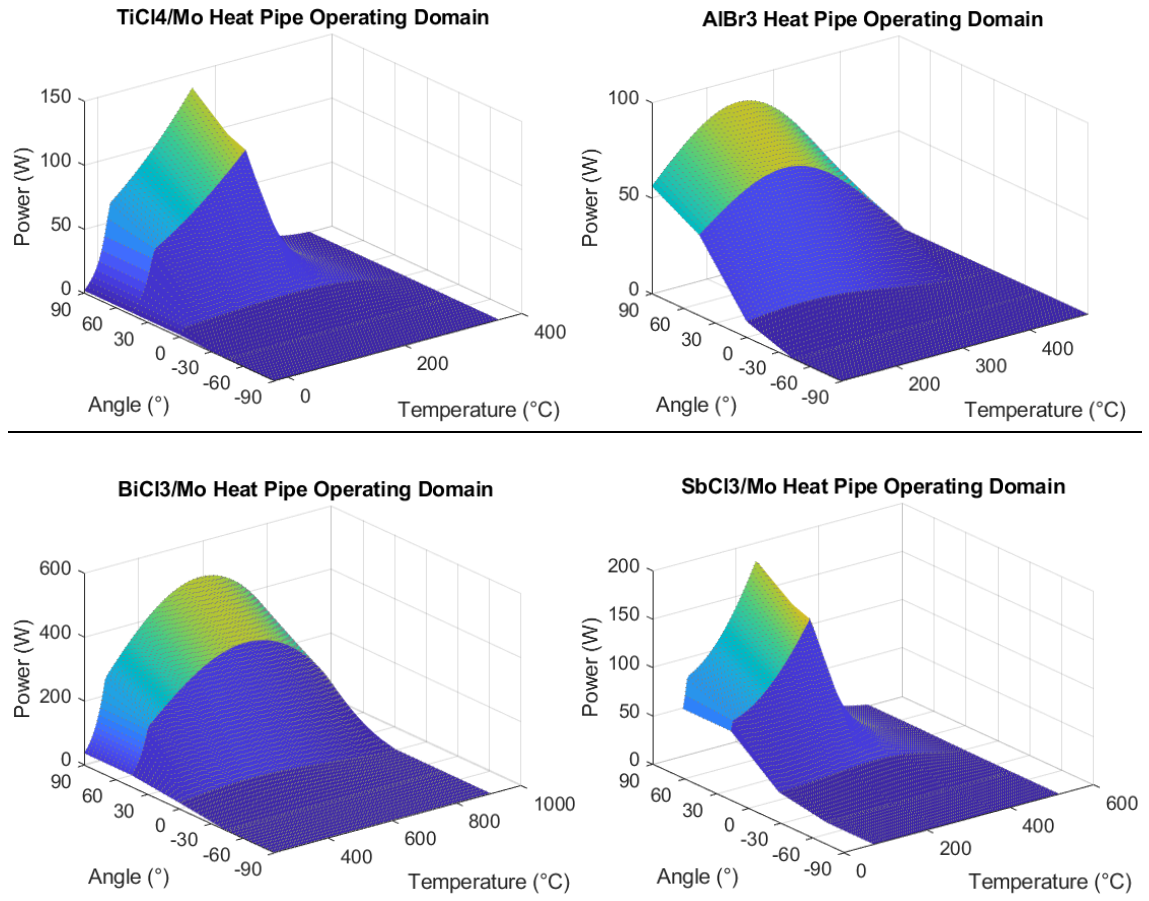


Figure 4-17 Heat pipe operating domains for previously studied fluids (TiCl4 and AlBr3) and current shortlisted fluids (BiCl3 and SbCl3)

One distinct quality which is apparent in all medium temperature fluids is their lack of ability to operate against gravity. While a mesh wick is certainly not an appropriate wick to use when building pipes specifically to operate against gravity, there appears to still be a distinct drop in performance when moving from a gravity aided to a gravity neutral

position which is much higher than that observed in water heat pipes for example (see Figure 4-18).

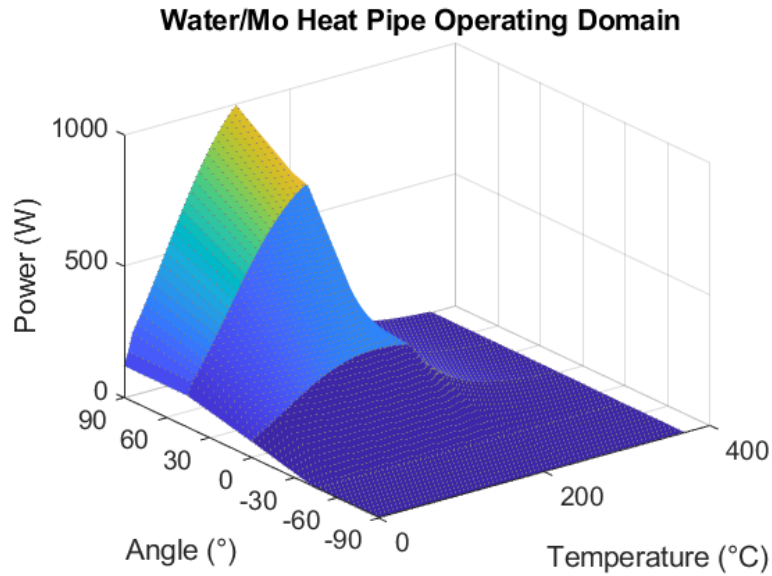


Figure 4-18 Heat pipe operating domains for a Water/Mo heat pipe

4.4.4 Results and discussion of fluid modelling

To assess the relative performances of horizontal wicked heat pipe model of each fluid, Table 4-8 shows a comparison between the thermal transport capacity and operating range of each fluid in the 45° gravity aided position. It can be observed that both Antimony Trichloride and Bismuth Trichloride reach their maximum thermal transport capacity within the medium temperature range. In general, the performance for Bismuth Trichloride exceeded that of Antimony Trichloride in when modelling equivalent heat pipes. Bismuth Trichloride also displays a working range spanning the entire 'medium' temperature range while Antimony Trichloride is only operational up to around 518°C. Both Antimony

Trichloride and Bismuth Trichloride however outperformed the fluids which were studied by Anderson et al. in all respects.

Table 4-8 Fluid output data from 45° gravity aided model

<i>Fluid</i>	<i>Min Operating Temp (°C)</i>	<i>Max Operating Temp (°C)</i>	<i>Temperature at max heat flux (°C)</i>	<i>Maximum thermal load at 45° gravity aided angle (W)</i>	<i>Maximum heat flux at evaporator (W/cm²)</i>	<i>Maximum heat flux at condenser (W/cm²)</i>
Bismuth Trichloride	230	905	585	353	8.85	6.02
Antimony Trichloride	73	518	263	142	3.55	2.41
Titanium Tetrachloride	-24	361	171	104	2.62	1.78
Aluminium Tribromide	117	487	242	65.2	1.63	1.1

Based on the modelled performance of mesh wicked heat pipe, Bismuth Trichloride has stood out as the strongest contender from the attained results. The use of cross-fluid data for this particular fluid does, however, substantially reduced the accuracy of the model results. Antimony Trichloride also is able to perform at a higher level than the last studied medium temperature fluids and has an exceptionally low cost when compared to all other fluids, hence this could still be put forward as a cost-effective solution in the medium temperature range for low heat flux applications.

4.5 Chapter Summary

A detailed explanation of the fluid selection process methodology, chronology and application has been presented. A framework has been constructed to enable the developed methodology to be applied universally why selecting a heat pipe fluid for any application. Appropriate constraints and selection criteria were chosen to determine optimal fluids which may be capable of operating in the medium temperature range for heat pipes based on a custom fluid property database containing 343 fluids at the time of writing. The shortlisted fluids from this analysis were Antimony Trichloride and Bismuth Trichloride. The heat pipe modelling code presented in Appendix F was successfully applied to the shortlisted fluids to predict their performances and compare these against the performance of fluids which were identified in previous medium temperature heat pipe studies. The key outcomes from this Chapter are:

- Development and demonstration of a universal fluid selection framework
- Development of an extensive inorganic fluid property database
- Development of a fluid/metal compatibility database
- Development of a metal property database
- Application demonstration of heat pipe numerical model presented in Chapter 3 and incorporation of the databases into the model
- Selection of Antimony Trichloride and Bismuth Trichloride as fluids of interest to take forward to testing phase

The fluid selection and modelling process brought forward Bismuth Trichloride as a strong contender for future work. Due to estimation of some of the fluid property data, however, the model predictions accuracy may be significantly lower than that of Antimony Trichloride. Further research is needed to acquire the true liquid thermal conductivity values, or alternatively, experimental verification of the liquid thermal conductivity is needed to progress with this fluid. Antimony Trichloride has presented itself as the next most viable fluid out of the database, though only partially covering the medium temperature range. It was concluded that Antimony Trichloride will be the chosen fluid to develop compatibility and wettability techniques due to its low cost and ease of handling. Other fluids of interest are Ruthenium Pentafluoride, Rhenium Heptoxide and Rhenium Heptafluoride which have the greatest thermal transport capacity in the medium temperature range, but also are very rare and expensive fluids – hence these should be studied in a specialised and specifically funded programmes.

Chapter V

Calculation, design and construction of a high temperature test rig for novel heat
pipes

5.1 Introduction

Using the proposed approach detailed in section 7 for heat pipe testing and qualification under the conditions outlined in the water heat pipe test matrix (see Chapter 7), a suitable test rig was required to be constructed which can accommodate the temperatures and thermal loads specified. The qualification tests have been separated into two categories: thermal heat transport performance and lifetime. The focus in this study is on the thermal heat transport performance testing which aims to quantify the steady state performance of the heat pipe at various conditions and compare these against numerical models. Although lifetime testing is also of vital importance to qualify the heat pipe in its long-term use, the results for these tests cannot be presented in the time frame of this study due to the length of time required to complete (first set of results is usually around 10000h of operation), though the test rig design and construction will also be reported in this section.

Test rigs which can perform the steady state analysis described in section 7 at or above 300°C are scarcely reported in literature. This is mainly due to the need for more specialist equipment due to the high temperatures the test rig components will be exposed to. Generally, higher operating temperature also cause an exponential increase in equipment price due to the operating challenges associated with this. Hence, a full development plan was put in place to design and construct a test rig within the required budget with the following key requirements:

- Capable of measuring the temperature across the length of pipe
- Capable of changing the heat pipe angle
- Capable of operating the heat pipe up to 600°C
- Capable of transmitting up to 1kW through a heat pipe (max range of water)
- Capable of measuring the inlet/outlet calorimeter temperatures
- Capable of controlling the calorimeter flow rate
- Capable of controlling the power input

Assuming all these criteria are achieved, the test rig will be capable of reaching all operation points dictated by the test matrix outlined in Chapter 7, allowing for a direct comparison of the acquired data to numerical models. This will allow for two key results; the validation of the numerical model against any tested fluids and the direct comparison of the performance of novel fluid against each other.

Following from similar testing undertaken by Min [60], Quo [73], Anderson [43], Khandekar [28] and Williams [107] where the performance of a wide range of heat pipes were quantified, the methodology developed for this testing is aimed at achieving and demonstrating the maximum working limitation at temperatures surrounding 300°C (the lower limit of the medium temperature range). In the case of water heat pipes, the boiling limit is the focus as this is predicted to be the working limitation at these temperature [1]. This can then be compared against various boiling limit equations such as those proposed by Rohsenow [30], Casswell [108], Ferrell [31] and Ivanovskii [109] as to determine the most appropriate correlations to be used for the particular heat pipe tested.

5.2 Engineering Design Assessment

The general design of the rig is geared towards flexible use by engineering it to cater for a range of potential future testing on heat pipes containing medium temperature fluids. To cater for the power input and extraction requirements, the rig will mainly consist of a high-power heating unit and a calorimeter able to reach very high circulator temperatures to operate the heat pipe in the medium temperature range.

This section of the study will highlight the design methodology surrounding each component of the test rig and present the final design used in the testing. Throughout the project, many iterations of each custom component were made to reach the final design, the drawings used to manufacture each iteration is presented in the appendices, here only the final drawings used will be presented.

To standardize the parts, each component was designed for use with 12mm OD heat pipes as were specified for the Innova Microsolar [110] thermal storage application as detailed in section 7 . The evaporator and condenser section dimensions were determined through available equipment sizes, geometric constraints, optimisation tests and calculations. The detailed design process for each of these parts will also be highlighted in this section.

5.2.1 General layout

Figure 5-1 shows the general layout of each component of the test rig to achieve the required steady state results. In preliminary tests, the setup was proven successful in its general operation in terms of flow control and temperature measurement hence no major changes to the layout were taken forward from the preliminary stage. The focus of the final design was to improve the individual components of the test rig to reach the required test criteria.

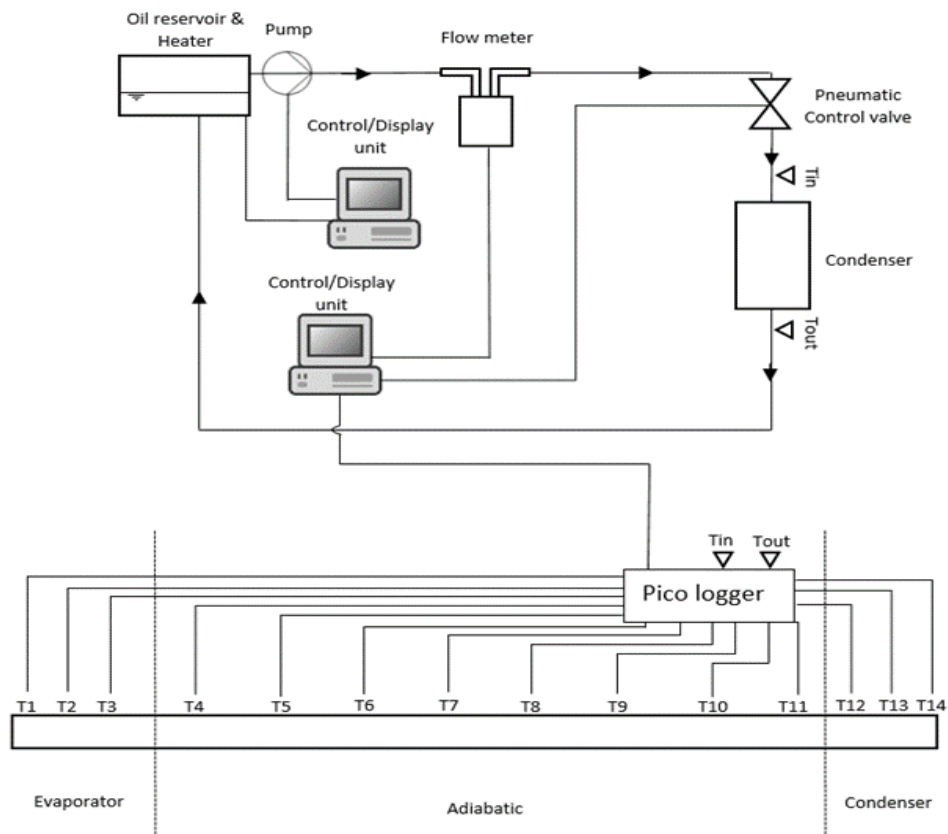


Figure 5-1 Test rig schematic

All connections between components were made through ¼ inch stainless steel pipes. This required the modification of various component fittings using custom made adaptors. Figure 5-2 shows a general layout for all components involved in the calorimeter loop.

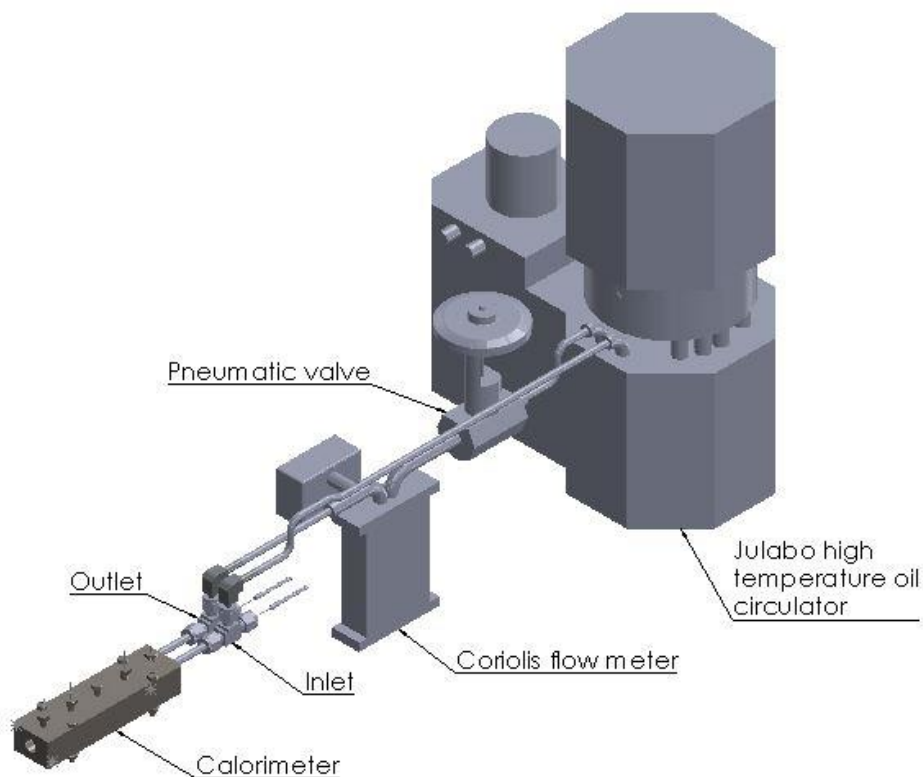


Figure 5-2 Calorimeter loop layout

Figure 5-3 presents the final iteration of the full test rig (with simplified tube connections). The layout presented allows the heat pipe to reach all experimental steady state conditions presented in Chapter 7. An additional support structure was built for the heat pipe assembly which allows the unit to alter its inclination angle for future testing as seen in Figure 5-4.

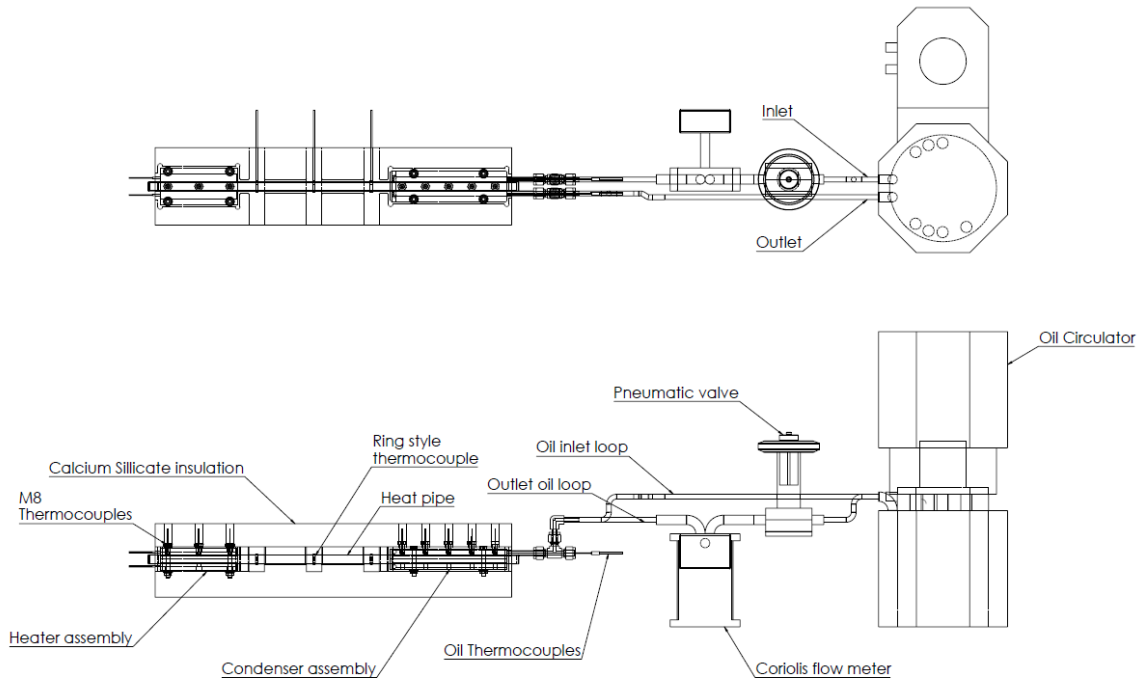


Figure 5-3 Full test rig diagram

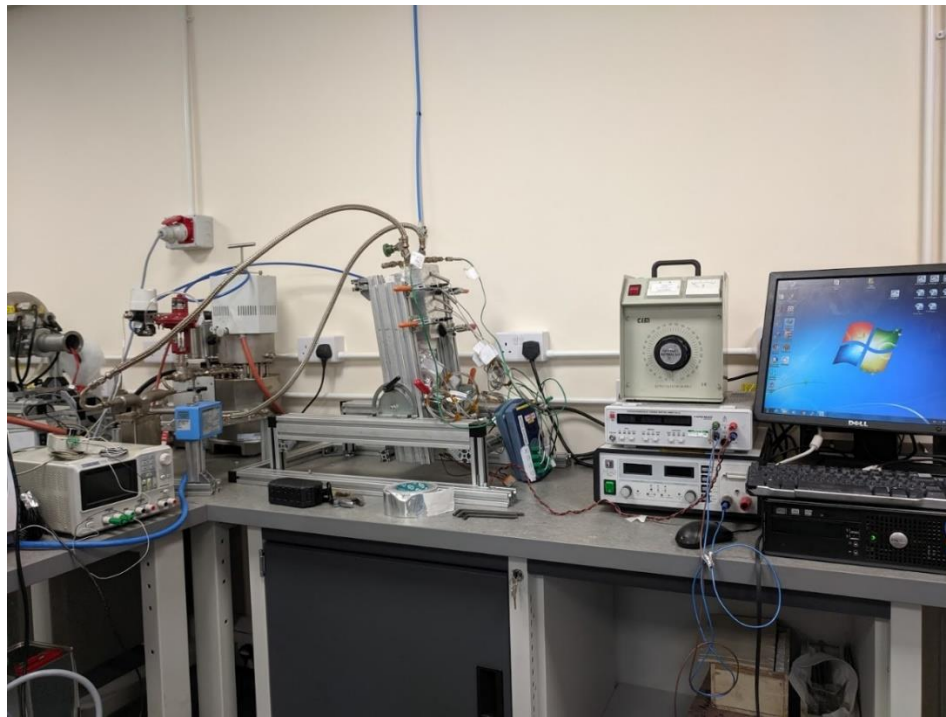


Figure 5-4 Figure of apparatus setup

5.2.2 Component assessment

To maintain the project within budgetary and time constraints, a cross examination of available equipment together with a general prediction of materials needed, costs, delivery times of any new equipment was taken into consideration. To minimise costs, it was decided to utilize the available equipment at Aavid Thermacore which would be suitable for maintaining condenser temperatures up to 350°C and construct the test rig to cater for the constraints found in the available lab facilities based in Aavid Thermacore. Table 5-1 shows the main component list taken forward. A preliminary test rig was set up to test incoming water heat pipes at high temperatures and experiment with using the equipment in various ways. From this, many challenges were encountered throughout the process which resulted in consequent modifications to the design plan. The main challenges observed for each component is highlighted in Table 5-1.

Based on this preliminary testing exercise, lab modifications were made to cater for the power and water-cooling requirement for the oil circulator and addition of a ventilation system was deemed necessary. Another point of observation was the insulation; in preliminary tests, a high temperature glass fibre insulation was used which was wrapped around each component prior to testing. This helped somewhat with reducing heat losses, however at the test temperatures required, it is unavoidable that large heat losses will occur unless the tests are conducted in a vacuum⁶.

⁶ While testing in vacuum was considered, it was determined that the costs for acquiring such a system and adapting all components to a vacuum rig would exceed budgetary requirements and prolong the development of the components beyond a reasonable timeframe.

The insulation casing for the test rig should be designed to both limit the heat losses during the testing, but also to maintain the exposed outer wall temperature at a safe level. From the preliminary experimentation, it was observed that for each test that was conducted with the glass fibre insulation, it would have to be either partially replaced or often completely replaced due to break down while loading or unloading the heat pipe. This led to the design of a solid Calcium Silicate insulation structure to replace the woven Glass Fibre for insulation of the condenser, heater and adiabatic section of the heat pipe. The design for this can be found in section 5.3.

The available oil circulator uses the silicone-based oil Thermal H350 (Dibenzyl toluene, 90-95%) and allows circulation of the fluid at normal pressures to reach up to 350°C. Supplier recommendations state that ¼ inch stainless steel pipes are optimal for use with the circulator due to pumping specifications. To standardise the rig, all inlets/outlets were designed to fit ¼ inch Swagelok compression fittings. Where possible, all components which comes in contact with the oil would also be designed in stainless steel 316L. This additionally caters for the eventuality of components needing to be welded, as stainless-steel welding facilities are readily available in both Aavid Thermacore and Nottingham University.

Table 5-1 Components list

Component	Function	Issues	Design changes
Julabo High Temperature Circulator	To cool and circulate the condenser fluid	Limitation of the circulator include: - Maximum pressure of 1.2bar - Maximum flow rate of 10Kg/min - Maximum temperature of 350°C	No design changes to circulator needed, the specs are within requirements, the other components are the main limiting factors
Badger Pneumatic valve	Accurately control the flow rate of the cooling oil and feedback to flow meter	-The valve is the main source of pressure loss through the system and one of the limiting factors in the maximum achievable flow rate (with the supplied pressure) - Changes to software annulled the flow rate readings and inhibited PID control	- Valve designed to maximum flow rate and temperature spec possible so no further changes could be made to the hardware - A manual override to control the valve was installed to replace PID
RHEONIC Flow meter	To measure the flow rate and control the valve	- Changes to software annulled the flow rate readings and inhibited PID control	- A long process of contacting the supplier to assist in hardware and software changes to cater for higher flow rates and calibrate the flow readings was necessary
Heater	To provide input heat flux to heat pipe	- The heater cartridges couldn't handle the high temperature - Reaction of copper with the insulation - Issues with cartridge heater tolerance limits inhibited insertion of some cartridges into designed block	- Specialist heater cartridge developer sourced, and new cartridges purchased - New designs using stainless steel instead of copper have been produced - New design of heater block using 'sandwich' method allowed for larger variations in tolerance
Condenser	To provide a sink for the heat flux	- Problems separating flow into two separate sections (upper and lower halves)	- Only used top half as an active calorimeter
Thermocouples	To measure the temperature across the heat pipe and the inlet/outlet temperature of the condenser oil	- Calibration at high temperature not possible - Large variance between thermocouples and unexpected results occurring - T type thermocouples showing wear with few uses	- Look for high temperature calibration standards - Source equipment able to calibrate up to 600°C - Possible use only K type metal sheathed thermocouples as these shows higher resistance to multiple uses - Source alternative thermocouple types and attachment methods
PICO logger temperature logging equipment	To record the temperature readings from each thermocouple over time	- Limited only to conventional thermocouple types, incompatible with higher accuracy PT100 sensors	- No need for higher accuracy thermocouples for initial testing, alternative logging equipment considered when higher accuracy needed

The thermocouple attachment method also presents a challenge. Normally, thermocouples are placed onto heat pipe walls via either high temperature tape or plastic spring-loaded mechanisms. In this case, neither of these methods would be possible due to the high temperatures involved. Welding the thermocouples onto the heat pipe would also be a challenge for a number of reasons; the heat pipe wall and thermocouple sheath metals are dissimilar, the thermocouple ends are very fragile (only roughly a 30% weld success rate was reported in preliminary tests) and any unconventional mass islands on the heat pipe surface would be extremely difficult to cater for in the heater and condenser designs and potentially add contact resistance. A bespoke heat pipe attachment solution based on the spring-loaded design was created to easily attach/detach the thermocouples to the heat pipe surface before and after testing and applied to the evaporator and condenser designs. The adiabatic section used Jubilee clips with embedded thermocouples. Both thermocouple types used are shown in Figure 5-5.



Figure 5-5 Thermocouple types

All components must be insulated due to the high temperatures involved, including pipe feeds, joints and valves. As the oil circulator would need to be moved to other test rigs when necessary, none of the piping could be permanently insulated as frequent access to the fittings would still be necessary. For this reason, the rig was routinely insulated with

the woven glass fibre before every test, though this did present a potential source of error in the results as it is difficult to exactly reproduce the insulation conditions from test to test. While this is not ideal, this was the only possible method of insulation due to lab constraints.

The frame to hold the condenser, heater, heat pipe and solid insulation underwent a variety of iterations in design. Some of these iterations can be found in Appendix H. The final iteration will be presented in section 5.5. The principal goal was to provide support for the components while maintaining minimal contact with any metal parts to minimise thermal conduction out of the heater and condenser. The rig also needs to cater for heat pipe angle adjustments from 0° to 90° for future work.

5.2.3 Test approach and strategy

The apparatus is designed to cater for a wide variety of test conditions aimed at the medium temperature range of heat pipe operation. The approach and strategy of each test must be carefully designed before initiating testing. In this study the test rig is used to validate high temperature water heat pipes, the strategy and approach developed using the apparatus described in this chapter can be found in Chapter 7.

5.3 Heater block design

The heater block simply serves to introduce a heat flux to the evaporator end of the heat pipe. This can be achieved using a variety of methods as listed in Table 5-2, each having their own advantages and disadvantages.

Table 5-2 Types of heater used in heat pipe test rigs

Hater block type	Advantages	Disadvantages
Induction	-Can potentially be constructed at relatively low price -No contact resistance -Lower potential thermal losses	-Requires secondary coolant system -More difficult/time consuming to model and assemble due to system complexity
Cartridge	-Substantially cheaper than alternatives -Easy to use and operate -Easy to model and assemble	-Can have large contact resistance -Usually has a low design tolerance
Heated fluid loop	-Can potentially deliver large thermal loads easily -Uses both conduction and convection	-Adds substantially more complexity to the overall rig -Less accuracy in delivered thermal load output

To focus efforts more on the condenser section of the test rig and decrease the complexity of other parts of the rig, the simplest heater design was preferable in this instance, leading towards the heater cartridge option. The readily available materials at low cost also contributed to the gravitation towards this design. The component design focused on minimising the distance between the cartridges and the heat pipe surface. This in turn minimises the temperature difference between the two components to keep the cartridge operating temperature below 1200°C (see appendix I for the chosen cartridge heater specifications).

5.3.1 Performance assessment

The initial conceptual design of the heater block can be seen in Figure 5-6. The design consists of four high temperature 250W heater cartridges equally spaced around the circumference of the heat pipe to provide an even heat flux around it. The principal design constraints which were considered in the design process are the following.

- The maximum operational temperature of the cartridges
- Minimal machinable distance
- Tolerancing
- The maximum space available to house the heater
- Must be designed to house the 12mm diameter heat pipe
- Easily assembled/disassembled in between tests

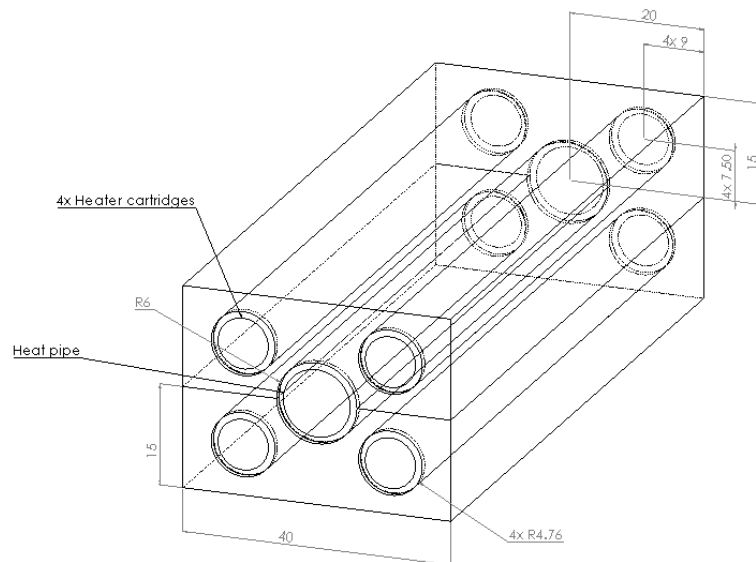


Figure 5-6 Cartridge heater concept model

To validate and improve the design, a CFD model was created to assess the maximum temperature difference between the cartridge and heat pipe surfaces. A thermal model built in Ansys Icepak is used to determine the surface temperature differences at various thermal load inputs. The boundary conditions taken into consideration were the input heat flux from the cartridge heaters, the thermal losses to the environment and the heat extraction rate (equivalent conductivity) of the heat pipe. The heat travelling radially out of the cartridge heater can be described through equation 61. The heater block was assessed as part of the full test rig CFD model presented in section 5.6.

$$\dot{Q} = 2\pi kl \frac{(T_1 - T_2)}{\ln\left(\frac{r_2}{r_1}\right)} \quad 61$$

Where ' k ' is the thermal conductivity of the heater block, ' r_1 ' is the radius of the heater cartridge and ' r_2 ' is the desired radial point for temperature measurement.

5.3.2 Final design

The final design can be seen in Figure 5-8 and consists of a four-piece structure which is bolted together in each corner holding four heater cartridges equidistant around the heat pipe which is in the centre. The design forgoes the need for thermal grease or any other thermal interface substance due to the clamping effect of the 'sandwich' design. This also allows for looser tolerancing which in turn reduced production costs.

Three thermocouple access holes are placed along the surface to enable the custom made 'blot' type thermocouples described in Section 5.5.2.1 to be inserted and removed with ease. Figure 5-7 shows the thermocouple mechanism in more detail.

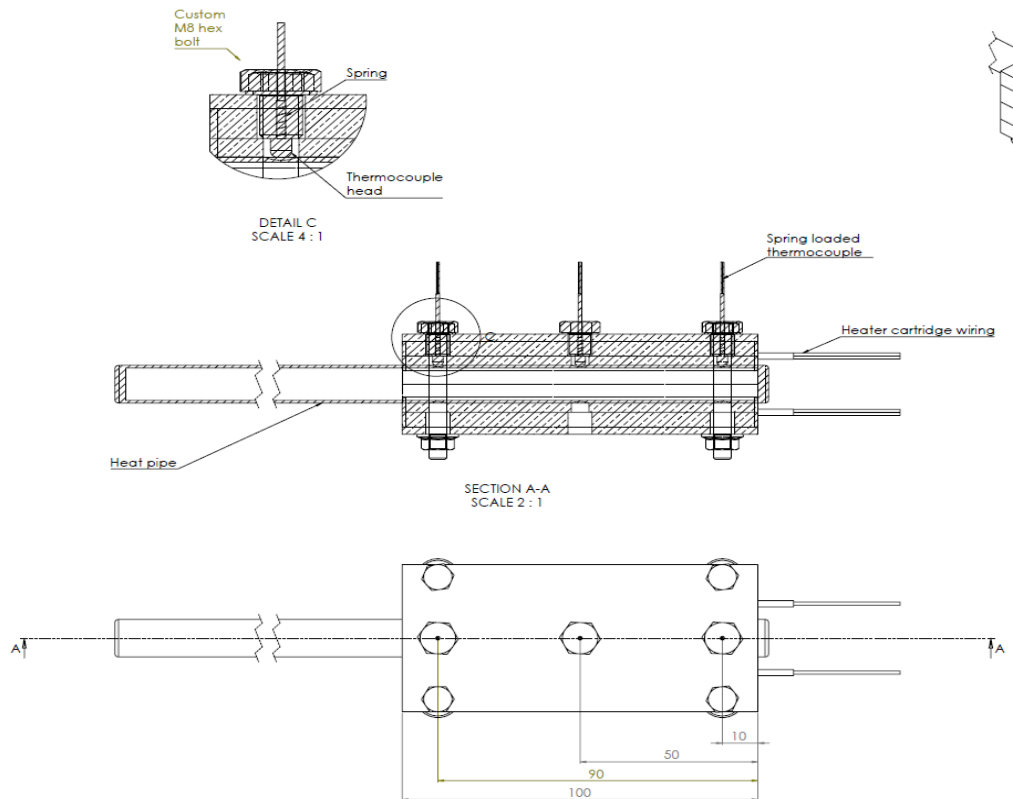


Figure 5-7 Final heater design engineering drawing

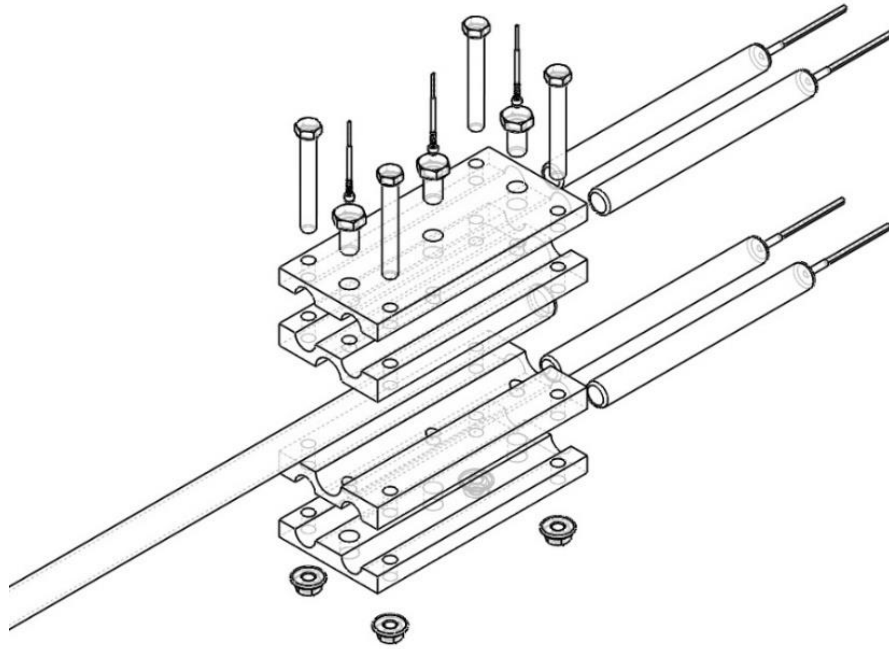


Figure 5-8 Final heater design exploded view

From the various design iterations seen in Appendix J, it was concluded that the tolerancing for the cartridge heater was too low to cater for through-hole designs as the hole would often need widening to fit the cartridge in. This would create large gaps in sections of contact creating increased thermal resistance. To solve this problem, a ‘sandwich’ design concept was taken forward which uses external pressure to minimise the contact gaps and allows for looser tolerancing due to the nature of the design. The final design of this type is presented below.

5.4 Calorimeter unit design

The calorimeter is the principal component of the test rig. This part is responsible for cooling the condenser section of the pipe and measuring the heat pipe thermal load. It is also the main point of control for the heat pipe vapour temperature which can be regulated by altering the circulator fluid temperature.

The basic working mechanism behind the calorimeter is the transformation of heat into a quantifiable measurement. This is done primarily by two common methods in industry; radiation or forced convection [111]. In the radiation method, the heat transfer is dictated by the Stephan-Boltzmann relationship seen in equation 62 [112].

$$\dot{Q} = \varepsilon\sigma A(T_h^4 - T_\infty^4) \quad 62$$

This method has three basic requirements; it must be conducted in vacuum; the surface temperature must be monitored, and the surrounding chamber must be kept at a constant temperature. Although the measurement technique for this method is relatively simple, it would require the construction of a costly vacuum chamber and the heat transfer rate is still relatively low even at elevated temperature, mainly due to the extremely low emissivity of Copper/Nickel alloys (~0.06). This limiting heat transfer rate would impede the heat pipes from reaching its maximum thermal load limitations and was determined to be too costly to implement.

The second method of calorimetry uses conduction and convection to transfer the heat into a fluid medium where the inlet and outlet temperatures are monitored. These are governed by the Fourier heat transfer relation seen in equation 63 [112] and the convective heat transfer relation seen in equation 64 [112]. These equations are used to determine the heat transfer through the calorimeter body and into the liquid convection medium. This allows the heat transfer from the heat pipe to the circulator fluid to be quantified experimentally via the heat capacity (equation 65) [112].

$$\dot{Q} = \frac{kA(T_{hp} - T_{cw})}{l} \quad 63$$

$$\dot{Q} = \alpha A(T_{cw} - T_f) \quad 64$$

$$\dot{Q} = \dot{m}c_p(T_{out} - T_{in}) \quad 65$$

Using the convection calorimetry concept, two initial calorimeter designs were created, one using concentric tubes to provide a surrounding cooling jacket to the pipe and one using straight channels. The final design consists of a silicone-based oil as the coolant with a high temperature circulator and a through channel design. The main reason for opting for this solution is the ease of manufacture compared to the gas gap design, which makes a significant difference in manufacturing time and cost.

Table 5-3 Calorimeter design table

Calorimeter design	Description	Advantages	Disadvantages
Concentric design	The design uses concentric channels to provide a full cooling jacket around the condenser section.	<ul style="list-style-type: none"> - Provides a homogenised temperature profile - Provides a larger surface area for heat extraction - Provides higher thermal extraction potential 	<ul style="list-style-type: none"> - Extremely difficult to assemble and large chance of error - Difficult to make a removable option, would have to be directly welded to the heat pipe - Limited material options if need to weld onto pipe
Chanel design	The design uses machined channels in solid blocks to direct the liquid around the condenser section.	<ul style="list-style-type: none"> - Simple to manufacture and relatively straight forward assemble - Is removable, so can be used on multiple heat pipes - Can be designed with common and cheap materials 	<ul style="list-style-type: none"> - Does not provide full coverage of the condenser so higher heat loss is expected

Figure 5-11 shows the final calorimeter design taken forward. This consists of a single channel design using the silicone-based oil and high temperature circulator. The silicone-based oil has the advantage of being able to reach up to 350°C through the circulator with minimal vapour formation. This allows for the ideal control of heat pipe vapour temperature above 300°C, though this would still be limited to vapour temperature up to around 450°C depending on the thermal load input. To further increase vapour temperature, either additional thermal resistance should be added in between the condenser section and the calorimeter, or the development of the gas gap calorimeter could be taken forward as future work.

5.4.1 Calorimeter performance qualification

In order to size and create the preliminary condenser design, two-dimensional analysis was conducted to determine the pressure drop and thermal performance of the

system. The estimate aimed to be conservative to intentionally slightly ‘over design’ the system to guarantee its performance.

The chosen coolant (or circulator fluid) was Thermal H350 (Dibenzyl toluene, 90-95%) as this was the high temperature oil supplied with the available circulator system. Fluid properties for the oil used in subsequent calculations were taken from supplier datasheets as presented in Appendix E.

The pressure drop across the calorimeter is estimated using the following equation:

$$\Delta P = K' \frac{\rho \bar{v}^2}{2} T^n \quad 66$$

$$K' = f \left(\frac{L}{d_h} \right) \quad 67$$

Where ‘ d_h ’ is the hydraulic diameter (in this case the true tube diameter), ‘ f ’ is the friction factor and ‘ T ’ is the viscosity ratio. The viscosity ratio is used to account for variation in viscosity due to temperature gradients in the flow. The value of ‘ n ’ recommended for this geometry case is $n = -0.25$ [113].

The friction factor can be calculated according to the Reynolds number in accordance to equations 68-70. [111], [112]

$$\text{For } Re \leq 2000 \quad f = \frac{16}{Re} \quad 68$$

For $2000 < Re < 4000$

$$f = 0.2088 - 0.1868 \left(\frac{Re}{1000} \right) + 0.0624 \left(\frac{Re}{1000} \right)^2 - 0.00656 \left(\frac{Re}{1000} \right)^3 \quad 69$$

For $Re \geq 4000$

$$f = 0.3164 Re^{-0.25} \quad 70$$

Where the Reynold's number is determined through equation 71. [111], [112]

$$Re = \frac{\rho u d}{\mu} \quad 71$$

Figure 5-9 shows the initial concept design used for calculations. The original concept design uses a two-channel system to provide heat transport from both the top and bottom of the condenser section of the heat pipe.

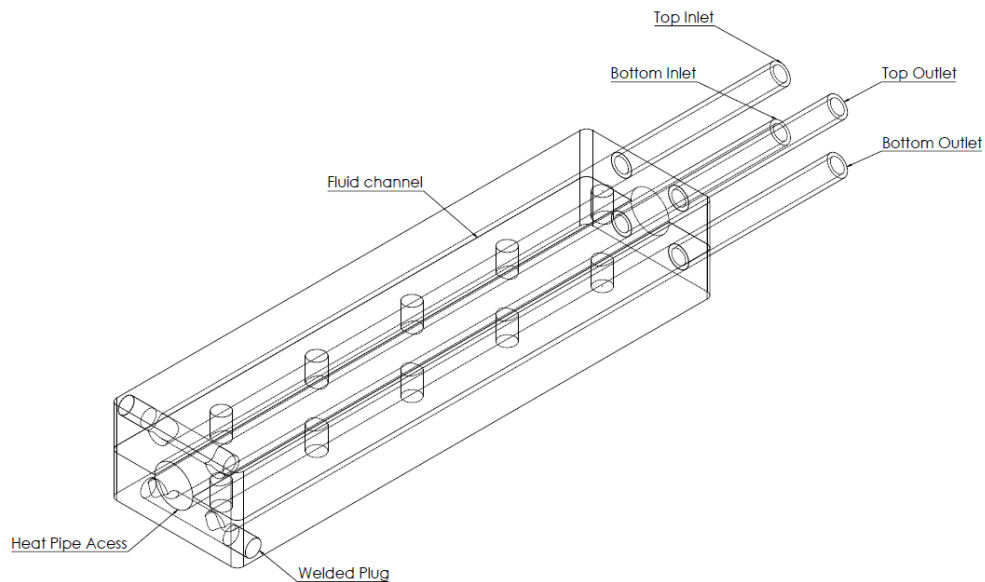


Figure 5-9 Initial calorimeter concept design

Initial system testing determined the flow rate through the system can be varied from a minimum of 0.0056 Kg/s to a maximum of 0.0167 Kg/s. The Reynolds number of maximum, minimum and medium flow rates were determined in for a pipe diameter of 6.15mm at a range of temperatures varying from 200°C to 320°C (determined by the temperature range the heat pipe will be tested in). At the maximum system flow rate, the fluid velocity reaches 0.62m/s to 0.68 m/s from 200°C to 320°C respectively.

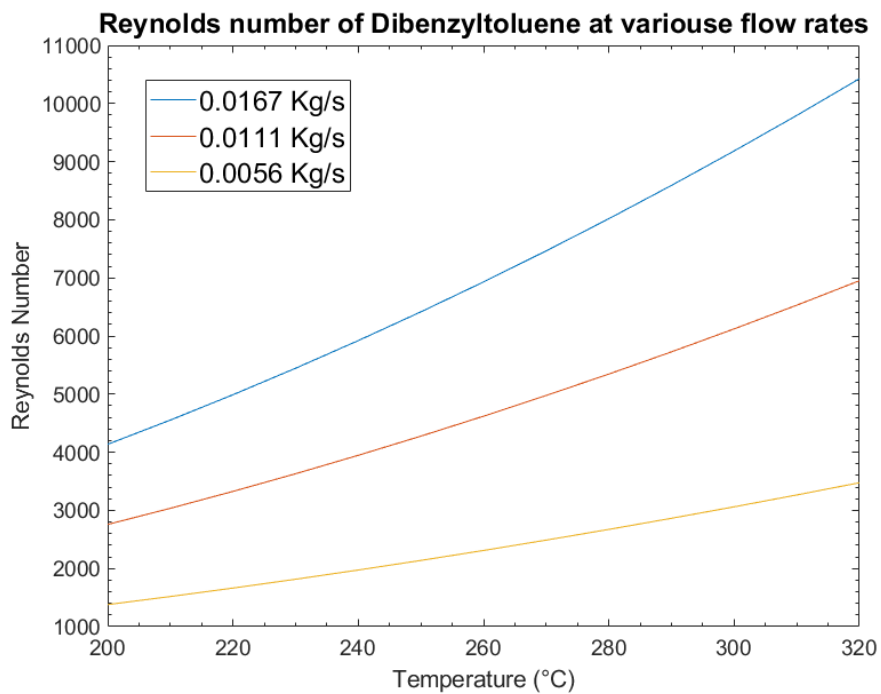


Figure 5-10 Reynolds number of Dibenzyltoluene for a rage of flow rates over expected operating temperature range

Figure 5-10 shows the calculated Reynold's number for each flow rate over the range of circulator oil temperatures expected. At low flow rates, the fluid flow starts in the laminar regime and becomes transient at temperature above roughly 240°C. At the flow rate of 0.011 Kg/s, the flow begins in the transient regime and becomes turbulent at temperatures above 240°C. At the highest flow rate, the flow regime is consistently

turbulent at the full temperature range. For ease of analysis, it is preferable that the fluid remains in one turbulence state throughout all tests. For this reason, the highest flow rate remains in one turbulence state throughout all tests. For this reason, the highest flow rate was chosen to take forward for further design of the condenser. In addition to this, heat transfer is generally promoted at higher turbulence states, causing an increasing the convective heat transfer coefficient compared to lower flow rates. As the flow rate through the top and bottom channels is measured in series with the flow meter, by the law of currents, the flow rate would in fact be halved through each channel using the two channel design in Figure 5-9. This led to the re-evaluation of the concept design to a single channel design instead as seen in Figure 5-11. This way the flow regime would remain turbulent through all testing and aid in simplifying the performance qualification.

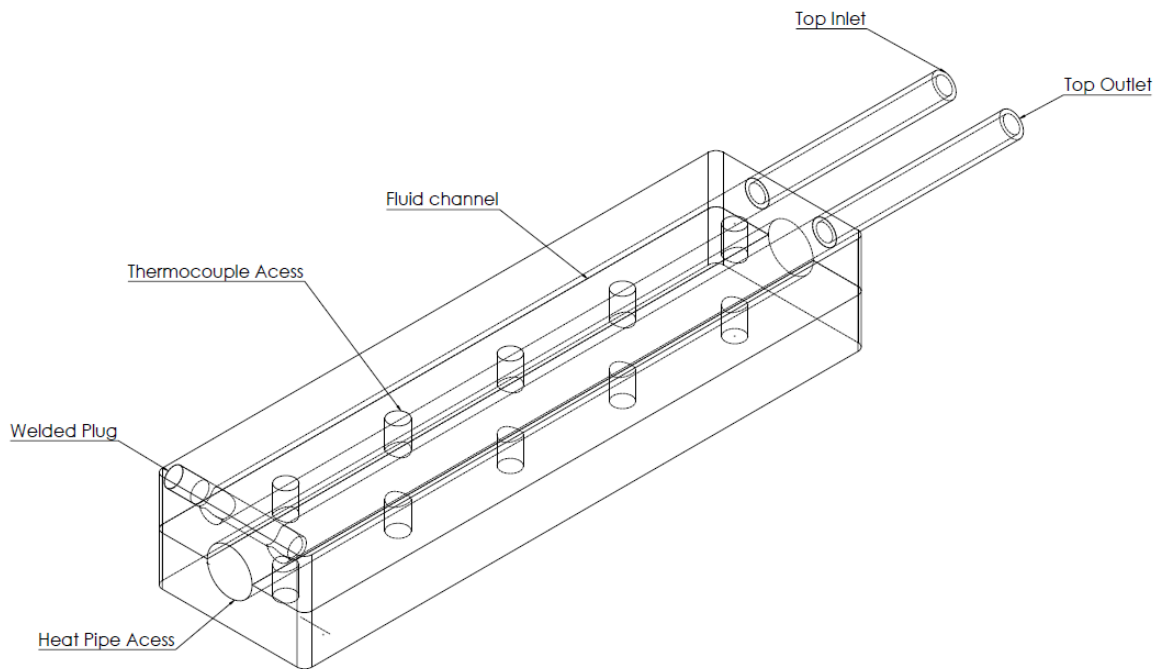


Figure 5-11 Final calorimeter design

5.4.1.1 Calorimeter heat transfer performance

To quantify the heat transfer performance of the calorimeter, the Nusselt and Prandtl numbers must first be determined for the calculated Reynolds number range for the operating conditions. The Prandtl number is defined as the ratio of momentum diffusivity to thermal diffusivity and is expressed through fluid properties as presented in equation 72. The Nusselt number is determined using the Gnielinski correlation represented in equation 13 using equation 70 to calculate the respective friction factor. This is valid for $3000 \leq Re \leq 5 \times 10^6$ and $0.5 \leq Pr \leq 2000$. [111], [112]

$$Pr = \frac{\mu c_p}{k} \quad 72$$

$$Nu = \frac{\left(\frac{f}{8}\right)(Re - 1000)Pr}{1 + 12.7\left(\frac{f}{8}\right)^{\frac{1}{2}}\left(Pr^{\frac{2}{3}} - 1\right)} \quad 73$$

The trend of Prandtl and Nusselt numbers at the given test temperature range was determined for Dibenzyl toluene in Figure 5-12. The given Nusselt number can then be used to predict the convective heat transfer coefficient through equation 74. [111], [112]

$$Nu = \frac{\alpha D}{k} \quad 74$$

Where ' α ' is the convective heat transfer coefficient, ' D ' is the channel diameter and ' k ' is the thermal conductivity of the fluid. Figure 5-12 shows the calculated Nusselt and Prandtl numbers for Dibenzyl toluene at the maximum flow rate of 0.0167 Kg/s and over the range of expected fluid temperatures.

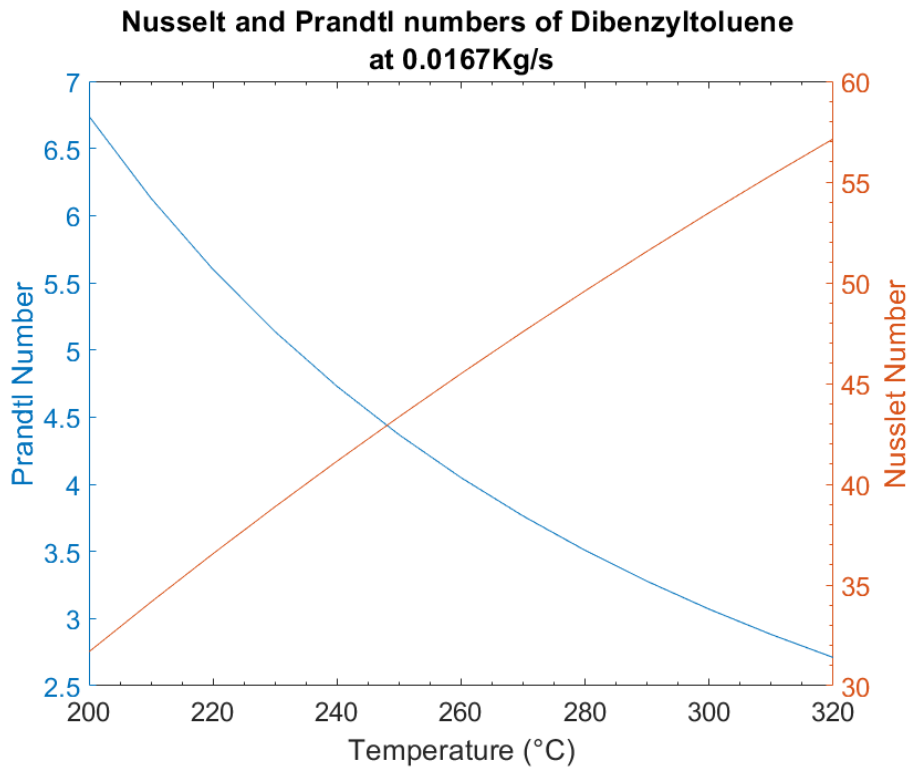


Figure 5-12 Dibenzyltoluene Nusselt and Prandtl number throughout operating temperature range

From the Nusselt number trend calculated in Figure 5-12, the convective heat transfer coefficient was then calculated using equation 74, presented in Figure 5-13. The expected temperature difference of the fluid over the range of expected thermal load inputs was determined for the maximum and minimum oil temperatures as presented in Figure 5-14.

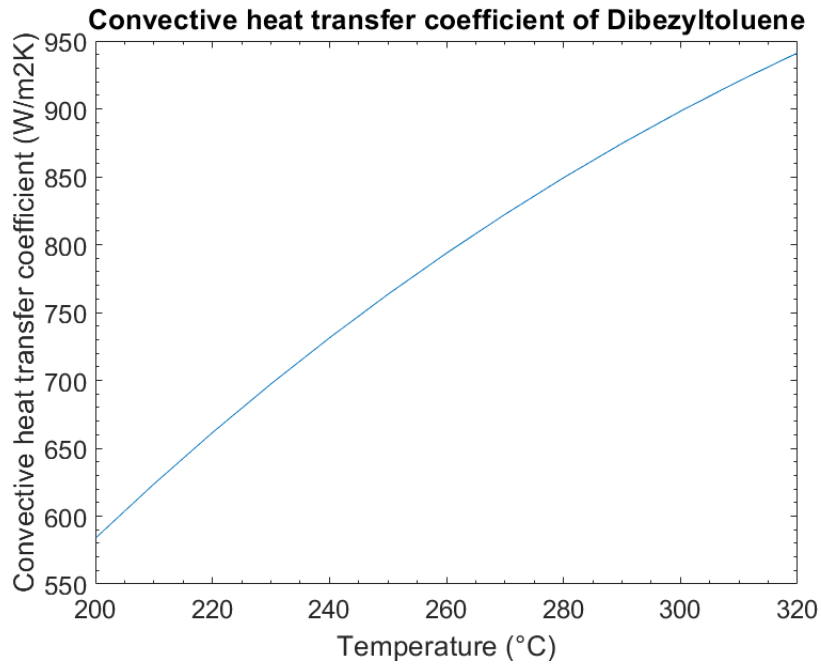


Figure 5-13 Convective heat transfer coefficient of Dibenzyltoluene through calorimeter channels over expected temperature range

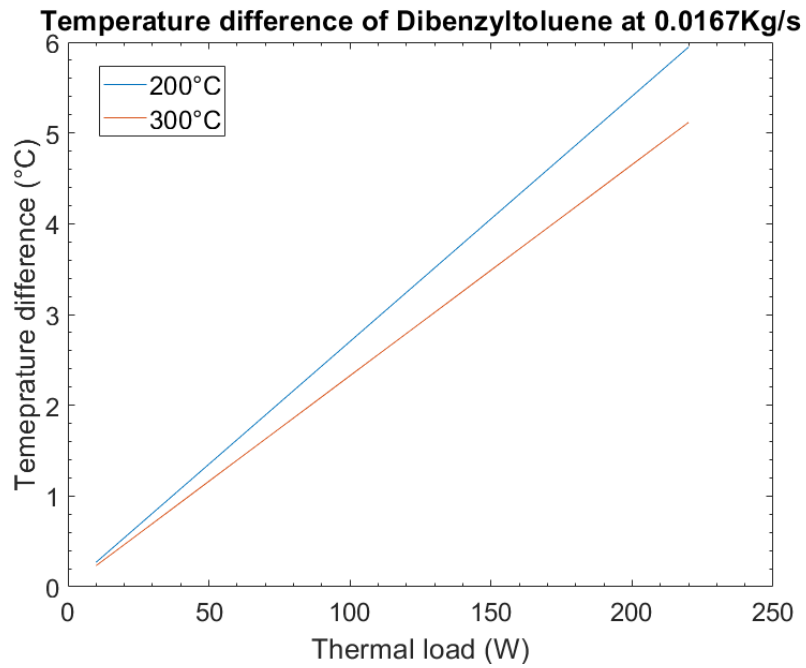
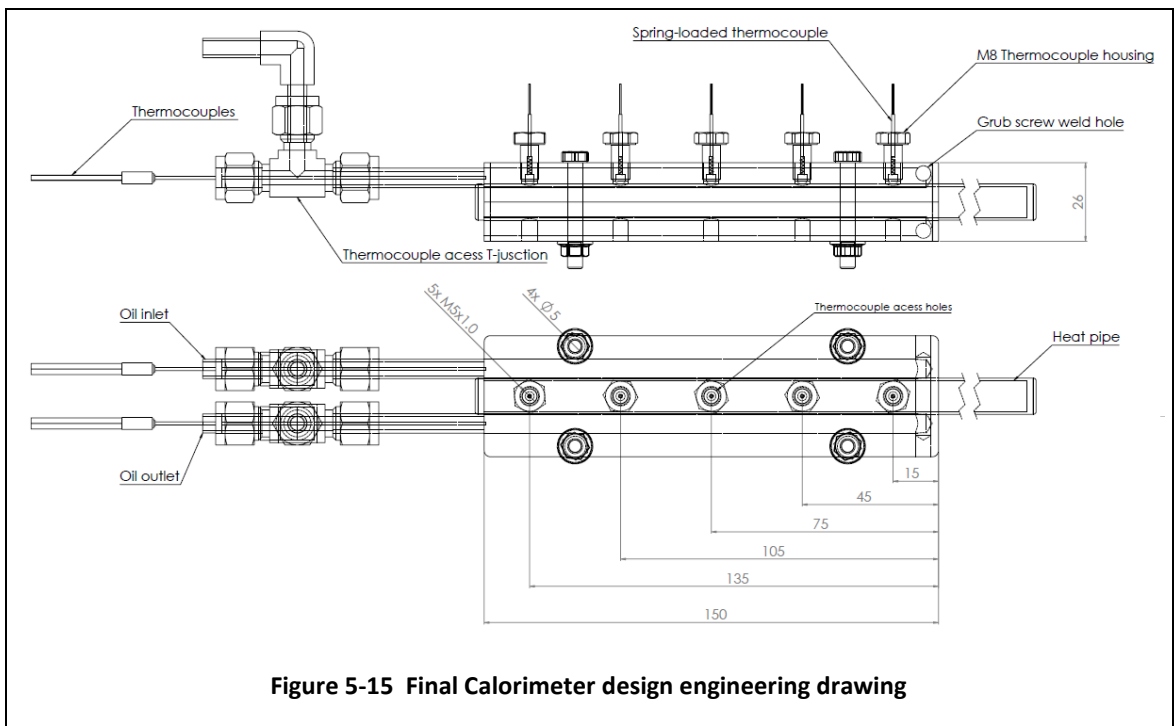


Figure 5-14 Calculated temperature difference at designated flow rate

5.4.2 Final calorimeter design

Based on the results from the calorimeter performance qualifications, and preliminary testing on various iterations, the final calorimeter design is given in Figure 5-15, Figure 5-16 and Figure 5-17. The design was aimed towards simplicity and ease of assembly. The top and bottom parts are kept together via four M4 screws which required a slight increase in width to allow the through hole clearance next to the fluid channels. The design is a one channel design with fluid only passing through the top part of the calorimeter, but with the possibility of adding a second oil channel in future. All parts are made of Stainless Steel 316L and the plug hole and oil inlet/outlet channels are welded to the calorimeter body.



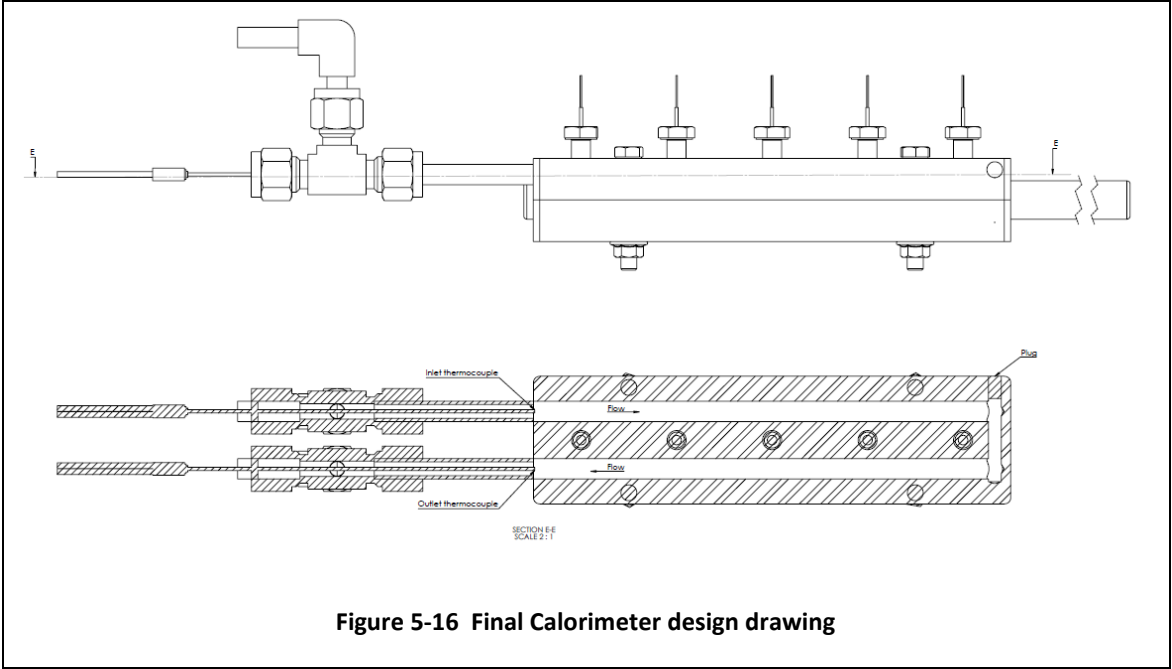


Figure 5-16 Final Calorimeter design drawing

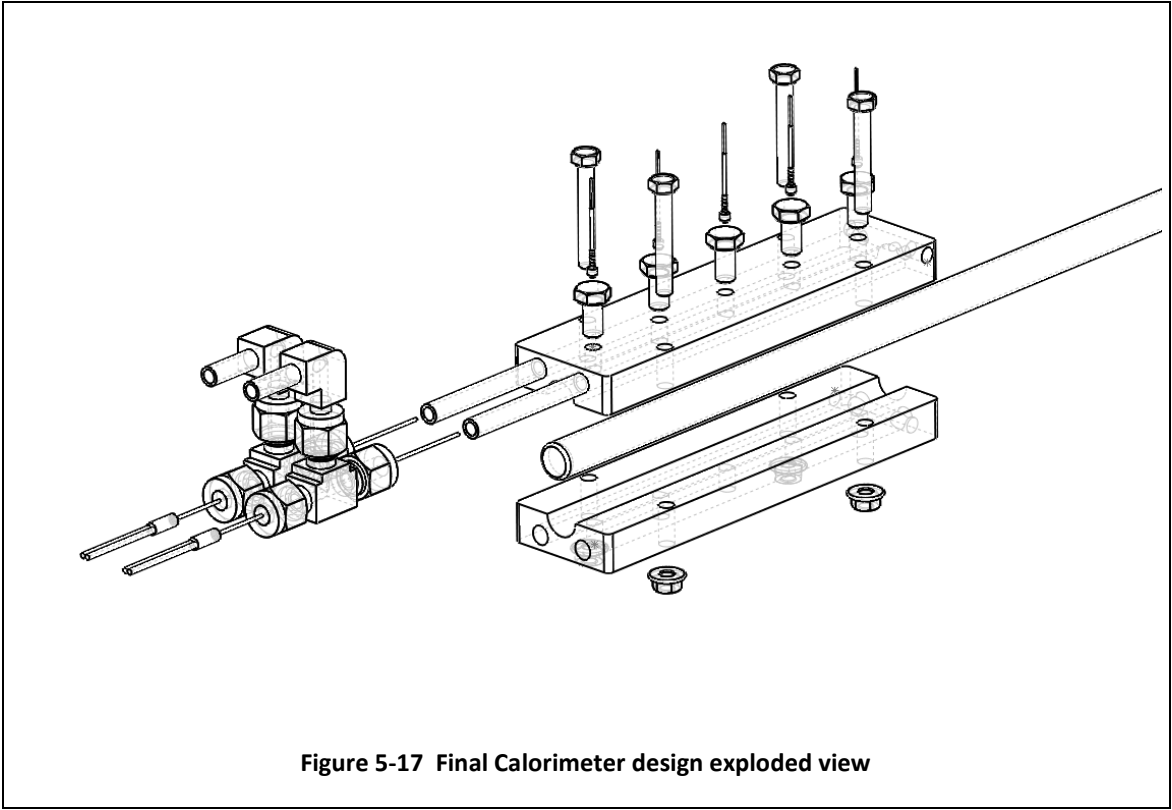


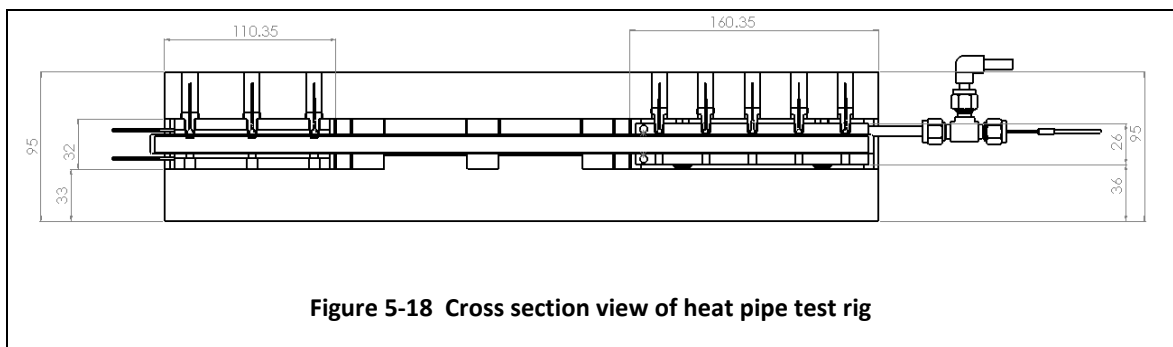
Figure 5-17 Final Calorimeter design exploded view

5.5 Final test rig design

The following section describes the final activities involved in quantifying the performance of the test rig to improve its design within the project constraints. The focus in the final design phase is predicting the heat loss experienced over the expected operating conditions, identifying the best hardware to collect data on temperature, flow rate and power input and determining an appropriate and accurate data acquisition and processing method.

5.5.1 Heat loss calculation

The heat losses from the test rig setup comes mainly from natural convective losses in air from the surrounding insulation. Figure 5-18 shows a general diagram of the proposed setup and insulation thickness. To estimate the heat losses, the thermal loss from each face of the insulation surrounding each component will be quantified. As the insulation around the adiabatic section of the heat pipe is much thicker compared to the heater and condenser section, heat loss forms the adiabatic section is assumed to be negligible compared to the rest.



The convective losses from both the condenser and heater sections are calculated for a rectangular object suspended in air. In general, the heat losses can be quantified according to equation 75. [111], [112]

$$\dot{Q} = \alpha A(T - T_{\infty}) \quad 75$$

Where ‘ α ’ is the convective heat transfer coefficient of air. This can be calculated using a similar methodology to the oil. In this case, the Nusselt number for vertical and horizontal flat surfaces proposed by Churchill and Chu [114] was used as follows:

For a vertical flat surface

$$Nu = \left(0.825 + \frac{0.87Ra^{\frac{1}{6}}}{\left[1 + \left(\frac{0.492}{Pr} \right)^{\frac{9}{16}} \right]^{\frac{8}{27}}} \right)^2 \quad 76$$

For a horizontal flat surface

$$Nu = 0.27Ra^{1/7} \quad 77$$

Where the Rayleigh number is defined as

$$Ra = \frac{\rho\beta\Delta Tl^3g}{\mu\alpha} \quad 78$$

From this the convective thermal conductivity from each face of the rectangular structure was assessed on the heater and calorimeter sides using the horizontal and vertical heat transfer correlations in equations 76 and 77. By further estimation of the bulk temperature of the heater and calorimeter by assuming the calorimeter remains near the oil circulation temperature and the heater will be higher by the calculated heat pipe temperature difference, the estimated heat losses for the full test rig are show in Table 5-4, Table 5-5, Table 5-6 and

Table 5-7.

Table 5-4 Heat loss calculations for 200°C circulator temperature

Circulator temperature (°C)	200							
Ambient temperatures (°C)	20							
	Variables					Heat loss Calculations		
Test series	Power input (W)	Heat pipe dT (°C)	Rough heater temperature (°C)	Rough Insulation wall temperature (°C)	Heater section (W)	Calorimeter (W)	Total estimated Heat loss (W)	
1.1	100	21.94	244.14	73.24	26.16	30.07	56.23	
1.2	120	28.24	251.07	75.32	27.11	31.14	58.25	
1.3	140	34.40	257.84	77.35	28.23	32.41	60.63	
1.4	160	40.82	264.90	79.47	29.46	33.80	63.26	
1.5	180	45.44	269.98	80.99	31.39	35.98	67.37	
1.6	200	51.55	276.71	83.01	32.30	37.00	69.30	
1.7	220	62.04	288.25	86.47	37.04	42.33	79.37	
1.8	240	106.00	336.60	100.98	46.55	52.99	99.54	

Table 5-5 Heat loss calculations for 250°C circulator temperature

Circulator temperature (°C)	250							
Ambient temperature (°C)	20							
	Variables					Heat loss Calculations		
Test series	Power input (W)	Heat pipe dT (°C)	Rough heater temperature (°C)	Rough Insulation wall temperature (°C)	Heater section (W)	Calorimeter (W)	Total estimated Heat loss (W)	
2.1	100	15.83	287.42	86.22	35.76	41.55	77.31	
2.2	120	20.88	292.97	87.45	36.77	42.70	79.47	
2.3	140	26.82	299.50	89.10	37.97	44.06	82.03	
2.4	160	33.29	306.62	90.75	39.28	45.55	84.83	
2.5	180	43.32	317.66	92.40	41.34	47.88	89.22	

2.6	200	47.98	322.78	94.05	42.30	48.97	91.27
2.7	220	71.88	349.06	95.70	47.32	54.65	101.97
2.8	240	117.87	399.66	97.35	57.33	65.91	123.24

Table 5-6 Heat loss calculations for 270°C circulator temperature

Circulator temperature (°C)		270							
Ambient temperature (°C)		20							
		Variables				Heat loss Calculations			
Test series	Power input (W)	Heat pipe dT (°C)	Rough heater temperature (°C)	Rough Insulation wall temperature (°C)	Heater section (W)	Calorimeter (W)	Total estimated Heat loss (W)		
3.1	100	15.22	308.00	92.40	39.67	46.22	85.89		
3.2	120	20.64	313.50	94.05	40.79	47.49	88.27		
3.3	140	29.39	319.00	95.70	42.59	49.54	92.13		
3.4	160	37.82	324.50	97.35	44.35	51.54	95.89		
3.5	180	49.04	330.00	99.00	46.72	54.22	100.94		
3.6	200	62.97	335.50	100.65	49.69	57.59	107.28		
3.7	220	80.88	341.00	102.30	53.58	61.98	115.56		
3.8	240	98.57	346.50	103.95	57.48	66.38	123.86		

Table 5-7 Heat loss calculations for 300°C circulator temperature

Circulator temperature (°C)		300							
Ambient temperature (°C)		20							
		Variables				Heat loss Calculations			
Test series	Power input (W)	Heat pipe dT (°C)	Rough heater temperature (°C)	Rough Insulation wall temperature (°C)	Heater section (W)	Calorimeter (W)	Total estimated Heat loss (W)		
4.1	100	13.93	341.00	102.30	45.64	53.34	98.98		
4.2	120	27.37	346.50	103.95	48.49	56.59	105.09		
4.3	140	42.06	352.00	105.60	51.66	60.19	111.85		
4.4	160	56.44	357.50	107.25	54.80	63.76	118.56		
4.5	180	62.04	363.00	108.90	56.04	65.15	121.19		
4.6	200	106.00	368.50	110.55	65.94	76.35	142.29		
4.7	220	120.00	374.00	112.20	69.17	79.98	149.16		
4.8	240	140.00	379.50	113.85	73.85	85.24	159.09		

5.5.2 Data acquisition and Methodology

The main form of data collection is by measurement of temperature values from each thermocouple over time. Other recorded data includes the flow rate of the coolant, power input, position of the thermocouples and photographic data of each test. The test

data are arranged by both data and test type in two separate folders. Key variables are noted before and during the test (if changed) and a description of the test and relevant notes is carried out afterwards. Various layouts for the data collection have been tested to facilitate the live heat pipe performance analysis to adjust flow rates and power input accordingly.

5.5.2.1 Thermocouples

The main chosen thermocouple type is the K-type mineral insulated stainless-steel thermocouples. From reporting and previous experience within the company these tend to be a very robust and reliable thermocouple type. The typical thermocouple accuracy for K-type thermocouples is $\pm 2.2^{\circ}\text{C}$ [115]. The thermocouple calibration equipment available at Aavid Thermacore is limited to temperatures up to 140°C only hence the thermocouples were instead calibrated in isothermal ovens at temperatures up to 1000°C . There are three types of thermocouple used as part of the test rig; 1mm mineral insulated, M6 spring loaded and ring types as seen in Figure 5-19. These thermocouples were all sourced from TC Direct [115].



Figure 5-19 Thermocouple types used

Future improvements to the temperature reading includes the potential use of PT100 sensors which provide an accuracy of $\pm 0.15^{\circ}\text{C}$ [115]. These, however, are substantially more expensive than conventional thermocouples and require a specialised data logging system hence were not considered for the testing presented in this thesis.

5.5.2.2 Flow meter programming & control

The flow meter used is a RHEONIC RHM 04 with a capacity of up to 10kg/min. The flow reading has an accuracy of 0.1% of the recorded flow rate and was originally sourced as a set from Bronkhorst using a Cori-flow Controller to automatically adjust the Badger pneumatic valve to a set flow rate. In this system, the Cori-flow controller both outputs the flow rate from the Rheonik sensor and controls the pneumatic valve to adjust the flow rate using a feedback loop using proprietary Bronkhorst software. Unfortunately, due to incompatibility of the Bronkhorst software with the Coriolis flow meter, there were serious reading discrepancies in this system which lead to the re-calibration of the flow meter and use of a proprietary Rheonik signal receiver and software in place of the Bronkhorst system. The Pneumatic valve was then reconfigured to be adjusted manually using a 0-16 mA signal converter. Appendix N shows the control screen for the proprietary Rheonik software used during the final tests.

5.5.2.3 Pico logger settings & automated calculations

The chosen temperature recording hardware and software was the PICO Technology Pico logger C06 and PicoLog 6 respectively. This was due to Aavid Thermacore possessing all the appropriate licensing required and having worked with such hardware extensively throughout the company. The hardware is compatible with a large range of thermocouples and provides an excellent interface to record temperature data and has great flexibility with automated calculations and data extraction. The device can be used with a wide range of thermocouple types and has a resolution of 0.025°C [116].

The pico logger allows for automated calculations to be added as an output function during testing. This allows for the real time heat flux output to be calculated even with a change in flow rate. Firstly, a linear equation correlating the specific heat capacity heat capacity with the average bulk fluid temperature. The volume flow rate of the fluid is then correlated with a stable temperature source (i.e. thermocouple calibrator). The temperature of the calibrator could then be changed to match the flow rate recorded. For the final tests however, only one flow rate was used, so the flow rate value was used directly in the variable equations. The linear approximations for the specific heat capacity and density were taken from the oil property tables provided by Julabo as seen in Appendix E.

5.6 Test rig CFD analysis

To validate the final design, a CFD model of the full rig assembly was built to simulate a range of test conditions. The simulations are used to predict the maximum temperature seen in the evaporator section in order to spec the heater cartridges as well as to validate the predicted heat losses calculated from numerical analysis. It also serves to identify any issues which may arise in the testing. Additionally, a preliminary heat pipe model is built in CFD using thermal conductivity values predicted from the heat pipe performance modelled in Chapter 4. This heat pipe CFD model can subsequently be used to compare against the experimental performance of medium temperature heat pipes and be adjusted/improved using empirical data.

5.6.1 CFD boundary conditions

To begin building the CFD model in Ansys Icepak, the CAD files used for each of the part drawings were assembled and encapsulated in a Calcium Silicate shell of the same dimensions which were used in the test rig. Figure 5-20 shows the full assembly CAD model used for the simulations. The heat pipe model consists of a 12mm diameter and 0.8mm thick Cu/Ni 60/30 shell with a solid interior user defined material with a thermal conductivity 6670 W/mK which is estimated through the thermal resistance model described in Chapter 2. Additionally, the heat pipe shell is split into 2mm thick sections at the location of each thermocouple in order to monitor the shell temperature at those positions.

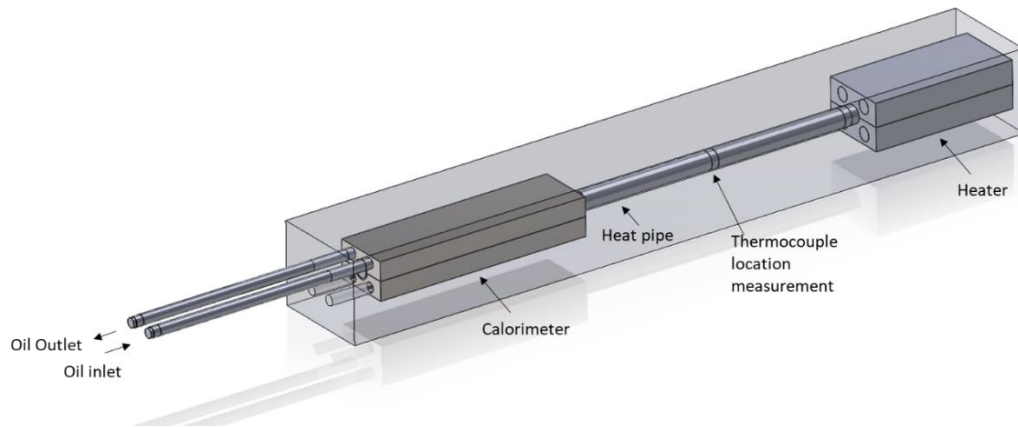


Figure 5-20 Thermocouple types used

Once each component in the assembly was modelled, a 720x270x255mm cabinet was modelled around them with the assembly centred. The cabinet is by default populated with air at 30°C (as measured within the cabinet during preliminary tests). On the upper and lower edges of the cabinet in the ‘y’ orientation, the boundaries were modelled as ‘openings’ as seen in Figure 5-21. All spaces occupying the inner channels of the calorimeter and tubing were modelled as Dibenzyltoluene with the fluid properties seen in Figure 5-22. The flow in the calorimeter was set as a turbulent flow using the enhanced k-epsilon turbulence model. Heat transfer due to radiation was ignored. The convergence criteria were set to that seen in Figure 5-22. The inlet conditions for Dibenzyltoluene was set to 200°C and 0.0167 Kg/s for all simulations. The total power input at the evaporator was split evenly between all four heater cartridges. Three power input conditions were chosen to analyse, these are 100W, 140W, 180W and 220W. The heat pipe was modelled as a solid rod with thermal conduction of 9000W/mK based on the predicted heat pipe performance of Water heat pipes modelled in Chapter 7.

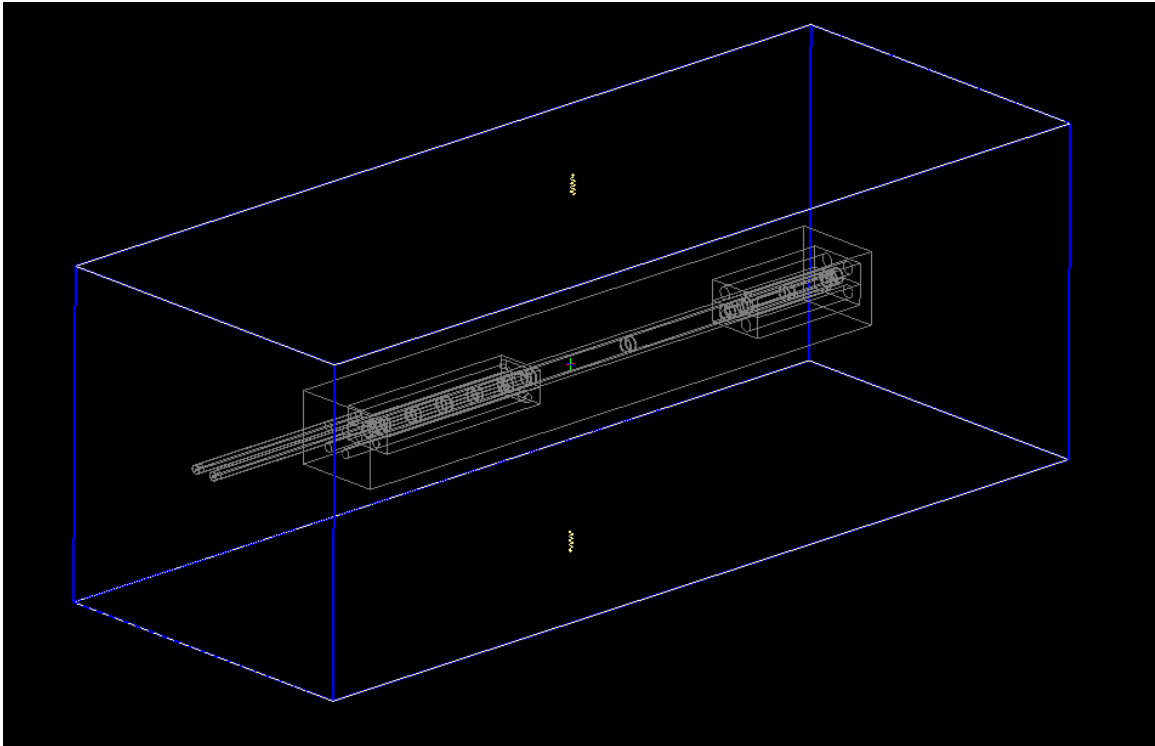


Figure 5-21 CFD model and cabinet in Ansys Icepak

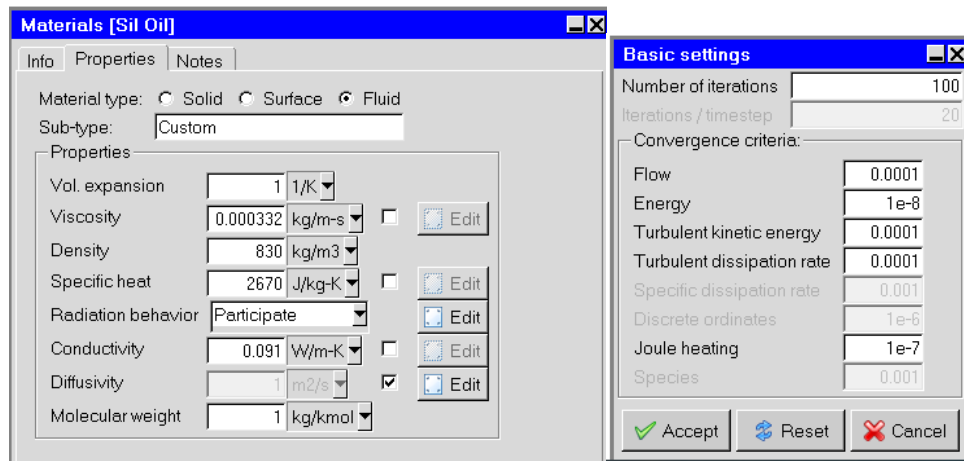


Figure 5-22 Dibenzyltoluene property data in Ansys Icepak and convergence criteria

5.6.2 Full assembly performance

To assess the performance of the heat pipes and test rig, CFD modeling at various input powers was undertaken to estimate the expected heat loss and heat pipe temperature profile. Figure 5-23 shows the expected heat pipe profile temperature at various power inputs. The heat output is calculated from the coolant temperature rise between the inlet and outlet of the calorimeter for each steady state condition. The heat input against heat output for each steady state is shown in Figure 5-24.

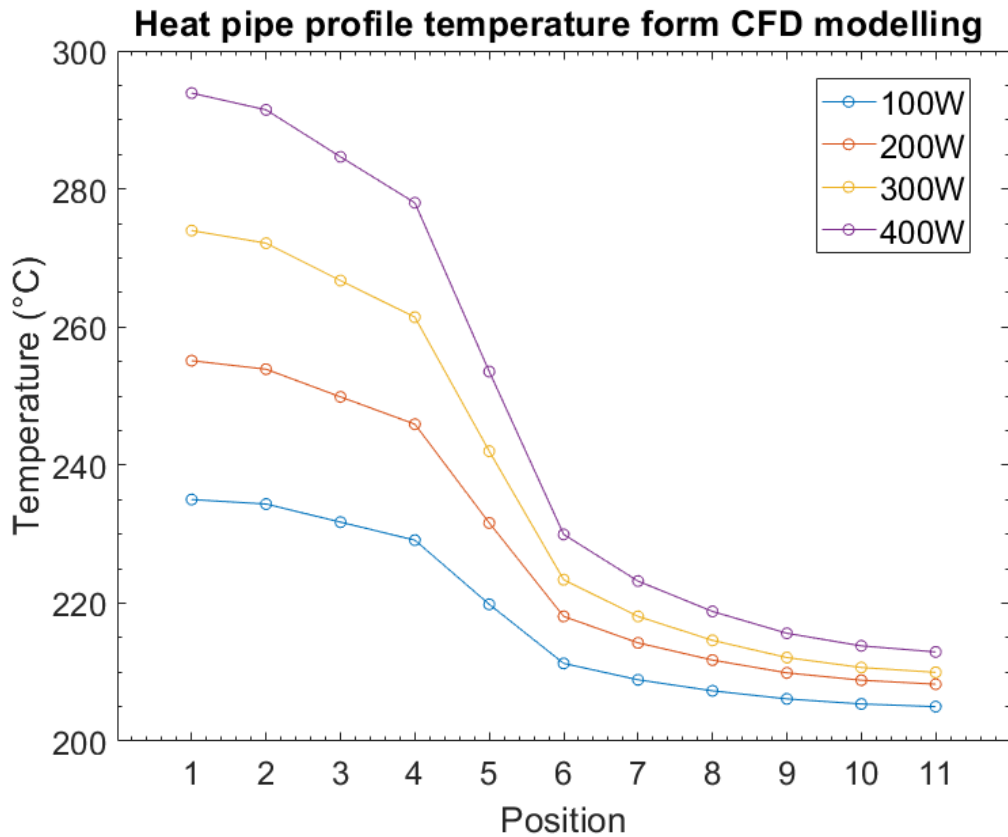


Figure 5-23 CFD heat pipe temperature profile at various input powers. The calorimeter temperature input is of 200°C and flow rate is 0.0167 Kg/s.

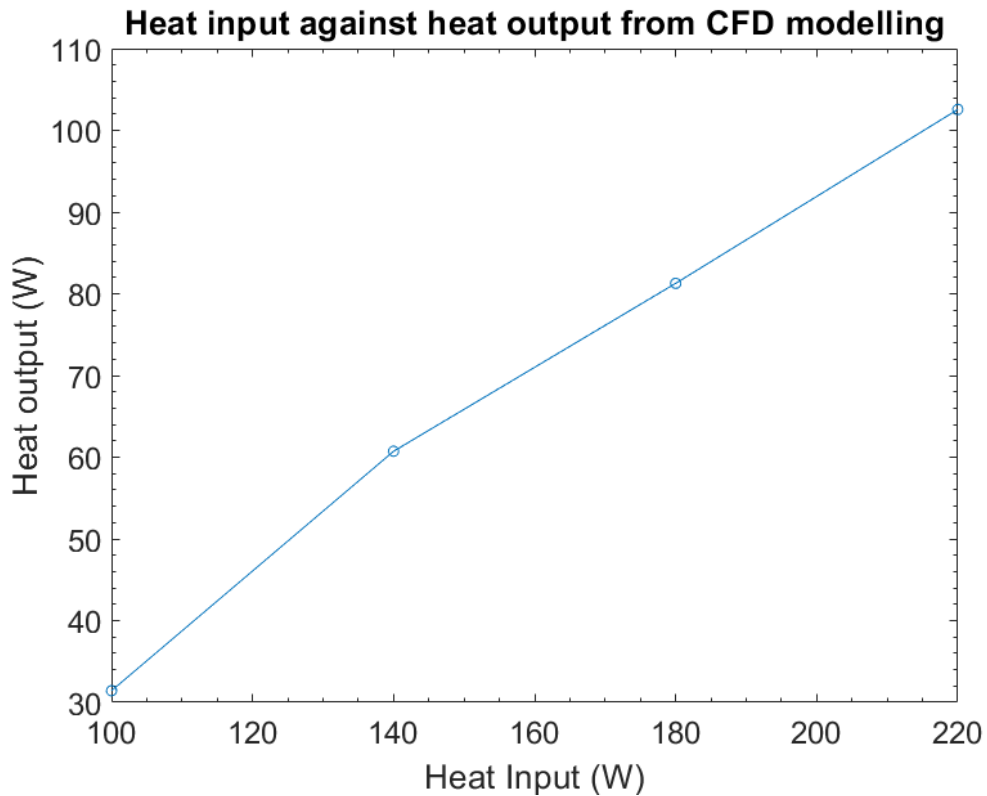


Figure 5-24 Heat input vs heat output from calorimeter.

From this analysis it is apparent that there is a relatively high heat loss experience by the test rig, even when operating the calorimeter at maximum flow rate. As this equipment was the only available within budget for high temperature tests, the experimental heat losses will be compared against the CFD for mutual validation, while future work will focus on reducing the experienced heat loss. A comparison of the numerical heat loss predictions against the CFD analysis is presented in Table 5-8. Here it can be seen that there is a divergence of heat loss estimations with an increase in power input. It can be assumed that the true heat loss will lie somewhere between the two estimations.

Table 5-8 Comparison of CFD and analytical heat loss predictions

CFD Heat loss estimation (W)	Analytical Heat loss estimation (W)
68.58	56.23
79.27	60.63
98.72	67.37
117.44	79.37

5.6.3 Heater block analysis

An analysis of the heater block internal temperature variation was done on highest power steady state condition in Figure 5-23. Figure 5-25 shows the results from this study. The maximum temperature reached by the heater cartridges is 312°C. the maximum temperature difference form the heat pipe wall to calorimeter walls experienced is of 17°C.

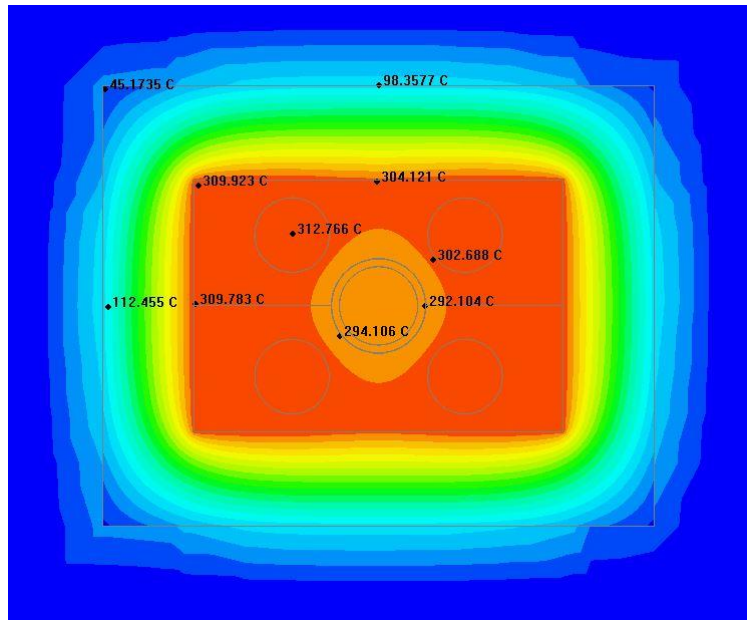


Figure 5-25 Heater block modelling results at 220W

These results were used in order to spec the heater cartridge maximum temperature capability and ensure the maximum temperatures experienced were at a reasonable magnitude for the materials in use (i.e. heater metal, surrounding insulation and heater cartridge).

5.7 Qualification testing

As part of the production procedure, there are various tests which must be completed to pass industrial standard production. Furthermore, preliminary tests which quantify the extent of heat loss and compare these to the predicted values are essential before carrying out any performance tests on the heat pipes. Figure 5-26 shows the production process flow chart of a typical heat pipe. A summary of each test is detailed in this section where full testing procedures are referenced in the appendices accordingly.

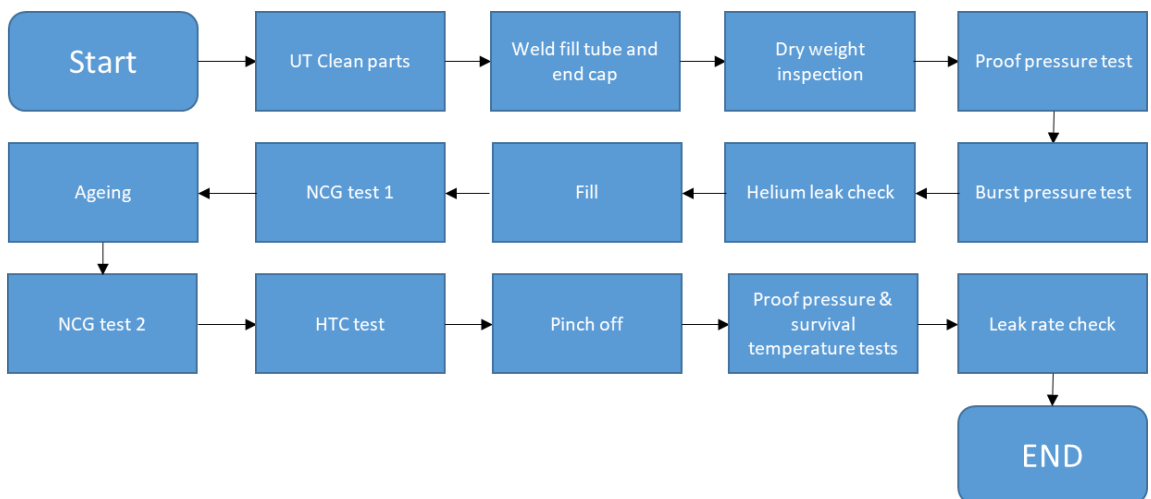


Figure 5-26 Heat Pipe production flow chart

After the heat pipes are manufactured, there are two main types of tests which will be carried out on the heat pipe to characterise their performance:

5.7.1 Dry-out tests

This test intends to verify the thermal load at which dry-out occurs in the horizontal and vertical positions (i.e. maximum and minimum thermal heat transport capabilities). Tests are run at 3 different temperatures pre-determined according to the fluid used. The tests are used to qualify the heat pipes and ensure they are operating within the desired thermal loads and temperature range.

5.7.2 Angle test

This test intends to further characterise the heat pipe determining the dry-out point at various angles. This is used if the application requires angular operation or to quantify the full operating range of the heat pipe. In this case, the angle tests performed were limited as the operation for the application in question in Chapter 7 was only in the horizontal position.

5.7.3 Heat loss tests

Prior to any heat pipe testing, it is essential to determine the performance of the test rig in terms of its heat loss and temperature drops in the piping. There are two main factors to be considered; the heat loss to be expected through the condenser block at a given temperature and the temperature drop from the heating element to the inlet of the condenser.

5.7.4 Baseline Testing

The first round of tests focused on high temperature water heat pipes and determining their maximum operational conditions. This has the principal goals of:

- Verifying the previously claimed compatibility between the given metal shell/wick material/working fluid combination
- Ensuring there are adequate production and assembly methods/procedures
- Comparing pipe performance against theoretical predictions
- Ensuring the viability of using water heat pipes in the determined temperature range
- Characterising the maximum performance limitations
- Determining improvements to be made (material/wick improvements)
- Comparing results to predicted performance data
- Completing all heat loss tests for the test rig

The main results attained are the heat loss tests for the preliminary test rig and the first condenser block design. A summary of each test conducted, and the main observations taken from them are detailed in Chapter 3.

5.8 Life test rig

Once the various selected fluids have been established in their thermal transport performance assessment, the long-term viability of the heat pipe must then also be assessed through what is known as ‘lifetime tests’. This can be done in various forms but there are generally two main types of tests are performed: cyclical and linear. The cyclical tests emulate heat pipe operation cycles by heating and cooling the heat pipe close to the amount of times that would be experience in the operation lifetime, but at an accelerated pace. This is useful for determining any issues with the start-up process and any degradation in functionality over the operation for a specific application. Linear tests are more geared toward fluid/metal compatibility over time. This keeps the heat pipe steadily in operation for a long period of time at the desired maximum operating temperature to analyses any NCG formation by detecting any changes in temperature difference in the vertical orientation. This is used for novel heat pipes to validate its metal/fluid compatibility and determine its lifetime expectancy at the desired temperature. This is the main form of lifetime test used in this case.

5.8.1 Accelerated life test theory and approach

Accelerated life tests can be performed in several ways. Generally, the tests aim to emulate the operational cycles at a much faster frequency to determine any corrosion, thermal fatigue, compatibility issues or fluid degradation and to quantify the heat pipe’s expected lifetime. Previous work by Anderson et. al [10][43], Rosenfeld et. al [80], Kenney et. al [41] and Martin et. al [89] has shown the compatibility of a variety fluid/metal

combinations through a variety of experimental and analytical techniques. In the case of this study, the approach taken is to construct a test rig which can maintain the evaporator of a heat pipe at a constant temperature for a long duration.

5.8.2 Life test rig design assessment

In industry the ‘life test’ of a product usually manifests itself in the form of cyclical tests taking the heat pipe from the lowest expected application temperature to the highest expected application temperature at a vastly accelerated rate. This is known as ‘accelerated life test’ and often forms a part of the heat pipe appraisal when adopting in new applications. In this case however, there is no specific application or minimum and maximum temperature requirements, simply a novel fluid/metal combination which requires long term compatibility validation. In these cases, a different approach is taken. The test consists only of keeping the heat pipe at the maximum operable temperature for an extended period. In this case, there are two different life tests to be completed, one with water/CuNi heat pipes at 300°C and the other with the SbCl₃ and GaCl₃ heat pipes at 400°C or above.

5.8.3 Life test strategy

The life tests aim to be as simple as possible in design in order to ensure longevity by ‘future proofing’ the test (e.g. ensuring the apparatus and instructions are as simple as possible so that others can extract data easily in future). The rig will consist of only

heater blocks and machined calcium silicate insulation. The power input will be a self-adjusting PID controller set to maintain the evaporator at a constant temperature.

5.8.4 Final test rig model

The final test rig design consists of a variety of Calcium Silicate insulation blocks stacked around the heat pipes. A small 40mmx60mm heater block with two heater cartridge in each is used to maintain the heat pipes at temperature as seen in Figure 5-27. The calcium silicate blocks are made in two sizes, one thin section and one thick section. The thin sections have larger hole diameters in order to fit ring type thermocouples onto the pipe. There are also small channels machined at the bottom of each thin section to feed the thermocouple wires through.

The control system consists only of a PID controller for each heater block and TC-08 Pico Technology thermocouple loggers to record the temperature of the heat pipes in 30min intervals. The test rig has been constructed, and one water heat pipe has been put in place to validate the long-term performance of the heat pipes developed in Chapter 7.

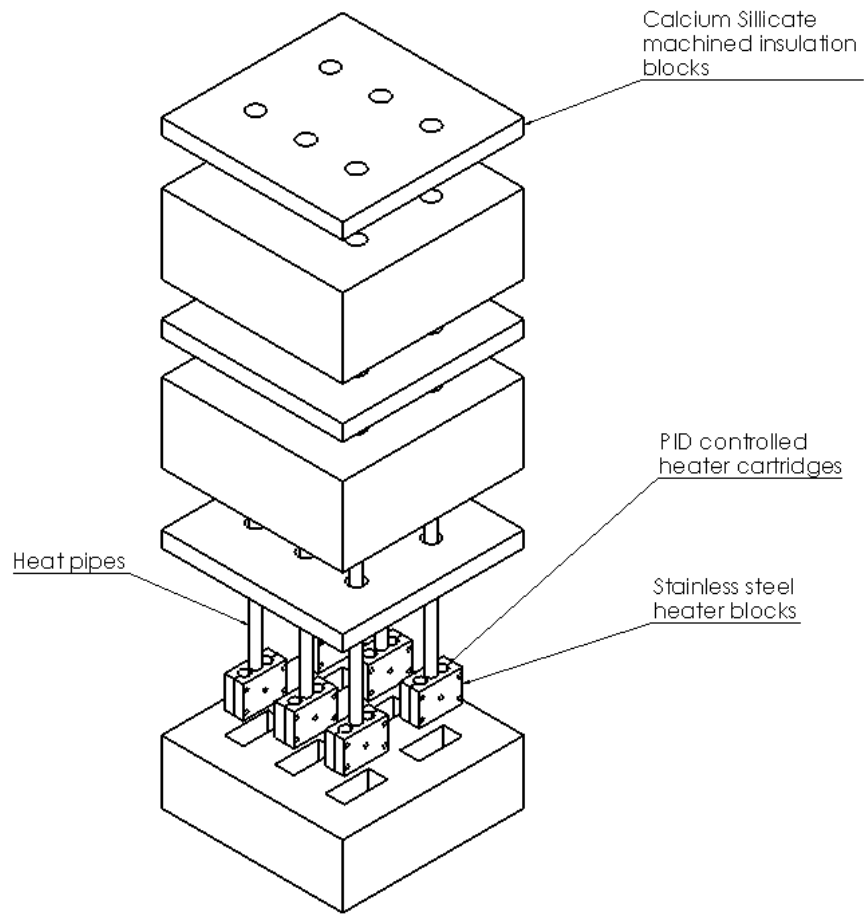


Figure 5-27 Life test rig exploded view

5.9 Chapter Summary

A test rig capable of achieving the specification outlined in Section 6.1 has been constructed. Each part of the test rig has been iteratively designed and tested to reach an optimised solution for the equipment and software available. The predicted performance of the evaporator and condenser has been calculated for the desired test conditions for water heat pipes. The conditions will be used as a baseline to compare the performance of selected medium temperature fluids in future work. The test rig itself has been validated through tests outlined in Chapter 3, showing the performance of each individual component in terms of estimated heat losses. The calibration and statistical accuracy of each component is also outlined in Chapter 3. Further to this work, water heat pipes will be tested and results using the developed test rig are presented in Chapter 7.

Additionally, a lifetime test rig has been modelled, designed and produced for future work. The water heat pipes used in Chapter 7 will begin their testing toward the end of this project, hence the results will only be available for future publications. The rig allows the future development of medium temperature heat pipes to also be lifetime tested once prototype development stage is reached.

Chapter VI

Experimental analysis of fluid/metal compatibility and wettability

6.1 Introduction

The next step in the development of a heat pipe which could hold the previously determined fluids (Antimony Trichloride and Bismuth Trichloride, see Chapter 4) is to determine the optimal metal which can be used as the heat pipe envelope and wick structure. The key attribute the metal must have are:

- Fluid compatibility over time (low NCG formation)
- Resistance to corrosion by fluid
- Good wettability

The wettability of the fluid is a key attribute which gives an indication towards the level of capillary action to be expected in the porous structure of the heat pipe. The higher the wettability of the fluid to the surface, the better the capillary action will be [117]. An investigation into the wettability of the metal surfaces is undertaken and the creation of new testing methodology to determine the wettability of Halide salts is proposed and tested. In addition to the wettability of the metal surface, the compatibility of the chosen fluids with a given metal surface is of vital importance to the functionality of the heat pipe. For this, the electromotive force for forward and backward reaction equations are analysed, this gives determination of which direction the reaction is likely to have most affinity towards.

Key performance indicators are selected to determine the most suitable metals by performing an extensive metal selection database search to determine the main compatible metals which could have the best long-term potential with a given fluid. Due to time limitation, however, a short-term compatibility investigation is devised to identify any immediate effects on the metal form exposure to the fluids and identify the most suitable long-term candidates. Analysis of the electrochemical properties of the metal and chosen chemicals are also performed. From these processes, three key phases were determined for the selection and testing processes.

- Metal selection
- Wettability testing
- Molten fluid compatibility testing

6.2 Material selection for Heat Pipe

The heat pipe material selection made use of ‘Citrix Database’ [118] to analyse a database of over 2000 metals, alloys and ceramic materials. This aims to narrow the search to only a few key metals based on their physical qualities – the chemical compatibility of these metals with chosen chemicals is then subsequently analysed.

The main selection criteria used to narrow the database are defined by the key desirable qualities of the material, these are listed as follows ranked in order of importance:

- Resistance to corrosive fluids
- Good weldability
- Resistance to stress corrosion cracking
- High tensile strength
- High Thermal conductivity
- Low price
- Low density

The selection process took place by comparing two key properties against each other and selecting a graphical region containing materials of the desired property. This took place iteratively until the material choices were narrowed to an acceptable quantity. The order by which the comparisons were made followed the importance ranking of each quality, for example, the first graph compares qualities 1 & 2, the second 2 & 3 and so forth

until an acceptable number of materials were selected. To begin the analysis a few key features were chosen to narrow the initial selection. The initial search parameters were the corrosion resistance, durability (towards weak acids) and processing properties (weldability).

From this initial filtering, 381 suitable metals were highlighted as suitable. To further narrow these options, four key metal properties were analysed: tensile strength, thermal conductivity, hardness and cost. The first pass plotted the results for tensile strength against thermal conductivity and the metals which were presented in the preferable range of the plot were selected to take forward. These can be seen in Figure 6-1.

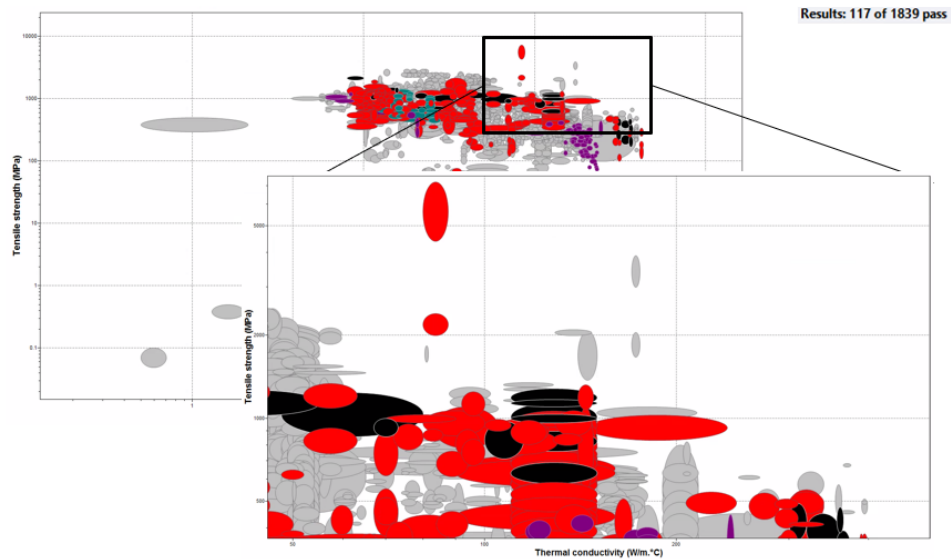


Figure 6-1 Tensile strength vs thermal conductivity metal search filter

The second pass narrowed the search to 117 metals and alloys to take forward. These were then further analysed comparing a plot of hardness against price. Figure 6-2 shows the plot results. The metals in the low-price range were selected for analysis.

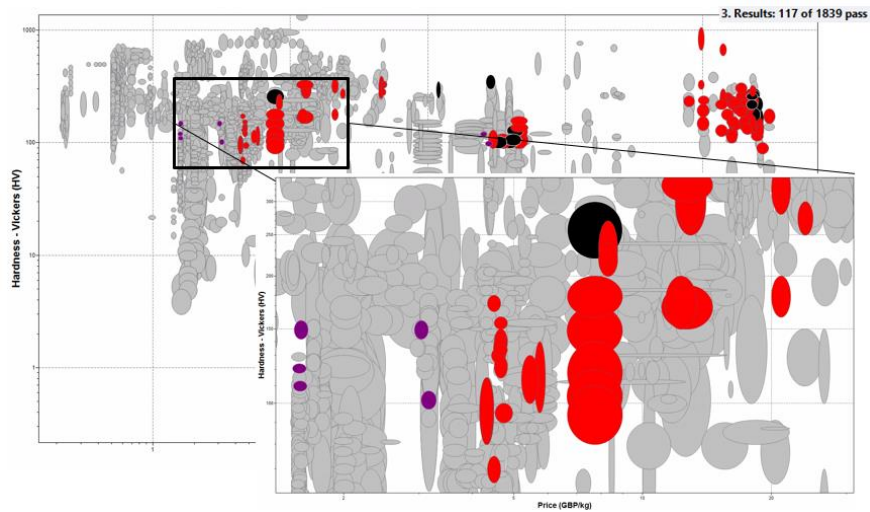


Figure 6-2 Hardness vs Price metal search filter

A detailed view of Figure 6-2 is presented in Figure 6-3 showing the listed metals and alloys from the outcome of this database search. In total 39 metals met the filter criteria with the overall general pure metals being Nickel, Molybdenum, Copper, Chromium and Aluminium as well as many alloy variations of these metals.

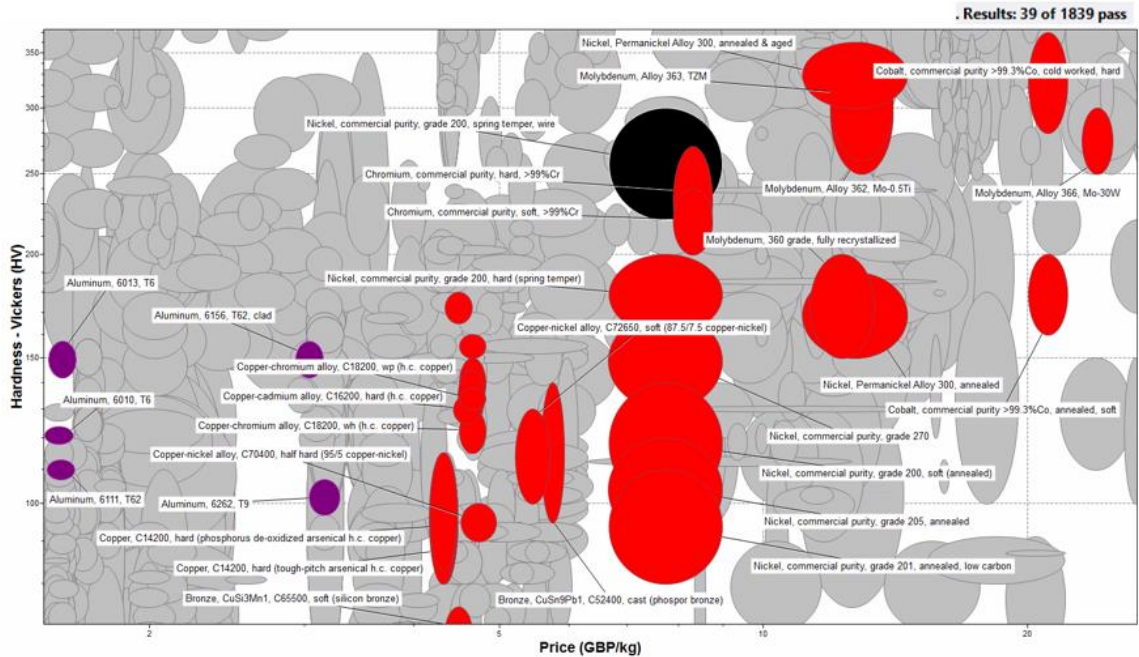
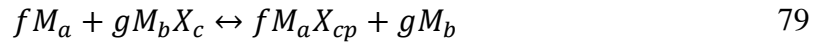


Figure 6-3 Final metal output from filter search

Though the database analysis has successfully narrowed the potential metals to a select few, the database does not consider the reactivity of the metals with the selected medium temperature fluids. Taking forward the results of this initial study, a compatibility model will be determined to assess the suitability of each to exposure to halides. The compatibility model and results are outlined in the next section.

6.2.1 Compatibility model

Using the Electromotive Force Difference (EMF) model described in section 2.4.2.2 is used to analyse the reactivity of a metal halide in contact with a metal container and characterised their relative stabilities. As described in equation ..., the general reaction can be expressed as follows:



Where the EMF can subsequently be calculated from equation ... and their stability analysed through the following statement by Saaski et al. [47]

$$\Delta E^0 = E_p(\text{product halide}) - E_p(\text{initial halide}) \quad 80$$

If the result returns a positive value, then spontaneous reaction will occur between the wall and the fluid. If the EMF is strongly negative the reaction between the fluid and the wall is insignificant. From this it can be inferred that the ideal combination would be to have fluids with high decomposition potentials and walls with low decomposition potentials. Table 6-1 shows the resultant electromotive force difference reaction of the two shortlisted fluids (SbCl₃ and BiCl₃) with the select metals identified from the Citrix database search as well as many common metals found in alloys used for conventional heat pipes. All EMF property data was taken from the CRC Handbook of Chemistry and Physics [119].

Table 6-1 Electromotive Force Difference potential of Antimony Trichloride and Bismuth Trichloride with various metals. Property data source: [119]

	Mo	Fe	Ni	Cu	W	Zr	Ti	Mn	Cr
SbCl ₃	-0.439	0.407	0.024	0.0441	-0.637	1.054	0.653	1.061	0.766
BiCl ₃	-0.394	0.452	0.069	0.0894	-0.591	1.099	0.698	1.107	0.811

In Table 6-1 it can be seen that Tungsten and Molybdenum have the least potential for reaction occurring with both SbCl₃ and BiCl₃, while conventional metals which are widely present in stainless steel alloys, such as Iron, Manganese and Chromium, have the highest likelihood for spontaneous reaction to occur.

6.3 Wettability study of chosen fluids on metals

The wetting of a fluid on a surface is caused by intermolecular reactions between a liquid and a solid. This allows the liquid to maintain its contact with the solid and reach mechanical equilibrium with the various interfacial forces acting upon it. The main qualification of such quantity is determined through the angle measurement of the curved fluid surface with respect to the metal surface (see Figure 6-4).

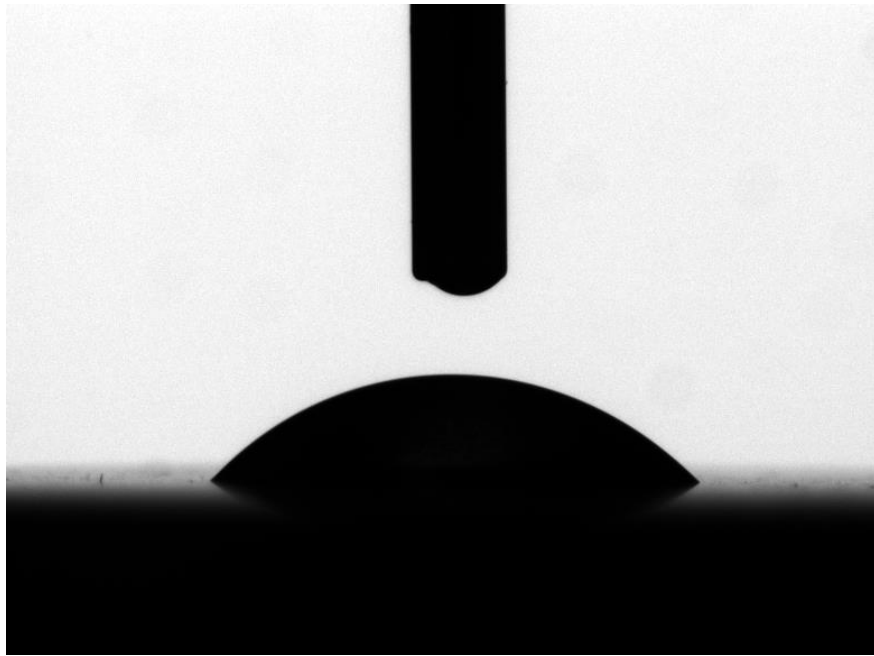


Figure 6-4 Contact angle test example

The degree of wetting experience is categorized in two forms: ‘wetting’ and ‘non-wetting’. For an interaction to be considered ‘wetting’, the angle of the fluid relative to the surface must be below 90° , therefore, for an interaction to be considered ‘non-wetting’ this angle must be above 90° [1], [120], [121].

The tensional forces action on the bodies can be described through Young's equation [122].

$$\cos \theta = \frac{\sigma_s - \sigma_{sl}}{\sigma_l} \quad 81$$

Where σ_s , σ_{sl} and σ_l are the tensional vectors of the solid-vapor interface, solid-liquid interface and liquid-vapor interface respectively. This assumes a rigid, smooth and chemical homogeneous substrate surface [123].

In a heat pipe, the wettability of the fluid to the metal surface can have an impact on two key aspects of its performance: the capillary action of the wick and the curvature of the evaporating/condensing interfaces. The effect of the surface tension on the capillary action is described by Hewett et. al [124] dictating that the capillary lift rises as a result of an increase in surface tension and decrease in contact angle. The capillary pressure in a heat pipe wick can be determined through equation 82.

$$\Delta P_c = \frac{2\sigma_l}{r_w} \cos \theta \quad 82$$

Where ΔP_c is the capillary pressure difference (Pa), σ_l is the liquid-solid surface tension (N/m), r_w is the radius of the wick (m) and θ is the contact angle ($^\circ$). Through this equation it is possible assert that as the contact angle tends towards 0, it will reach its maximum capillary pressure, confirming the statement by Hewett et. al.

The effect found on the liquid-vapour interface of the heat pipe is described by Ochterbeck [114]. At a microscopic level, it is a volumetric transition zone where the molecular density varies considerably. At a macroscopic level, the interface is described entirely by its surface tension where:

$$\sigma = \left(\frac{\partial E}{\partial A_s} \right)_{T,n} \quad 83$$

Where E is the total energy (J), A is the area (m^2) and σ is the surface tension (N/m).

The techniques, equipment and procedures used to determine the contact angle of the various fluids and metal surfaces is described in Chapter 3. The tests were divided into three groups by fluid. The metals used in this study were determined in Chapter 4 through the metal selection process and compatibility modelling of the fluid/metal reactions. The chemicals under analysis are Water, Antimony Trichloride and Gallium Trichloride. The water analysis serves as a baseline study to compare against the Antimony Trichloride and Gallium Trichloride tests. These will then be cross examined to provide an assessment of the predicted capillary action between the two chosen chemicals on the various metal surfaces.

6.3.1 Test samples

To provide comparable results, the sample size and surface finish was standardised across all tests. The samples consisted of a 15x15mm cylinder with smooth, polished ends

using 4um grit surface (see Figure 6-5). In some cases, slightly larger or smaller diameter samples were used due to availability, but the variation was kept to within 10% of the diameter size to minimise impact on the tests.



Figure 6-5 Metal sample example

Each sample was logged in the format shown in Appendix A where the size, polish finish type, weight and chemical to be reacted was recorded. The table also records the testing and imaging done for each sample to keep track of each of them and perform multiple tests in parallel. Table 6-2 shows an extract of the sample log for each of the samples produced for wettability testing.

Table 6-2 Sample log extract. See full log in Appendix A.

<i>Name</i>	<i>Date received/ Produced</i>	<i>Size</i>	<i>Polished grade</i>	<i>Weight (after polish)</i>	<i>Roughness</i>	<i>Reacted With</i>
Mo4	01-Jan	15x15	P1200	26.7400	0.12	SbCl3
TZM4	01-Jan	15x15	P1200	26.8100	0.06	SbCl3
Ta4	27-Feb	15x15	P1200	44.4800	0.15	SbCl3
Nb4	27-Feb	15x15	P1200	22.9000	0.16	SbCl3
316SS4	24-Jul	15.875x15	P1200	23.4900	0.04	SbCl3

6.3.2 Water test results

Water was first used to compare the wettability of each material to a common and nontoxic substance. In accordance with ISO 828-2013 [125] each droplet had a volume of 4 μ l. The test was set up as described in Chapter 3 and an image was taken for each droplet. The roughness of each sample surface was reduced to the minimum possible to avoid the effect of surface artefacts on the contact angle measurement. As stated by Yuan et al. [126] the Young's equation fails to consider surface topography, hence to accurately approximate the Young's contact angle using experimental methods, the surface must be smooth and chemically heterogeneous. Additionally, it has been shown that the measure of contact angle on rough surfaces has no correlation to Young's equation [127]. In the case of hysteresis, the advancing contact angle is generally used as a good approximation to Young's contact angle, whereas receding angles tend to have less reproducibility due to liquid sorption or solid swelling [126]. To counter these effects, the droplet was randomly placed each time to eliminate any systematic error due to small surface condition variations. Each sample was polished to the same grit size of 6 μ m; however, the surface

roughness tests did present slight variance in values between different metals. This can be attributed to the hardness of each material causing different levels of material removal rates when polishing. Figure 6-1 shows the measured contact angles of each sample prior to testing. Figure 6-6 shows the relative difference in roughness levels between the samples. Here it can be seen that Zirconium had the highest roughness of 0.13ra and Stainless Steel 316 had the lowest roughness at 0.038 ra. As stated by Yuan et al. [126], there are no specific guidelines on the maximum surface roughness permissible, only the recommendation that the sample ‘be prepared as smoothly as possible’. To comply to this, all samples were polished down to the smallest possible grit size and kept for 20mins.

Table 6-3 Roughness test results, average peak length, Ra (μm)

<i>Sample</i>	<i>1</i>	<i>2</i>	<i>3</i>	<i>4</i>	<i>5</i>	<i>6</i>	<i>7</i>	<i>8</i>	<i>9</i>	<i>10</i>	<i>Av</i>
Mo3	0.05	0.08	0.05	0.09	0.06	0.06	0.06	0.08	0.06	0.05	0.06
Tzm3	0.06	0.06	0.05	0.06	0.06	0.05	0.06	0.05	0.07	0.05	0.06
CuNi3	0.07	0.05	0.08	0.05	0.08	0.05	0.06	0.05	0.07	0.05	0.06
W3	0.05	0.05	0.05	0.05	0.06	0.06	0.08	0.1	0.05	0.05	0.06
Ta3	0.1	0.13	0.1	0.12	0.13	0.11	0.09	0.14	0.13	0.08	0.11
Zr3	0.14	0.12	0.13	0.12	0.12	0.15	0.14	0.11	0.13	0.14	0.13
Nb3	0.08	0.07	0.12	0.11	0.15	0.16	0.08	0.08	0.11	0.17	0.11
316SS 3	0.04	0.04	0.03	0.05	0.03	0.03	0.03	0.05	0.03	0.04	0.04
304SS 3	0.03	0.05	0.03	0.06	0.03	0.04	0.04	0.04	0.05	0.04	0.04

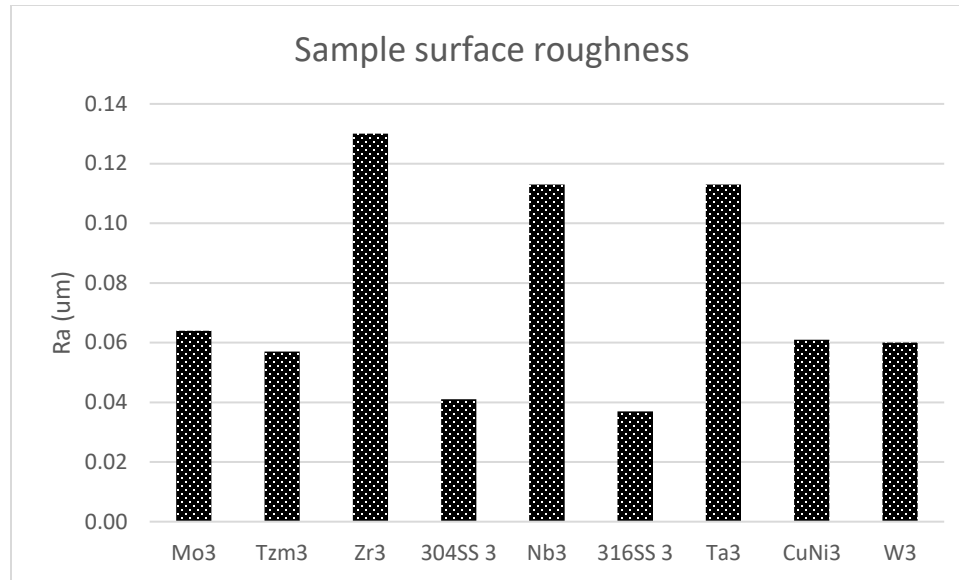


Figure 6-6 Average sample roughness chart

The static contact angle can present some degree of variability which according to Marmur [121] can “depend on the initial kinetic energy and dynamics of vibrations it experiences after landing on the surface”. For this reason, the study has taken measurements from 3 separate sessions each which have adhered to identical procedures to determine the repeatability of the tests. The results presented in Table 6-4 and Table 6-5 show the average contact angle measurement from each session. Averages were taken from 10 individual images in each session for static measurements and for the advancing measurements. The advancing method tends to have higher reproducibility. In this case the for a single experiment average contact angle was calculated from approximately 200 frames. In total 4 videos of each sample were taken (each test denotes a video). These were produced over two separate sessions.

Table 6-4 Static contact angle test results

<i>Test type</i>	<i>Sample</i>	<i>Test 1</i>	<i>Test 2</i>	<i>Test 3</i>	<i>Average</i>
Static	Mo	50.72	66.73	63.84	60.43
	TZM	60.20	75.18	73.12	69.50
	Zr	51.44	72.11	68.97	64.17
	304SS	76.93	75.10	74.14	75.39
	Nb	47.39	52.66	58.30	52.78
	316SS	53.50	79.09	70.04	67.54
	Ta	52.20	75.18	51.97	59.78
	CuNi	88.84	92.89	81.38	87.70
	W	50.64	84.44	72.04	69.04

Table 6-5 Advancing contact angle test results

<i>Test type</i>	<i>Sample</i>	<i>Test 1</i>	<i>Test 2</i>	<i>Test 3</i>	<i>Test 4</i>	<i>Average</i>
Advancing	Mo	39.44	44.90	42.74	56.04	45.78
	TZM	56.67	49.41	64.84	68.35	59.82
	Zr	49.71	50.72	62.05	55.51	54.49
	304SS	60.87	66.83	67.29	64.23	64.81
	Nb	50.28	48.19	42.49	46.74	46.93
	316SS	64.43	62.60	54.53	54.64	59.05
	Ta	49.48	57.21	50.31	45.28	50.57
	CuNi	90.93	88.59	82.15	80.50	85.54
	W	51.87	56.47	64.51	58.36	57.80

Figure 6-7 shows the average contact angle values over all sessions for the static measurements. The error bars indicating the standard error between the mean values obtained in each session. Here it is observed that the refractory metals Molybdenum, Tantalum and Zirconium do not significantly differ in wettability towards water. The main differentiating samples from the group are the Copper-Nickel alloy and Niobium. The Copper-Nickel alloy has the worst wettability of water showing a clear statistical deviation from the sample trend. On the other end, Niobium has presented the lowest mean wetting

angle demonstrating its wettability to water through another clear statistical difference in the opposing direction.

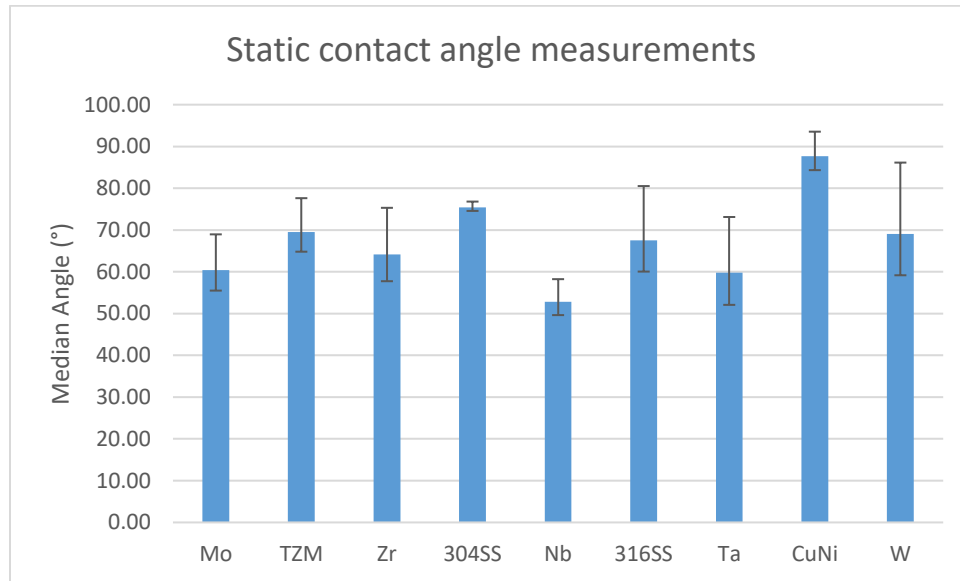


Figure 6-7 Static contact angle results chart

In order to further validate the pattern demonstrated in Figure 6-7 the last test to take place on the samples was the advancing contact angle. As described in Chapter 3, this method uses a similar technique to the static angles, but the contact angle is measured by filming the droplet's expansion over time and resolving each image instead of analysing only one still image. Figure 6-8 shows the results obtained for the advancing angle measurements. Here it can be seen that the exact same trend occurred where the Copper-Nickel alloy has the worst wettability of water and Niobium has presented the lowest mean wetting angle signifying the best wettability.

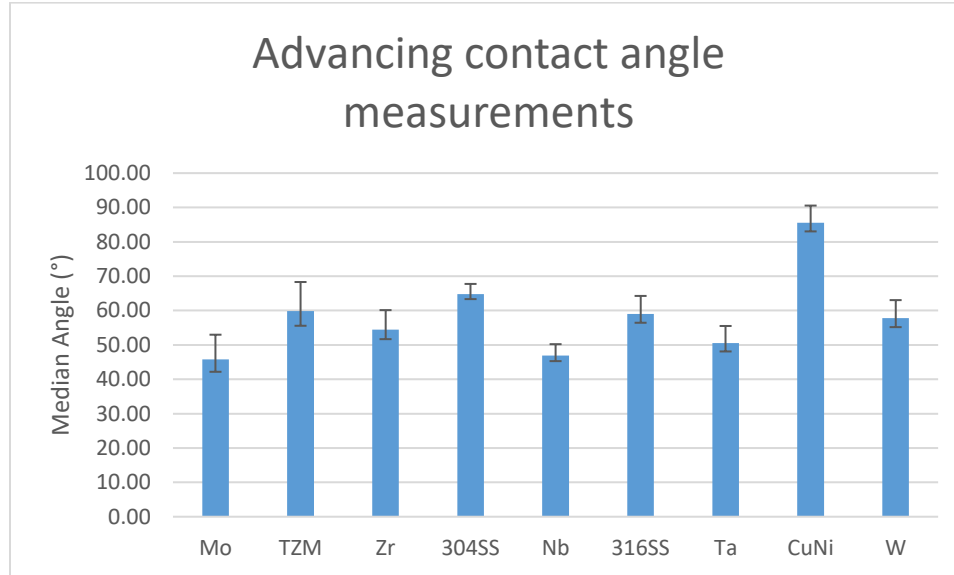


Figure 6-8 Advancing contact angle results chart

Each set of measurements was then compared in Figure 6-9 to determine whether the wettability trend for each sample matched using each method. Observing Figure 6-11 the relative trends are consistent showing the exact same wettability pattern over the spread of samples. The results shown for advancing contact angle experiments are systematically lower than the static experiments. It can be determined, therefore, that there is a clear systematic error encountered using one method over the other. As described by Yuan et al. [126], the probability of error is higher in the static measurements due to the high complexity of the surface/liquid interaction and the large number of factors that can affect it. As the tests are photographing only one state of the droplet, there is a high likelihood that this could be affected by external influences even with all the error mitigations in place. The advancing contact angle measurement, on the other hand, utilises multiple changing states of the droplet over a much larger data range giving it a higher potential precision,

though the statistical accuracy in each case does not seem to be significantly different. While the contact angle trend does definitively show the differences in relative wettability of the fluids, it was expected that the advancing contact angle would present higher results than the static tests. This discrepancy may have been caused by cohesive forces toward the central syringe which would cause a slight upward mass displacement, and hence, reducing the relative angle. Further analysis on this discrepancy should be evaluated in future work.

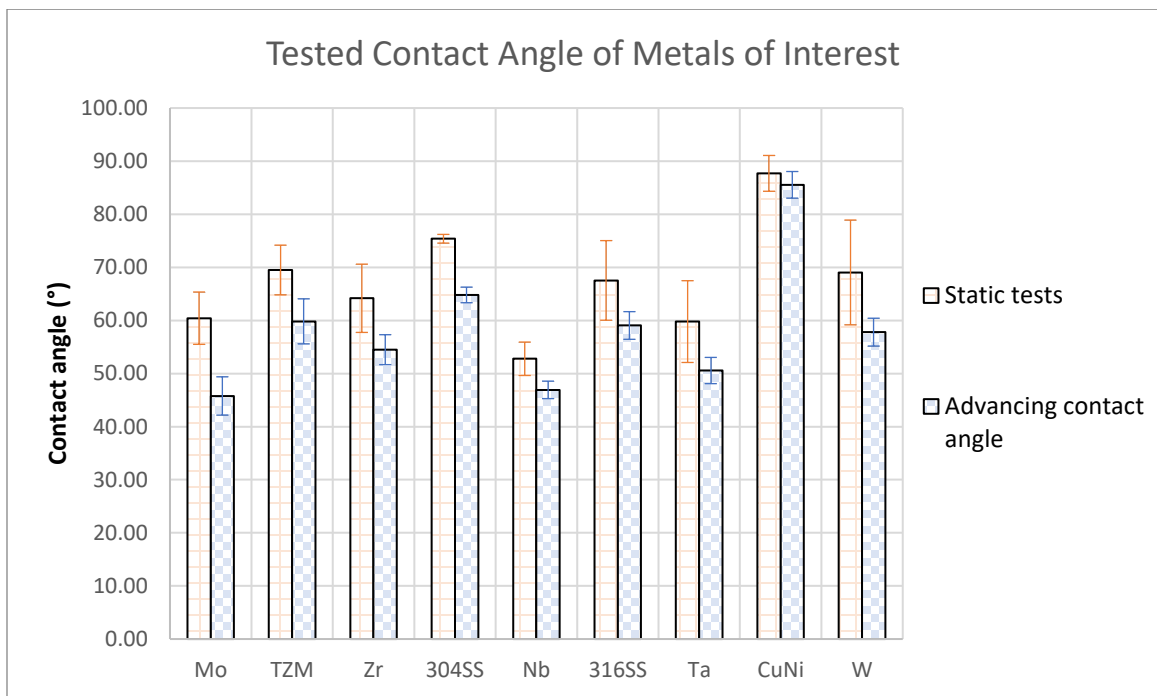


Figure 6-9 Comparison of static and advancing contact angle results

The goal of this exercise is to study the methods by which the contact angle could be measure and give an initial indication of metals which show high wettability with water for potential use in water heat pipe applications. This gives an indication as to the deviation to be expected in the tests developed for the reactive fluids which only uses static contact angle tests.

The methodology developed for contact angle measure of air sensitive fluids can only cater for static contact angle tests due to the high reactivity of the fluids. Using such reactive fluids, with a relatively high melting point also, makes providing a continuous feed off the fluid technically challenging and subsequently very costly. For this reason, only static tests were developed for this research, however implementation of angled tests once the technique is perfected could be a possibility. Due to the time constraints and budgetary limits, it was not possible to explore this option.

6.3.3 Antimony Trichloride test results

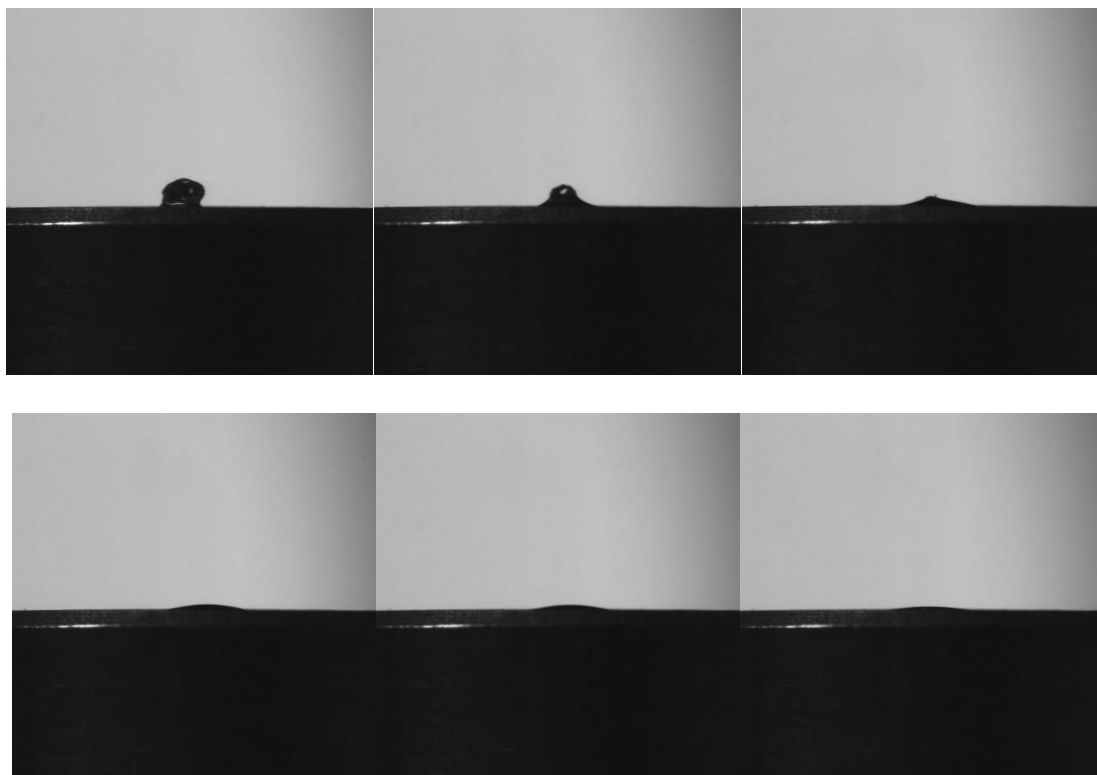


Figure 6-10 Time-lapse image of SbCl_3 melting on Molybdenum surface

To perform the same type of experimentation on Halides - the identified fluid type for operation in the medium temperature range – new test methodology had to be developed to cater for the air sensitivity of these types of fluids. Another challenge is that in most cases Halides are in solid form at ambient conditions, hence the tests would also have to include a heating mechanism. The methodology developed to cater for these constraints is described in Chapter 2. The sample containing the metal surface and a small quantity of the chemical (approximating the weight needed to produce 4ul volume when melted) is kept in an inert Argon atmosphere in a small sealed container. The sample is heated up to the melting point of the fluid using a heat gun. The temperature is monitored using a laser thermometer. Figure 6-10 shows an example of the melting process of Antimony Trichloride on a Molybdenum metal surface.

Due to the complexity and logistical constraints of the tests, only three metals were able to test with Antimony Trichloride: Molybdenum, TZM and Stainless Steel 316. Figure 6-11, Figure 6-12 and Figure 6-13. show the attained results for roughly the last 40 frames of each test. The starting point was chosen as the point where all the solid had been fully melted.

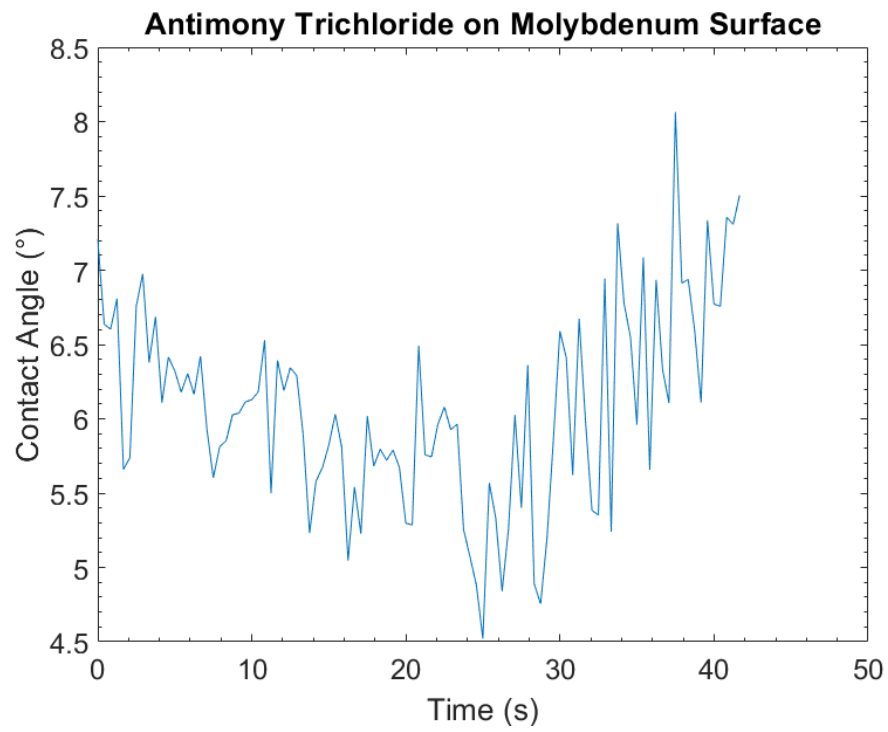


Figure 6-11 Contact angle measurement over time for SbCl₃ on Molybdenum surface

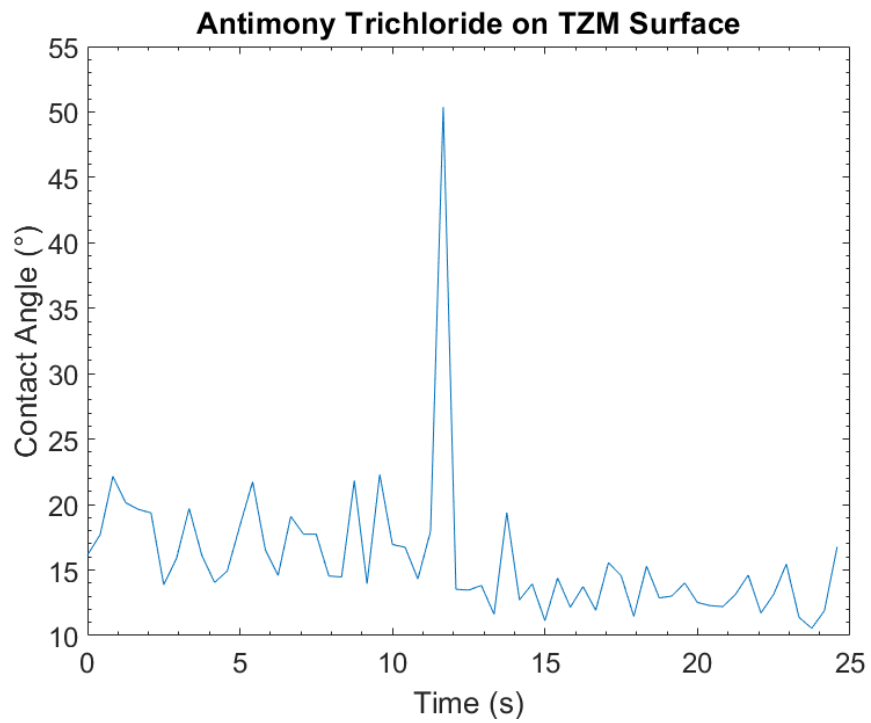


Figure 6-12 Contact angle measurement over time for SbCl₃ on TZM surface

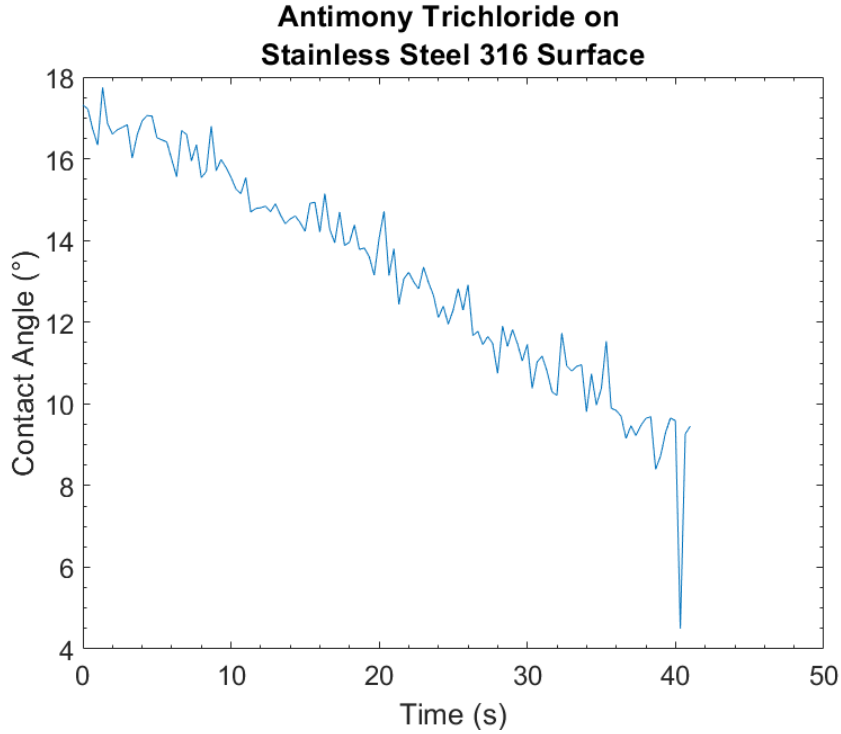


Figure 6-13 Contact angle measurement over time for SbCl₃ on Stainless Steel 304 surface

To assess the relative contact angles of each metal with relation to Antimony Trichloride, the average contact angle over the measured time in Figure 6-11, Figure 6-12 and Figure 6-13 were taken. Table 6-6 presents the attained results.

Table 6-6 Contact angle of Antimony Trichloride on various metal surfaces

Metal	Measured Mean Contact Angle
316SS	13.2
TZM	15.9
Mo	6.1

From Table 6-6, Molybdenum presents the highest relative degree of wettability and TZM the lowest. In general, Antimony Trichloride has demonstrated to have a much

higher potential wettability compared to water base on the initial testing results. To determine with higher precision what the true Young's contact angle is experimentally further testing must be conducted in future work using the developed methodology. This work has demonstrated the ability to conduct these tests in controlled environments and has given an initial estimation of Halide wettability with refractory and common metals. In general Antimony Trichloride has demonstrated a high wettability towards the tested metals compared to water showing that there is a strong potential for capillary action in heat pipe applications.

6.4 Compatibility study of fluid with selected metals

Compatibility tests aim to determine the extent of compatibility of each metal with the chosen baseline Halide, Antimony Trichloride. The tests expose each metal to the Halide in liquid state and observes any reaction which may occur on the metal surface together with any reaction of the fluid itself.

The test samples used for these tests are detailed in Table 6-7. The surface was polished at a relatively high roughness to increase the surface area and incentive any surface reaction to occur in order to mimic a ‘worst case scenario’. The surface roughness of each sample was assessed beforehand and recorded. This will serve as an additional indicator for the compatibility of the metal.

Table 6-7 List of metal samples

Sample Table						
Status	Name	Date received or produced	Size	Polish	Weight (after polish)	Roughness (um)
✓	Mo	1-Jan	15x15	P240	26.6100	0.36
✓	TZM	1-Jan	15x15	P240	26.7700	0.18
✓	W	27-Feb	15x15	P240	50.8800	0.29
✓	CuNi	7-Jun	12.7x15	P240	16.6800	0.21
✓	316SS	24-Jul	15.875x15	P240	23.4400	0.21
✓	304SS	24-Jul	15x15	P240	20.9400	0.11
✓	Ta	27-Feb	15x15	P240	43.3300	0.41
✓	Zr	27-Feb	15x15	P240	17.1700	0.21
✓	Nb	27-Feb	15x15	P240	22.5200	0.58

6.4.1 Compatibility test

The test procedure follows the outlined process described in Chapter 2. The samples were each exposed to molten Antimony Trichloride in vacuum over a period of 24h. Table 6-8 shows the test progression for each sample. The first observations from the test is the colour change of the fluid through each test. In most cases, the fluid changes from a clear liquid to a ‘milky’ white liquid over time. The change occurs consistently around the 6-hour mark in each case. This is likely a reaction with residual moisture within the sample or from degradation of the sample seal slowly introducing moisture from the outside air. When removing the sample after the tests, it was apparent that the vacuum was at a reduced level in most cases (though it was not possible to measure the reduction). It can therefore be assumed that in most cases that there are small amounts of Antimony Oxychloride present due to reduced seal integrity at around the 6h mark giving the ‘milky’ colour through the following reaction:



The only exception to this was the TZM sample which maintained its vacuum level through testing and therefore did not undergo this colour change, presumably due to the lack of moisture ingress. The main attributes to look for is any colour change outside of that created by SbOCl. This would give an indication of the formation of other chlorinated compounds by a substitution mechanism.

Table 6-8 Compatibility test progression timeline for each sample. Images show a snapshot of the molten $SbCl_3$ exposed sample at each time step.

	0h	3h	6h	8h	24h
Niobium					
Molybdenum					
TZM					
Tantalum					
Stainless Steel 304					
Stainless Steel 316					
Copper Nickel					
Tungsten					
Zirconium					

A better sign of reaction occurring between the metal sample and the molten fluid is by observing the colour changes at the 3h mark. The cases of all refractory metals

(Molybdenum, TZM, Niobium, Tantalum and Zirconium) the fluid remains a colourless liquid. In the case of Tungsten, the 'milky' colour begins to occur at this point already possibly indicating early degradation of the seal. In the cases of both Stainless-Steel alloys and the Copper Nickel alloy, there is a clear colour change to green in the case of Stainless-Steel samples and light brown in the case of the Copper Nickel sample.

To quantify and compare the extent of the reaction on the surface of each metal, various quantitative and qualitative methods were used, these include:

- The measure of surface roughness change
- Imaging of the sample under Microscope
- SEM imaging of regions of interest
- EDX analysis of regions of interest

The principal results of each analysis method and a discussion on the significance of these findings is presented in the following section.

6.4.2 Results and Analysis

Table 6-10 shows the macrostructure of the sample surface before and after the compatibility tests with Antimony Trichloride were completed. All images were taken with the Leica microscope. This give a first analysis of compatible and incompatible surfaces form observing the general surface changes and any corrosion which may have occurred.

From observation of Table 6-10 it is apparent that the surface groves cause by the polishing can be a good indicator of corrosion. In the cases of Molybdenum, Tungsten, TZM and Zirconium, there is not a significant change in the surface features. Within this group, Molybdenum and TZM appear to be largely unaffected with only very light staining and minimal surface deposits. Zirconium and Tungsten appear to have slightly more staining and signs of some solid deposits on the surfaces.

From further analysis of Table 6-10, Tantalum and Niobium appear to have a more significant change in surface condition with a visual change in surface features and moderate deposits and staining on the surface. The Stainless Steel and Copper Nickel alloys presented a high level of corrosion with no comparable surface features, high level of staining and deposits and visible pitting corrosion indents. To further analyse these metals, the results were arranged into three groups as presented in Table 6-9.

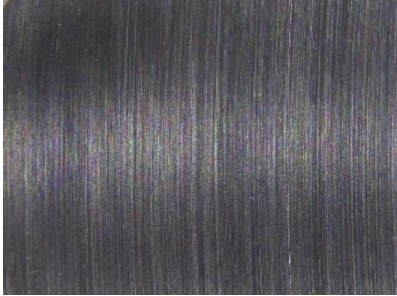
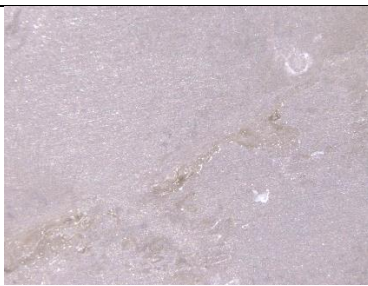
Table 6-9 Compatibility results

Group	Description	Metals
1	High compatibility	Molybdenum, Tungsten, TZM and Zirconium
2	Medium Compatibility	Tantalum and Niobium
3	Low Compatibility	Stainless Steels and Copper Nickel

Table 6-10 Microscope images of top and bottom of metal samples before and after compatibility testing

Sample	Top		Bottom	
	Before	After	Before	After
Molybdenum				
TZM				

Tungsten				
Copper/Nickel Alloy (60/40)				
Stainless Steel 316				

<p>Stainless Steel 304</p>				
<p>Tantalum</p>				
<p>Niobium</p>				

Zirconium



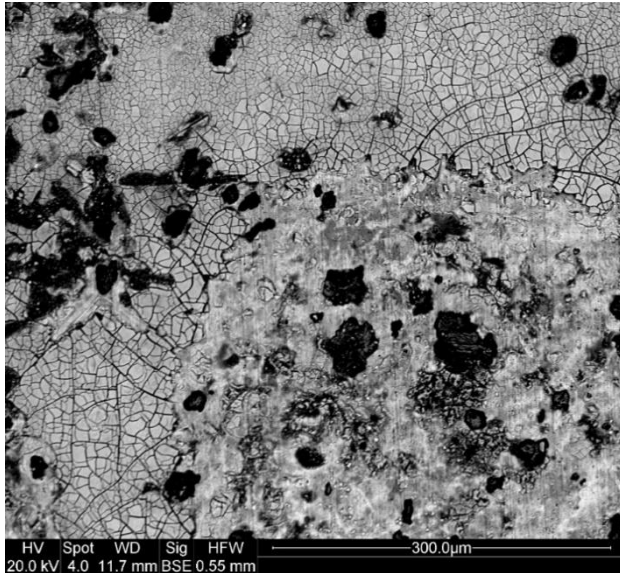
To condense the study, only one metal will be analysed from each category as a representative of that group. The full SEM and EDX results of all metals can be found in Appendix K.

6.4.2.1 Stainless Steel 304 compatibility with Antimony Trichloride

Stainless Steel is known to have a low compatibility with Antimony Trichloride due to the high electromotive force potential of Nickel in molten chlorinated halide solution [57]. The green colour change to the Antimony (III) Chloride is indicative of Nickel (II) Chloride formation from the following reaction mechanism:



The reaction causes severe damage to the metal surface and lead to pitting corrosion as seen in Figure 6-14.



	Initial Ra (µm)	Post tests Ra (µm)
Top	0.10	0.92
Bottom	0.19	0.82

Figure 6-14 SEM image of Stainless Steel 304 surface

The table presented in Figure 6-14 shows the change in surface roughness before and after testing for both the top and bottom surfaces. The top surface had the highest increase of 0.82ra from the original measurement and the bottom surface displayed a 0.63ra increase. It is clear from the images that the surface has been unacceptably damaged from the displacement reaction showing the necessary disqualification of any Nickel bearing alloy as the heat pipe wall material for Antimony Trichloride and likely many other Chlorinated Halides. The lack of brown or black colouring in the molten Antimony Trichloride suggests that anhydrous Copper and Iron Chloride formation did not occur in any of the cases. To corroborate this observation, a line scan of the sample surface was taken using EDX as seen in Figure 6-15. This shows the presence of Antimony, Chromium and Iron on the surface and no substantial presence of Nickel. This infers that the Nickel present on the immediate surface has been removed by the formation of Nickel Chloride and the other constituents of the alloy remained.

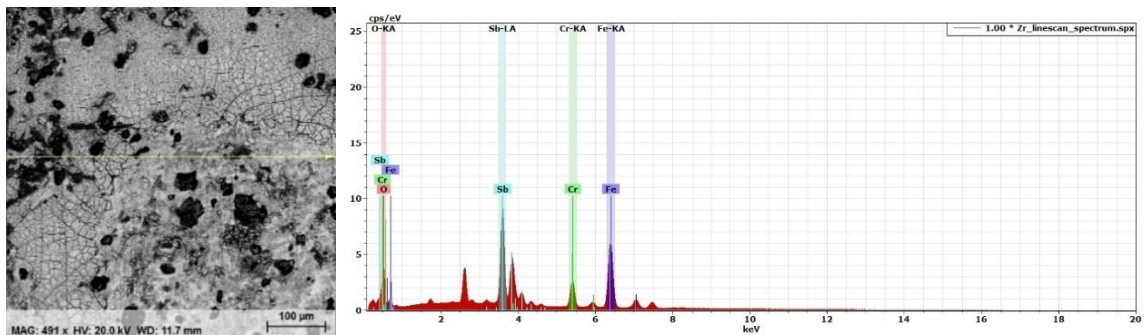
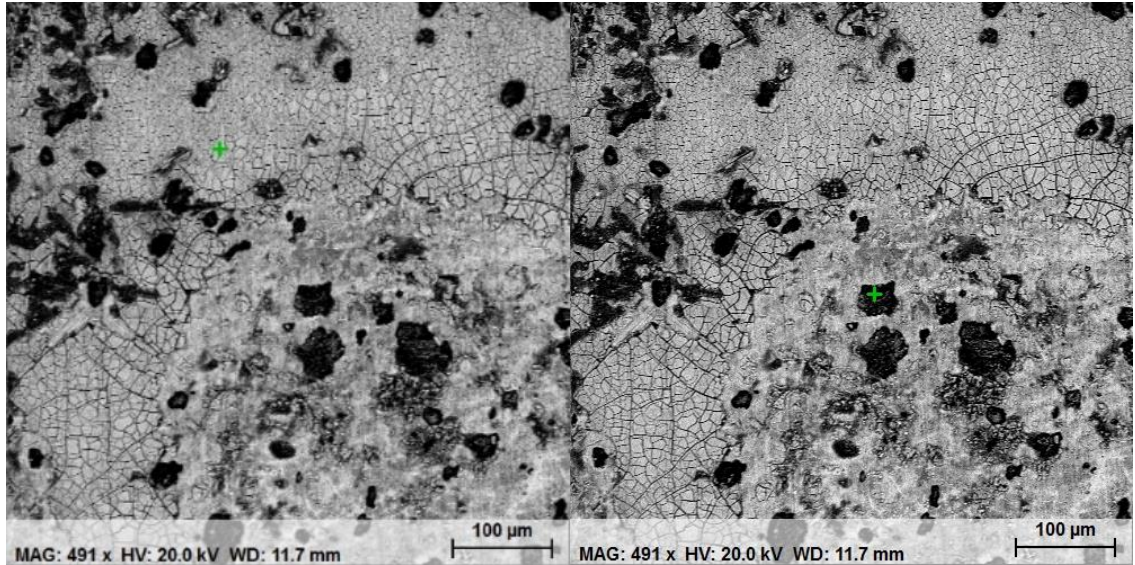


Figure 6-15 EDX line scan of Stainless Steel 304 sample

Further EDX analysis was made at two key points on the surface to attempt to detect the presence of Nickel within the deeper crevices cause by the pitting which could uncover

still unreacted Nickel deeper down. Figure 6-16 shows this analysis and the proportion of elements found on each point.



Element	Series	unn. C [wt.%]	norm. C [wt.%]	Atom. C [at.%]	Error (3 Sigma) [wt.%]
Oxygen	K-series	8.27	11.37	40.34	4.09
Chlorine	K-series	7.19	9.88	15.83	0.86
Iron	K-series	9.37	12.88	13.10	0.98
Antimony	L-series	47.91	65.87	30.72	4.35

Total:		72.74	100.00	100.00	

Element	Series	unn. C [wt.%]	norm. C [wt.%]	Atom. C [at.%]	Error (3 Sigma) [wt.%]
Oxygen	K-series	9.32	8.12	23.13	6.05
Chlorine	K-series	2.94	2.56	3.29	0.50
Chromium	K-series	17.49	15.24	13.35	1.72
Iron	K-series	78.55	68.44	55.84	6.73
Nickel	K-series	6.48	5.64	4.38	1.01

Total:		114.77	100.00	100.00	

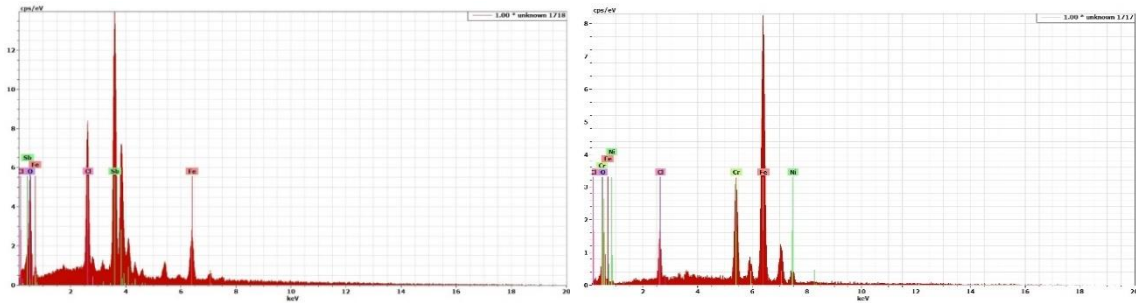


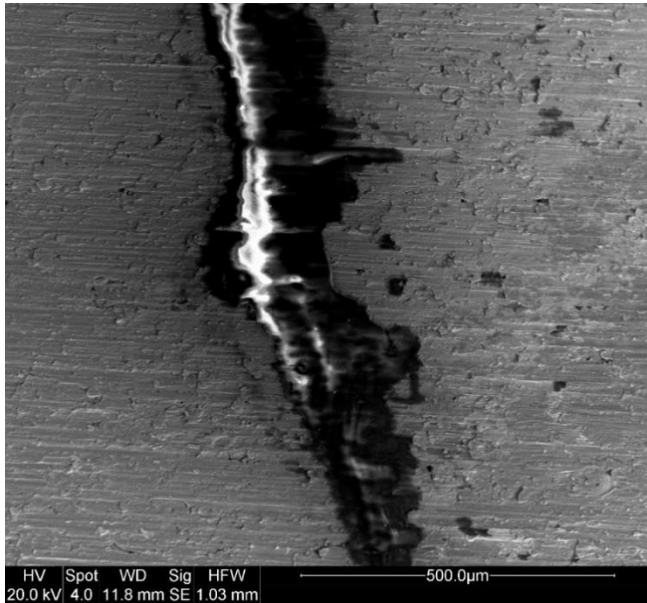
Figure 6-16 EDX Point analysis on Stainless Steel 304 sample

From observing Figure 6-16, the point on the sample surface did indeed show no substantial sign of Nickel and had a similar profile to the line scan presented in Figure 6-15. Point 2, which looked at a point inside a relatively deep pit, did in fact pick up the presence

of a small amount of Nickel showing that the Nickel is indeed the cause of the pitting corrosion and is the principal cause of incompatibility of Nickel bearing alloys with Antimony Trichloride.

6.4.2.2 Niobium compatibility with Antimony Trichloride

From the analysis made previously most refractory metals should be resistant to degradation by Antimony Trichloride and similar chlorinated Halides, due to the low potential for chloride bond formation for these metals. Figure 6-17 shows a feature of the resultant Niobium surface from the compatibility test. Although initial images in Table 6-10 appeared to have some level of surface condition change, SEM images show only a higher-level solid Antimony Trichloride residue on the surface. The constitution of the metal itself appears to be largely unchanged with no signs of corrosion present.



	Pre-test Ra (μm)	Post-test Ra (μm)
Top	0.59	0.61
Bottom	0.58	0.62

Figure 6-17 SEM image of Niobium surface

The lack of corrosion is verified by the measure of surface roughness change. It is seen from this that the top surface only sees an increase of 0.02ra and the bottom surface of 0.04ra. Both surface roughness changes can be considered negligible when considering the spread of data over 10 measurements displayed an error range of +0.02/-0.04 for the top surface and +0.03/-0.02 for the bottom surface. Hence, the addition of Antimony Trichloride deposits on the surface tended to increase the roughness, but only by an amount within the expected error range, signifying that the surface topography has suffered a negligible physical change from the Antimony Trichloride exposure.

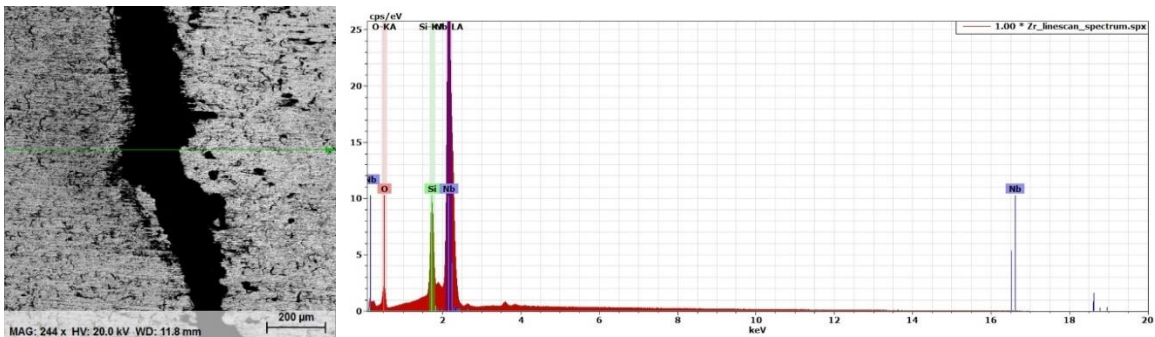


Figure 6-18 EDX line scan of Niobium sample

The line scan conducted via EDX in Figure 6-19 shows the primary present elements to be Niobium with traces of Silicone (a common impurity to find on metal surfaces). The oxygen detection could be indicative of the presence of Antimony Oxychloride from the hydrolysis of Antimony Trichloride through reaction below (though minimal amounts of antimony were detected through the line scan).

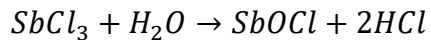
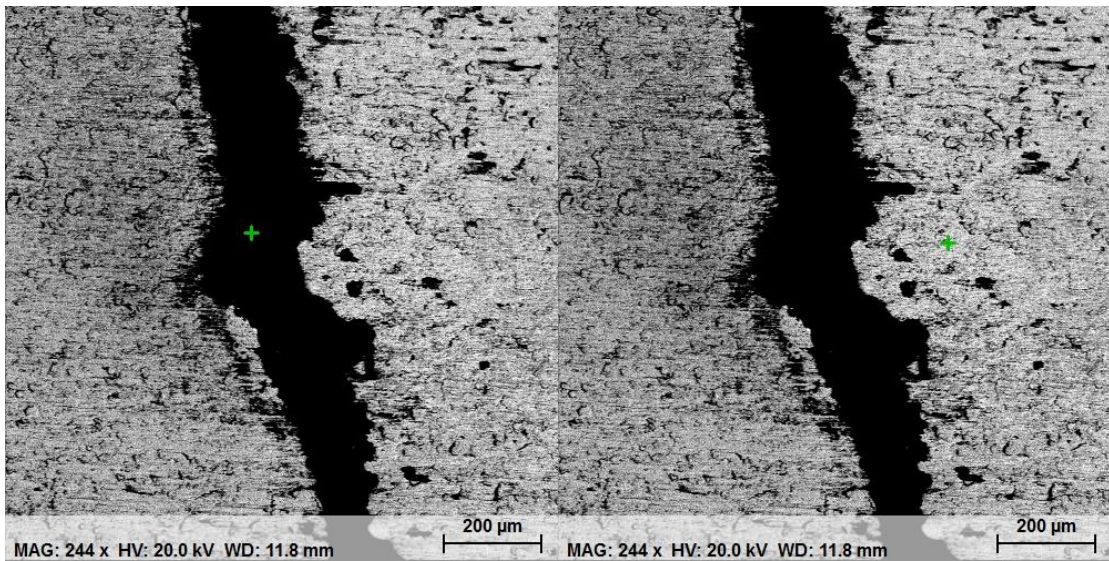


Figure 6-19 show a point EDX analysis on two points of interest on the surface to further analyse the surface conditions on the deposit and on the bare surface of the sample. The first point is in the central section of the analysed deposit. Interestingly, Silicone was the largest peak detected followed by Oxygen and Antimony. This is likely due to the presence of impurity when preparing the sample for examination which has been attracted by the Antimony containing compounds. Nevertheless, it is clear that the deposits are a result of Antimony Trichloride oxidation or attraction to the surface only, with no presence of other heavy metals indicating that no substitution reactions have occurred.



Element	Series	unn. C [wt.%]	norm. C [wt.%]	Atom. C [at.%]	Error (3 Sigma) [wt.%]	Element	Series	unn. C [wt.%]	norm. C [wt.%]	Atom. C [at.%]	Error (3 Sigma) [wt.%]
Oxygen	K-series	19.27	34.92	49.64	9.63	Oxygen	K-series	4.06	4.77	22.54	3.72
Silicon	K-series	33.84	61.31	49.66	4.46	Niobium	L-series	81.00	95.23	77.46	9.05
Antimony	L-series	2.08	3.77	0.70	0.39						
Total: 55.20 100.00 100.00						Total: 85.06 100.00 100.00					

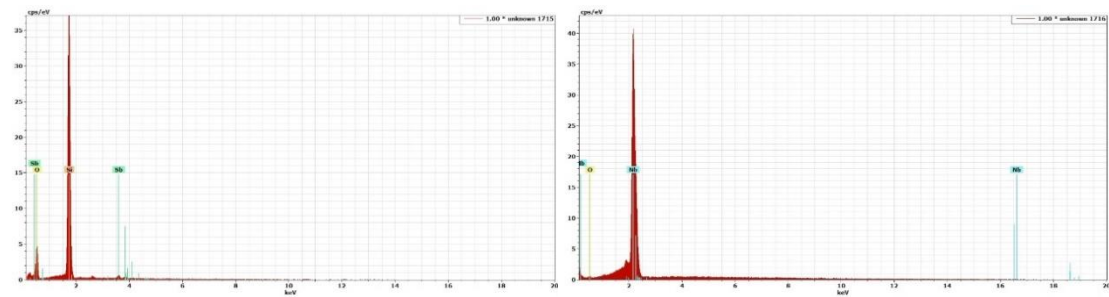
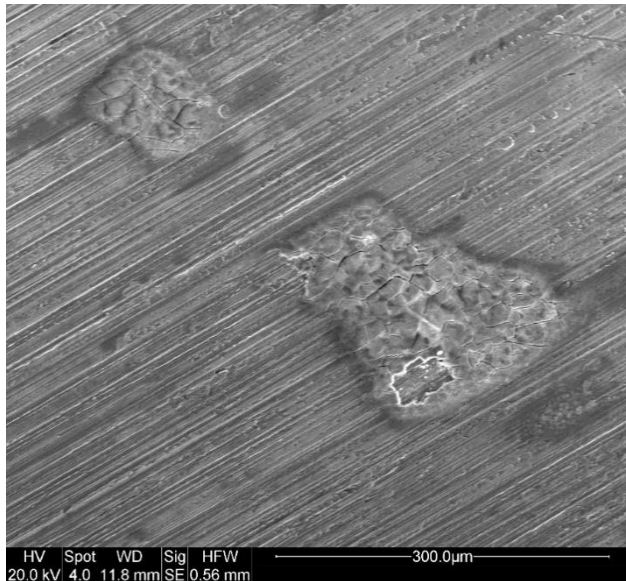


Figure 6-19 EDX Point analysis on Niobium sample

Point 2 in Figure 6-19 shows the EDX analysis of a random point on the exposed metal surface. This has indicated only the presence of Niobium and Oxygen, with Niobium comparison of over 95% of the atomic weight distributions. This shows that there is no substantial presence of oxides and other corrosion-related elements on the bare Zirconium surface indicating a good compatibility of Zirconium with Antimony Trichloride.

6.4.2.3 Molybdenum compatibility with Antimony Trichloride

From the compatibility model, Molybdenum presented the highest potential for corrosion resistance. The initial test images show good promise towards this premise. The surface appears to not have suffered any substantial changes other than the presence of some solid deposits. Figure 6-20 shows an SEM image of one of the deposits used to quantitatively analyse the metal surface.



	Pre-tests Ra (μm)	Post-tests Ra (μm)
Top	0.37	0.35
Bottom	0.33	0.34

Figure 6-20 SEM image of Molybdenum surface and roughness test results

The surface roughness tests show no significant change in the surface roughness of the sample before and after the tests were conducted. All measured values after the compatibility tests show a discrepancy lower than the calculated error of the measurement. Figure 6-21 shows an EDX line scan of the surface across bare and surface deposit sections. The spectra analysis shows a combination of Molybdenum, Antimony, Chlorine and Oxygen as expected.

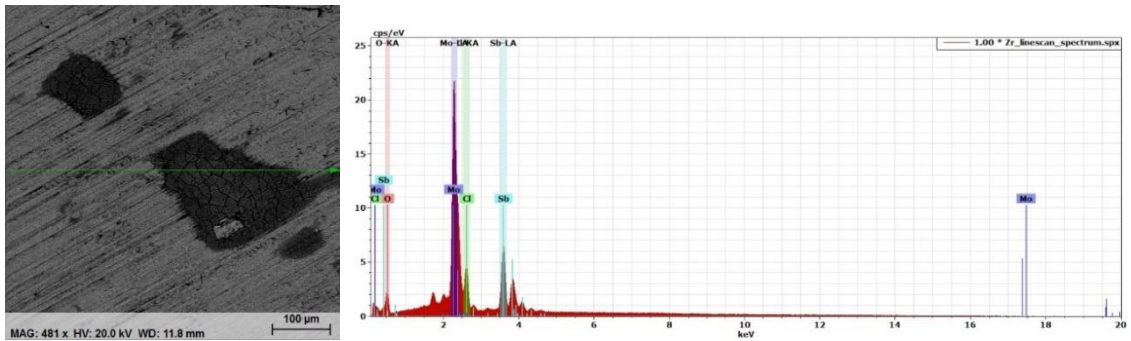
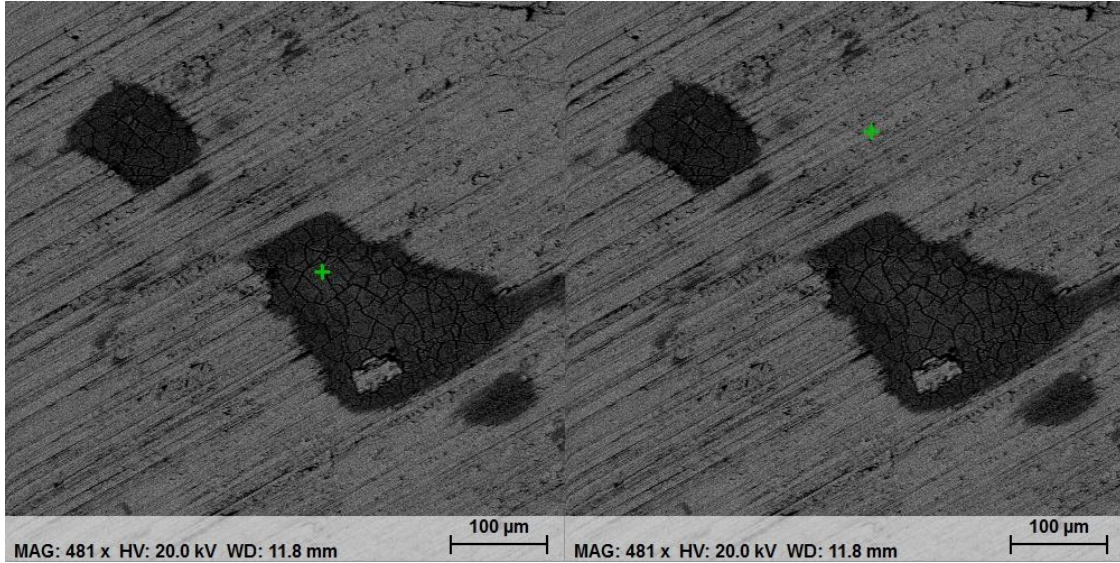


Figure 6-21 EDX lines can on Molybdenum sample

Figure 6-22 shows two points chosen for EDX analysis on the deposit and base sample surface. Point 1 shows the analysis taken on the deposit surface demonstrating the presence of Antimony, Chlorine and Oxygen only showing that no substitution reaction has occurred with Molybdenum. Point 2 then shows the bare surface of the sample with the presence of only Molybdenum and Oxygen, once more indicating that only slight surface oxidation has occurred, but the surface chemistry has not changed due to exposure to liquified Antimony Trichloride.

These tests are in line with the predicted compatibilities through EMF analysis confirming the validity of the theory. To further analyse these properties, longer tests can now be considered for future work to verify the long-term compatibility as a heat pipe fluid.



Element	Series	unn. C [wt.%]	norm. C [wt.%]	Atom. C [at.%]	Error (3 Sigma) [wt.%]	Element	Series	unn. C [wt.%]	norm. C [wt.%]	Atom. C [at.%]	Error (3 Sigma) [wt.%]
Oxygen	K-series	6.01	7.77	31.22	3.29	Oxygen	K-series	6.06	7.27	31.99	5.53
Chlorine	K-series	12.06	15.60	28.30	1.35	Molybdenum	L-series	77.31	92.73	68.01	8.37
Antimony	L-series	59.27	76.64	40.48	5.34						
Total: 77.34 100.00 100.00						Total: 83.38 100.00 100.00					

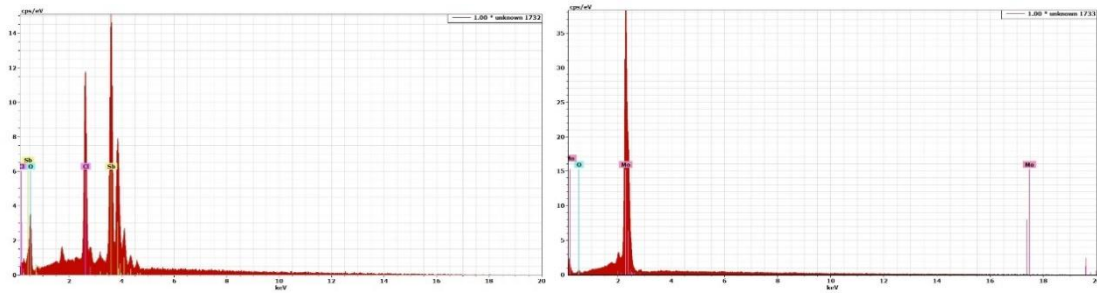


Figure 6-22 EDX Point analysis on Molybdenum sample

6.5 Chapter Summary

An analysis of the most likely metals to be compatible with chlorinated halides was made and a wide selection of refractory metals were used for testing, as well as some commonly used alloys for comparison purposes. The tests were conducted with only one representative halide, Antimony Trichloride, which was one of the highest-ranking halides in the fluid analysis for medium temperature applications. Future tests should be aimed towards verifying other potential halides such as Bismuth Trichloride, Bismuth Tribromide and Antimony Tribromide.

From this study it is concluded that Molybdenum presents the most likely best compatibility and wettability qualities out of the identified metals. The long-term compatibility of the metal and fluid is still to be determined through lifetime testing, the minimum term for qualifying results is 1 Year. Niobium and Tantalum also show good compatibility with Antimony Trichloride and are shown to have similar wettability properties from water CA analysis. Further work should be directed towards developing the CA measuring technique for air sensitive and high melting point fluids to validate the preliminary results achieved in this study. The main conclusions can be summarised as follows:

- A group of refractory metals were identified as the best compatible fluid with Antimony Trichloride (as well as other similar chlorinated halides). Particular attention was brought to Molybdenum due to its superior machinability and better potential for welding.

- Molybdenum was identified as the most ‘wetable’ metal in the water contact angle study comparing 9 different metals.
- Preliminary results for wettability of 3 different metals with Antimony Trichloride indicate that Molybdenum presents the highest wettability still, though these results need to be further tested due to the limited data that was able to be collected.
- The compatibility study shows that any alloys containing Nickel are not compatible with Antimony Trichloride due to excessive levels of pitting corrosion.
- All refractory metals showed a good level of corrosion resistance to molten Antimony Trichloride over a 24h period.
- SEM imaging and EDX analysis showed that no reaction occurred on the refractory metal surfaces and only Antimony Trichloride residues were found.

Chapter VII

Experimental analysis of water heat pipe thermal transport limitations

7.1 Water Heat Pipe thermal performance analysis

The following chapter outlines the thermal transport testing done on Water based heat pipes approaching their maximum working temperature. As discussed in Chapter 2, the lower end of the ‘medium’ temperature range is defined by the maximum working temperature of water heat pipes. By analysing the performance characteristics of water heat pipes in their maximum temperature range, a baseline performance indicator is given for fluids which may exceed these temperatures. New testing methods and techniques are explored which aim to attain the upper working limit of water heat pipes using the test rig developed in Chapter 5. In addition to this, water heat pipes are commonly developed for a range of markets and current applications in Thermacore Europe Ltd. The heat pipes used in this testing section were developed for use in a PCM thermal storage application and these tests are used to quantify and validate the heat pipe performance at a system level.

The experimental setup, procedures, test methods and analytical methods used to attain the results outlined in this chapter are detailed in Chapters 3 and 5. Previous tests by Anderson et al. , [43], Sarraf et al. [42] and William et al. [98] show other similar techniques used in testing the thermal transport performance of a heat pipes to the ones developed in this chapter, however, some fundamental changes - particularly towards the methodology of the testing – were applied as detailed below:

- Taking the heat pipe up to the thermal transport limitation to identify the limitation boundary and quantify their change in performance.

- Tests intend to emulate realistic application conditions in presence of air, and hence, the quantification of heat losses form a part of the assessment.
- The experimental design was tailored specifically to achieve the above two points, deviating from traditional experimental techniques which do not tend to aim towards these objectives.

The test was primarily aimed towards determining the boiling limit of the heat pipe as this was determined to be the main limiting phenomena at the given test temperatures through the modelling described in Chapter 4. The test methodologies and test rig design were developed considering three main questions:

- How can a specific vapour temperature be reached and maintained?
- How can the thermal transport through the heat pipe be maximized at a specific vapour temperature?
- At what point can the operating limit be defined experimentally? (i.e. which indicator or combination of indicators can best describe this point)

These questions formed the basis of the experimental design. By answering these, it was possible to formulate a strategy by which the test rig could be best utilized to attain the desired results. A critical analysis of the results attained is presented in section 7.2 of this chapter. The results of this study intend to set the experimental process for further testing on the selected medium temperature fluids in future work. The full characterization of the above described heat pipes allows to confirm the adequate production and manufacturing processes to be used for this type of heat pipe,

validate the numerical modelling solutions and provide baseline data for future development of heat pipes in this temperature range and above.

The general objective of these tests is to determine the performance of Copper Nickel (CuNi30Mn1Fe) heat pipes using water as the working fluid whilst approaching the maximum temperature limitation of water. Water is predicted to work effectively at up to 350°C (provided the heat pipe can withstand these vapour pressures) [1], [42], [43], [98], [128], [129]. Copper Nickel has a relatively high strength compared to other common heat pipe metals. This allows the pipe to be able to withstand the high vapour pressures with minimal wall thickness. Extensive data for the performance of Copper Nickel pipes at high temperatures is currently limited. The thermal transport performances of these heat pipes at their upper temperature limits is of critical importance for validation of numerical models. These could subsequently be used to identify new potential medium temperature fluids which could offer better heat transport in the medium temperature range.

Although many life tests have been conducted with Cu-Ni heat pipes using water as the working fluid, proving their long term compatibilities, studies showing the thermal transport performance limitations (i.e. the maximum thermal transport performance as determined by boiling, capillary, sonic and entrainment limitations) of these heat pipes at elevated temperatures are scarce and for the particular alloy chosen for this study there is currently no data. This set of data also may serve as a comparative measure against other working fluids which may be tested in this temperature range.

7.1.1 Heat Pipe Design

The dimensions of a heat pipe are highly dependent on the application. Usually the application would primarily dictate the outer geometry of the heat pipe (shape, diameter, angle, etc.) and thermal optimization is applied to the inner geometry (wall thickness, wick thickness, wick porosity, vapour space, etc.) [1], [32]. In this study, there is no specific geometry dictated due to the end application spanning a variety of potential technologies. For this reason, the key considerations taken into account for the desired heat pipe are listed in Table 7-1.

Table 7-1 Heat pipe design considerations

<i>Quality</i>	<i>Purpose</i>	<i>Constraint</i>
Must provide sufficient vapour space	To increase sonic and entrainment limits	Minimum vapour space
Must be representative of a typical heat pipe used in industry	To have a higher chance of being taken forward into market	Cylindrical shape
Must allow for adequate capillary action to be demonstrated	Demonstrate the functionality as a heat pipe	Some form of wick structure must be present at a suitable thickness
Must contain a higher vapour volume than liquid volume	To prevent entrainment	Minimum vapour space of 2.83E-3 m ³
Must allow for adequate thermocouple attachment	Ease of measurement	Accessible thermocouple attachment areas
Must be relatively easy to manufacture	Decrease cost and lead times	Simple shape with minimal welding

One closely linked heat pipe application involving PCM storage units utilizes water heat pipes at up to 300°C. This is a development by the H2020 fund and ran by Innova Microsolar with partnerships with several institutions including Aavid Thermacore Ltd. [110]. Details about this application and its various requirements can

be found in Chapter 8. The final heat pipe design followed the constraints presented by the Innova project as this also fell in line with the design constraints presented in Table 7-1. The final heat pipe design undertook several iterations throughout the test rig development to cater for further constraints such as manufacturing, materials and cost. A full breakdown of the design process and final iterations is shown in Table 7-2. All CAD and engineering drawings can be found in Appendix L.

Table 7-2 Heat pipe design summary

Iteration	Description	Drawing
1	Initial design – first concept heat pipe design using two weld joints for the end cap and fill tube	D-A18721-550-B
2	Length decrease for adaptation to test rig	D-A21738-550-A
3	Reduction to one weld joint for fill tube only and fill tube re-design	D-A22430-550-B

The heat pipe design used in the water heat pipe testing and Molybdenum and TZM welding trials was Design 2. Design 3 was then adopted for all subsequent heat pipes. A full list of the heat pipes produced can be found in Table 7-4. The final heat pipe dimensions chosen are highlighted in Table 7-3.

Table 7-3 Final heat pipe dimensions

Measurement	Value
Heat Pipe Length (m):	0.46
Evaporator Length (m):	0.1
Condenser Length (m):	0.15
Adiabatic Length (m):	0.21
Effective Length (m):	0.335
Diameter (mm):	12
Wall Thickness (mm):	0.8
Wall Conductivity (W/mK):	29
Orientation:	Horizontal
Screen Conductivity (W/mK):	50
Minimum Operating Temperature (C):	50
Maximum Operating Temperature (C):	300
Max Operating Power in application (W):	150

Table 7-4 Heat pipe list summary

Heat pipe name	Design	Material	Wick	Fluid	Fill volume (cc)	Length (mm)	Accepted/Rejected
CuNi HP1	2	CuNi	PhosB Mesh 300	Water	10	460	Accepted
CuNi HP2	2	CuNi	PhosB Mesh 300	Water	10	460	Accepted
CuNi HP3	2	CuNi	PhosB Mesh 300	Water	10	460	Accepted
CuNi HP4	2	CuNi	PhosB Mesh 300	Water	10	460	Accepted
CuNi HP5	2	CuNi	PhosB Mesh 300	Water	10	460	Rejected
CuNi HP6	2	CuNi	PhosB Mesh 300	Water	10	460	Rejected
TZM1	3	TZM	No wick	N/A	N/A	300	Rejected
TZM2	3	TZM	No wick	N/A	N/A	200	Rejected

7.1.2 Material analysis

Various authors have conducted both analytical and experimental studies on the identification of medium temperature fluids as well as compatible metal combinations [43], [46], [56], [98], [129], [130]. Studies by Sarraf et. al. [42] and Groll [6] looks into various metals which could be compatible with water at high temperatures. Potential candidate metals were then constructed, and life tested to assess their compatibilities were undertaken. The selected wall material for the thermal storage application was CuNi30Mn1Fe due to its ready availability, high strength, high conductivity, high corrosion resistance and relatively low cost.

Table 7-5 shows some of the previous wall materials used in high temperature water heat pipe compatibility testing and how the selected wall material compares against these.

Table 7-5 Water heat pipe metal envelope alloys

<i>Metal</i>	<i>Ref</i>	<i>Composition</i>	<i>Tensile Stress (at 300°C) (N/mm²)</i>	<i>Wall thickness (mm)</i>	<i>Conductivity (W/mK)</i>
Monel 400	[131]	Ni, Mn, Fe, Si, Cu	380	0.7	30.1
Monel K500	[132]	Ni, Mn, Fe, Cu, Al, Ti	980	0.27	25.4
OFHC Copper	[133]	Cu (Ag)	265	1.00	386
CuNi10Fe	[134]	Cu, Ni, Fe	412	0.64	50.15
CP Ti	[135]	Ti	448	0.6	17
CuNi30Mn1Fe	[135]	Cu, Ni, Mn, Fe	441	0.6	29

Previous testing from Sarraf et al. and Groll et al. show life tests for the first five metals detailed in Table 7-5. These were conducted at 277°C and with a 325W thermal load input in Sarraf's tests [42] and at a temperature of 200°C with unknown thermal load input for Groll's tests [6]. All tests were successful at up to 5000 hours, after which the Titanium heat pipes started to develop NCG's. Report show that other

heat pipes showed no signs of decay with CuNi10Fe reaching over 17500 hours of testing.

7.1.3 Aim and setup

The main aim of the thermal transport performance tests is to determine the maximum working limitation point of the heat pipe at the given temperatures. Initially the tests set out to answer the three principal question posed at the start of the chapter; how can a specific vapour temperature be reached and maintained? How can the heat load through the heat pipe be maximized at a specific vapour temperature? At what point can the transport limit be defined experimentally?

These points were explored in the preliminary testing phase, where the individual components of the test rig were assessed and optimized towards the posed questions. Figure 7-1 shows the types of testing done for each test rig component. These are summarized in section 7.3 where the drawn conclusions are analysed, and experimental settings established.

The test rig is designed to characterize these heat pipes and assess their performance compared to predicted values. The main objectives of this test are as follows:

- To determine experimentally the optimal charge volume (horizontal)
- To determine the maximum heat pipe thermal performance at 4 different condenser temperatures (200, 250, 270 and 300°C).

- To verify the primary form of limitation (boiling or capillary) at three different temperature ranges
- To compare this data against prediction calculations and previous tests conducted in such ranges

7.1.3.1 Test rig

The experimental facilities consist of an oil circulator with programmable temperature control capable of operating up to 350°C, a high temperature flow meter, a pneumatic valve and Pico logger for thermocouple signal processing. Condenser and heater blocks were custom built to fit the heat pipe and the power supply could deliver a power of up to 1kW to the heat pipe.

The circulator is able to deliver a flow rate of up to 0.035 Kg/s and provides a temperature reading accuracy of 0.01°C. The flow meter is capable of reading the flow rate, density and temperature of the oil at an accuracy of 0.0001kg/s, 0.1kg/m³ and 0.01°C respectively. K-type thermocouples were used for temperature measurement along the heat pipe and at the inlet and outlet of the condenser block with a post-calibrated accuracy of 0.1°C. Two separate control systems were used, one to control the circulator and the other to control the pneumatic valve and take readings from the Pico logger and flow meter. Table 7-6 details the list of apparatus used in the test rig construction while the test setup diagram can be seen in Figure 3-13.

Table 7-6 Test component list

Apparatus	Function
Coolant circulator	To provide coolant re-heating & pumping
Flow meter	To measure the fluid flow
Heater block	To provide heat flux to heat pipe evaporator
Pneumatic valve	To control flow rate through condenser block
T-type Thermocouples	Temperature measurement
K-type Thermocouples	Temperature measurement
H350 Thermal bath fluid	Coolant

7.1.3.2 Test structure: Preliminary tests and optimisation

Preliminary testing serves to determine the main test parameters and adjust and components, as necessary. Figure 7-1 outlines the various preliminary tests needed on each individual test rig component. These tests also serve to determine the amount of heat loss to be expected from each component and will be compared against the predicted values in Chapter 3.

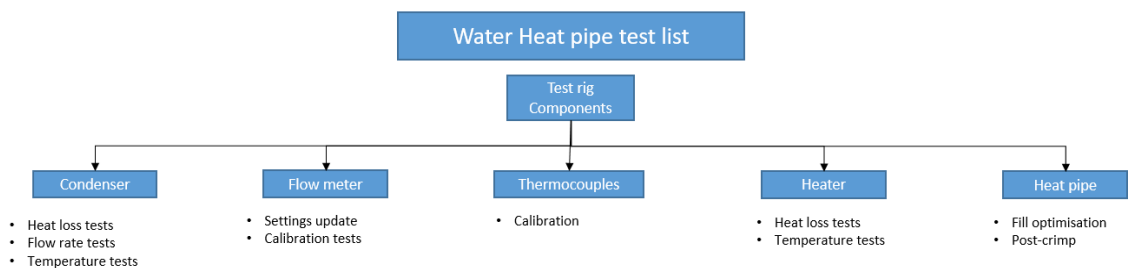


Figure 7-1 Component testing diagram

Figure 7-2 shows the flow diagram of the tests to be carried out. The main outputs from the tests are symbolised by triangular extracts. These come mostly in the form of linear equations relating the expected heat loss or temperature difference to the active component temperature.

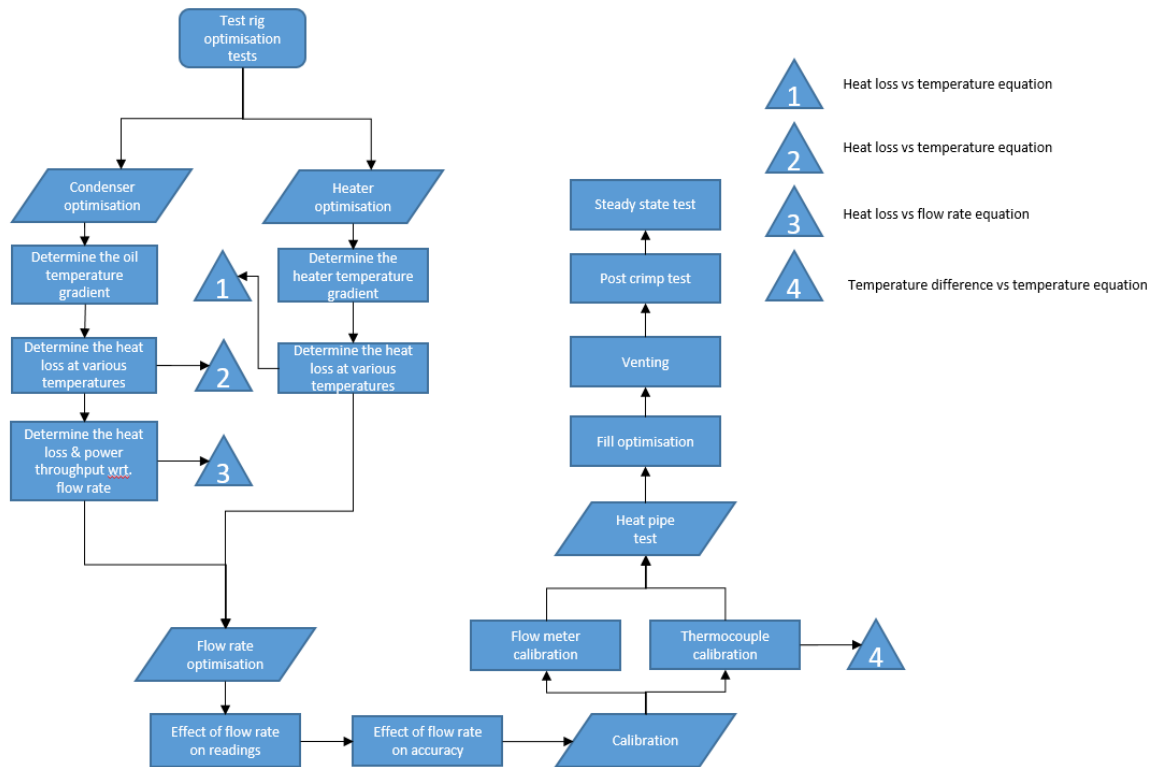


Figure 7-2 Test process flow chart

7.1.4 Heat pipe testing approach and methodology

The main objective of the thermal transport performance tests is to accurately assess the performance of the heat pipe close to its maximum operating limits. In this case, the limits of interest are those around 300°C for any given heat pipe (as testing will start at the lower limit of the medium temperature zone). To begin with, water heat

pipes have been selected to be tested and used as a baseline indicator for thermal heat transport in the lower end of the medium temperature range.

Determinants of the heat pipe performance are the thermal resistance (R), the average temperature difference of the heater and condenser section (ΔT_{av}) and the effective conductivity (k_{eff}) of the heat pipe. These are characterised through equations 84, 85 and 86 respectively [1], [32].

$$R = \frac{T_e - T_{co}}{Q} \quad 87$$

$$T_{av} = Av(E1 \rightarrow E4) - Av(C1 \rightarrow C6) \quad 88$$

$$k_{eff} = \frac{l_{eff}}{A_{xs}R} \quad 89$$

Where ' T_e ' is the average evaporator temperature ($^{\circ}\text{C}$), ' T_c ' is the average condenser temperature ($^{\circ}\text{C}$), ' l_{eff} ' is the effective heat pipe length (m), ' A_{xs} ' is the heat pipe cross sectional area (m^2) and ' Q ' is the heat output (W).

These quantities can be used to aid in any subsequent system modelling which would utilise these heat pipes. Additionally, a cross examination of each of these values is made to estimate the limitation point of the heat pipe and show the behaviours of the heat pipe around this point in practise.

7.1.5 Test matrix

Out of these variables there are 1, 4 and 6 ‘levels’ chosen for the flow rate, circulator temperature and power input respectively to adequately quantify the heat pipe performance. The response variable in all experiments is the thermal load output. The uncontrolled parameters for each test case are:

- Ambient temperature
- Pipework heat loss
- Condenser/Heater heat loss

The effect of these factors intends to be minimised through repeated experiments in varying conditions. Once the baseline data is determined according to the methodology laid out in Chapter 3, the test rig and heat pipe is determined suitable to begin the principal heat pipe thermal heat transport tests. These have the aim of determining the dry-out limit of the heat pipe in the horizontal orientation. For this, the parameters set out in Table 7-7 must be determined from the baseline testing. The experimental design follows a ‘Latin square’ approach [136] where the main variables are defined to be:

- Flow rate
- Circulator temperature
- Power input

Table 7-7 Latin square example with test parameters

Experiment number	Flow rate (Kg/s)	Circulator temperature (°C)	Power inputs (W)
1	x	a	l, m, n, o, p, q
2	x	b	l, m, n, o, p, q
3	x	c	l, m, n, o, p, q
4	x	d	l, m, n, o, p, q

7.2 Thermal transport performance testing on Water Heat pipes

The following section outlines the thermal transport performance of the water/CuNi6030 heat pipes approaching dry-out conditions in the 200°C to 300°C range. The tests aim to determine the maximum heat transfer rate which can be achieved in this temperature range before dry-out occurs and compare this to numerical prediction. Further to this, a quantitative analysis is made on key performance indicators for the heat pipe such as the equivalent thermal conductivity and thermal resistance. The tests serve as a demonstrator of the operating potential of the test rig and set out standard operating procedures for testing heat pipes at the medium-high temperature range.

7.2.1 Test plan

Through preliminary testing, the most suited flow rate to be used was determined to be 0.0167Kg/s. The minimum power input needed to overcome heat losses and start normal heat pipe operation in most cases was determined to be 100W. The circulator temperature is used to control the steady state vapour temperature. The temperature difference from the circulator outlet to the condenser inlet with respect to the set temperature can be determined from line equations set out in Chapter 3 but on average tends to be around 15°C. The maximum circulator temperature is set to 300°C which would give a condenser inlet temperature of around 280/285°C. This allows the evaporator temperature to rise above 300°C for the testing and achieve a vapour temperature of around 300°C for the maximum dry-out conditions.

Preliminary testing has determined the degree to which the vapour temperature is raised with relation to the power input to the heat pipe. This in turn can be used to determine the pre dry-out temperature/power input gradient to achieve any vapour temperature required.

The test intends to reach four boiling limit points in the 250 to 300°C range. To achieve this, 4 circulator temperatures were selected: 200, 250, 270 and 300. These would equate to lower condenser temperatures, as seen in Table 7-8, but should achieve vapour temperatures in the same region as the circulator temperature. The test layout is outlined in Table 7-8 and the procedure is detailed in short form below.

Table 7-8 Test parameters

Test number	Flow rate (Kg/s)	Circulator temperature (°C)	Power inputs (W)
1	0.0167	200	100, 120, 140, 160, 180, 200
2	0.0167	250	100, 120, 140, 160, 180, 200
3	0.0167	270	100, 120, 140, 160, 180, 200
4	0.0167	300	100, 120, 140, 160, 180, 200

7.2.1.1 Procedure

- Set the pre-determined flow rate and circulator temperature
- Begin temperature data recording
- Set the power to 100W
- Wait until steady state is reached (temperature variance of <0.5°C)
- Stop temperature recording and save file

- Begin new temperature recording
- Increase power by 20W
- Repeat steps 4 to 7 until obvious dry-out is reached or vapour temperature becomes $> 320^{\circ}\text{C}$

7.2.2 Theory

During production testing, the main identifier for the heat pipe functionality is the temperature differential of the heat pipe extremities (ΔT_{e2e} , see Table 7-9). This, however, does not give a complete picture of the heat pipe performance within a system as it does not serve as measure of the heat flux at the evaporator and condenser or provide any measure of the axial heat flux. Using the experimental equipment and procedure detailed in section 2.2, various heat pipe performance indicators were determined before testing which would provide a better understanding of the heat pipe behaviour. First, the various experimental measures of temperature difference were identified as seen in Table 7-9. Further determinants of the heat pipe performance are the thermal resistance (R), the average temperature difference of the heater and condenser section (ΔT_{av}) and the effective conductivity (K_e) of the heat pipe. These are characterised through equations 87, 88 and 89 respectively.

All these qualities can act as an indicator to when a limitation point is reached. In this study, a quantitative analysis of these properties is reported from and experimental data to aid in any subsequent system modelling which would utilize these heat pipes. Additionally, a cross examination of each of these values is made to

determine the limitation point of the heat pipe and show the behaviours of the heat pipe around the boiling limit.

Table 7-9 Various experimental temperature difference definitions. The 'E' and 'C' variables are temperature readings in the positions indicated in

<i>Formula</i>	<i>Description</i>
$dT_{e2e} = E1 - C6$	End to end heat pipe dT
$dT_{av} = Av(E1 \rightarrow E4) - Av(C1 \rightarrow C6)$	Average heat pipe dT
$dT_{adi} = E4 - C1$	Adiabatic dT
$T_e = Av(E1 \rightarrow E3)$	Average evaporator temperature
$T_c = Av(C2 \rightarrow C6)$	Average condenser temperature
$dT_R = T_e - T_c$	Thermal resistance dT
$T_{vap} = Av(T_e, T_c)$	Vapour temperature
$dT_e = T_e - T_{vap}$	Evaporator dT
$dT_{max} = Max(E1 \rightarrow E4) - Min(C1 \rightarrow C6)$	Maximum recorded temperature difference

7.2.2.1 Predicted heat pipe performance

The heat pipe numerical modelling uses selected empirical formulae to quantify each heat pipe limitation curve. The principal limitations which are of interest in this study are the capillary and boiling limits as these are the dominant limitations at the upper operating temperatures. The capillary limit is the point at which the sum of the liquid, vapour and gravitational pressure differentials become greater than the capillary pressure [1], this is demonstrated in Equation 90.

$$\Delta P_{c,max} \geq \Delta P_l + \Delta P_v + \Delta P_g \quad 90$$

From substituting the empirical correlations for each pressure value in Equation 90, this balance can be expressed as seen in Equation 91 [1].

$$\frac{2\sigma}{r_{eff}} \geq \frac{\mu_l Q l_e}{\pi(r_w^2 - r_v^2)\epsilon r_c^2 \rho_l h_{fg}} + \frac{8\mu_v Q}{\pi\rho_v r_v^4 h_{fg}} + \rho_l g(l_e + l_a) \sin \theta \quad 91$$

The boiling limit (i.e. the determination of the critical heat flux for the specified heat pipe conditions) of choice which best suits mesh wick heat pipes according to previous studies [1], [32], [11] is that by Ivanovski et. al. [8] as described in Chapter 2, equation 16. The equation used shall be presented again below.

$$Q_b = \frac{2\pi l_e K T_v}{h_{fg} \rho_v \ln\left(\frac{r_i}{r_v}\right)} \left(\frac{2\sigma}{r_n} - P_{c,max} \right) \quad 92$$

The boiling and capillary limits form the principal power limitation modelling of the heat pipe, giving origin to the heat pipe thermal limitation curves seen in Figure 7-3. Other limitation such as the sonic, entrainment and viscous limit were also modelled and showed to have no effect on the operation of the heat pipe at high temperatures and in this case even throughout the entire operating range. This is also ascertained by Reay and Kew [1] who demonstrate that these equations are relevant only at start-up and low temperature conditions in high density and high viscosity fluids (such as liquid metals) due to the low pressure gradients which lead to high vapour velocities, high shear stress on the vapour/liquid boundary and high shear within the liquid saturated porous structure.

Figure 7-3 shows the resultant thermal power limitations form modelling equations 91 and 92 over the majority of its operating range using the heat pipe

geometry seen in Table 7-3. Details of the code used to undertake the modelling can be found in Appendix F and G. It is determined from this model that the maximum thermal power the heat pipe is able to carry is 280W when operating at 150°C. From a temperature above 200°C, the boiling limit start to take effect causing a more rapid decrease in thermal power capacity compared to the capillary limit. This graph suggests that in the temperature range of interest for the current testing (200°C to 300°C), the dominant thermal performance limitation will be the boiling limit. For this reason, the analysis will concentrate on quantifying the boiling limitation point experimentally and analyse the change in performance of the heat pie around this point.

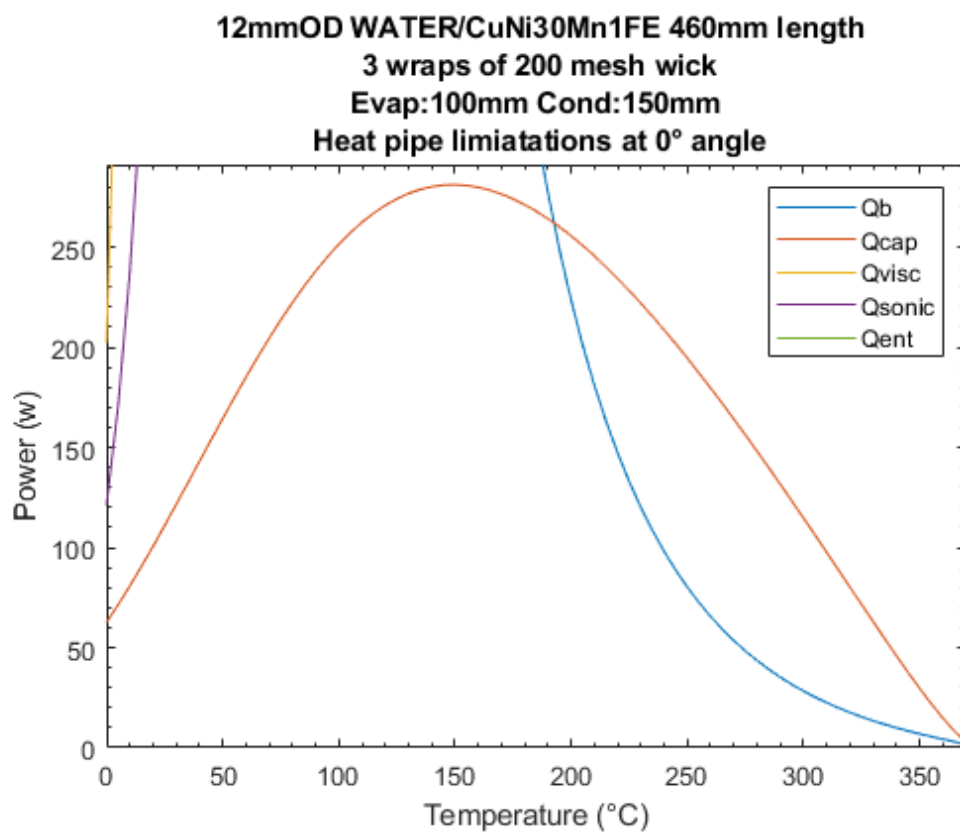


Figure 7-3 All limitations for horizontal water heat pipe

To further describe the thermal performance, Figure 7-4 shows the radial heat flux to the evaporator and condenser sections when reaching the maximum thermal power limitations determined in Figure 7-3. Here it can be observed that the maximum heat flux experienced in the system is 70.3 kW/m² at the evaporator when operating at 150°C. At temperatures above 200°C, the maximum heat flux at the evaporator is 66.1 kW/m² and at the condenser is 44.9 kW/m².

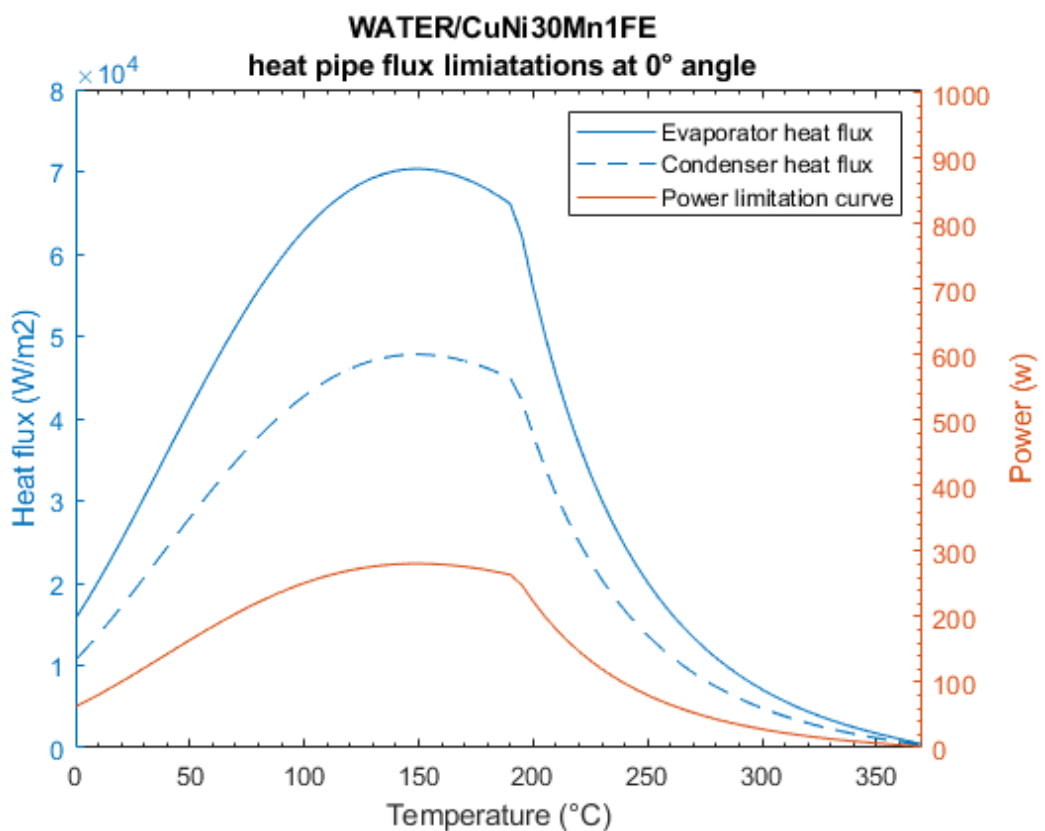


Figure 7-4 Evaporator and Condenser heat fluxes associated with maximum thermal power capacity from Figure 7-3

7.3 Results and Discussion

To determine where the heat transport limit lies in the heat pipe at vapour temperatures approaching and above 280°C, the test requires the heat pipe to slowly approach the operating limit by increasing the thermal load in small steps. To regulate the vapour temperature and alter the point at which the limitation is reached, the condenser oil loop was set to four different temperatures; 200, 250, 270 and 300°C. Various flow rates were initially explored to determine the highest possible heat extraction without compromising the accuracy of the output thermal load readings. Once this was determined, the heat input was increased in steps of 20W, starting from 100W, until dry-out was reached at each condenser temperature.

The main objectives of the test is to measure the change in performance at and beyond the heat transportation limit, identify the indicators (i.e. heat pipe temperature difference, vapour temperature or thermal resistance) that could best describe the point at which the capillary or boiling limits are reached experimentally and, from this, determine the range of maximum nucleation radius values, ' r_n ', which would best describe the heat pipe boiling limit numerically. Each experimental data point in Figure 7-5 indicates the steady state vapour temperature and maximum thermal load achieved for the each input power step at a constant condenser temperature.

7.3.1 Heat pipe heat transport limit analysis

The first impression taken from the experimental data presented in Figure 7-5 is that there appears to be a 'transition zone' in which the heat pipe can still effectively

transport heat, but there is a clear break from the linear trend line of increasing thermal load input suggesting that the boiling limit has been reached. After this point, a further power increase results only in the increase of the vapour temperature with a plateau in output thermal load – a clear indication that wick dry-out has occurred. Before the plateau occurs, however, there is a steady change in trend where the heat pipe thermal load outputs correlate with a range of nucleation radius values.

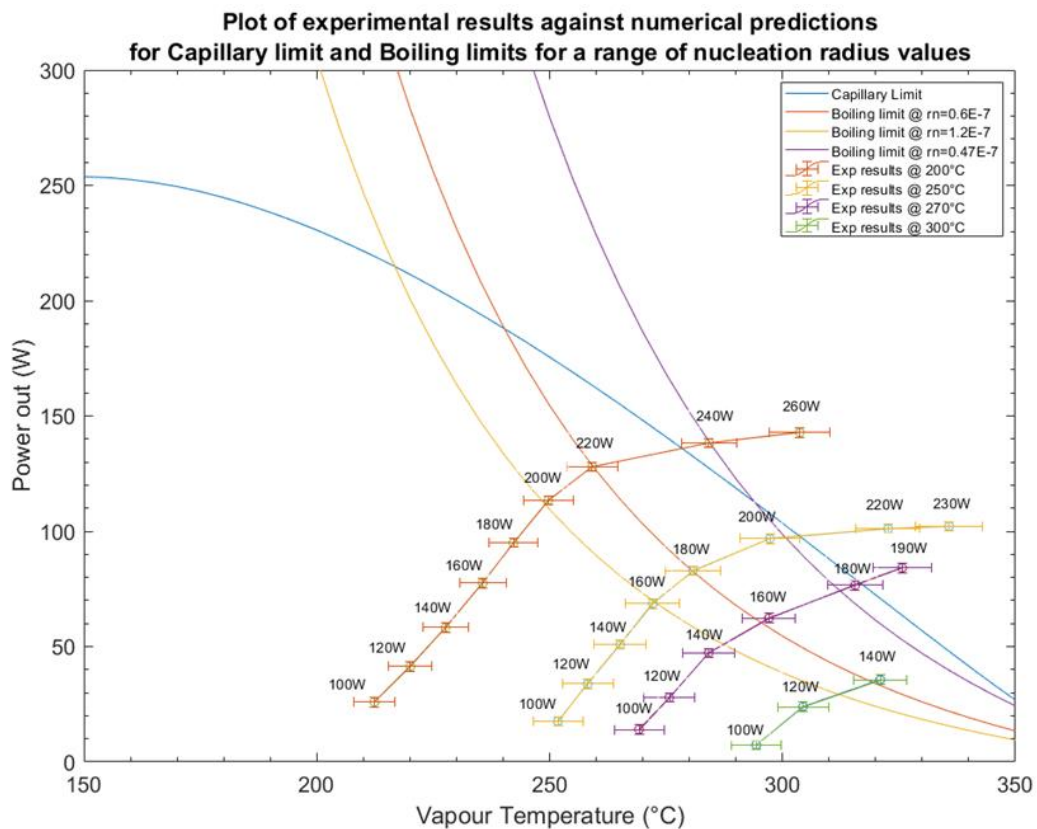


Figure 7-5 Experimental and numerical thermal heat transport prediction results. Values next to experimental data points indicate the input power for the steady state condition. The points correlating with the range of calculated boiling limit curves are proposed as the ‘transition’ zone. The error bars are calculated from instrument error propagation theory.

Figure 7-6, Figure 7-7 and Figure 7-8 show the calculated output heat load of a range of nucleation radii against the experimental output heat load of the water heat pipe. The results show that the estimated point of transition using experimental methods correlates within a 1% accuracy when adjusting the nucleation radius values between $0.47\text{E-}7$ and $1.2\text{E-}7$. This indicated that the maximum nucleation radius the heat pipe can achieve is $1.2\text{E-}7$ before the bubbles begin to occupy the majority of the evaporator wick structure.

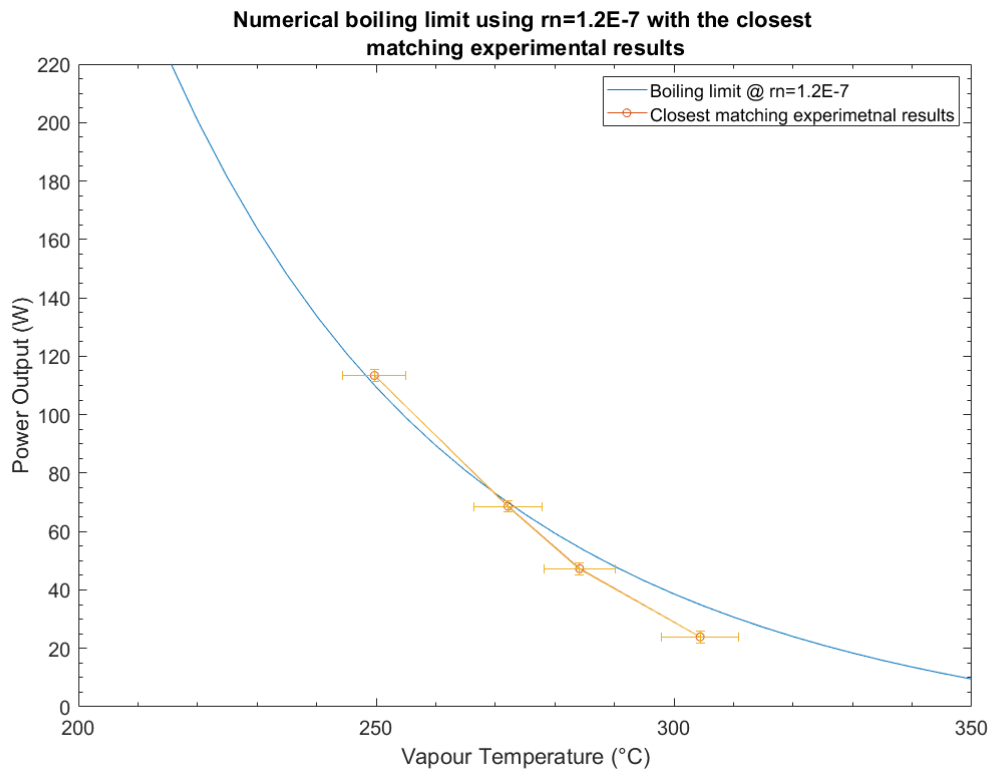


Figure 7-6 Graph of experimental steady state values correlating with a nucleation radius of $1.2\text{E-}7$

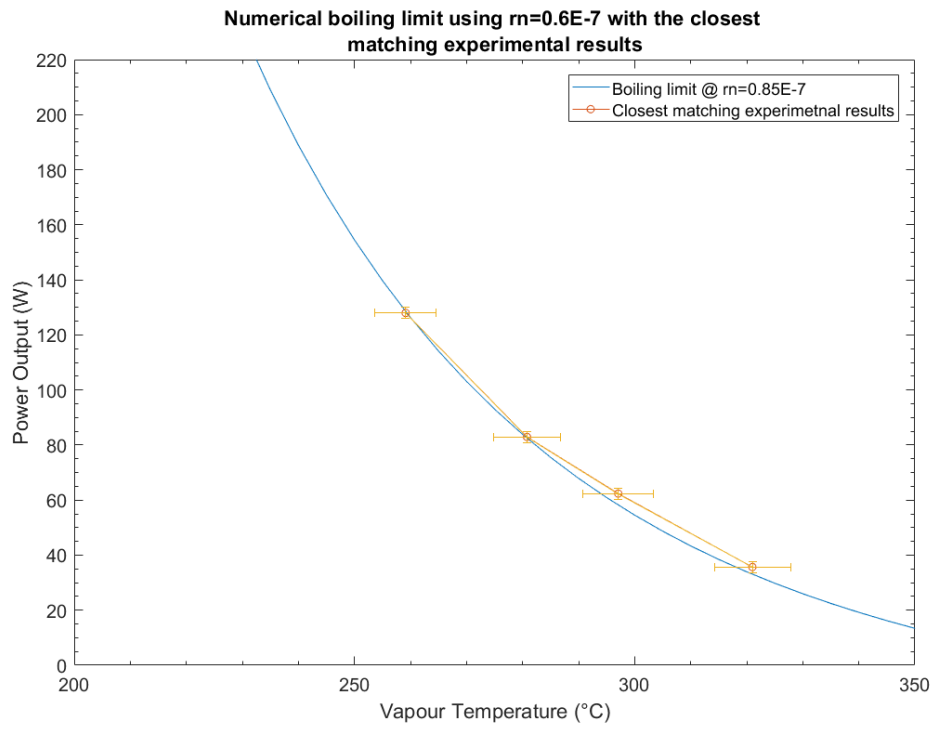


Figure 7-7 Graph of experimental steady state values correlating with a nucleation radius of 0.6E-7

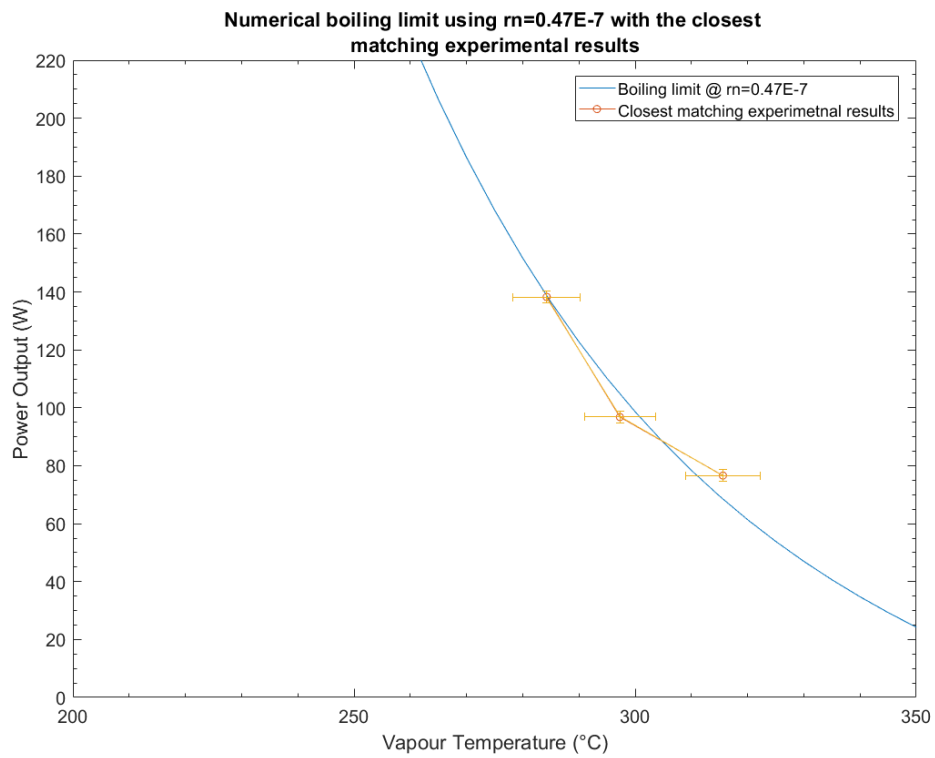


Figure 7-8 Graph of experimental steady state values correlating with a nucleation radius of 0.47E-7

This first experimental analysis shows that the boiling limit may encompass a ‘range’ where the numerical predictions correlate with experimental values. This range is primarily dictated by the minimum and maximum nucleation radius values, r_n . This range could be described as the range of radii in which there will either be a partial or full dry-out of the wick, though experiments have proven that operating the heat pipe in partial wick dry out conditions may still be effective. Regardless of this, this transition zone remains a highly unpredictable region due to the number of factors which could influence the nucleation radius.

To further analyse the ‘transition zone’, key qualities of the heat pipe, such as the temperature difference, thermal resistance and effective thermal conductivity will be analysed in this transition region to identify some indicators which may be of use to pinpoint a more precise transition point and analyse the performance of the heat pipe in this region.

7.3.2 Heat pipe temperature difference analysis

One key point of discussion is in the measure of temperature difference of the heat pipe and how these measurements can be used and interpreted. To calculate the theoretical temperature difference, a thermal resistance network is usually employed where the sum of the thermal resistances of the wall material and wick gives the total thermal resistance across the heat pipe. In an application, however, it is unlikely that these will be the only thermal resistances present between the heat sources and sink. Other factors, such as contact resistance, radiation and parasitic heating/cooling all influence the measurement of the heat pipe wall temperature. This is demonstrated in

the variety of temperature differences that can be extracted from the data as seen in Table 7-9. The main measurements are ‘end to end’ temperature difference, average temperature difference, adiabatic temperature difference and maximum temperature difference. These are all valid quantities which can be use in the thermal resistance and equivalent conductivity calculations. It is important to consider which one to use in any subsequent calculations as these will each give a different interpretation of the functionality of the heat pipe. For this study, the average temperature difference was chosen as the preferable option as this averages any potential temperature gradients within the heater and condenser blocks. It also gives a more representative value towards the final application which will use a similar measure to determine the effectiveness of the heat pipe and system.

Figure 7-9 shows the trend of average temperature difference values for each experiment as the power to the evaporator end is increased. It is expected that the temperature difference at each power input would be the same across all circulator temperatures (if it’s within the limitation curve). It can be observed that the temperature difference values remain within a consistent range until the transition point is achieved. At circulator temperatures of 250 and 270°C, the temperature difference is consistent for power inputs of 100W to 140W, remaining within a 10% range. For a circulator temperature of 200°C, the values still follow the general trend, however, they appear to incur a systematic error throwing them out of range from the 250°C and 270°C values. This of course may have been the consequence of the presence of some systematic error in the 200°C condenser tests cause by an unexpected change in ambient conditions or a change in the insulation uniformity and packing density or most likely a small

variation in the inclination angle – all of which are a very difficult factor to monitor and keep consistent from test to test.

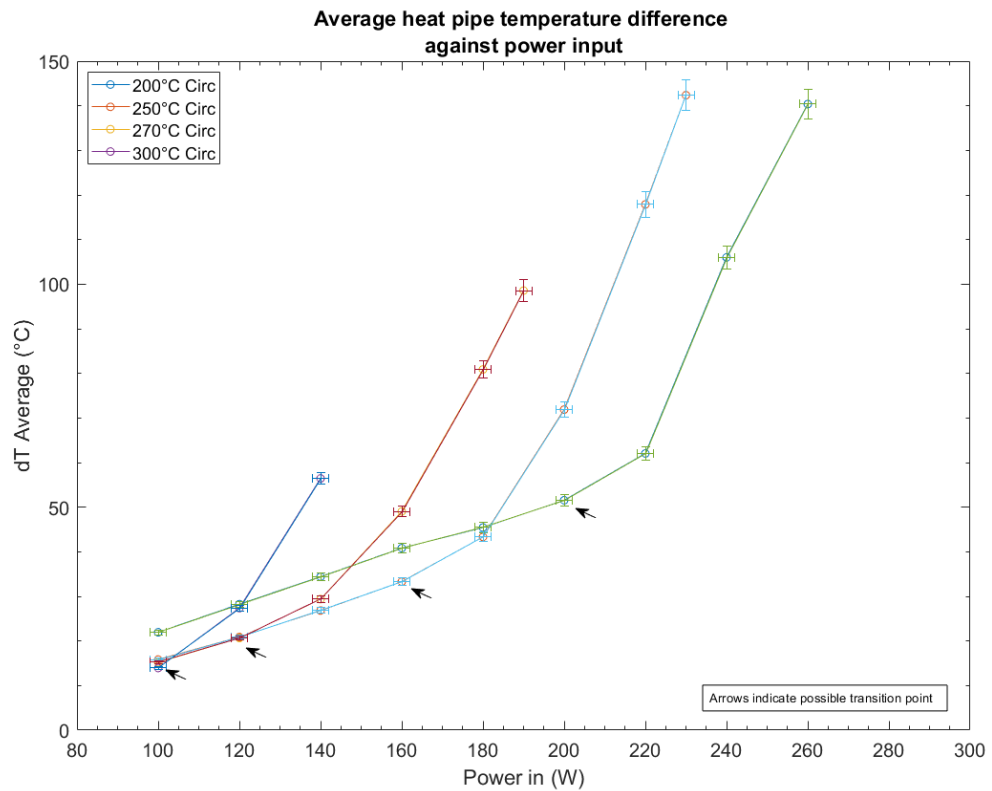


Figure 7-9 Average temperature difference against the input power for experimental steady state results

The highlighted values in Figure 7-9 indicates the observed point at which the linear trend increase is broken at each condenser temperature. This may give the first indication as to a fixed point where the boiling limit is reached. Taking the points highlighted in Figure 7-9, and assuming they give a good representation of the boiling limit of the heat pipe, these points can be plotted against the numerical dT predictions as shown in Figure 7-10.

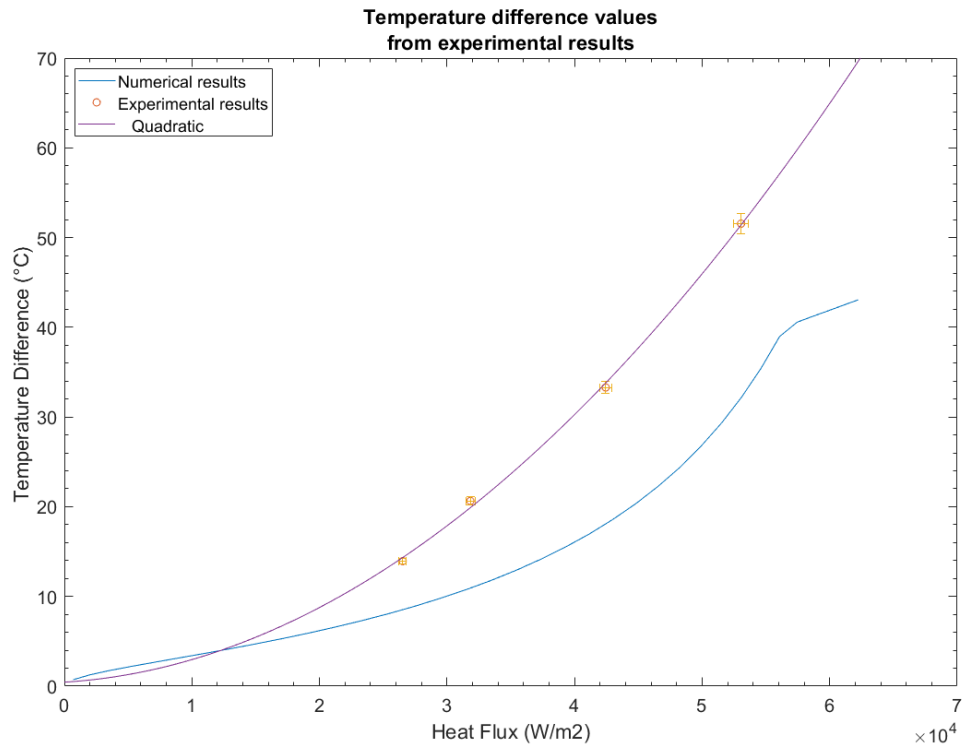


Figure 7-10 Experimental average temperature difference values at estimated boiling limit against the heat flux input compared to numerical predictions

Figure 7-10 shows that the experimental values for the average temperature difference experienced by the heat pipe at the transition points are substantially larger than that predicted by the thermal network method.

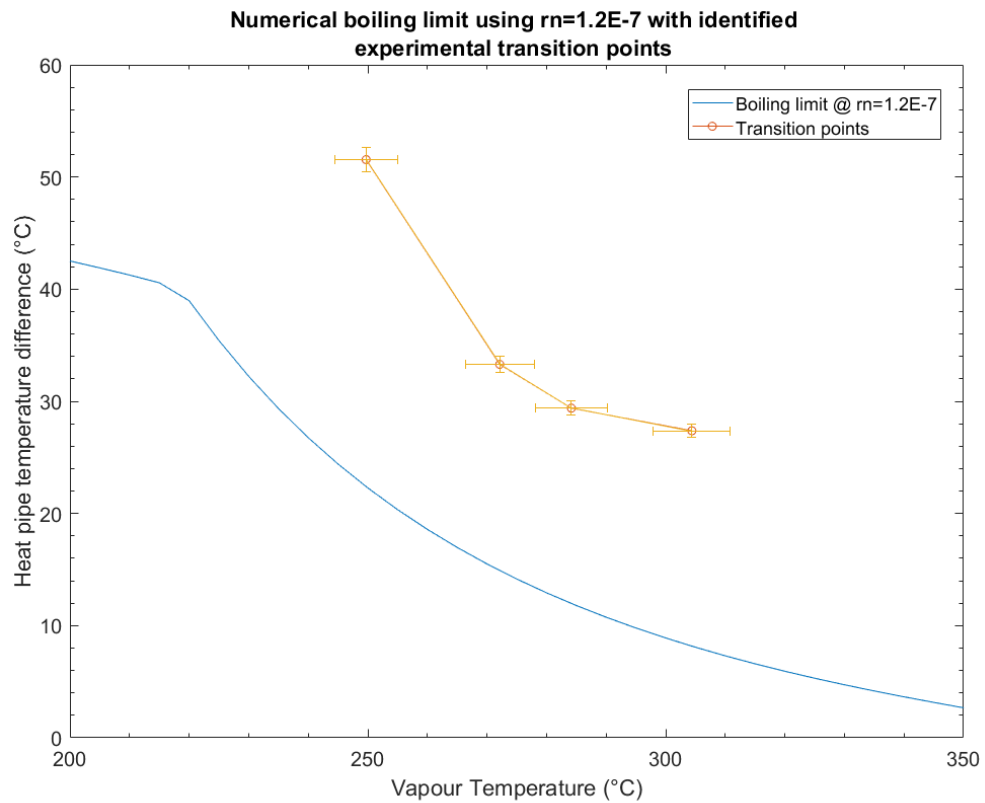


Figure 7-11 Experimental average temperature difference values at estimated boiling limit against the calculated vapour temperature for each steady state value compared to predicted trend

7.3.3 Heat pipe thermal resistance analysis

At lower condenser temperatures of 200°C and 250°C, there is a clear change in gradient indicating a heat transport limitation has been reached. The numerical model for the boiling limit was calculated for a range of maximum nucleation radii from 1.1E-7 and 0.6E-7. The boiling limit curves showed trend lines correlating with the start and end of the proposed ‘transition zone’. At higher condenser temperatures of 270°C and 300°C, there becomes a less defined limitation point with a smoother gradient change. This may indicate that the heat pipe is already operating at or near its operating limit but is still able to transfer heat somewhat effectively. Another indicator for the transition point in these cases are the thermal resistance as shown in Figure 7-12.

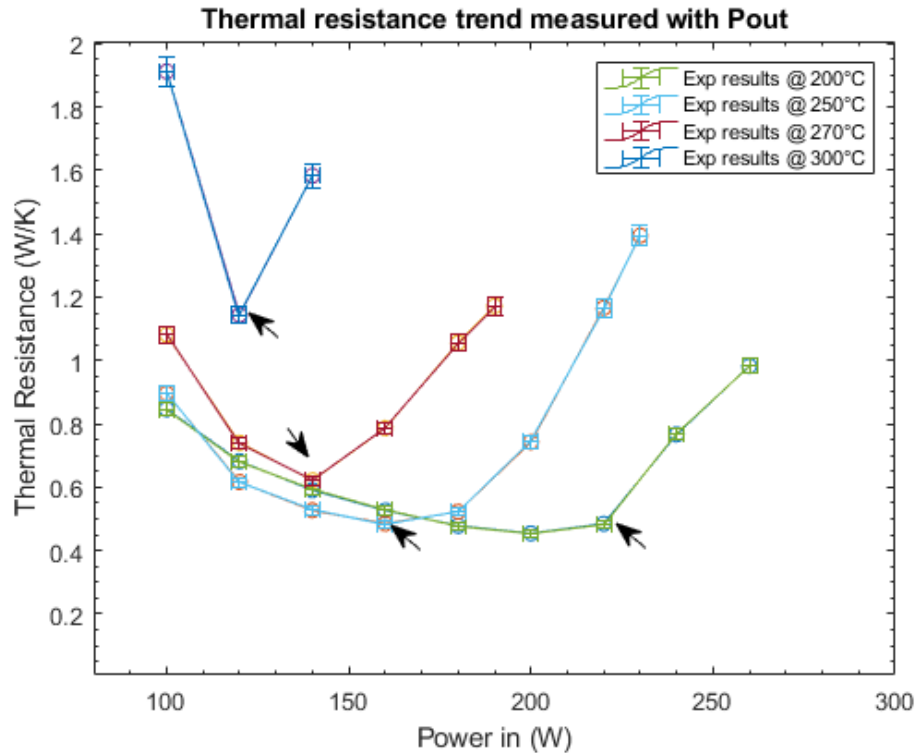


Figure 7-12 Thermal resistance at each experimental steady state against the input thermal load for thermal resistance calculated from the output thermal load (measure by calorimeter). Highlighted points show an alternative indication for the ‘transition’ zone. Here the transition point for 270°C and 300°C circulator temperature differs from those indicated in Figure 7-5.

Figure 7-12 shows the thermal resistance trend of each test series where the thermal resistance, denoted by equation 87, is calculated against the heat output of the heat pipe (i.e. that measure by the calorimeter) as this is assumed to be the total heat travelling through the pipe after heat losses.

It is observed that in the case of the 270°C and 300°C condenser temperatures, there is a clear change in thermal resistance which could serve as an alternative indicator for the limitation point where the ‘transition zone’ is less defined though the vapour temperature data alone. These, however, differ from the points identified in Table 7-10 as they occur at higher thermal loads for circulator temperatures of 270°C

and 300°C respectively. This is a good example of the various ways in which the boiling limit could be identified and how the various indicators suggest different points.

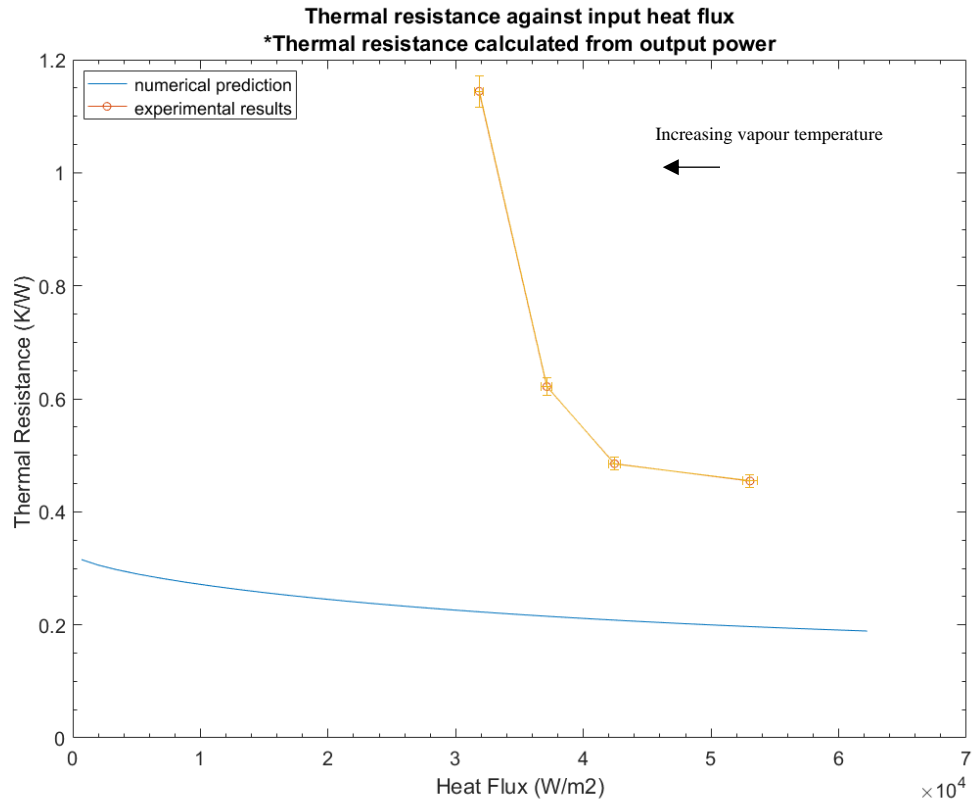


Figure 7-13 Thermal resistance of transition zone points against heat flux input

Figure 7-13 shows the trend in experimental thermal resistance at the determined transition points in Figure 7-12 against the calculated thermal resistance at the boiling limit for the thermal resistance calculated from the measured thermal load from the calorimeter. It can be seen that although there is an agreement with trend prediction for the higher vapour temperature values, due to the large discrepancy between experimental and numerical heat pipe temperature differences the experimental thermal resistances are much greater than predicted. There also seems to be a rapid increase in thermal resistance above a vapour temperature of 280°C in the experimental results. This highlights the shortfall of using a thermal network in

predicting the heat pipe temperature difference, particularly along the boiling limit line. The complexity of the boiling kinetics in the wick structure appear to hugely impact the temperature difference across the wick in ways which are hard to predict using equivalent conductivities for liquid filled porous structures. Another factor which may have impacted the temperature difference measurement is the angle measurement of the heat pipe. Small changes in angle can cause a huge impact in the horizontal orientation and angle measurement accuracy was capable of being measured to $\pm 0.1^\circ\text{C}$. The heat pipe was adjusted so that the average angle measurement was negative in each case (i.e. the heat pipe was acting slightly against gravity) as this would be the conditions specified for the end application. The difference seen in the thermal resistance reported against the input and output thermal loads also highlights the various interpretations that can be made of the experimental results.

7.3.4 Effective conductivity quantification and analysis

The effective conductivity is a product of both the temperature difference and the output thermal load of the heat pipe (as seen in equation 89). For this reason, although the experimental output thermal load tends to correlate with predicted values, the discrepancy in the temperature difference of the heat pipe observed compared to the predicted values is bound to have a negative impact on the effective thermal conductivity compared to numerical predictions. Indeed, Figure 7-14 shows a plot of all of the effective conductivities calculated from the steady state values within the ‘transition zone’ range. It can be seen that the experimental results present a much lower effective thermal conductivity than predicted by numerical modelling. A quadratic trend line of all experimental results shows an estimate of the expected thermal

conductivity at any given vapour temperature in the 250°C to 320°C range. This can subsequently be used in system modelling to more accurately depict the heat pipe performance using empirical data.

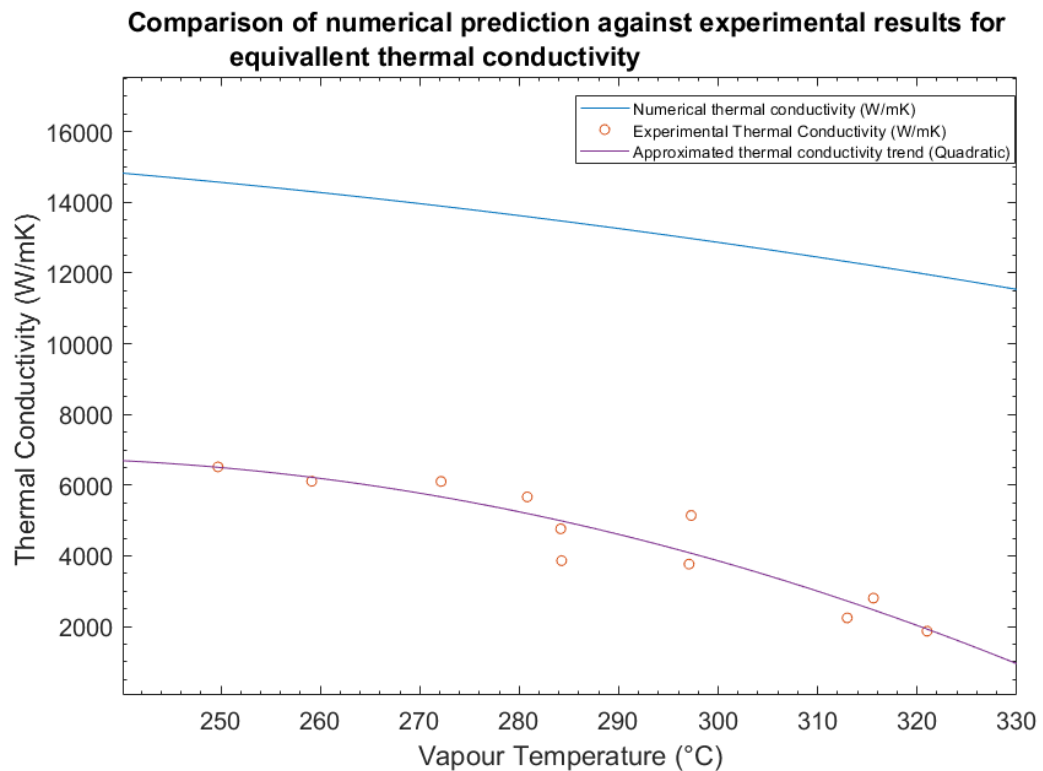


Figure 7-14 Scatter plot of all the calculated effective conductivities of steady state values within the 'transition zone'.

These results indicate that the temperature difference modelling approach tends to overestimate the heat pipe performance in the boiling limit region. It is suggested that an alternative approach to temperature difference modelling should be the focus of future work to improve this discrepancy.

7.3.5 Boiling point identification, quantification and analysis

Table 7-10 presents the results of the steady state tests that present the maximum effective thermal conductivity denoted by the line in Figure 7-15. From this data, it can be observed that there is a large increase in the thermal resistance as vapour temperature increases, particularly in the 270°C to 300°C condenser temperature values. The effect of increasing the condenser temperature in step of 50°C, 20°C and 30°C appeared to have relatively uniformly increased the boiling limit vapour temperature by roughly 20°C at each step, whereas the output thermal load at the transition point tended to decrease in near equivalent steps to the condenser temperature step magnitudes at 61.1W, 20.6W and 26.7W thermal load difference respectively. Theoretically, the effective thermal conductivity should decrease as the vapour temperature increases as the liquid thermal conductivity tends to decrease which results in an overall increase of the wick thermal resistance. This remained true for the effective conductivity trend seen in the experimental results.

Table 7-10 Heat pipe performance at transition point indicated in Figure 7-15.

Circulator temperature (°C)	Vapour Temperature at transition point (°C)	Thermal resistance at transition point (K/W)	Output thermal load at transition point (W)	dTav at transition point (°C)	dTadi at transition point (°C)	Effective thermal conductivity at transition point (W/mK)
200	259.1	0.43	144	62	13.5	6668.5
250	280.8	0.52	82.9	43.3	9.8	5499
270	297	0.79	62.3	49	9.1	3653.6
300	321	1.58	35.6	56.4	10	1815

Scatter plot of all steady state conditions

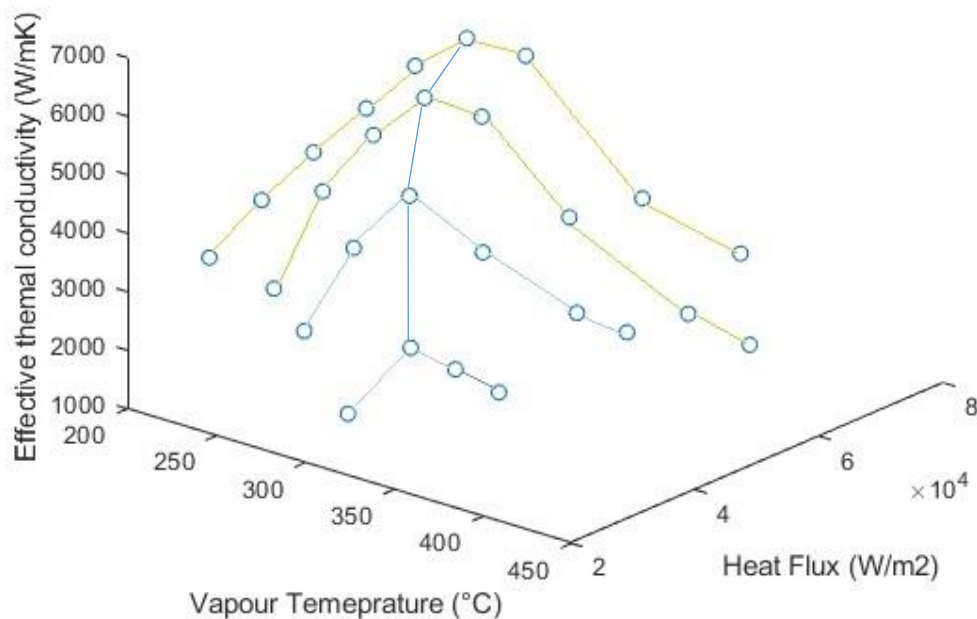


Figure 7-15 Multi variable scatter plot of steady state conditions. Line represents the maximum thermal conductivity path which can be used as the transition point.

7.3.6 Error analysis

The error analysis methodology is largely outlined in section 3.4. The data presented in this study has an N value of 2 due to the length of time taken to both build the test rigs and to acquire one steady state value point (run time for a single test usually exceeds 1 working day). For this reason, it was not possible to acquire multiple sets of all steady state data, however, tests at 200°C were able to be repeated up to 3 times to ensure the repeatability of the methodology. The error displayed in previously presented graphs are derived from propagation theory of instrument error (as presented in chapter Error analysis3.4). Table 7-11 presents the repeated tests for a circulator temperature of 200°C with the statistical error presented. In all test cases, the heat pipe

angle was kept as close to 0° as possible with error only in the positive direction of up to +0.2°.

Table 7-11 Repeatability of 200°C circulator temperature tests

Power in (W)	<i>Output thermal load (W)</i>					
	Test 1	Test 2	Test 3	Mean	SD	SDOM (%error)
100	25.93	30.19	-	28.06	2.13	1.51
120	41.40	41.66	45.01	42.69	1.64	0.95
140	58.22	60.62	62.71	60.52	1.84	1.06
160	77.50	77.99	79.69	78.39	0.94	0.54
180	94.96	96.61	99.40	96.99	1.83	1.06
200	113.43	114.81	117.14	115.13	1.53	0.88
220	127.98	123.46	123.46	124.97	2.13	1.23

7.3.7 Discussion

The methods and results put forward in this experiment show four-point indicators which can be used to identify the heat pipe limitation using relatively simple techniques applied in a unique way to allow for testing of heat pipes at elevated temperatures. The test not only successfully demonstrates the use of a previously untested alloy, CuNi30Mn1Fe, as a viable heat pipe wall material, but also demonstrated its medium-term compatibility with water. A demonstration of the high temperature heat pipe limitations in practice was achieved, and the results largely agree with one-dimensional model predictions in terms of maximum thermal load delivery of the heat pipes in the boiling limit region.

The study successfully lays out an experimental method for identifying the maximum heat transport limit (in this case the boiling limit) at high vapour temperatures

of water using analyses on the power output and heat pipe wall temperature. The use of water filled copper alloy heat pipes for use in thermal storage applications at temperatures above 280°C has been demonstrated to be somewhat effective should the condenser temperature be kept below 300°C. When the condenser is operating at this temperature, particularly in the horizontal orientation, the pipe is susceptible to rapid decline in thermal conductivity due to reaching the boiling limit at a relatively low input thermal loads. Operation in the identified ‘transition zone’, however, is still able to effectively transport heat without too much detriment.

From this analysis clearly there is a change in behaviour of the heat pipe beyond a certain vapour temperature corresponding to the boiling limit equation with a nucleation radius between 0.6E-7 and 1.1E-7. As the vapour temperature increases, the transition point becomes less pronounced. It has been shown in these cases that the thermal resistance values could give an alternative indication of when the boiling limit occurs. Results showing the performance of the heat pipe at each experimental boiling limit point is presented with the calculated equivalent thermal conductivity. The main conclusions of the study are as follows:

- Experimental results show that the boiling limit could lie between maximum nucleation radii of 1.1E-7 and 0.6E-7 in the proposed boiling equation by Chi [32] and Faghri [11].
- Thermal resistance values can give an alternative indicator of reaching the boiling limit where the transition zone is less pronounced. This may differ from that defined by the vapour temperature.
- Equivalent thermal conductivity values have been calculated for a copper alloy/water heat pipe operating at the boiling limit above 280°C

- At vapour temperature above 250°C the thermal resistance substantially increases, but effective heat transfer can still occur up to the output thermal loads presented in Table 7-10.

As the main application concerns the PCM thermal storage unit, in which the heat pipes operate horizontally, the water filled Cu/Ni heat pipes were tested only in the horizontal position. Not only does this demonstrate the limitations of a water filled heat pipe operating above 280°C but also this gives an empirical value to the conductivity and thermal resistance of the heat pipes which can be used in subsequent thermal storage simulations.

7.4 Summary and Conclusions

Though experimentation with novel water heat pipes, the outlined study in this chapter has achieved the following:

- Proven the functionality, accuracy, and repeatability of tests using the designed test rig at the lower end of the medium temperature range with water-based heat pipes
- Results for the water heat pipe have provided a baseline for medium temperature heat pipes operating up to 320°C
- The water heat pipe testing has validated the use of Water/CuNi meshed heat pipes for applications operating up to 300°C
- A study on the boiling limit of meshed water heat pipes determined that the empirical equation proposed by Chi [32] and Faghri [11] is valid for nucleation radii between $1.1E-7$ and $0.6E-7$

From the results attained in this chapter, the validation of both the test rig components and the 1D numerical modelling was possible. The test rig can now confidently be used on novel heat pipes in the medium temperature range. Future work primarily aimed at the manufacturability of refractory metals is the next step to producing a medium temperature heat pipe prototype. Once this is completed, the same procedure outlined in this study should be used to assess the limitations of the prototype across the medium temperature range.

Chapter VIII

Heat Pipe fabrication and industrial case study

8.1 Introduction

As well as providing the theoretical scientific method for determining the optimal metals and fluids to take forward, this study has used a myriad of quantitative and qualitative analysis methods to prove the viability of the selected fluids and metals from the fluid selection process. The medium temperature test rig has been validated and its capabilities for testing in the medium temperature range has been proven. Moving forward with the tested fluids and metals over this study, the next phase of research should be directed towards prototype production. Although significant efforts were made over the duration of this project to manufacture a viable medium temperature heat pipe prototype, the production process met a series of challenges which could not be overcome using the available equipment and budget.

This chapter will outline the research that was undertaken with regard to the potential production methods as well as report the attempts that were made to manufacture a prototype and analyse the successes and failures of in the process. Based on this first-hand experience, the recommendation for how to proceed with production subject to further funding opportunities will be highlighted.

8.2 Fabrication methods

One major conclusion from this study is that the use of conventional metals and alloys for medium temperature heat pipes is not possible. The identified metals which would be suitable fall within the refractory metal category. Two major contenders are Molybdenum and the Molybdenum alloy TZM for further development. In most cases, refractory metals can present a challenge when welding due to a high tendency to oxidise at temperatures above 350°C causing reduced ductility in the weld joints [137]. In the case of Molybdenum and alloys, rapid oxidation starts at around 500°C if in contact with air, and if the temperature is elevated to above 778°C (the eutectic temperature of MoO₂-MoO) oxides become volatile and the oxidation rate accelerates considerably [137].

This section will discuss the general process and the possible fabrication methods which could be used in developing a medium temperature thermosyphon and heat pipe prototype. An outline of the general manufacturing process for a standard heat pipe is outlined. In the case of medium temperature heat pipes, the joining, filling and crimping procedures may need to be modified to cater for sensitive fluids and materials. The possible approaches to these processes will be discussed.

8.2.1 General manufacturing process

Figure 8-1 shows a general outline of the manufacturing processes involved in the production of a liquid metal (Sodium) heat pipe. This represents some of the most

involved preparation and filling procedures currently employed in Aavid Thermacore USA.

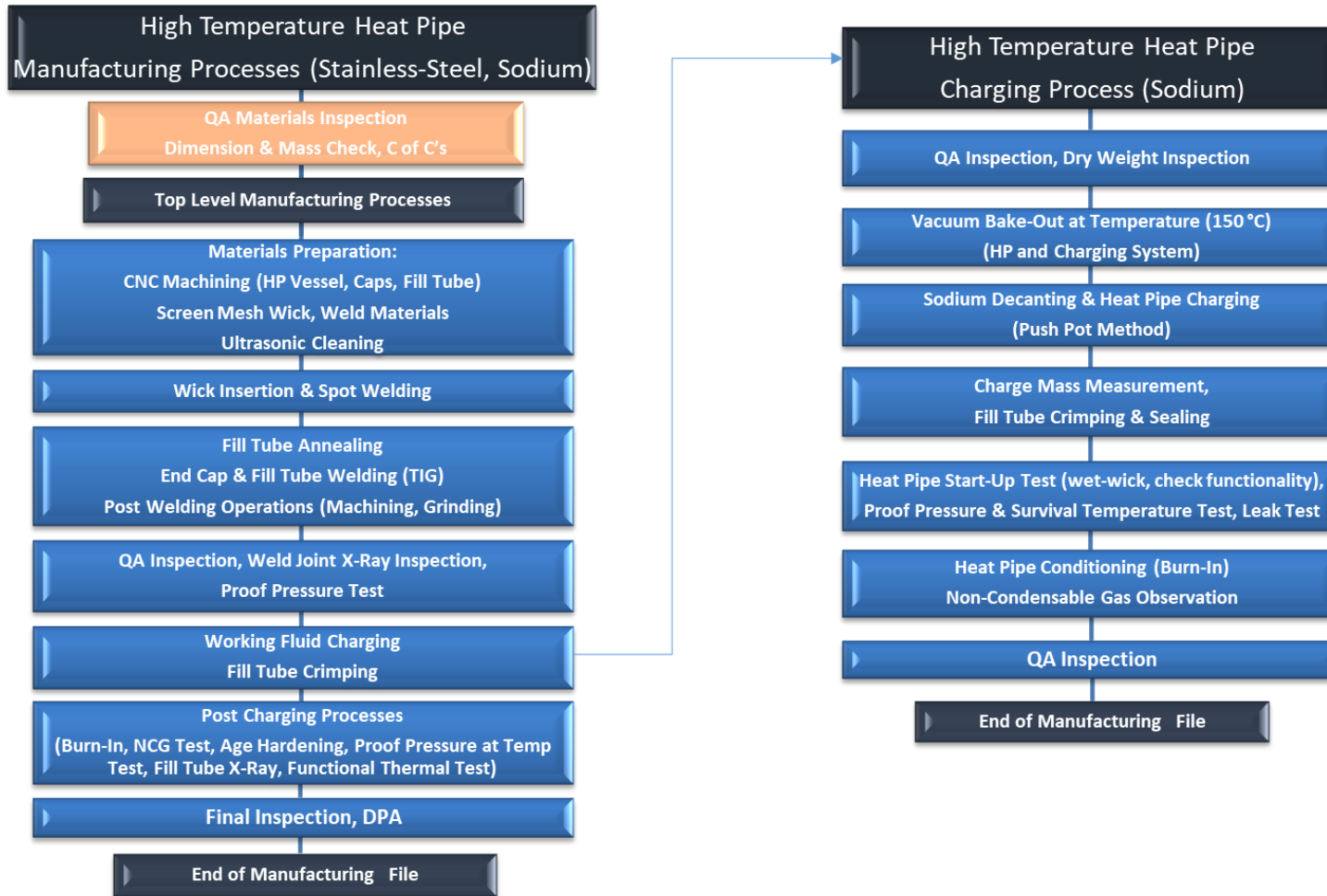


Figure 8-1 Manufacturing process for sodium/stainless steel heat pipe

8.2.2 Joining methods

Molybdenum and TZM have been identified and experimentally confirmed as a preferred vessel material, however, manufacturing process research has identified that joining of the materials is inherently challenging. The following table lists challenges associated to various joining techniques:

Table 8-1 Potential Tungsten Joining Technique Analysis:

Method	Description	Issues	Suitable (Y/N)	Recommendation Notes
TIG Welding	<ul style="list-style-type: none"> Welding in inert gas atmosphere. Dissimilar metal filler wire added to joint (Rhenium / Tantalum) 	<ul style="list-style-type: none"> Pre-heating Required Parts likely to be brittle below transition temperature 	N	<ul style="list-style-type: none"> Low quality weld joint expected Embrittlement likely to be induced
Laser / EB Welding	<ul style="list-style-type: none"> Low voltage and slow travel rates advised 	<ul style="list-style-type: none"> EB potentially can lead to micro-fractures in weld joint 	Y	<ul style="list-style-type: none"> Not a lot of data on improvement in weld quality over TIG, however EB and laser welding are potential options.
Plasma Arc Welding	<ul style="list-style-type: none"> The plasma jet is being explored by for use in welding of tungsten 	<ul style="list-style-type: none"> Limited information and results from tests 	?	<ul style="list-style-type: none"> Potential for narrower heat affected zones than conventional arc processes, but limited information of success in using the technique
Resistance Spot Welding	<ul style="list-style-type: none"> Electric current locally melts and fuses material between two electrodes 	<ul style="list-style-type: none"> Only focuses on a spot / does not weld entire seam. Intermediate metal foil / plates required to aide welding 	N	<ul style="list-style-type: none"> Multiple spot welds expected to lead to porosity in joints / create mechanical issues Filler materials typically have lower melting temperature than the base metal.
Vacuum Brazing (Conventional non-reactive braze alloys)	<ul style="list-style-type: none"> A braze material (foil / filler wire) is compressed between two surfaces that are heated, melting the material. Cooling solidifies the material forming the joint 	<ul style="list-style-type: none"> Conventional Braze Alloys have much lower melting point than Tungsten 	N	<ul style="list-style-type: none"> Braze joint expected to melt during operation of the heat pipe.

Vacuum Brazing (Novel reactive braze alloys)	<ul style="list-style-type: none"> • As per conventional alloy vacuum brazing. • Low melting point braze alloy forms a high melting point alloy during braze process 	<ul style="list-style-type: none"> • Availability of novel braze alloys • Process development and qualification testing required 	Y	<ul style="list-style-type: none"> • Platinum-Boron (2%) vacuum brazing of Tungsten has been shown to re-alloy increasing the Eutectic melting point from ≈ 830 °C to 2100 °C to 2150 °C
Additive Manufacturing	<ul style="list-style-type: none"> • Laser Powder Bed Fusion / 3D Printing of subsequent powder layers to create a 3D part. • Has been demonstrated to create medical devices for storage / handling of radioactive materials 	<ul style="list-style-type: none"> • New technique / new alloy for 3D printing • Requires development activity 	Y	<ul style="list-style-type: none"> • Aavid UK hold the patent on additive manufactured heat pipe capillary structures, therefore are experienced in this type of technology

Electron Beam / Laser welding, vacuum brazing utilising reactive alloys and additive manufacturing have been identified as candidate joining techniques, however all four techniques have challenges to address to prove feasibility. The preferred joining option is additive manufacturing, however further research into the process is required.

8.2.3 Wick Structure design

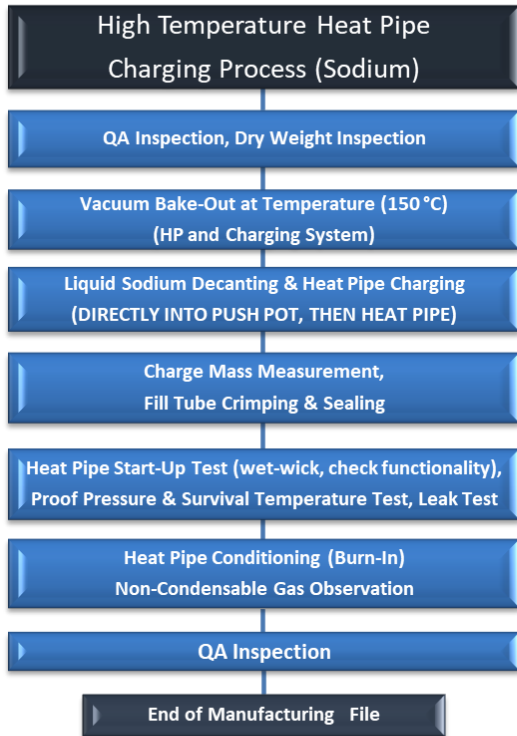
Initial prototypes are highly recommended to be thermosyphons due to the lower cost and complexity to build. This will allow for long term compatibility tests to be undertaken with selected fluids and metals. Once the compatibility has been verified, simple wick structures such as channels and arteries could be used to enhance heat transfer for applications requiring only gravity aided or horizontal applications. Further on, sintered wicks are most likely to be the primary wick option as the cost of sinter powder is much lower than the cost of mesh structures.

8.3 Filling methods

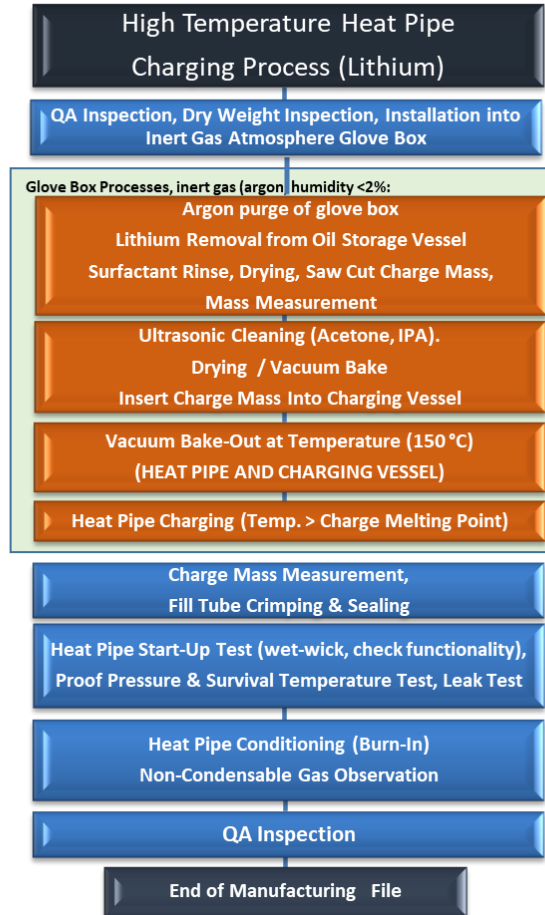
Once the fabrication method for both the heat pipe envelope and wick structure have been defined, the next challenge lies in the successful filling of the heat pipe. Due to the nature of the selected medium temperature fluids, the filling process is met with a series of challenges in order to keep the fluid from reacting with either moisture in the air or any of the materials in the filling process.

The following flow charts show the overall manufacturing processes for liquid metal heat pipe that is used as a reference. Due to the reactivity of the chosen fluids (Bismuth Trichloride, Antimony Trichloride and Bismuth Tribromide) the filling mechanism may follow a slightly modified procedure to a traditional sodium hat pipe.

FULLY SEALED VACUUM SYSTEM



INERT GAS GLOVE BOX SYSTEM



RELAXED VACUUM / BENCHTOP

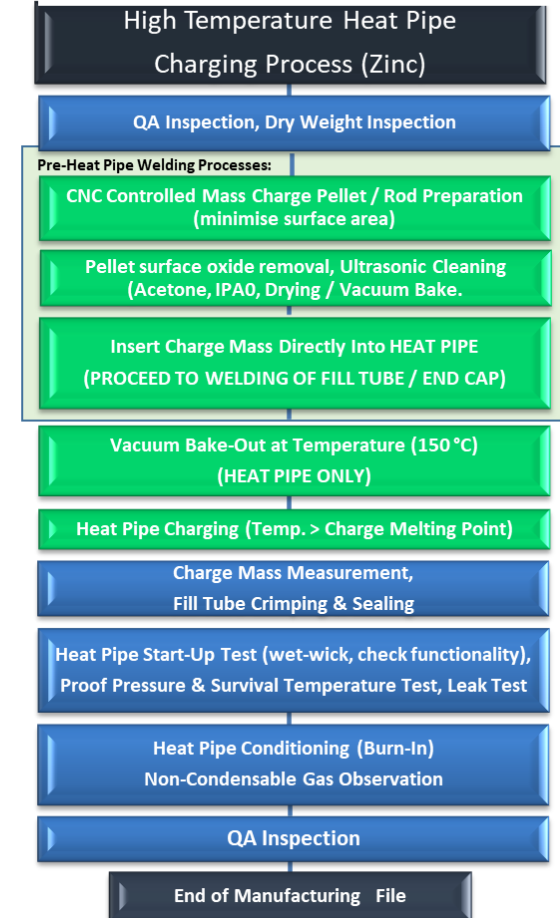


Figure 8-2 Charging processes

Focusing on the working fluid charging processes, the following three flow charts compare the sodium charging process flow with proposed modified charging processes for halide fluids. For Gallium Trichloride, it can be seen that due to rapid reaction of the solid material in air, it is required to store the material in inert atmosphere at all times and handle using an inert gas purged glove box. The GaCl₃ sample must then be weighed to size using mass measured with equipment installed within the glovebox, before transferring a directly into the push-pot. The vacuum bake and charging processes that follow are then similar to the sodium charging processes. The complexity of halides charging is greater than for sodium.

8.3.1 Conventional fill method

Considering the charging process for conventional fluids, usually they are non-reactive in air, therefore is easily handleable without personal protective equipment. Ideally a fluid which is solid at room temperature could be placed directly into a partially assembled heat pipe, which then progresses immediately to cap welding a vacuum bake-out to prevent deoxidisation. This process could potentially be achieved with Bismuth Trichloride and Antimony Trichloride, though this would still require a highly clean and

8.3.2 Push-pot fill method

A high purity fluid supply is stored within a bulk storage vessel, that is elevated above the work-piece location. An external heater jacket elevates the storage vessel to above the melting point of the fluid, transitioning it into the liquid phase. A valve at

the base of the vessel allows for decanting of the fluid into a measurement vessel (push-pot).

The push-pot assembly in turn is elevated above the work piece and has an outlet port / valve at the bottom of the vessel, that allows the fluid to flow into the heat pipe. The push-pot, transport lines, valve and heat pipe test piece are vacuum baked to remove moisture and air before sodium charging. At elevated temperature, the sodium charge mass is decanted into the push-pot, then is charged into the heat pipe. The heat pipe then undergoes a burn-in period that conditions the pipe to achieve maximum functionality.

In the case of a halide heat pipes, an additional process is proposed that to remove moisture / oxygen from within the heat pipe vessel, to minimise internal evaporation of the vessel wall at temperatures $> 300\text{ }^{\circ}\text{C}$.

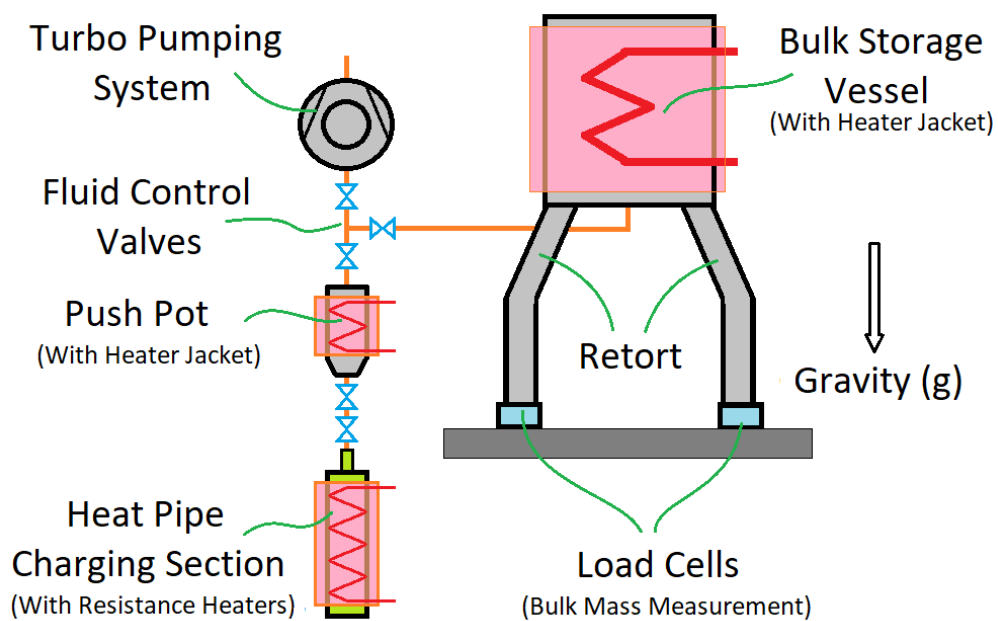


Figure 8-3 Schematic Diagram Showing the Main Elements of a High Temperature Heat Pipe Charging Facility

A preliminary charging process could be used to remove oxygen / moisture from within the heat pipe. One potential method would be to pre-charge the heat pipes with ammonia, that acts to draw moisture and oxygen into the fluid. The ammonia can then be removed, before proceeding to vacuum bake process. Ammonia charging facilities are available within Aavid UK.

8.3.3 Inert atmosphere/vacuum fill method

The procedure for filling the heat pipe using either an inert atmosphere or a vacuum environment would still be the same as conventional method but with the added cost of preparing either an inert or vacuum chamber containing all necessary equipment inside. Though the procedure itself would only have minor logistical factor on top of the conventional method (i.e. keeping everything within reach of the access point), the main disadvantage is the high cost of initial equipment investment should this equipment not already be available.

8.3.4 Crimping

Once filling and evacuation is complete, the standard crimping process follows that seen in Figure 8-4. This comprises of a pneumatic crimping tool which is used to keep the fill tube sealed while the valve is sawn off and the end is welded shut. It is currently unknown whether this process would be adequate for the metals in question. Once a prototype is constructed, the crimping process will have to undergo trial and error to determine if it is an adequate procedure. The metals in question are significantly stronger than conventional metals, hence it is predicted that the crimping force would

have to be much higher for refractory metals. The crimping tool does have the capability of reaching crimping strengths significantly higher than that used on regular metals though.

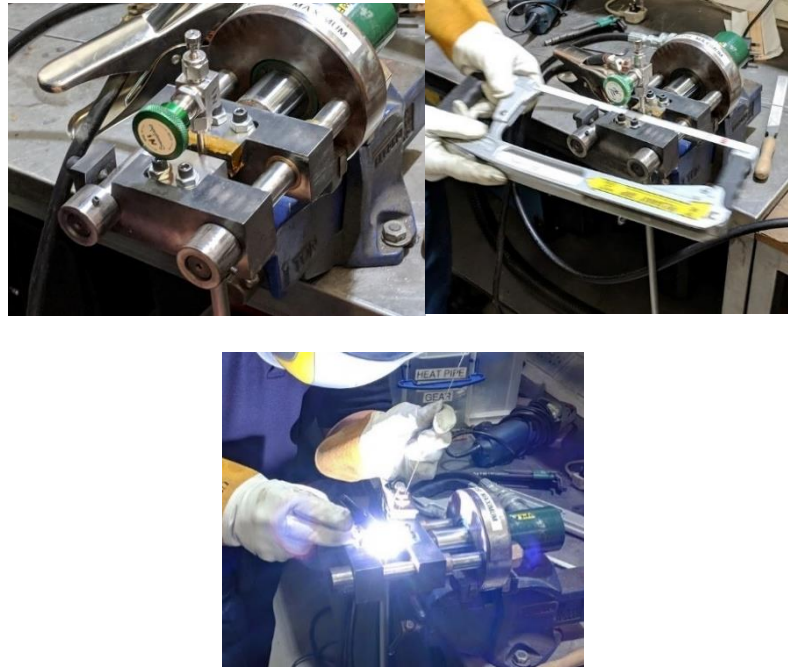


Figure 8-4 Standard crimping process

8.4 Fabrication attempts

Over the duration of this project, many attempts were made to produce a Molybdenum and TZM heat pipe prototype. The principal difficulty encountered during these trials is with the weldability of these metals. Although there are some studies which claim that these metals are weldable using conventional welding techniques such as TIG and MIG [137] [138], the studies clearly state that this must be done in a vacuum or inert atmosphere. Using the equipment available at Aavid Thermacore, an inert atmosphere glovebox with welding capability was constructed to trial welding the Mo and TZM prototype designs together.

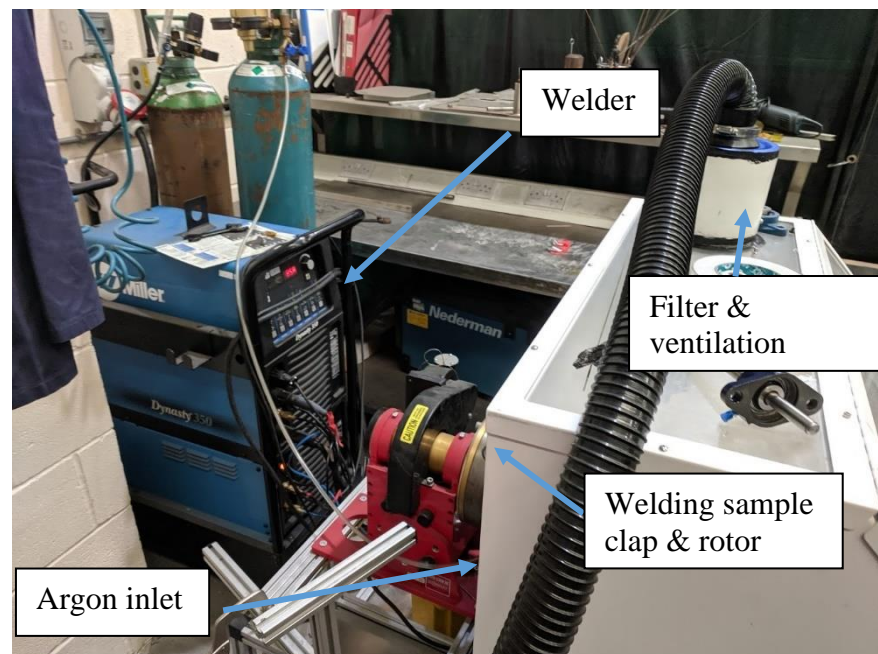


Figure 8-5 Custom built argon purged welding chamber



Figure 8-6 Argon purged welding attempt

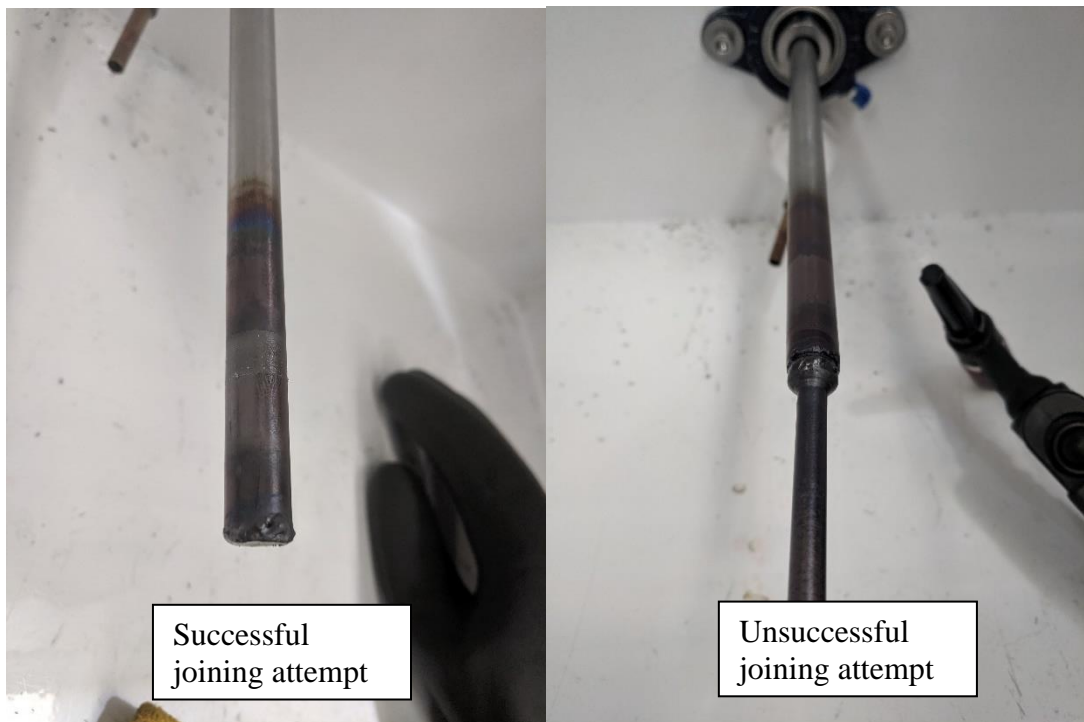


Figure 8-7 Argon purged welding results

8.5 Fluid selection analysis case study

In this thesis, a variety of methods and techniques have been used to validate the theory behind the modelling, compatibility and provide evidence of the viability of a variety metals and fluids in their use within the medium temperature range. Although these methods were directed a specific temperature range in this case, there is no reason why this fluid and metal optimisation process could not be conducted in any other temperature range also. For this reason, over the duration of the project I have set out to create a ‘framework’ by which the methods used in this study could be applied to any other temperature range of any heat pipe application.

This ‘framework’ is the basis of the content presented in Chapter 4. The framework intends to be an exhaustive consolidation of every method used in this study to enable rapid experimentation of new fluids to be considered for use in heat pipes. The method may also be used to either validate a fluid which is currently being used in an application or identify a more suitable alternative in accordance to changing application criteria. The ‘weighted selection’ methodology can consider a wide variety circumstances and identify the most suitable fluid out of those which have available fluid property data. Using the extensive fluid property databases which were also created during this study, this framework could be a valuable tool for industry to optimise their heat pipe designs and potentially identify cheaper, easier and more effective fluids for any number of applications in any temperature range.

Over the duration of this project, this framework has had the opportunity to be applied in other industrial applications to verify its usefulness and versatility. This

section will present a case study whereby the exact framework which was outlined in Chapter 4 was used in a feasibility study for the application of heat pipes as a thermal conduction enhancement in Nuclear Fusion application.

8.5.1 Application example

The UK Atomic Energy Authority proposed a feasibility study directed towards the viability of implementing heat pipes into plasma facing components of TOKAMAK nuclear reactors. The industry has previously conducted prototype testing on Lithium heat pipes which was met with a series of issues primarily involving material failure [139]. Other issues with the utilisation of Lithium prototypes is in the cost involved in producing such heat pipes due to the difficulty in handling the fluid and the materials involved.

The STEP Work Package 5 (Resilient Nuclear Components) wishes to harness industrial expertise in heat pipe design outside the fusion community and to identify whether this expertise can be applied to developing an innovative heat pipe concept design for the STEP diverter target. Further in-depth design and testing, to be carried out during the STEP programme conceptual design phase (2020-2025), is contingent on an initial feasibility study or studies to be carried out in 2019, expressed in terms of a “design challenge,”. The design challenge is ultimately concerned with the feasibility of implementation for a heat pipe high heat flux handling solution within the diverter region of a fusion reactor. The applications for the use of heat pipes in fusion applications are not necessarily limited to this application.

8.5.2 Fluid analysis

A fluid selection procedure was undertaken to select the most viable fluids which could be used in the application. From this study, 7 fluids were selected to take forward for further analysis. The figure below shows the Heat Transport Capacity (or Merit Number) of each fluid, this is the first method used to compare the functionality of the fluids over the desired temperature range.

Another important quality to analyse in each fluid is the Vapour Pressure. This determines whether the heat pipe internal pressure is within a functional range i.e. low enough to not cause any damage to the heat pipe walls and large enough to overcome viscous forces in the wick structure.

Once the Merit Number and Vapour Pressure analysis were completed, other important fluid properties were analysed, such as the fluid stability in air (at room temperature), the toxicity and ease of handling, the magnetic susceptibility and the cost. From this analysis, each property was assigned a score from 1 to 3 (1 indicating low performance and 3 indicating high performance). The fluids were then collated in a weighted analysis table seen below to rank the effectiveness of each fluid. From this analysis two fluids were shown to be equally viable as top candidate; hence these were taken forward into further analysis.

Using acquired property data for each of the shortlisted fluids, it is possible to model the maximum operating limits of heat pipes using each of the fluids. The images below show the 'operating domain' of each fluid. This encompasses the maximum heat

transfer rate which can be achieved with changes in both angle and temperature of the heat pipe.

The conclusion of this study brought forward two fluids which were of main interest to the UKAEA. To further analyse the use of these fluids with a Tungsten heat pipe body, an FEA study was conducted on the heat pipe structure operating at the maximum allowable temperature to determine the maximum von mises stress experienced.

8.6 Chapter Summary

This chapter has explored some of the methods which could be applied to future work to manufacture and develop medium temperature heat pipes. The attempts at manufacturing these using conventional techniques available at Aavid Thermacore have been highlighted and the end results confirm that more specialised techniques are required. This chapter has also highlighted the use of the ‘fluid assessment framework’ in industry by presenting a real case study where the framework and modelling was used with great success.

Chapter IX

Conclusions and Recommendations

9.1 Conclusions

This thesis has set out to build a framework by which medium temperature heat pipe fluids can be further explored. Throughout this project, modelling and experimental techniques have been developed not only to provide the necessary equipment and tools to accelerate the development of medium temperature heat pipes in future, but to provide commercial value to the project as these are tools and techniques which can be used to verify the use of heat pipes in commercial systems.

9.1.1 Summary of thesis

A summary of the key conclusion from the overall thesis follows:

- An analysis of 350 inorganic fluids concluded that Antimony Trichloride and Bismuth Trichloride are the highest ranking current medium temperature fluids when considering cost and ease of handling. Other fluids of interest are Ruthenium Pentafluoride, Rhenium Heptoxide and Rhenium Heptafluoride which have the greatest thermal transport capacity in the medium temperature range, but are very rare and expensive fluids – hence these should be studied in a specialised and specifically funded programmes.
- Electromotive force difference modelling indicates that refractory metals are the most likely compatible metals with Antimony Trichloride. It also indicates that commonly available metals and alloys such as

Stainless Steel are highly incompatible. This has been validated through short term compatibility testing.

- Wettability tests indicate that some refractory metals may have favourable wettability with water compared with conventional metals. Preliminary tests using novel wettability measuring techniques for air sensitive fluids indicate that Antimony Trichloride has excellent wettability with Molybdenum, Tungsten and TZM.
- Experimental results for high temperature water heat pipes have validated the predicted Boiling limit using the Ivanovskii et al [8] equation.
- The thermal resistance model has not provided accurate temperature difference predictions compared to experimental values. This model must be further development to enable accurate prediction of the heat pipe effective conductivity.
- The fluid selection process developed has successfully identified both ideal fluids to take forward in the medium temperature range as well as alternative fluids in other temperature ranges with higher cost-effectiveness to apply in commercial applications.

9.1.2 Originality and contributions

1. Develop a new, more accessible and more extensive databases of fluid properties, metal properties and fluid/metal compatibilities.
 - A database of 350 inorganic fluids has been created with the pending addition of 1000 organic fluids
 - A metal property database was created with the identified metals
 - A comprehensive database of all previous fluid/metal compatibility tests has been successfully created
 - The databases are able to interact seamlessly with MATLAB code and a variety of analytical programmes have been developed to study the database
2. Develop a new heat pipe modelling code which can easily incorporate the databases.
 - A MATLAB heat pipe modelling code was developed using one dimensional analysis of heat pipe limitations
 - The MATLAB code call and model any fluid or metal from the databases – this will be continually updated to provide even better user experience and further modelling capability in future
3. Develop a framework by which fluids can be rapidly identified and selected for testing.
 - A comprehensive fluid selection framework has been developed and proven through academic and commercial application

- The framework has successfully identified and empirically justified two key fluids, Antimony Trichloride and Bismuth Trichloride, which are the best candidates to move forward with out of currently available fluids
4. Perform extensive metal search and compatibility modelling to select likely compatible metals.
 - An extensive metal database search was performed, and key metal groups identified
 - Compatibility modelling techniques were used to determine the most likely compatible metals to take forward to treating. Refractory metals were identified as highly compatible metals, in particular Molybdenum and its alloys
 5. Develop methods and test rigs to perform compatibility tests and wettability tests on the selected fluids and metals.
 - The compatibility of Antimony Trichloride with various selected metals has been tested and verified using a test process developed for air sensitive fluids
 - The wettability of Antimony Trichloride with various selected metals has been tested and verified using a test process developed for air sensitive fluids
 6. Develop a test rig which can support heat pipe testing in the medium temperature range.
 - A medium temperature heat pipe test rig was successfully developed, and each component optimised as much as possible
 7. Validate the test rig at the lower end of the medium temperature range using water heat pipes.

- Water heat pipes have been extensively analysed over their boiling limit and have validated the functionality of the medium temperature test rig
- Novel research establishing the boiling limit boundary and quantifying the heat pipe performance at that boundary has been published through this research

9.2 Recommendations and future work

While this work has progressed research for medium temperature heat pipe development, there is still much further work to be done. This includes:

1. Compatibility and wettability testing
 - Further testing is needed on the wettability of Antimony Trichloride with all refractory metal samples using the developed methods
 - Once adequate results for Antimony Trichloride are achieved, progress to testing with Bismuth Trichloride
 - Short term compatibility tests are needed with Bismuth Trichloride using the developed methods
 - Once the development of a prototype is possible, long term compatibility tests must be carried out using the developed long-term compatibility test rig
2. Medium temperature test rig
 - The development of a gas gap condenser may be beneficial to test at higher temperatures
 - If possible to conduct tests in vacuum, this would be highly advisable to reduce heat losses
3. Modelling and databases
 - Continual improvements to MATLAB model are always possible aimed at reducing running time, improving user experience and incorporating new features such as predicting the performance of bent pipes

- Continual improvement to databases by adding as many fluids and metals as possible would increase the capability of the fluid selection framework and modelling code
- Development of an improved or alternative version of the thermal resistance network to predict the heat pipe temperature difference would be advisable
- Development of CFD modelling which is capable of predicting the boiling limit

4. Water heat pipe testing

- Further testing at lower temperatures to identify the capillary limit point experimentally would be of interest
- Testing the performance of the heat pipe at various inclinations would be of interest

5. Prototype development

- Study joining techniques to join refractory metals
- Develop a filling rig for air sensitive fluids
- Create thermocypions for compatibility analysis
- Develop adequate wick structures
- Create a medium temperature heat pipe for thermal transport performance testing

6. Medium temperature fluid development

- Perform analysis on other shortlisted fluids such as Rhenium Heptoxide and Ruthenium Pentafluoride which offer excellent heat transport in intermediate temperature range but at a higher capital cost

- Perform fluid property testing on fluids which are missing fluid property data
- Develop new potential medium temperature fluids using conventional or azeotropic mixtures and determine their fluid properties through experimentation

References

- [1] D. Reay and P. Kew, *Heat Pipes theory and design*. 2006.
- [2] R. S. Gaugler, “Heat transfer device,” 1944.
- [3] G. M. Grover, “Evaporation- Condensation Heat Transfer Device,” 1966.
- [4] T. Cotter, “Theory of heat pipes,” 1965. [Online]. Available: <https://www.osti.gov/scitech/servlets/purl/4619147>.
- [5] F. Dobran, “Heat pipe research and development in the Americas,” *Heat Recover. Syst. CHP*, vol. 9, no. 1, pp. 67–100, 1989, doi: 10.1016/0890-4332(89)90140-3.
- [6] M. Groll, “Heat pipe research and development in western Europe,” *Heat Recover. Syst. CHP*, vol. 9, no. 1, pp. 19–66, 1989, doi: [http://dx.doi.org/10.1016/0890-4332\(89\)90139-7](http://dx.doi.org/10.1016/0890-4332(89)90139-7).
- [7] F. Polášek, “Heat pipe research and development in east european countries,” *Heat Recover. Syst. CHP*, vol. 9, no. 1, pp. 3–17, 1989, doi: [http://dx.doi.org/10.1016/0890-4332\(89\)90138-5](http://dx.doi.org/10.1016/0890-4332(89)90138-5).
- [8] M. N. Ivanovski, V. P. Sorokin, and I. V Yagodkin, *Physical principles of heat pipes* . 1982.
- [9] A. Faghri, “Review and advances in heat pipe science and technology,” *J. Heat Transfer*, vol. 134, no. 12, pp. 1–18, 2012, doi: 10.1115/1.4007407.
- [10] W. G. Anderson, P. M. Dussinger, and D. Sarraf, “High temperature water heat pipe life tests,” *AIP Conf. Proc.*, vol. 813, pp. 100–107, 2006, doi:

10.1063/1.2169185.

- [11] A. Faghri, *Heat pipe science and technology*. Taylor & Francis, 1995.
- [12] C. A. Bankston and J. H. Smith, “Incompressible laminar vapour flow in cylindrical heat pipes,” *ASME*, 1971.
- [13] A. R. Rohani and C. L. Tien, “Analysis of the effects of vapour pressure drop on heat pipe performance,” *Int. J. Heat Mass Transf.*, vol. 17, pp. 61–67, 1974.
- [14] C. A. Busse, “Pressure Drop in Vapor Phase of Long Heat Pipes,” 1967.
- [15] J. E. Deverall, J. E. Kemme, and L. W. Flarschuetz, “Sonic Limits & Startup Problems of heat pipes,” 1970.
- [16] J. E. Kemme, “Ultimate Heat Pipe Performance,” in *IEEE Transactions on Electron Devices*, 1968, pp. 717–723.
- [17] F. C. Blake, “F. C. Blake,” *Trans. Amer. Inst. Chem. Engrs.*, no. 14, pp. 415–421, 1922.
- [18] G. M. Grover, J. E. Kemme, and E. S. Keddy, “Advance in heat pipe technology.”
- [19] D. Chimcholm, J. B. Googacre, G. Rattcliff, D. A. Reay, and G. Rice, “Heat pipes - properties of common small-pore wicks,” *ESDU 79013*, no. November, 1979.
- [20] S. W. Chi, “Heat Pipe Theory and Practice.” 1976.
- [21] D. Chisholm, *The heat pipe*. Mills and Boon, 1971.
- [22] B. Fadhl, L. C. Wrobel, and H. Jouhara, “Numerical modelling of the temperature distribution in a two-phase closed thermosyphon,” *Appl. Therm.*

- Eng.*, vol. 60, no. 1–2, pp. 122–131, 2013, doi:
10.1016/j.applthermaleng.2013.06.044.
- [23] B. Fadhl, L. C. Wrobel, and H. Jouhara, “CFD modelling of a two-phase closed thermosyphon charged with R134a and R404a,” *Appl. Therm. Eng.*, vol. 78, pp. 482–490, 2015, doi: 10.1016/j.applthermaleng.2014.12.062.
- [24] M. Arab and A. Abbas, “A model-based approach for analysis of working fluids in heat pipes,” *Appl. Therm. Eng.*, vol. 73, no. 1, pp. 751–763, 2014, doi: 10.1016/j.applthermaleng.2014.08.001.
- [25] Z. J. Zuo and A. Faghri, “A network thermodynamic analysis of the heat pipe,” *Int. J. Heat Mass Transf.*, vol. 41, no. 11, pp. 1473–1484, 1998, doi: 10.1016/S0017-9310(97)00220-2.
- [26] P. J. Marto and L. V. J. Lepere, “Pool boiling heat transfer from enhanced surfaces to dielectric fluids,” *J. Heat Transfer*, vol. 104, no. 2, pp. 292–299, 1982, doi: 10.1115/1.3245086.
- [27] D. Bachurina *et al.*, “Joining of tungsten with low-activation ferritic–martensitic steel and vanadium alloys for demo reactor,” *Nucl. Mater. Energy*, vol. 15, no. November 2017, pp. 135–142, 2018, doi: 10.1016/j.nme.2018.03.010.
- [28] S. Khandekar, Y. M. Joshi, and B. Mehta, “Thermal performance of closed two-phase thermosyphon using nanofluids,” *Int. J. Therm. Sci.*, vol. 47, no. 6, pp. 659–667, 2008, doi: 10.1016/j.ijthermalsci.2007.06.005.
- [29] S. Khandekar, P. Charoensawan, M. Groll, and P. Terdtoon, “Closed loop pulsating heat pipes - Part B: Visualization and semi-empirical modeling,”

- Applied Thermal Engineering*, vol. 23, no. 16. pp. 2021–2033, 2003, doi:
10.1016/S1359-4311(03)00168-6.
- [30] W. M. Rohsenow and P. Griffith, “Correlation of maximum heat flux data for boiling of saturated liquids,” *Tech. Rep. no. 6, MIT Cambridge*, 1955.
- [31] J. FERRELL, E. ALEXANDER, and W. PIVER, “Vaporization heat transfer in heat pipe wick materials,” in *7th Thermophysics Conference*, American Institute of Aeronautics and Astronautics, 1972.
- [32] S. W. Chi, *Heat Pipe Theory and Applications*. 1976.
- [33] P. Griffith and J. D. Wallis, “The role of surface conditions in nucleate boiling,” *Chem. Eng. Prog., Symp. Ser.*, vol. 56, no. 30, pp. 49–63, 1960, doi:
10.1063/1.3013567.
- [34] D. B. Marcus, “Theory and design of variable conductance heat pipes,” *J. Chem. Inf. Model.*, vol. 53, no. 9, pp. 1689–1699, 1972, doi:
10.1017/CBO9781107415324.004.
- [35] E. K. Levy, “Theoretical investigation of heat pipes operating at low vapor pressures,” *J. Manuf. Sci. Eng. Trans. ASME*, vol. 90, no. 4, pp. 547–552, 1968, doi: 10.1115/1.3604687.
- [36] C. A. Busse, “Theory of the ultimate heat transfer limit of cylindrical heat pipes,” *Int. J. Heat Mass Transf.*, vol. 16, no. 1, pp. 169–186, 1973, doi:
10.1016/0017-9310(73)90260-3.
- [37] F. C. Prenger, F. S. Walter, and J. E. Runyan, “Development of Cryogenic heat pipe,” *Los Alamos Natl. Lab.*, 1993, doi: 10.1115/1.3445564.
- [38] M. Ishii and M. A. Grolmes, “Inception criteria for droplet entrainment in two-

- phase concurrent film flow,” *AIChE J.*, vol. 21, no. 2, pp. 308–318, 1975, doi: 10.1002/aic.690210212.
- [39] I. Kataoka, K. Mishima, and M. Ishii, “Generation and size distribution of droplet in annular two-phase flow.,” vol. 105, no. 83, 1983.
- [40] B. KIM, G. PETERSON, and K. KIHM, “Experimental investigation of entrainment in heat pipe wicking structures,” 1993, doi: 10.2514/6.1993-281.
- [41] D. D. Kenney and J. Feldman, K. T., “Heat pipe life tests at temperatures up to 400 C,” 1978.
- [42] D. B. Sarraf and W. G. Anderson, “High-temperature water heat pipes,” *Proc. - 2006 IMAPS Int. Conf. Exhib. High Temp. Electron. HiTEC 2006*, no. December, pp. 549–556, 2006.
- [43] W. G. Anderson, R. W. Bonner, P. M. Dussinger, J. R. Hartenstine, D. B. Sarraf, and I. E. Locci, “Intermediate temperature fluids life tests - Experiments,” *5th Int. Energy Convers. Eng. Conf.*, vol. 2, no. June, pp. 926–941, 2007, doi: 10.2514/6.2007-4808.
- [44] R. Hay and W. G. Anderson, “Water-titanium heat pipes for spacecraft fission power,” *13th Int. Energy Convers. Eng. Conf.*, pp. 1–12, 2015.
- [45] J. H. Rosenfeld, G. Y. Eastman, and J. E. Lindemuth, “Sulfur heat pipes for 600 K space heat rejection systems,” *AIP Conf. Proc.*, vol. 1170, no. 1992, pp. 1170–1176, 1992, doi: 10.1063/1.41780.
- [46] L. R. Grzyll, D. D. Back, C. Ramos, and N. A. Samad, “Characterization and testing of novel two-phase working fluids for spacecraft thermal management systems operating between 300°C and 400°C,” 1994.

- [47] E. W. Saaski and P. C. Owzarski, "Two-Phase Working Fluids for the Temperature Range 50° to 350°C," *Heat Transf. Therm. Control Syst.*, pp. 63–79, 1978, doi: 10.2514/5.9781600865343.0063.0079.
- [48] E. W. Saaski, "Two Phase working fluids for the temperature range 100°C to 350°C."
- [49] E. W. Saaski and J. H. Hartl, "Two-Phase Working Fluids for the Temperature Range 50° to 350°C - Phase II," *NASA Lewis Res. Cent.*, vol. 2, 1980.
- [50] L. R. Grzyll, "Investigation of heat pipe working fluids for thermal control of the sodium/sulfur battery," in *Proceedings of the Intersociety Energy Conversion Engineering Conference*, 1991, vol. 3, pp. 390–394.
- [51] I. B. Johns, E. A. McElkill, and J. O. Smith, "Thermal Stability of organic compounds," *Clay-Containing Polym. Nanocomposites*, no. 44, pp. 243–261, 1962, doi: 10.1016/b978-0-444-59437-2.00007-7.
- [52] S. Benson and W. Sidney, *The Foundations of Chemical Kinetics*. Division of Chemical Education, 1960.
- [53] K. U. Ingold, "Peroxy Radicals," *Acc. Chem. Res.*, vol. 2, no. 1, pp. 1–9, 1969, doi: 10.1021/ar50013a001.
- [54] D. R. Miller and K. F. Barber, "Working Fluids for Automotive Rankine Engines." .
- [55] W. G. Anderson, S. Tamanna, C. Tarau, J. R. Hartenstine, and D. L. Ellis, "Intermediate temperature heat pipe life tests and analyses," *43rd Int. Conf. Environ. Syst.*, pp. 1–23, 2013.
- [56] W. G. Anderson, "Intermediate temperature fluids for heat pipes and loop heat

- pipes,” *Collect. Tech. Pap. - 5th Int. Energy Convers. Eng. Conf.*, vol. 2, no. June, pp. 1147–1164, 2007.
- [57] C. Tarau, D. B. Sarraf, I. E. Locci, and W. G. Anderson, “Intermediate temperature fluids life tests - Theory,” *AIP Conf. Proc.*, vol. 880, no. May 2017, pp. 137–146, 2007, doi: 10.1063/1.2437450.
- [58] A. Devarakonda, D. Xiong, and D. E. Beach, “Intermediate temperature water heat pipe tests,” *AIP Conf. Proc.*, vol. 746, no. March 2005, pp. 158–163, 2005, doi: 10.1063/1.1867130.
- [59] L. L. Vasil’ev, G. M. Volokhov, A. S. Gigevich, and M. I. Rabetskii, “Heat pipes based on naphthalene,” *J. Eng. Phys.*, vol. 54, no. 6, pp. 623–626, 1988, doi: 10.1007/BF01102648.
- [60] K. P. Min and H. B. Joon, “Thermal Performance of a Heat Pipe for Medium-Temperature thermal Storage System,” *10th Int. Heat Pipe Symp.*, pp. 13–18, 2011.
- [61] D. D. Kenney and J. Feldman, K. T., “Heat pipe life tests at temperatures up to 400 C,” *13th Intersociety Energy Conversion Engineering Conference*. 1978.
- [62] T. Yamamoto, K. Nagata, M. Katsuta, and Y. Ikeda, “Experimental study of mercury heat pipe,” *Exp. Therm. Fluid Sci.*, vol. 9, no. 1, pp. 39–46, 1994, doi: [http://dx.doi.org/10.1016/0894-1777\(94\)90006-X](http://dx.doi.org/10.1016/0894-1777(94)90006-X).
- [63] W. G. Anderson, “Evaluation of Heat Pipe Working Fluids In The Temperature Range 450 to 700 K,” *AIP Conf. Proc.*, vol. 20, no. 2004, pp. 20–27, 2004, doi: 10.1063/1.1649553.
- [64] P. M. Dussinger, W. G. Anderson, and E. T. Sunada, “Design and testing of

- titanium/cesium and titanium/potassium heat pipes,” *Collect. Tech. Pap. - 3rd Int. Energy Convers. Eng. Conf.*, vol. 2, pp. 1088–1096, 2005.
- [65] M. S. El-Genk and J.-M. P. Tournier, “Uses of Liquid-Metal and Water Heat Pipes in Space Reactor Power Systems,” *Front. Heat Pipes*, vol. 2, no. 1, 2011, doi: 10.5098/fhp.v2.1.3002.
- [66] J. T. Sena and M. A. Merrigan, “Niobium-1% Zirconium/Potassium life-test heat pipe design and testing,” *28th Aerosp. Sci. Meet.*, 1990.
- [67] J. Tom Sena and M. A. Merrigan, “Niobium-1% zirconium/potassium and Titanium/Potassium life-test heat pipe design and testing,” *28th Aerosp. Sci. Meet. 1990*, 1990.
- [68] R. S. Reid, M. A. Merrigan, and J. T. Sena, “Review of liquid metal heat pipe work at Los Alamos,” *AIP Conf. Proc.*, vol. 999, no. May, pp. 999–1008, 1991, doi: 10.1063/1.40058.
- [69] I. E. Locci, A. Devarakonda, E. H. Copland, and J. K. Olminky, “Analytical and experimental thermo-chemical compatibility study of potential heat pipe materials,” *Collect. Tech. Pap. - 3rd Int. Energy Convers. Eng. Conf.*, vol. 2, no. August, pp. 1285–1292, 2005, doi: 10.2514/6.2005-5666.
- [70] A. Akbari and M. H. Saidi, “Experimental investigation of nanofluid stability on thermal performance and flow regimes in pulsating heat pipe,” *J. Therm. Anal. Calorim.*, vol. 135, no. 3, pp. 1835–1847, 2019, doi: 10.1007/s10973-018-7388-3.
- [71] Z. hua Liu, J. guo Xiong, and R. Bao, “Boiling heat transfer characteristics of nanofluids in a flat heat pipe evaporator with micro-grooved heating surface,”

- International Journal of Multiphase Flow*, vol. 33, no. 12. pp. 1284–1295, 2007, doi: 10.1016/j.ijmultiphaseflow.2007.06.009.
- [72] W. S. Han and S. H. Rhi, “Thermal characteristics of grooved heat pipe with hybrid nanofluids,” *Therm. Sci.*, vol. 15, no. 1, pp. 195–206, 2011, doi: 10.2298/TSCI100209056H.
- [73] J. Qu, H. ying Wu, and P. Cheng, “Thermal performance of an oscillating heat pipe with Al₂O₃-water nanofluids,” *Int. Commun. Heat Mass Transf.*, vol. 37, no. 2, pp. 111–115, 2010, doi: 10.1016/j.icheatmasstransfer.2009.10.001.
- [74] M. Ghanbarpour, “Investigation of Thermal Performance of Cylindrical Heat pipes Operated with Nanofluids.” 2017.
- [75] J. H. Jang, “Study of Startup Characteristics of Potassium Heat Pipe from Frozen State.” 1992.
- [76] R. S. Reid, J. T. Sena, and A. L. Martinez, “Heat-Pipe Development for Advanced Energy Transport Concepts Final Report Covering the Period,” *Los Alamos Natl. Lab*, no. September, 2001.
- [77] W. W. Wits and G. J. te Riele, “Modelling and performance of heat pipes with long evaporator sections,” *Heat Mass Transf. und Stoffuebertragung*, vol. 53, no. 11, pp. 3341–3351, 2017, doi: 10.1007/s00231-017-2040-5.
- [78] S. T. Tu, H. Zhang, and W. W. Zhou, “Corrosion failures of high temperature heat pipes,” *Eng. Fail. Anal.*, vol. 6, no. 6, pp. 363–370, 1999, doi: 10.1016/S1350-6307(98)00057-0.
- [79] X. Meng *et al.*, “Compatibility of Molybdenum, Tungsten, and 304 Stainless Steel in Static Liquid Lithium Under High Vacuum,” *Plasma Phys. Reports*,

vol. 44, no. 7, pp. 671–677, 2018, doi: 10.1134/S1063780X18070036.

- [80] J. H. Rosenfeld and N. J. Gernert, “Life test results for water heat pipes operating at 200 °C to 300 °C,” *AIP Conference Proceedings*, vol. 969, pp. 123–130, 2008, doi: 10.1063/1.2844957.
- [81] A. Basiulis and M. Filler, “Operating Characteristics and Long Life Capabilities of Organic Fluid Heat Pipes,” vol. 29, pp. 431–444, 1972.
- [82] M. Ghanbarpour, N. Nikkam, R. Khodabandeh, M. S. Toprak, and M. Muhammed, “Thermal performance of screen mesh heat pipe with Al₂O₃ nanofluid,” pp. 213–220, 2015.
- [83] W. G. Anderson, D. B. Sarraf, S. D. Garner, and J. Barth, “High temperature titanium-water heat pipe radiator,” *AIP Conf. Proc.*, vol. 813, no. August 2015, pp. 91–99, 2006, doi: 10.1063/1.2169184.
- [84] J. H. Rosenfeld, I. E. Locci, J. L. Sanzi, D. R. Hull, and S. M. Geng, “Post-Test Analysis of a 10-Year Sodium Heat Pipe Life Test,” no. December 2011, 2011.
- [85] J. E. Deverall and J. E. Kemme, “High thermal conductance devices - Boiling Li or Ag.” 1965.
- [86] W. G. Anderson, R. Bonner, J. Hartenstine, and J. Barth, “High temperature titanium - water heat pipe radiator.” .
- [87] J. H. Rosenfeld, B. L. Drolen, and C. Y. Lu, “Design, fabrication, and testing of high capacity high-temperature monel/water heat pipes,” *AIP Conf. Proc.*, vol. 813, pp. 117–125, 2006, doi: 10.1063/1.2169187.
- [88] D. A. Jaworske, J. L. Sanzi, M. A. Gibson, and E. A. Sechkar, “Thermal interface evaluation of heat transfer from a pumped loop to titanium-water

- thermosyphons,” *7th Int. Energy Convers. Eng. Conf.*, 2009, doi: 10.2514/6.2009-4532.
- [89] J. J. Martin and R. S. Reid, “Methodology for Life Testing of Refractory Metal-Sodium Heat Pipes.pdf.” 2006.
- [90] X. Yang, “The Investigations of Lightweight Heat Pipes - Fundamental Studies on Magnesium Alloy Heat Pipes,” no. June, 2011.
- [91] Hideo Nakae, Ryuichi Inui, Yosuke Hirata, and Hiroyuki Saito, “Effects of surface roughness on wettability,” *Acta Mater.*, vol. 46, no. 7, pp. 2313–2318, 1998, doi: 10.1016/s1359-6454(98)80012-8.
- [92] K. T. Hong, H. Imadojemu, and R. L. Webb, “Effects of oxidation and surface roughness on contact angle,” *Exp. Therm. Fluid Sci.*, vol. 8, no. 4, pp. 279–285, 1994, doi: 10.1016/0894-1777(94)90058-2.
- [93] B. J. Ryan and K. M. Poduska, “Roughness effects on contact angle measurements,” *Am. J. Phys.*, vol. 76, no. 11, pp. 1074–1077, 2008, doi: 10.1119/1.2952446.
- [94] A. Toloei and V. Stoilov, “The relationship between surface roughness and corrosion,” 2016, pp. 1–10.
- [95] G. Launay, “PyDSA_core: Drop shape analysis in Python.” 2018, [Online]. Available: https://framagit.org/gabylaunay/pyDSA_core.
- [96] ASTM-E220, “Calibration of Thermocouples By Comparison Techniques,” pp. 1–16, 2013, doi: 10.1520/E0220-13.2.
- [97] J. R. Taylor, *An introduction to error analysis*. University Science Books, 1997.

- [98] W. G. Anderson, "Evaluation of heat pipes in the temperature range of 450 to 700 K," *AIP Conf. Proc.*, vol. 746, pp. 171–178, 2005, doi: 10.1063/1.1867132.
- [99] W. G. Anderson and T. Stern, "Water heat pipe radiator trade study for the 300-550 K temperature range," *AIP Conf. Proc.*, vol. 746, pp. 187–194, 2005, doi: 10.1063/1.1867134.
- [100] D. B. Sarraf and W. G. Anderson, "Heat pipe for high temperature thermal management," in *2007 Proceedings of the ASME InterPack Conference, IPACK 2007*, 2007, vol. 1, pp. 707–714, doi: 10.1115/IPACK2007-33984.
- [101] C. L. Yaws, *Chemical Properties Handbook*. The McGraw-Hill Companies, Inc, 1999.
- [102] Dechema, "Detherm." <https://dechema.de/en/detherm.html>.
- [103] NIST, "REFPROP." <https://www.nist.gov/srd/refprop>.
- [104] Coolprop, "Coolprop." <http://www.coolprop.org/>.
- [105] CDS, "National Chemical Database Service."
<https://www.rsc.org/NCD/denial.asp?path=http://detherm.cds.rsc.org/detherm/mixture.php>.
- [106] W. G. Anderson, S. Tamanna, C. Tarau, J. R. Hartenstine, and D. L. Ellis, "Intermediate temperature heat pipe life tests and analyses," *43rd Int. Conf. Environ. Syst.*, pp. 1–23, 2013.
- [107] R. R. Williams and D. K. Harris, "A device and technique to measure the heat transfer limit of a planar heat pipe wick," *Exp. Therm. Fluid Sci.*, vol. 30, no. 3, pp. 277–284, 2006, doi: 10.1016/j.expthermflusci.2005.07.008.

- [108] B. F. Casswell and R. E. Balzheiser, “The critical heat flux for boiling metal systems,” in *Chemical Engineering Progress Symposium Series of Heat Transfer*, 1966, p. 64.
- [109] J. Wang and I. Catton, “Enhanced evaporation heat transfer in triangular grooves covered with a thin fine porous layer,” *Applied Thermal Engineering*, vol. 21, no. 17, pp. 1721–1737, 2001, doi: 10.1016/S1359-4311(01)00044-8.
- [110] “Innova Microsolar Project.” <http://innova-microsolar.eu/>.
- [111] J. J. Martin, R. S. Reid, E. T. Stewart, and J. D. Davis, *Design of Refractory Metal Heat Pipe Life Test Environment Chamber , Cooling System , and Radio Frequency Heating System*, no. February 2011. 2019.
- [112] T. D. Eastop and A. McConkey, *Applied Thermodynamics for Engineering Technologists*, 5th ed. Pearson Prentice Hall.
- [113] M. Furukawa, “Empirical expressions selected as a common basis of heat-transfer and pressure drop calculations,” *Trans. Jpn. Soc. Aeronaut. Space Sci.*, vol. 36, no. 113, pp. 188–208, 1993.
- [114] A. Bejan and A. D. Kraus, *Heat Transfer Handbook, Volume 1*. 2003.
- [115] “TC Direct.” <https://www.tcdirect.co.uk/>.
- [116] “Picotechnology: Picologger TC-08.” <https://www.picotech.com/data-logger/tc-08/thermocouple-data-logger>.
- [117] B. D. Iverson, T. W. Davis, S. V. Garimella, M. T. North, and S. S. Kang, “Heat and mass transport in heat pipe wick structures,” *J. Thermophys. Heat Transf.*, vol. 21, no. 2, pp. 392–404, 2007, doi: 10.2514/1.25809.

- [118] “Citrix Database.” <https://docs.citrix.com/en-us/xenapp-and-xendesktop/7-15-ltsr/technical-overview/databases.html>.
- [119] W. M. Haynes, “Handbok of Chemistry and Physics. 99th Edition.,” *CRC Handb. Chem. physics, 98th Ed.*, vol. 94, pp. 4.43-4.101, 2018, [Online]. Available: <http://scholar.google.com/scholar?hl=en&btnG=Search&q=intitle:Magnetic+Susceptibility+of+the+Elements+and+Inorganic+Compounds#0>.
- [120] J. M. Ochterbeck, “Heat Pipes,” *NASA Contract. Reports*, pp. 1181–1230, 1975.
- [121] A. Marmur, “Solid-surface characterization by wetting,” *Annu. Rev. Mater. Res.*, vol. 39, pp. 473–489, 2009, doi: 10.1146/annurev.matsci.38.060407.132425.
- [122] T. Young, “An essay on the cohesion of fluids,” *Philos. Trans. R. Soc. London. B, Biol. Sci.*, vol. 303, no. 1113, pp. 1–62, 1983, doi: 10.1098/rstb.1983.0080.
- [123] H. Yildirim Erbil, G. McHale, S. M. Rowan, and M. I. Newton, “Determination of the receding contact angle of sessile drops on polymer surfaces by evaporation,” *Langmuir*, vol. 15, no. 21, pp. 7378–7385, 1999, doi: 10.1021/la9900831.
- [124] G. F. Hewitt, G. L. Shires, and T. R. Bott, *Process heat transfer*. 1994.
- [125] “BS EN 828 Adhesives - Wettability - Determination by measurement of contact angle and surface free energy of solid surface,” 2013.
- [126] Y. Zhu, R. Wang, and Y. Zhang, “Modeling and optimization of isolated heat pipe heat exchange system based on Matlab,” *2010 IEEE Int. Conf. Autom.*

- Logist. ICAL 2010*, pp. 211–215, 2010, doi: 10.1109/ICAL.2010.5585281.
- [127] G. Bracco and B. Holst, *Surface science techniques*, vol. 51, no. 1. 2013.
- [128] J. H. Rosenfeld and N. J. Gernert, “Advances in high temperature titanium-water heat pipe technology,” *AIP Conf. Proc.*, vol. 880, pp. 129–136, 2007, doi: 10.1063/1.2437449.
- [129] A. Devarakonda and W. G. Anderson, “Thermo-physical properties of intermediate temperature heat pipe fluids,” *AIP Conf. Proc.*, vol. 746, no. February 2005, pp. 179–186, 2005, doi: 10.1063/1.1867133.
- [130] A. Devarakonda and J. K. Olminsky, “An evaluation of halides and other substances as potential heat pipe fluids,” *Collection of Technical Papers - 2nd International Energy Conversion Engineering Conference*, vol. 1. pp. 471–477, 2004.
- [131] Smiths Metals, “Monel® Alloy 400.”
- [132] Smiths Metals, “Monel® Alloy k500.”
- [133] Smiths Metals, “Oxygen-free Copper Cu-OF.”
- [134] Smiths Metals, “Copper-Nickel 90/10 and 70/30 Alloys Technical Data.”
- [135] Smiths Metals, “Titanium Alloy Data Sheet.”
- [136] M. Cavazzuti, “Optimization methods: From theory to design scientific and technological aspects in mechanics.” pp. 1–262, 2013, doi: 10.1007/978-3-642-31187-1.
- [137] E. E. Levi, “Refractory metals.” <https://www.welding-advisers.com/Refractory-metals.html#:~:text=Niobium%2C tantalum%2C and>

their alloys,when welding tungsten and molybdenum.

[138] N. E. Weare and R. E. Monroe, “Welding and brazing of molybdenum.”

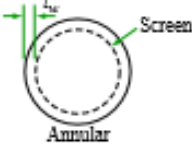
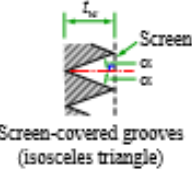
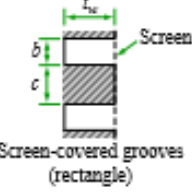
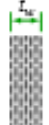
[139] G. F. Matthews *et al.*, “Testing of a high temperature radiatively cooled Li/Ta heat pipe in Magnum-PSI,” *Fusion Eng. Des.*, 2019, doi: 10.1016/j.fusengdes.2018.12.096.

Appendix A Compatibility and Wettability
test sample log table

Sample Table

Status	Name	Date rece	Size	Polished?	Weight (g)	Roughness	Microscope	Reacted With	Low temp tested?	Microscope	SEM	Post low?	Re-Roughness tested?
✓	Mo1	1-Jan	15x15	P240	26.6100	0.37	11-Sep	SbCl3	✓	✓	✓	✓	✓
✓	Mo2	1-Jan	15x15	P240	26.6900	0.16	11-Sep	N/A	N/A	N/A	N/A	N/A	N/A
✓	Mo3	1-Jan	15x15	P1200	26.7300	0.06	12-Sep	N/A	N/A	N/A	N/A	N/A	N/A
✓	Mo4	1-Jan	15x15	P1200	26.7400	0.12	11-Sep	N/A	N/A	N/A	N/A	N/A	N/A
-	Mo4	1-Jan	15x15	P1200	-	-	-	N/A	N/A	N/A	N/A	N/A	N/A
✓	TZM1	1-Jan	15x15	P240	26.7700	0.19	11-Sep	SbCl3	✓	✓	✓	✓	✓
✓	TZM2	1-Jan	15x15	P240	26.7100	0.23	12-Sep	N/A	N/A	N/A	N/A	N/A	N/A
✓	TZM3	1-Jan	15x15	P1200	26.6000	0.06	12-Sep	N/A	N/A	N/A	N/A	N/A	N/A
✓	TZM4	1-Jan	15x15	P1200	26.8100	0.06	11-Sep	N/A	N/A	N/A	N/A	N/A	N/A
-	TZM4	1-Jan	15x15	P1200	-	-	-	N/A	N/A	N/A	N/A	N/A	N/A
✓	W1	27-Feb	15x15	P240	50.8800	0.29	11-Sep	SbCl3	✓	✓	✓	✓	✓
✓	W2	27-Feb	15x15	P240	50.8100	0.37	12-Sep	N/A	N/A	N/A	N/A	N/A	N/A
✓	W3	27-Feb	15x15	P1200	50.7200	0.06	12-Sep	N/A	N/A	N/A	N/A	N/A	N/A
-	W4	27-Feb	15x15	P1200	50.8300	-	-	N/A	N/A	N/A	N/A	N/A	N/A
-	W4	27-Feb	15x15	P1200	-	-	-	N/A	N/A	N/A	N/A	N/A	N/A
✓	CuNi1	7-Jun	12.7x15	P240	16.6800	0.23	11-Sep	SbCl3	✓	✓	✓	✓	✓
✓	CuNi2	7-Jun	12.7x15	P240	16.6900	0.23	12-Sep	N/A	N/A	N/A	N/A	N/A	N/A
✓	CuNi3	7-Jun	12.7x15	P1200	16.8000	0.06	12-Sep	N/A	N/A	N/A	N/A	N/A	N/A
-	CuNi4	7-Jun	12.7x15	P1200	16.9600	-	-	N/A	N/A	N/A	N/A	N/A	N/A
-	CuNi4	7-Jun	12.7x15	P1200	-	-	-	N/A	N/A	N/A	N/A	N/A	N/A
✓	316SS1	24-Jul	15.875x15	P240	23.4400	0.11	11-Sep	SbCl3	✓	✓	✓	✓	✓
✓	316SS2	24-Jul	15.875x15	P240	23.2600	0.07	12-Sep	N/A	N/A	N/A	N/A	N/A	N/A
✓	316SS3	24-Jul	15.875x15	P1200	23.6400	0.04	12-Sep	N/A	N/A	N/A	N/A	N/A	N/A
-	316SS4	24-Jul	15.875x15	P1200	23.4900	-	-	N/A	N/A	N/A	N/A	N/A	N/A
-	316SS4	24-Jul	15.875x15	P1200	-	-	-	N/A	N/A	N/A	N/A	N/A	N/A
✓	304SS1	24-Jul	15x15	P240	20.9400	0.10	11-Sep	SbCl3	✓	✓	✓	✓	✓
✓	304SS2	24-Jul	15x15	P240	20.9600	0.11	12-Sep	GaCl3					
✓	304SS3	24-Jul	15x15	P1200	20.9800	0.04	12-Sep	N/A	N/A	N/A	N/A	N/A	N/A
-	304SS4	24-Jul	15x15	P1200	20.8700	-	-	N/A	N/A	N/A	N/A	N/A	N/A
-	304SS4	24-Jul	15x15	P1200	-	-	-	N/A	N/A	N/A	N/A	N/A	N/A
✓	Ta1	27-Feb	15x15	P240	43.3300	0.41	12-Sep	SbCl3	✓	✓	✓	✓	✓
✓	Ta2	27-Feb	15x15	P240	43.9600	0.39	12-Sep	N/A	N/A	N/A	N/A	N/A	N/A
✓	Ta3	27-Feb	15x15	P1200	44.3700	0.11	12-Sep	N/A	N/A	N/A	N/A	N/A	N/A
✓	Ta4	27-Feb	15x15	P1200	44.4800	0.15	12-Sep	N/A	N/A	N/A	N/A	N/A	N/A
-	Ta4	27-Feb	15x15	P1200	-	-	-	N/A	N/A	N/A	N/A	N/A	N/A
✓	Zr1	27-Feb	15x15	P240	17.1700	0.21	12-Sep	SbCl3	✓	✓	✓	✓	✓
✓	Zr2	27-Feb	15x15	P240	17.3300	0.25	12-Sep	N/A	N/A	N/A	N/A	N/A	N/A
✓	Zr3	27-Feb	15x15	P1200	17.3900	0.13	12-Sep	N/A	N/A	N/A	N/A	N/A	N/A
✓	Zr4	27-Feb	15x15	P1200	17.3200	0.13	12-Sep	N/A	N/A	N/A	N/A	N/A	N/A
-	Zr4	27-Feb	15x15	P1200	-	-	-	N/A	N/A	N/A	N/A	N/A	N/A
✓	Nb1	27-Feb	15x15	P240	22.5200	0.59	12-Sep	SbCl3	✓	✓	✓	✓	✓
✓	Nb2	27-Feb	15x15	P240	22.6300	0.62	12-Sep	N/A	N/A	N/A	N/A	N/A	N/A
-	Nb2	27-Feb	15x15	P1200	-	-	-	N/A	N/A	N/A	N/A	N/A	N/A

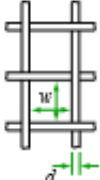
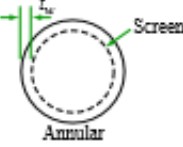
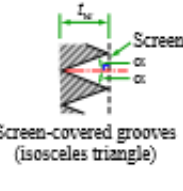
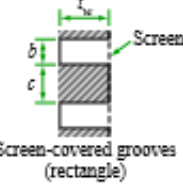
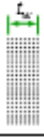
Appendix B Improved wick conductivity and mesh property equations

Wick Type*		Thermal conductivity		Porosity
		Equation†	Derivation Numbers (see Section 6)	
Single-layer wire mesh screens (heat-pipe axis in plane of paper in this sketch)	 Annular	$\lambda_w = \lambda_f$	—	$\epsilon = 1$
	 Screen-covered grooves (isosceles triangle)	$\lambda_w \approx 0.85\lambda_s[\lambda_f/(\lambda_s \sin \alpha)]^{0.63}$ (1)	18, 31	$\epsilon = 0.5$
	 Screen-covered grooves (rectangle)	$\lambda_w \approx \epsilon\lambda_f + (1-\epsilon)\lambda_s$	26, 28	$\epsilon = \frac{b}{b+c}$
 Multiple wire mesh screens†, plain or sintered (screen dimensions as for single layers illustrated above)	$\lambda_w \approx \frac{\lambda_f[\lambda_f + \lambda_s - (1-\epsilon)(\lambda_f - \lambda_s)]}{\lambda_f + \lambda_s + (1-\epsilon)(\lambda_f - \lambda_s)}$ (2)	19, 21, 25, 26	Best obtained experimentally, but can be estimated from the equation for single screens $\epsilon \approx 1 - \frac{\pi Nd}{4}$	
 Unconsolidated packed spherical particles (d = average particle diameter)	Plain	$\lambda_w \approx \frac{\lambda_f[2\lambda_f + \lambda_s - 2(1-\epsilon)(\lambda_f - \lambda_s)]}{2\lambda_f + \lambda_s + (1-\epsilon)(\lambda_f - \lambda_s)}$ (3)	4, 26	Depends on packing mode and should be measured. A very rough estimate can be obtained assuming cubic packing, $\epsilon \approx 0.48$
	Sintered	$\lambda_w \approx \frac{\lambda_s[2\lambda_s + \lambda_f - 2\epsilon(\lambda_s - \lambda_f)]}{2\lambda_s + \lambda_f + \epsilon(\lambda_s - \lambda_f)}$	19, 21, 28	
 Sintered felted metal fibres‡ (d = fibre diameter)	$\lambda_w \approx \epsilon\lambda_f + (1-\epsilon)^2\lambda_s + \frac{4\epsilon(1-\epsilon)\lambda_f\lambda_s}{\lambda_f + \lambda_s}$ (4)	11, 19, 22, 30, 33	Obtain ϵ experimentally or use manufacturer's data	

* In the sketches the axis of the heat pipe and therefore the direction of fluid flows are normal to the plane of the paper unless stated otherwise.

† Figures in brackets refer to notes in Section 7.2.

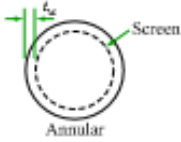
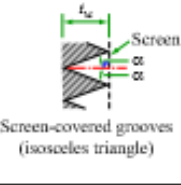
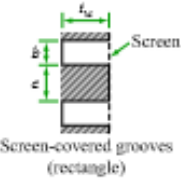
‡ These wicks are positioned so that the layers follow the contour of the inner surface of the heat-pipe wall.

Wick Type [†]		Minimum Capillary Radius					
		Equation [‡]	Derivation Numbers (see Section 6)	Accuracy Information			
Single-layer wire mesh screens (heat-pipe axis in plane of paper in this sketch)  $\frac{1}{N} = d + w$ N = number of apertures per unit (m) of screen	 Annular	$r_{\sigma} = \frac{1}{2N}$ (5), (6), (7)	6, 9, 12, 15, 23, 27	80% of data lie within 0.8 to 1.2 times value given by equation			
	 Screen-covered grooves (isosceles triangle)						
	 Screen-covered grooves (rectangle)						
	Multiple wire mesh screens [‡] , plain or sintered (screen dimensions as for single layers illustrated above)	$r_{\sigma} = \frac{1}{2N}$ (5), (8)	7, 8, 13, 15, 16, 19, 20, 21	80% of data lie within 0.5 to 1.5 times value given by equation			
	Unconsolidated packed spherical particles (d = average particle diameter)	<table border="1"> <tr> <td>Plain</td> <td rowspan="2"> $r_{\sigma} = 0.21d$ (9) </td> </tr> <tr> <td>Sintered</td> </tr> </table>	Plain	$r_{\sigma} = 0.21d$ (9)	Sintered	7, 8, 10, 16, 21, 23, 29, 32	80% of data lie within 0.7 to 1.3 times value given by equation
Plain	$r_{\sigma} = 0.21d$ (9)						
Sintered							
	Sintered felted metal fibres [‡] (d = fibre diameter)	$r_{\sigma} = \frac{d}{2(1-\epsilon)}$ (10)	7, 8, 19, 23	80% of data lie within 0.5 to 1.5 times value given by equation			

[†] In the sketches the axis of the heat pipe and therefore the direction of fluid flows are normal to the plane of the paper unless stated otherwise.

[‡] Figures in brackets refer to notes in Section 7.2

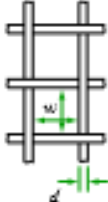
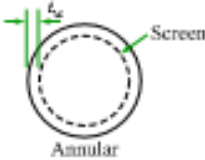
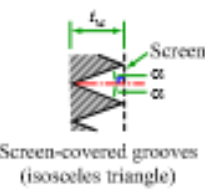
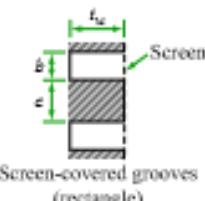
[‡] These wicks are positioned so that the layers follow the contour of the inner surface of the heat-pipe wall.

Wick Type*		Permeability				
		Equation†	Derivation Numbers (see Section 6)	Accuracy information		
Single-layer wire mesh screens (heat-pipe axis in plane of paper in this sketch)  $\frac{1}{N} = d + w$ <i>N</i> = number of apertures per unit (m) of screen	 Annular	$K = \frac{\epsilon^3}{12}$ (11)	5	Equations apply strictly to these shapes with smooth surfaces in place of screens and are then accurate to within $\pm 5\%$. The effect of screens is uncertain but it is expected to be small		
	 Screen-covered grooves (isosceles triangle)	$K = F \epsilon_w^2 \epsilon$ where <i>F</i> is given in Figure 1				
	 Screen-covered grooves (rectangle)	$K = F b t_w \epsilon$ where <i>F</i> is given in Figure 2				
	Multiple wire mesh screens‡, plain or sintered (screen dimensions as for single layers illustrated above)	$K = \frac{d^2 \epsilon^3}{122(1 - \epsilon)^2}$ (8), (12)	7, 8, 13, 14, 15, 16, 19, 21	Equation from Derivation 14; 80% of data from other Derivations lie within 0.5 to 2.0 times value given by equation		
	<table border="1"> <tr> <td>Plain</td> <td rowspan="2"> $K = \frac{d^2 \epsilon^3}{150(1 - \epsilon)^2}$ (13) </td> </tr> <tr> <td>Sintered</td> </tr> </table> Unconsolidated packed spherical particles (<i>d</i> = average particle diameter)	Plain	$K = \frac{d^2 \epsilon^3}{150(1 - \epsilon)^2}$ (13)	Sintered	7, 8, 10, 14, 16, 21, 29, 32	Equation from Derivation 14; 80% of data from other Derivations lie with in 0.8 to 1.7 times value given by equation
Plain	$K = \frac{d^2 \epsilon^3}{150(1 - \epsilon)^2}$ (13)					
Sintered						
	Sintered felted metal fibres‡ (<i>d</i> = fibre diameter)	$K = \frac{C_1(y^2 - 1)}{y^2 + 1}$ (14) where $y = 1 + \frac{C_2 d^2 \epsilon^3}{(1 - \epsilon)^2}$ $C_1 = 6.0 \times 10^{-10} \text{ m}^2$ $C_2 = 3.3 \times 10^7 \text{ l/m}^2$	7, 8, 19, 23, 24, 33	80% of data lie within 0.75 to 1.25 times value given by equation		

* In the sketches the axis of the heat pipe and therefore the direction of fluid flows are normal to the plane of the paper unless stated otherwise.

† Figures in brackets refer to notes in Section 7.2.

‡ These wicks are positioned so that the layers follow the contour of the inner surface of the heat-pipe wall.

Wick Type*		Equivalent Diameter	Reynolds Number Criterion		
<p>Single-layer wire mesh screens (heat-pipe axis in plane of paper in this sketch)</p>  <p>$\frac{1}{N} = d + w$ N = number of apertures per unit (m) of screen</p>	 <p>Annular</p>	$D_E = 2t_w$	$Re_i < 2000$ (15)		
	 <p>Screen-covered grooves (isosceles triangle)</p>	$D_E = \frac{2t_w \sin \alpha}{1 + \sin \alpha}$			
	 <p>Screen-covered grooves (rectangle)</p>	$D_E = \frac{2bt_w}{b + t_w}$			
 <p>Multiple wire mesh screens†, plain or sintered (screen dimensions as for single layers illustrated above)</p>	$D_E = \frac{d\epsilon}{1 - \epsilon}$	$Re_i < 10$			
 <p>Unconsolidated packed spherical particles (d = average particle diameter)</p>	<table border="1"> <tr> <td>Plain</td> <td rowspan="2">$D_E = \frac{2d\epsilon}{3(1 - \epsilon)}$</td> </tr> <tr> <td>Sintered</td> </tr> </table>		Plain	$D_E = \frac{2d\epsilon}{3(1 - \epsilon)}$	Sintered
Plain	$D_E = \frac{2d\epsilon}{3(1 - \epsilon)}$				
Sintered					
 <p>Sintered felted metal fibres† (d = fibre diameter)</p>	$D_E = \frac{d\epsilon}{1 - \epsilon}$				

* In the sketches the axis of the heat pipe and therefore the direction of fluid flows are normal to the plane of the paper unless stated otherwise.

† These wicks are positioned so that the layers follow the contour of the inner surface of the heat-pipe wall.

Appendix C SEM/EDX imaging procedure

Full details on SEM setup and imaging process can be found here:

<https://www.chems.msu.edu/resources/tutorials/SEM/generic-operation>

Appendix D Thermocouple calibration test
results

Liquid temperature measurement calibration results

<i>Temp</i>	<i>Ref</i>	<i>Top In</i>	<i>Top Out</i>	<i>Bot In</i>	<i>Bot Out</i>	<i>A</i>	<i>B</i>	<i>C</i>	<i>D</i>
30	29.66	29	29.23	29.43	29.53	29.03	29.25	29.57	29.52
50	49.31	48.42	48.64	48.89	48.99	48.53	48.74	49.2	49.02
70	68.75	67.97	68.18	68.46	68.54	68.23	68.43	69.01	68.64
90	88.29	87.71	87.9	88.2	88.28	88.01	88.21	88.96	88.44

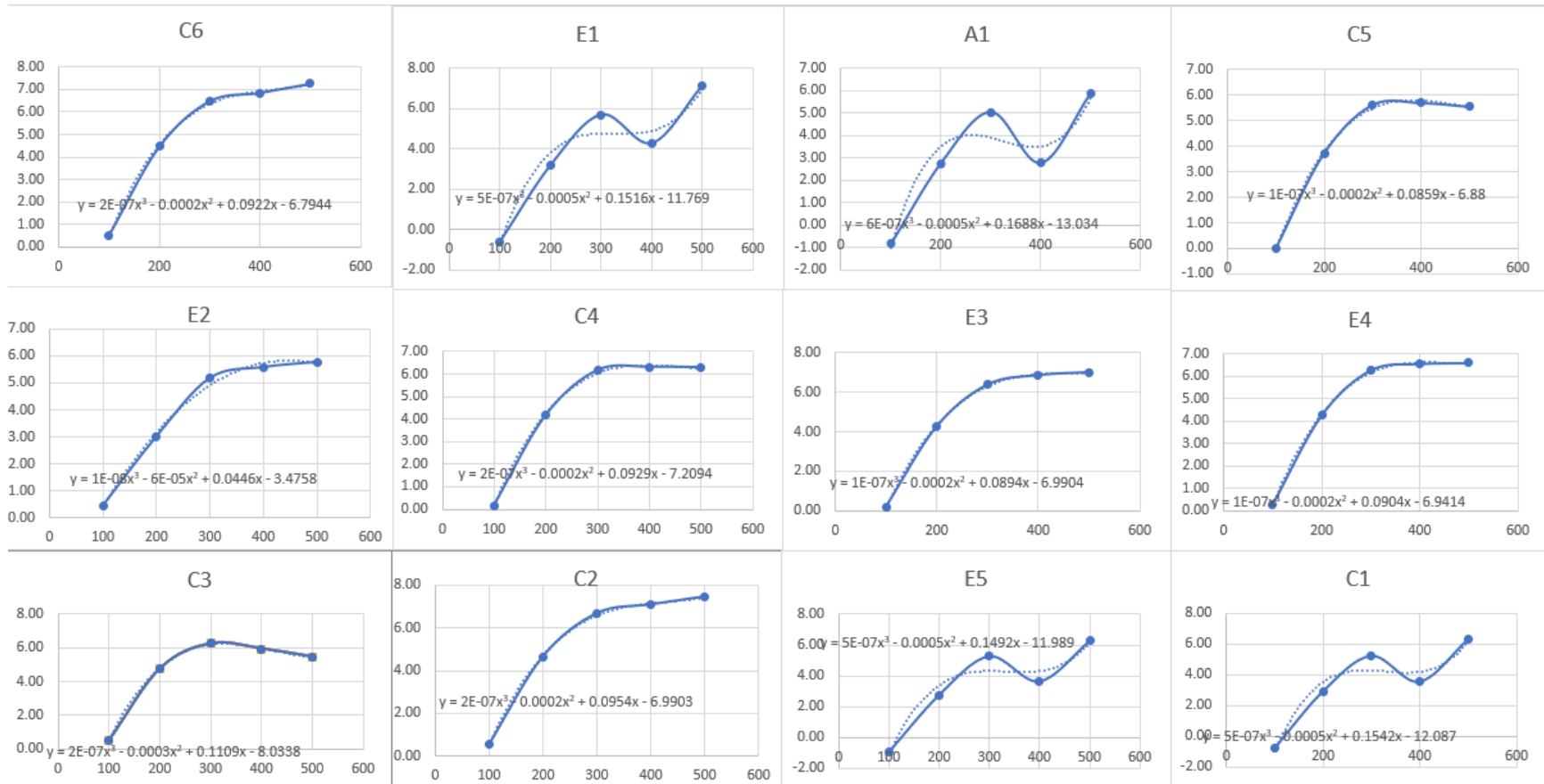
<i>dt Tin</i>	<i>dT Tout</i>	<i>dT Bin</i>	<i>dT Bout</i>	<i>dTA</i>	<i>dTB</i>	<i>dTC</i>	<i>dTD</i>
-0.66	-0.43	-0.23	-0.13	-0.63	-0.41	-0.09	-0.14
-0.89	-0.67	-0.42	-0.32	-0.78	-0.57	-0.11	-0.29
-0.78	-0.57	-0.29	-0.21	-0.52	-0.32	0.26	-0.11
-0.58	-0.39	-0.09	-0.01	-0.28	-0.08	0.67	0.15

Solid temperature measurement calibration results

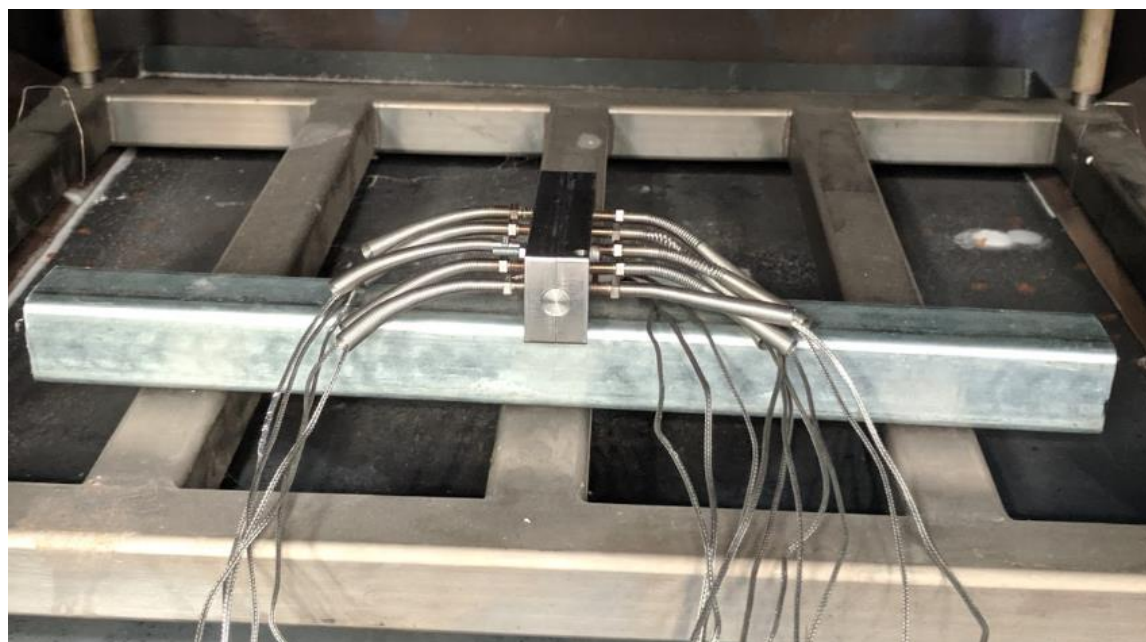
<i>Reference temp</i>	<i>C5 Type K</i>	<i>C4 Type K</i>	<i>C3 - Type K</i>	<i>C2 - Type K</i>	<i>C6 - Type K</i>	<i>X1 Type K</i>	<i>E4 Type K</i>	<i>ref 1 Type K</i>	<i>ref2 Type K</i>	<i>E2 Type K</i>	<i>E3 Type K</i>	<i>E1 Type K</i>	<i>C1 Type K</i>	<i>A1 Type K</i>	<i>E5 Type K</i>
100	100.02	99.83	99.49	99.45	99.50	99.59	99.73	99.78	101.04	99.56	99.81	100.60	100.79	100.83	100.97
200	196.28	195.83	195.22	195.34	195.54	195.51	195.74	195.75	197.38	197.00	195.73	196.80	197.08	197.24	197.25
300	294.37	293.84	293.75	293.32	293.52	293.46	293.72	293.73	294.98	294.83	293.61	294.29	294.75	294.97	294.71
400	394.29	393.69	394.06	392.91	393.15	393.09	393.44	393.45	396.93	394.43	393.14	395.71	396.43	397.23	396.34
500	494.44	493.71	494.54	492.55	492.74	492.83	493.40	493.27	494.11	494.24	492.99	492.84	493.70	494.11	493.71
<i>Reference temp</i>	<i>C5</i>	<i>C4</i>	<i>C3</i>	<i>C2</i>	<i>C6</i>	<i>X1</i>	<i>E4</i>	<i>ref 1</i>	<i>ref2</i>	<i>E2</i>	<i>E3</i>	<i>E1</i>	<i>C1</i>	<i>A1</i>	<i>E5</i>
100	-0.02	0.17	0.51	0.55	0.50	0.41	0.27	0.22	-1.04	0.44	0.19	-0.60	-0.79	-0.83	-0.97
200	3.72	4.17	4.78	4.66	4.46	4.49	4.26	4.25	2.62	3.00	4.27	3.20	2.92	2.76	2.75
300	5.63	6.16	6.25	6.68	6.48	6.54	6.28	6.27	5.02	5.17	6.39	5.71	5.25	5.03	5.29
400	5.71	6.31	5.94	7.09	6.85	6.91	6.56	6.55	3.07	5.57	6.86	4.29	3.57	2.77	3.66
500	5.56	6.29	5.46	7.45	7.26	7.17	6.60	6.73	5.89	5.76	7.01	7.16	6.30	5.89	6.29

<i>Reference temp</i>	<i>Mean</i>	<i>SD</i>	<i>SDOM</i>
100	-0.06611	0.597055	0.154159
200	3.753779	0.788321	0.203544
300	5.87643	0.59762	0.154305
400	5.447529	1.54028	0.397699
500	6.454664	0.65767	0.16981
		Av	0.215903

Thermocouple error vs temperature



High temperature calibration block photos



Appendix E Dibenzyl toluene, 90-95%
property data

<i>Thermal H350</i>						
Temperature [°C]	Kinematic viscosity [mm ² /s]	Dynamic viscosity [Pa.s]	Density [kg/m ³]	Specific heat capacity [kJ/kg K]	Thermal conductivity [W/m K]	Vapor pressure [hPa]
0	321	0.339618	1058	1.48	0.133	-
20	47	0.049068	1044	1.55	0.131	-
40	16.5	0.016995	1030	1.62	0.128	-
60	8.1	0.0082296	1016	1.7	0.125	-
80	4.7	0.0047047	1001	1.77	0.123	-
100	3.1	0.0030597	987	1.85	0.12	-
120	2.3	0.0022379	973	1.92	0.117	-
140	1.8	0.0017244	958	1.99	0.115	0.1
160	1.4	0.0013216	944	2.07	0.112	0.5
180	1.2	0.001116	930	2.15	0.11	1.7
200	0.92	0.0008418	915	2.22	0.107	5
220	0.77	0.00069377	901	2.29	0.104	12
240	0.65	0.00057655	887	2.37	0.102	27
260	0.57	0.00049761	873	2.44	0.099	54
280	0.5	0.000429	858	2.52	0.096	98
300	0.45	0.0003798	844	2.59	0.094	200
320	0.4	0.000332	830	2.67	0.091	315
340	0.36	0.0002934	815	2.74	0.088	560
360	0.32	0.00025632	801	2.82	0.086	860

Safety Data Sheet / Product Details

Thermal H350

Version: 2.1

Reviewed on -15.5.2015

Julabo

Print date: 26.05.15

SECTION 1. Identification of the substance/preparation and of the company

Product details

Product Name : Thermal H350

Order-No. (5 Liter) : 8940111

Order-No. (55 Gal Drum): 8891308

Company: : JULABO USA, INC
Manufactured for: 884 Marcon Blvd
ALLENTOWN, PA 18109 / U.S.A.

Phone : [+1] 610-231-0250

Fax : [+1] 610-231-0260

E-mail : info@julabo.com

Internet : www.julabo.com

Emergency Information : CHEMTREC 1-800-424-9300

Material name/category: : Methyl bis-(phenylmethyl) benzene; dibenzyltoluene

Recommended use of the chemical and restrictions on use

Recommended use : High temperature heat transfer fluid;

JULABO Forte HT systems working temperature range +50 °C to +350 °C

SECTION 2. Hazards identification

Classification of the substance or mixture

Classification (REGULATION (EC) No 1272/2008)

Chronic aquatic toxicity Category 4

May cause long lasting harmful effects to aquatic life

Aspiration hazard Category1

May be fatal if swallowed and enters airways.

Classification (67/548/EEC, 1999/45/EC)

May cause long-term adverse effects in the aquatic environment.

Label elements

Labeling (REGULATION (EC) No 1272/2008)

Hazard pictograms



Signal word

Danger

Hazard statements

H304

May be fatal if swallowed and enters airways.

H413

May cause long lasting harmful effects to aquatic life.

Precautionary statements

P273

Avoid release to the environment.

P301 + P310

IF SWALLOWED: Immediately call a POISON CENTER or doctor / physician.

P331

Do NOT induce vomiting.

P405

Store locked up.

P501

Dispose of contents / containers to an approved waste disposal facility.

Other hazards

JULABO USA, Inc.

www.julabo.com

Page 1 of 10

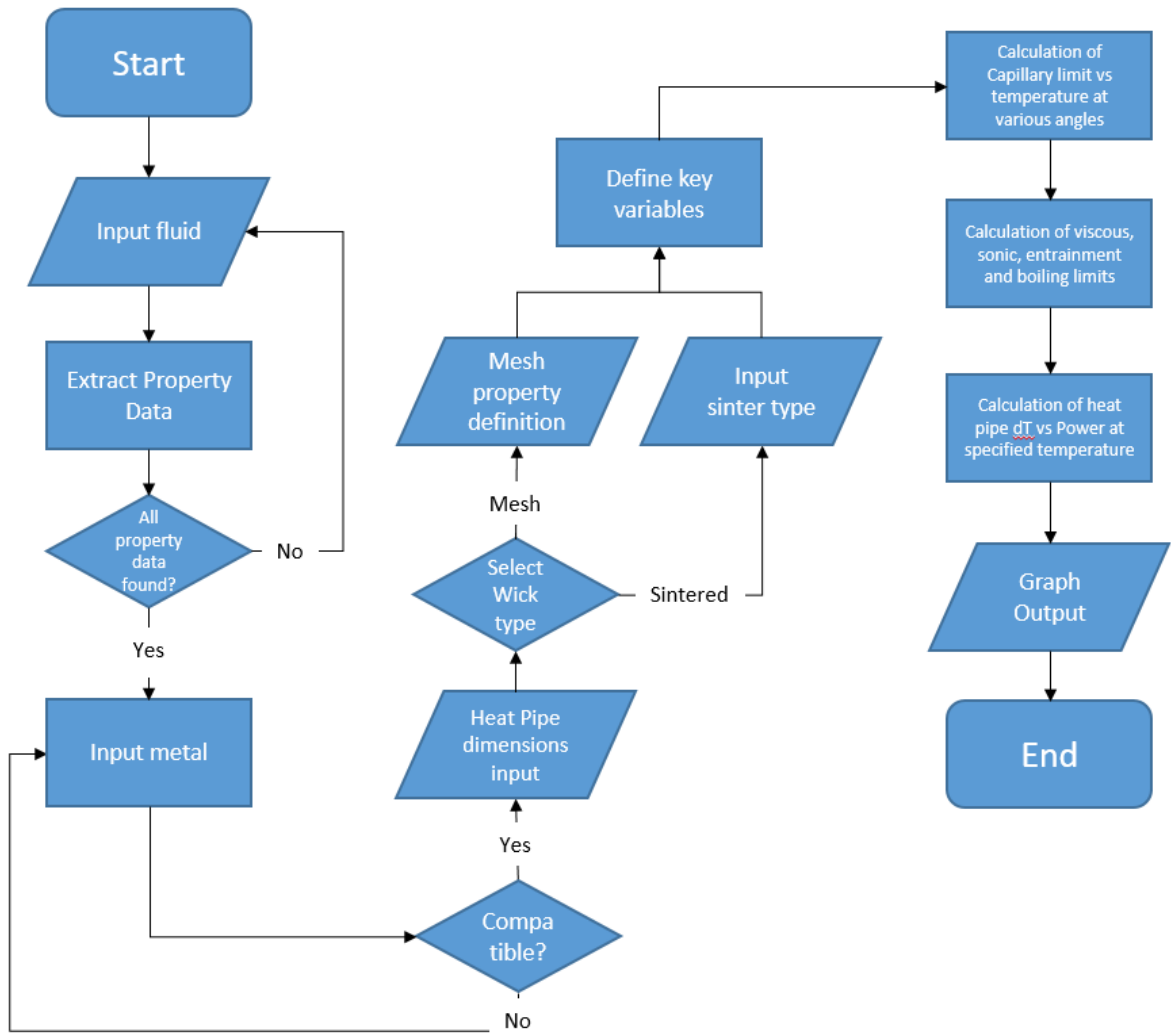
Appendix F MATLAB heat pipe model code
development

Using the theory outlined in section 2 a code was developed which would model the heat pipe working limitations using any of the fluids listed in the fluid property database (assuming all the property data is complete). The model uses the empirical data to map the limitation curves for a variety of input parameters. The capability of modelling a variety of wick structures is also in built. Calculations for the heat pipe limitations include:

- Capillary limit
- Capillary limit with annulus gaps in wick
- A choice of 4 boiling limit correlations
- Sonic limit
- Entrainment limit
- Viscous limit

Additionally, a variety of subsequent calculations include:

- Fill mass/volume calculations
- Temperature difference calculation
- Effective conductivity calculation
- Calculation of capillary limit at a variety of angles



MATLAB modelling structure

MATLAB Heat Pipe Modelling Code

The one-dimensional empirical equations outlined in chapter 2.3 form the basis of the coding used to assess the fluid performance within a heat pipe. The fluid performance is determined mainly by its capillary limit as this generally tends to be the limiting factor in the majority of cases. Another performance indicator is the temperature difference between the two ends of the heat pipe (although this tends to also be affected by the heat pipe wall thickness and metal conductivity). A comparison between these key performance indicators are used to evaluate each fluid and compare these against the baseline fluid (water) and each other.

The code performs three key functions in sequence; extracts all of the property data for the fluid selected, defined the key variables relating to the heat pipe geometry and wick structure, performs the performance limitation and temperature difference calculations and lastly presents the results in a graphical format. Each of these sections is detailed below

User input

The first section of code takes the user defined fluid input and locates the relevant property data stored as a .csv file in a database folder. The file is then stored as a Tabular text containing 9 columns and variable number of rows (varies according to the temperature range of the fluid).

```
Fluid = WATER ;
Metl = Copper ;
WICK_TYPE = orange ;

HP_Length = 250 ;           %Heat Pipe Length, mm
COND_Length = 70 ;         %Condenser Length, mm
EVAP_Length = 130 ;        %Evaporator Length, mm
HP_Angle = 45 ;           %Operating Angle, °
OP_Temp = 200 ;           %Operationg Tempeprature, °C
HP_Diameter = 6 ;         %Heat pipe diameter, mm
T_WALL = 1 ;             %Wall Thickness, mm
N_WRAPS = 3 ;            %Number of Wraps, #
MESH_NUMBER = 200 ;      %Mesh Number, #
WICK_K = 200 ;          %Wick Thermal Conductivity, W/mK
Rn = 6e-9 ;             %Nucleation Radius Value, m
```

Variable Definition

This section serves to define all of the required variables relating to the heat pipe geometry, wick structure and any area/volume calculations necessary. It also serves to extract the property data of the fluid from the tabular text data store and saves individual property data at each temperature increment as single column matrices.

```
if (wick_type=="mesh")           % Conditions for wick types chosen
    NW = N_WRAPS;                % Input the number of wraps in the mesh
    N = MESH_NUMBER;            % Input the screen type

if N == 100

    d_scr_in = 0.1E-3;           % Wire Diameter (m)
    w = 0.154E-3;               % Aperture (m)

    (...)

    rc1 = (1/(2*N))*2.54/100;     % Pore radius
    rc2 = ((1/N+d_scr_in*100/2.54)/2)*2.54/100; % Alternative Pore
    radius calculation

    twick = (2*d_scr_in*NW);     % Wick Thickness
    rv = (do-(2*twall)-(2*twick))/2; % Radius of Vapour Space
    po = 1-((1.05*pi*N*d_scr_in*100/2.54)/4); % Porosity
    pe = (d_scr_in)^2*po^3/(122*(1-po)^2); % Permeability

elseif (wick_type=="sintered")
    po = input('enter the porosity '); % Input the porosity
    rc1 = input('enter the pore radius '); % Input the pore radius
    rc2 = rc1;
    pe = input('enter the permeability '); % Input the permeability
    dm_mm = input('mandrel diameter (mm) '); % Input mandrel diameter
    dm = dm_mm/1000;
    kwick = input('powder conductivity (w/mk) '); % Enter powder
    conductivity
    twick = do/2-twall-dm/2; % Wick Thickness
    rv = (do-(2*twall)-(2*twick))/2; % Radius of Vapour Space
```

```
kwick = WICK_K; % Input screen conductivity
A = pi*((do-2*twall)/2)^2; % Total inner area
Av = pi*rv^2; % Area of vapour space
Aw = pi*(((do-2*twall)/2)^2)-rv^2); % Area of wick
Akeff = pi*(do/2)^2; % Area for effective conductivity
```

```
Sz_table = size(P_read);
Tmin = T(1); % Min operating temp
Tmax = T(Sz_table(1)); % Max operating temp
g = 9.81; % Gravity
theta = HP_Angle; % Angle of heat pipe
h = -l*sin(theta*2*pi/360); % Height of evap
Aevap = do*le*pi+2*pi*(do/2)^2; % Area of evaporator
Acond = lc*do*pi+2*pi*(do/2)^2; % Area of condenser
```

Capillary limit

The Capillary limitation is first calculated without the use of an ‘annulus gap’, referring to the gap present between mesh wick structures when these are the chosen wick type (if sintered wick is chosen this capillary limit is chosen by default). The calculation of the capillary limit makes use of two ‘for’ loops which iterate the ‘Qcap’ value until a residual value below ‘-0.001’ is reached. The magnitude of the residual value is determined by the magnitude of the iteration used in the second ‘for’ loop (in this case set at 0.01 to minimise calculation time). This can be changed within the code to improve the residual value. The gravitational, vapour and liquid pressure balance equations are used within the ‘for’ loop to determine maximum capillary limit of the system. These are equated to the maximum theoretical capillary pressure in the iterative cycle. See the extract below as an example of the ‘for’ loop used in this case.

```

Qcap_ant = zeros(Sz_table(1),1);           % Creates an empty matrix

for x = 1:Sz_table(1)

    for x0 = 1:n

        for Qcap_an = 0:0.1:100000

P_cmax = 2*(st_l(x,x0)/rc1);
% Maximum capillary limit Pc_max = 2*(ST/rc)
dPl_an = (mu_l(x,x0)*leff*Qcap_an)/(rho_l(x,x0)*k_gap(5)*(pi*((do/2-
twall)^2-(do/2-twall-gap(5))^2))*lhc(x,x0));
% Liquid pressure difference with annular gap dPl =
(mu_l*leff*Qcap_an)/(rho_l*k_gap*(pi*((do/2-twall)^2-(do/2-twall-
gap)^2))*lhc)
dPg_an = rho_l(x,x0)*g*h;
% Gravitational pressure difference dPg = rho*g*L*Sin(theta)
dPv_an = (Qcap_an*mu_v(x,x0)*8*leff)/(rho_v(x,x0)*pi*rv^4*lhc(x,x0));
% Vapour pressure difference dPv = (8*mu_v*Qcap*leff)/(rho_v*Pi*rv^4*lhc)
Prem_an = P_cmax - dPg_an - dPv_an - dPl_an;
% Pressure balance

        if Prem_an < -0.001                   % Break condition
            break
        end
        Qcap_ant(x,x0) = Qcap_an;           % Output calculated values into
empty matrix
        end
    end
end

```

Capillary limit at various angles

In addition to the calculations described previously, it is of interest to assess the performance of the heat pipe at various angles (in addition the one set by the user in the variable definition section). This give a fuller picture of the heat pipe performance in terms of the capillary limitation and dictates the ‘operating domain’ of the heat pipe, that is, the full characterisation of the heat pipe operation with respect to angle, temperature and heat flux. This ‘for’ loop performs the capillary limit with annulus gap equations but with the addition of an angle variable defined by another sub ‘for’ loop. This outputs six single column matrices defining the capillary limit at in 30° angle increments (varying form -90° to +90°) .

```

theta_range = -90:45:90; %
Angle of heat pipe
h_range = -1*sin(theta_range.*2*pi/360); %
Height of evap
%Qcap_rant = zeros((Sz_table(1)*10),1);

gap = 0.000127 % Wick gap
k_gap = 2*(gap.^2)./24; % Permiability of wick gap
x1=1;
for hx = h_range
    for x = 1:Sz_table(1)
        for Qcap_ran = 0:0.1:100000

P_cmax = 2*(st_l(x)/rc1);
% Maximum capillary limit Pc_max = 2*(ST/rc)
dPl_ran = (mu_l(x)*leff*Qcap_ran)/(rho_l(x)*k_gap(5)*(pi*((do/2-
twall)^2-(do/2-twall-gap(5))^2))*lhc(x)); % Liquid pressure difference
with annular gap
dPg_ran = rho_l(x)*g*hx;
% Gravitational pressure difference dPg = rho*g*L*Sin(theta)
dPv_ran = (Qcap_ran*mu_v(x)*8*leff)/(rho_v(x)*pi*rv^4*lhc(x));
% Vapour pressure difference dPv =
(8*mu_v*Qcap*leff)/(rho_v*Pi*rv^4*lhc)
Prem_ran = P_cmax - dPg_ran - dPv_ran - dPl_ran;

        if Prem_ran < -0.001
            break
        end
    end
end

Qcap_rant(x1,1) = Qcap_ran;
x1=x1+1;
end
end

Qcap_m90 = Qcap_rant(1:Sz_table(1));
Qcap_m45 = Qcap_rant(Sz_table(1)+1:Sz_table(1)*2);
Qcap_0 = Qcap_rant(Sz_table(1)*2+1:Sz_table(1)*3);
Qcap_45 = Qcap_rant(Sz_table(1)*3+1:Sz_table(1)*4);
Qcap_90 = Qcap_rant(Sz_table(1)*4+1:Sz_table(1)*5);

```

Other Heat Pipe limitations

Further to the capillary limitation of the heat pipe, the viscous, sonic, entrainment and boiling limits are analysed to validate the temperature range in which the capillary limit can be used as the dominating limitation. Often at higher temperature limits the boiling limit can become the predominant limitation and at lower temperatures the sonic or entrainment limits can dominate. It is rare that the viscous limit should dominate at such temperatures unless a highly viscous fluid is used.

```
%%%%%%%%%% Heat Pipe Limitations

%%%%%%%%%%%%%%%%%%%%%%%%%%%%%%%%%%%%%%%%%%%%%%%%%%%%%%%%%%%%%%%%%%%%%%%%%%
%/////////////////VISCOUS LIMIT EQUATION////////////////////////////////////
qvisc = (((rho_v.*P_v).*rv^2).*lhc)./((16*mu_v.*leff));
Qvisc = qvisc.*(pi*rv^2);

%/////////////////SONIC LIMIT EQUATION////////////////////////////////////
qsonic = (((rho_v.*P_v).^0.5).*lhc).*0.474);
Qsonic = qsonic.*(pi*rv^2);

%/////////////////ENTRAINMENT LIMIT EQUATIONS////////////////////////////////////

qent = (((((lhc.^2).*(rho_v.*2*pi)).*st_1)./rc2).^0.5);
Qent = qent.*(pi*rv^2);

%///////////////// Boiling limit Equations////////////////////////////////////
%///////////////// Chi/Faghri ///////////////////////////////////
rn = Rn;
Ke = (K_l.*((K_l+kwick)-((1-po)*(K_l-kwick))))./((K_l+kwick)+((1-
po)*(K_l-kwick)));
Qb = ((T_k'.*(Ke.*2*pi*le))./((lhc.*rho_v).*log((do/2)-
twall)/rv)).*(((st_1.*2)./rn)-P_cmax);
```

Heat Pipe Thermal Network

The temperature difference between the evaporator and condenser is evaluated in this part by adding the thermal resistances of each section of the heat pipe. Below is an extract of the code used to evaluate this at a fixed temperature and over a range of heat fluxes. The heat pipe thermal resistance network follows the theory presented in section

```
%%%%%%%%%%%%%% dT Calculation for varying heat fluxes %%%%%%%%%%  
  
dT_wall_evap = (Q_min.*twall)./(kwall*pi*do*le);  
dT_wick_evap = (Q_min.*twick)./(Ke.*pi*(do-2*twall)*le);  
dT_wall_cond = (Q_min.*twall)./(kwall*pi*do*lc);  
dT_wick_cond = (Q_min.*twick)./(Ke.*pi*(do-2*twall)*lc);  
  
dT_tot = [dT_wick_cond + dT_wick_evap + dT_wick_evap +  
dT_wall_evap].';  
  
Res = dT_tot./Q_min;  
K_eff = (A*Res).^(-1)*leff;
```

Databases

One crucial part to analysing these fluids is creating a database of both property data and fluid compatibility to incorporate into the heat pipe model. This provides the baseline property data needed to be incorporated into the modelling process. As the modelling used incorporates such extensive property data (8 individual property data sets needed per fluid) it is imperative to create an efficient and accessible database system which can be easily updated when new fluids are to be analysed. The methods chosen to combine both excel and MATLAB data basing systems which will be described in this section.

The fluid property database is a tool to collate all fluid property data found from numerous sources and provide a straightforward interface to access this data on demand. The data has successfully been integrated with MATLAB code to search, extract and use the property data within calculations. This data tends to be derived directly from empirical data, where the individual data points are given in the data source (as opposed to curve fitting equations).

Matlab database code

In addition to the Excel property database, a MATLAB based database was developed in order to extract large amounts of data from curve fitting equations. The code contains a database of polynomial variables for each fluid property. Once a fluid is selected, the code runs all variables in their relevant polynomial equations and outputs the property data in both tabular and graphical form.

```
%//////////////////////////////////// Data Extraction //////////////////////////////////////
```

```
load('Enthalpy of Vaporisation.mat');  
load('Liquid Density.mat');  
load('Surface Tension.mat');  
load('Thermal Conductivity Liquid.mat');  
load('Thermal Conductivity Vapor.mat');  
load('Vapour Pressure.mat');  
load('Viscosity Liquid.mat');  
load('Viscosity Vapor.mat');  
load('Metal Propoperties Database.mat');
```

```
Met2 = cell2mat(M2(2));  
Met2_select = Met2(str2double(Met1),:);
```

```
%//////////////////////////////////// Variable identification //////////////////////////////////////
```

```
MP_met1 = Met2_select(3);  
MAX_met1 = Met2_select(4);  
YM_max = Met2_select(5);  
YMA = Met2_select(6);  
YMB = Met2_select(7);  
YMC = Met2_select(8);  
YMD = Met2_select(9);  
UTS_max = Met2_select(10);  
UTSA = Met2_select(11);  
UTSB = Met2_select(12);  
UTSC = Met2_select(13);  
UTSD = Met2_select(14);  
Kmet_max = Met2_select(15); (...)
```

```
%%%%%%%%%%%%%%%%%%%%%%%%%%%%%%%%%%%%%%%%%%%%%%%%%%%%%%%%%%%%%%%%%%%%%%%% Data Extraction %%%%%%%%%%%%%%%%%%%%%%%%%%%%%%%%%%%%%%%%%%%%%%%%%%%%%%%%%%%%%%%%%%%%%%%%%
```

```
P_Pv = cell2mat(Pv(2));  
P_Pv_select = P_Pv(str2double(Fluid),:);
```

```
% Property data extraction from database
```

```
APv = P_Pv_select(4);  
BPv = P_Pv_select(5);  
CPv = P_Pv_select(6);  
DPv = P_Pv_select(7);  
EPv = P_Pv_select(8);  
MW = P_Pv_select(11);  
Tc = P_Pv_select(12);
```

```
x = 1;  
for T = Trange % Property data matrix creation
```

```
Pv =  
((10^(APv+(BPv/(T+273.15))+CPv*log10(T+273.15)+DPv*(T+273.15)+EPv*(T+273.15)^2))/750.06156130264); % Polynomial expression
```

```
Pvx(x,1) = Pv;  
x = x+1;  
end
```

Fill volume analysis

```
% Fill Volume Calculation %%

dp = do; % Diameter unit conversion
di_tube = dp-2*twall;

if (wick_type=="mesh")
di_vap = di_tube-2*(NW*2.2*d_scr_in); % Vapor space diameter
else
di_vap = di_tube - 2*twick;
end

Area_wick = (pi*(di_tube^2-di_vap^2))/4; % Wick area
Area_vap = (pi*di_vap^2)/4; % Vapor space area
Vol_wick = l*Area_wick; % Wick volume
Vol_vap = l*Area_vap; % Vapor space volume

Sat_wick = Vol_wick*po*1E6; % Wick saturation volume (cc)

% Find rho_v at operating temperature
T_rho_v = [T',rho_v];
find_rho_v = find(T_rho_v(:,1)>=Op_temp-2 & T_rho_v(:,1)<=Op_temp+2);
size_T_rho_v = size(T_rho_v);
rho_v2 = T_rho_v(round(find_rho_v+(size_T_rho_v(1))));

% Find rho_l at operating temperature
T_rho_l = [T',rho_l];
find_rho_l = find(T_rho_l(:,1)>=Op_temp-2 & T_rho_l(:,1)<=Op_temp+2);
size_T_rho_l = size(T_rho_l);
rho_l2 = T_rho_l(round(find_rho_l+(size_T_rho_l(1))));

Sat_vap = ((rho_v2*Vol_vap)/rho_l2)*1E6; % Vapor space volume (cc)
Losses = 0.06*Sat_wick; % Losses

Fill_Volume = Sat_wick + Sat_vap + Losses % Fill Volume (cc)
Fill_Mass = rho_l2*Fill_Volume*1E-3 % Fill mass (g)
```

Wall thickness analysis

```
T_uts = [T',utsx];
find_utsx = find(T_uts(:,1)>=Op_temp-2 & T_uts(:,1)<=Op_temp+2);
Operating_Temperature = T(find_utsx);
size_utsx = size(T_uts);
M_UTS_max = T_uts(round(find_ymx+(size_ymx(1))));

max_stress = (M_UTS_max/1E6)/4;
atm = 0.101325;
sf = 2;

% input('What safety factor would you like to include? ' )
t1 = [(((Pv/1000000)-atm)*((do/max_stress)/2)*1000)*sf]; % mm
if t1 <= 1;
    t=1;
else if t1 > 1;
    t = t1;
end
end

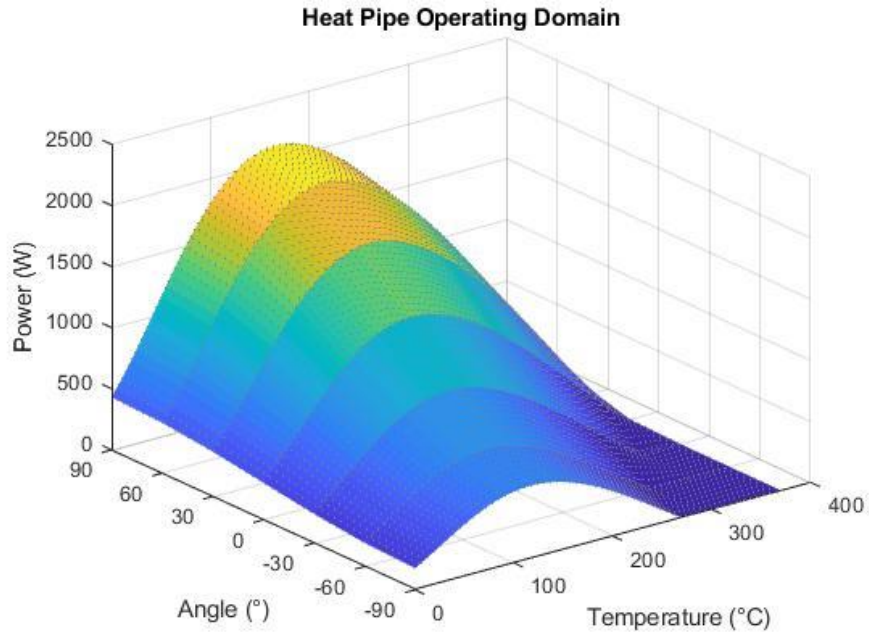
error1 = isempty(t1);
if error1 == 1
    disp('You have selected an operating temeprature out of range for
your fluid');
return
end
```

Appendix G General MATLAB graph output
description

The following document shows the output results for the input parameters described in the table below and a run through of each graphical output with a more detailed explanation of each is outlined.

Parameter	Input
Fluid	Water
Length	100mm
Evap length	20mm
Cond length	20mm
Wick	Mesh
Wraps	3
Count	200
Position	0°
Wall thickness	1mm

Output graph 1 – Heat pipe operating domain



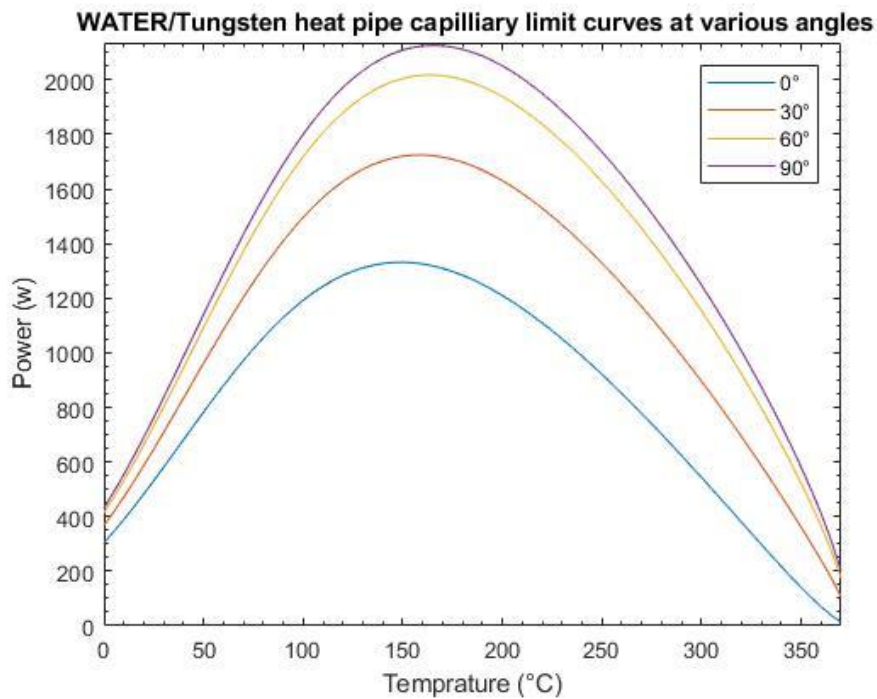
Water heat pipe operating domain

shows the first output graph detailing the ‘heat pipe operating domain’. This is a combination of three separate operating conditions, and the limitation equations associated with each. The output is a three-dimensional curved plain which demonstrates the output thermal load expected at any given angle and temperature within range.

The graph serves as a general overview of how the heat pipe will perform over its entire operating limit. It is important to note that output only makes use of the Capillary limit equations, which generally tend to be main limiting factor over the operating temperature range, the output thermal loads at the beginning and end may be reduced due to other

limitations which tend to affect only the start and end limit. The maximum heat transport point is always limited by the Capillary limit, so the graphs gives a good indication of what angle and temperature the maximum heat transport can be delivered at.

Output graph 2 – Capillary limit curve at various angles

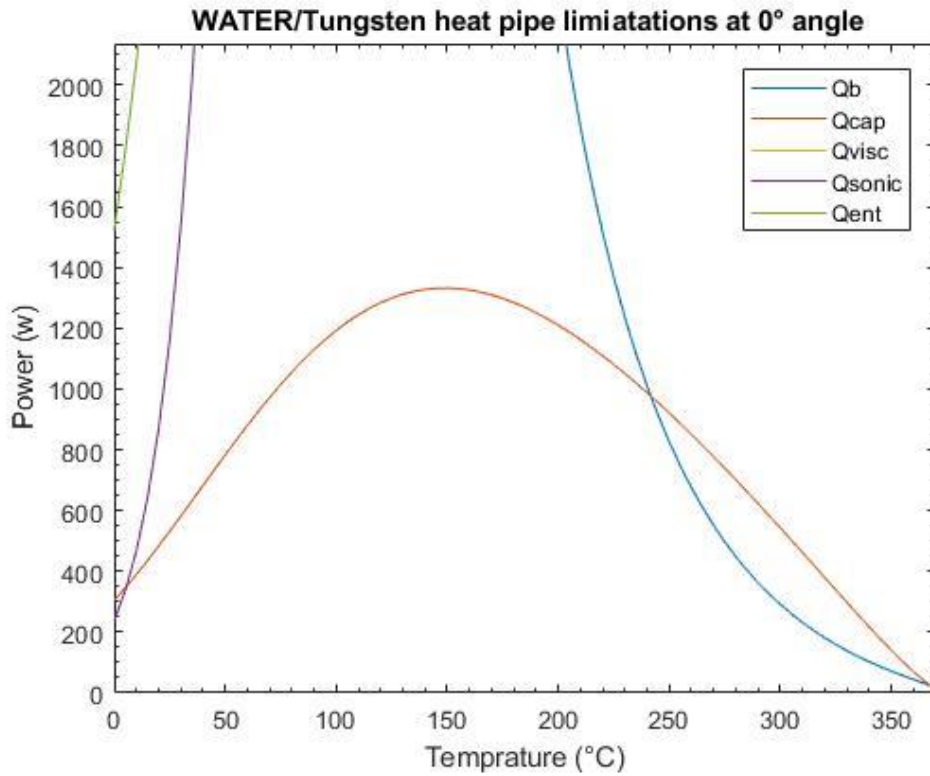


Water/Tungsten capillary limit at various angles

The second output figure seen in is a two dimensional view of . This is utilised to pinpoint exact operating conditions and enable a better reading of the thermal load to be expected at that point. A map of various operating conditions can then be made if there are various

operating condition to be expected in the application. The graph can also be easily adapted to include other specific operating angles.

Output graph 3 – Limitations at 0° angle



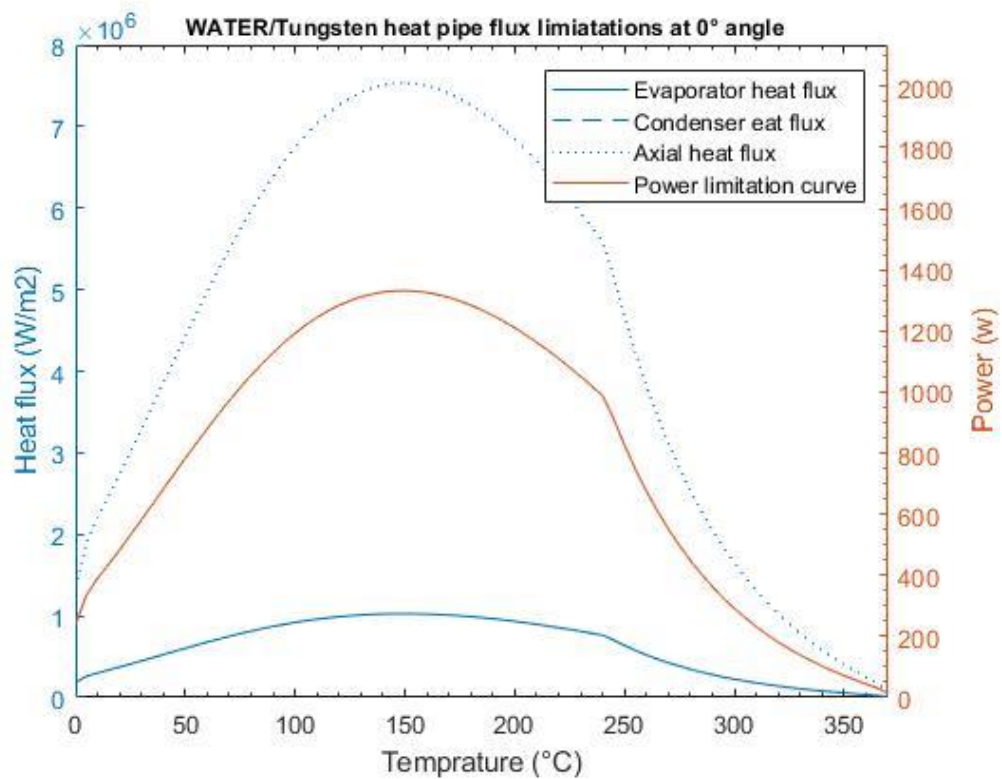
Water/Tungsten heat pipe limitations operating angle

shows the third output graph. When setting the input parameters, the main angle that the heat pipe is operated at is determined. This graph shows all the operating limitations over the entire operating temperature range of the heat pipe. In this case the Sonic limit only barely affects the start-up limit, but the boiling limit shows a large effect on the upper temperature range. The various operating limits are affected by a large number of factors,

hence it is important to analyse the full limitation graph for each operating condition to be expected in the application.

By observing the various limitation curves, it is possible to provide measures to reduce them, for example, in this case if the heat pipe were to be operated at high temperatures, the boiling limit could be increased by using an alternative wick type. Of course, this would then lead to a cost-benefit analysis on the proposed change.

Output graph 4 – Heat pipe flux limitations at 0° angle

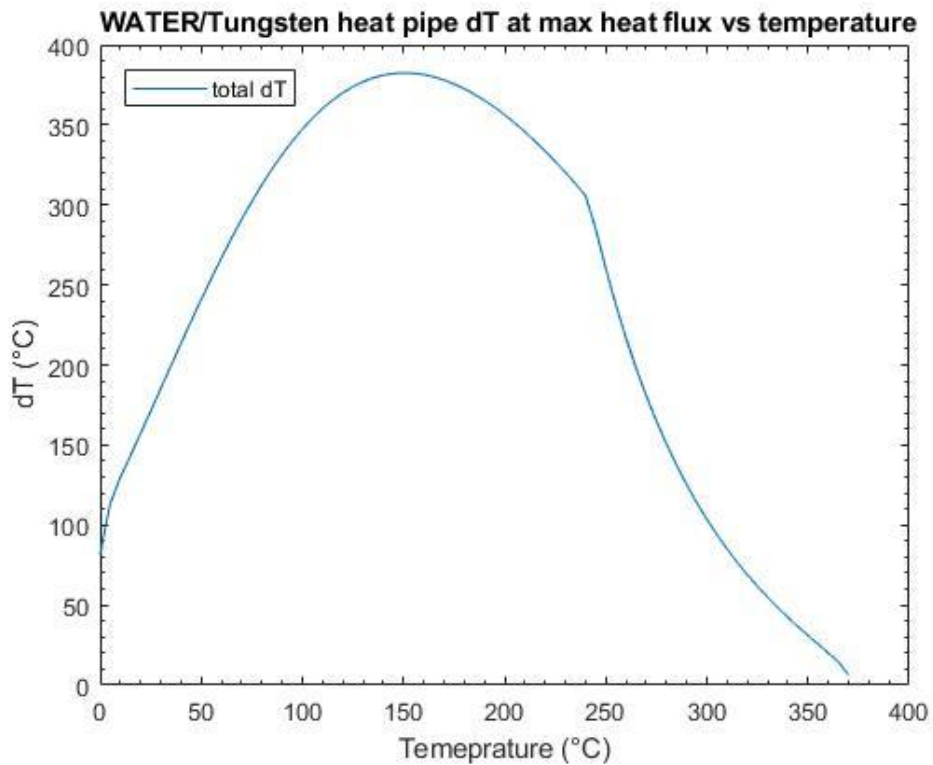


Water heat pipe heat flux limitations operating angle

The fourth output graph displayed in shows the full range of the thermal transport limit on the right axis considering all limitation equations and the corresponding evaporator, condenser and axial heat flux is displayed on the left axis.

This serves to translate the operating heat transport limitations into the maximum application heat flux which can be applied to each section of the pipe. In this case, as the evaporator and condenser areas are equal, they present the same maximum heat flux condition.

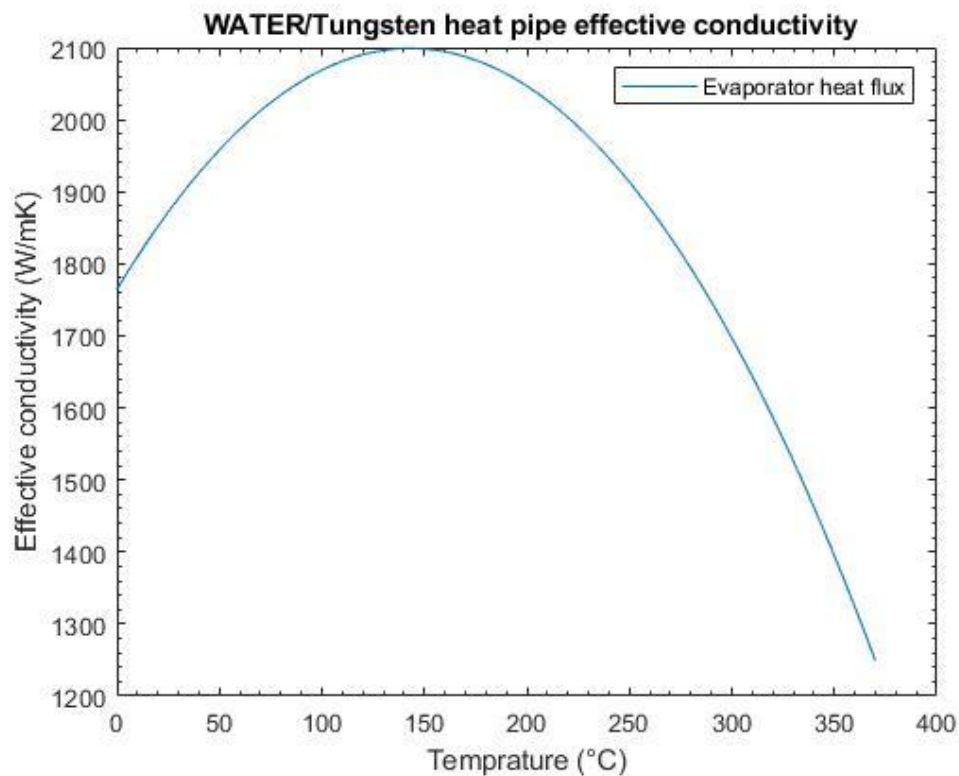
Output graph 5 – Heat pipe dT at max heat flux vs temperature



Water heat pipe temperature difference at limitation curve

The fifth output, seen in , shows the predicted temperature difference from the thermal resistance network equations when at the maximum thermal load conditions. As the model uses a simplistic approach to the problem, the results tend to over predict the expected temperature difference due to the simplified approach to modelling the wick structure thermal resistance. In reality, the wick structure provides a much more complex interface which is difficult to model as a single thermal resistance value. Improved versions of this model are still being research and the code is updated as this progresses for a more accurate temperature difference prediction.

Output graph 6 – Heat pipe effective conductivity



Water heat pipe equivalent conductivity trend

The last output graph, shown in , is the calculation of the effective conductivity corresponding to the heat transport curve displayed in . Within this temperature range, the minimum effective thermal conductivity (measured as the conductivity at the operating limits) can be calculated through the temperature difference profile in using equation 1. When performing the calculation at each datapoint along the heat transport limitation curve in , the end result is the effective conductivity trendline seen in .

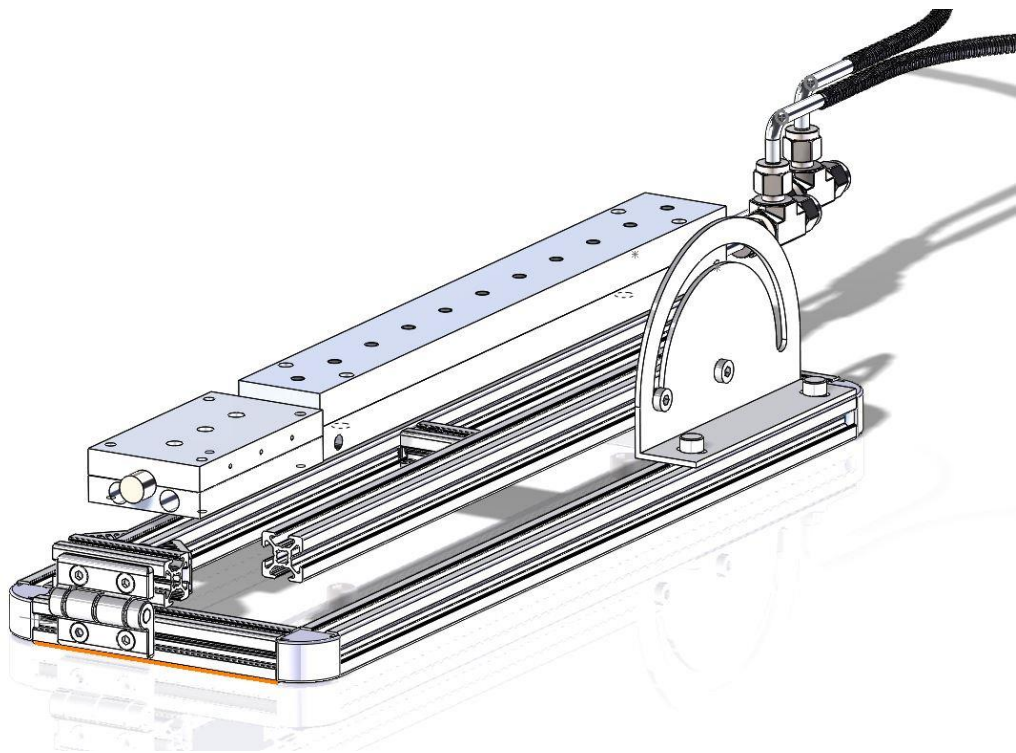
As mentioned previously, the temperature difference tends to be lower than the predicted values, which result in a lower effective thermal conductivity prediction to reality. This graph, therefore, serves as a 'worst case scenario' for the equivalent thermal conductivity over the heat pipe operating range.

Appendix H Test rig frame design iterations

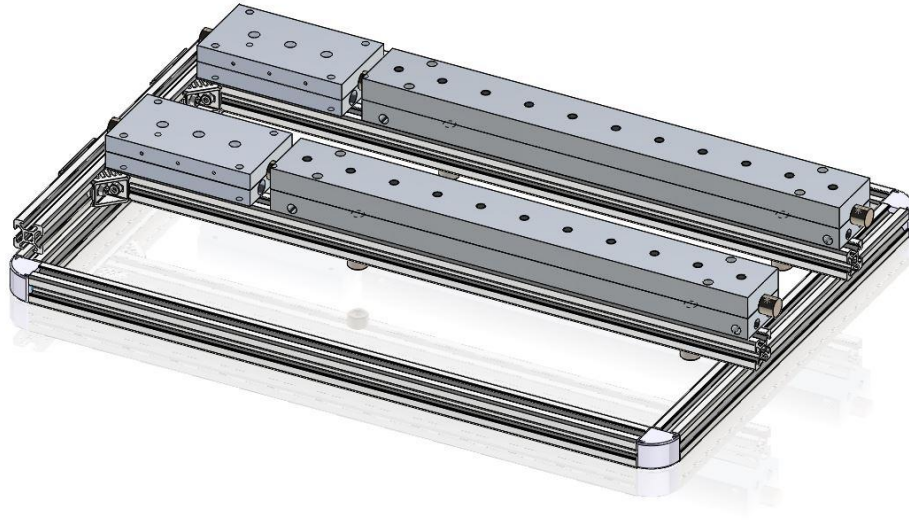
Design 1



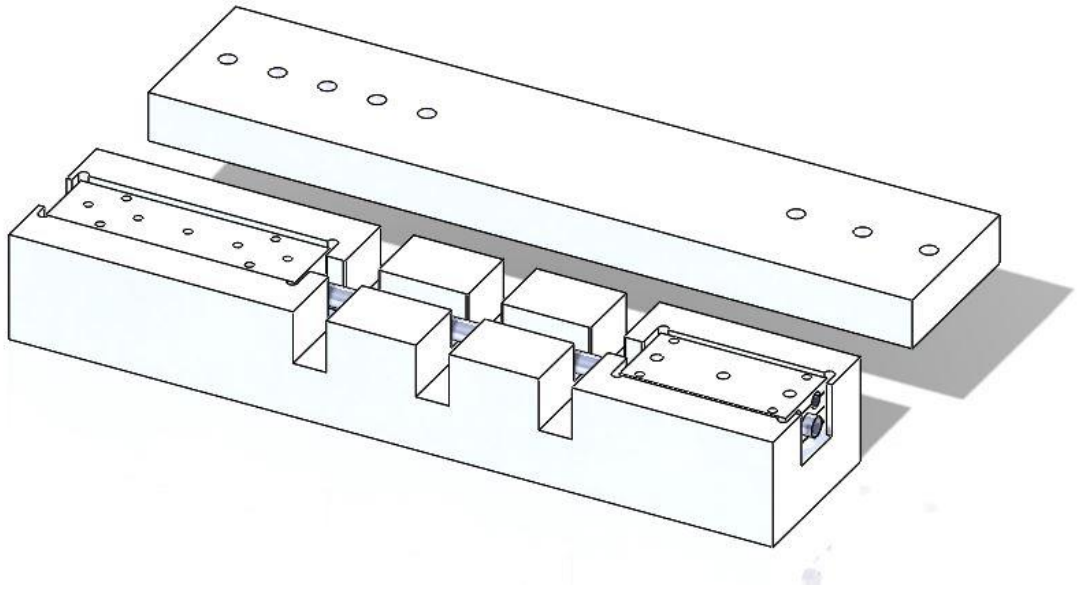
Design 2



Design 3



Design 4



Appendix I Cartridge heater specifications

Heating Element, 100mm, 500 W, 230 V

RS Stock No.: 374-2498 | Mfr. Part No.: H16X100X500 | Brand: Acim Jouanin



Technical Reference

[Cartridge Heater Data Sheet](#)

Legislation and Compliance

[RoHS Certificate of Compliance](#)

[Statement of conformity](#)

COO (Country of Origin): **FR**

Product Details

High-load heating cartridges

Heater cartridges very quickly raise the temperature of solid masses by conduction.
Stainless steel body for applications up to +750 °C max.
Plasma-welded completely sealed base.

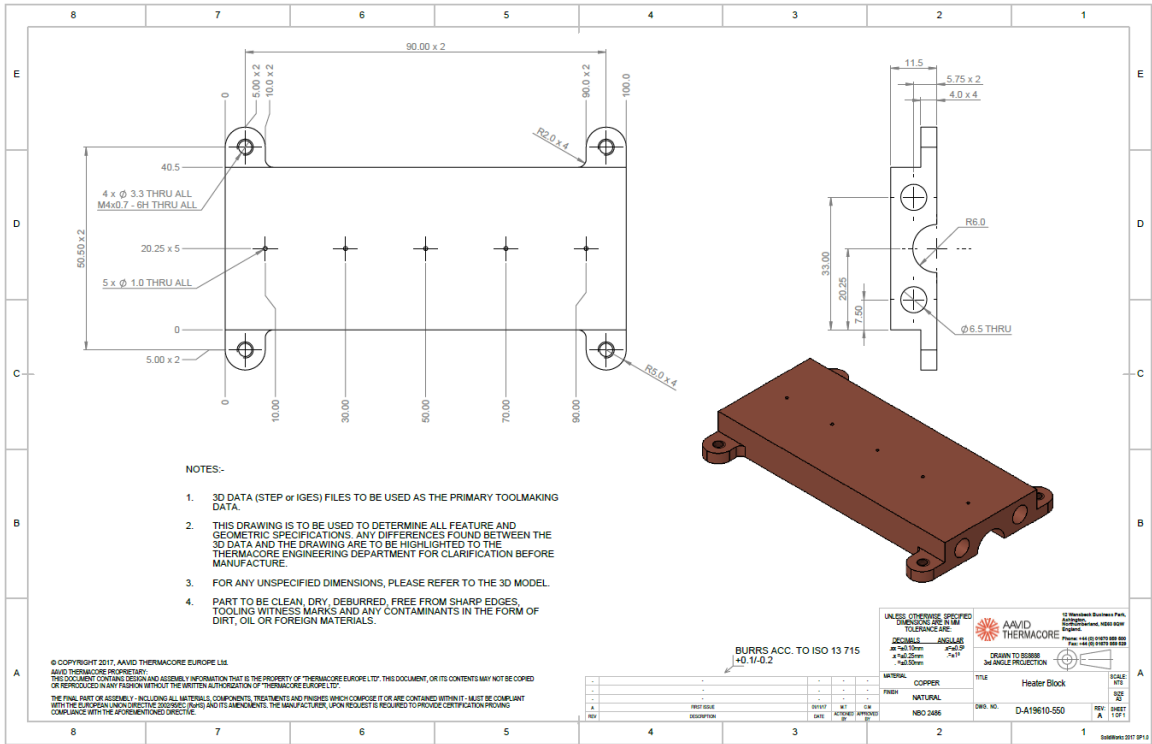
Cartridge Heaters

In order to obtain optimum performance from these products, it is advised that temperature sensing and control elements be used with them.

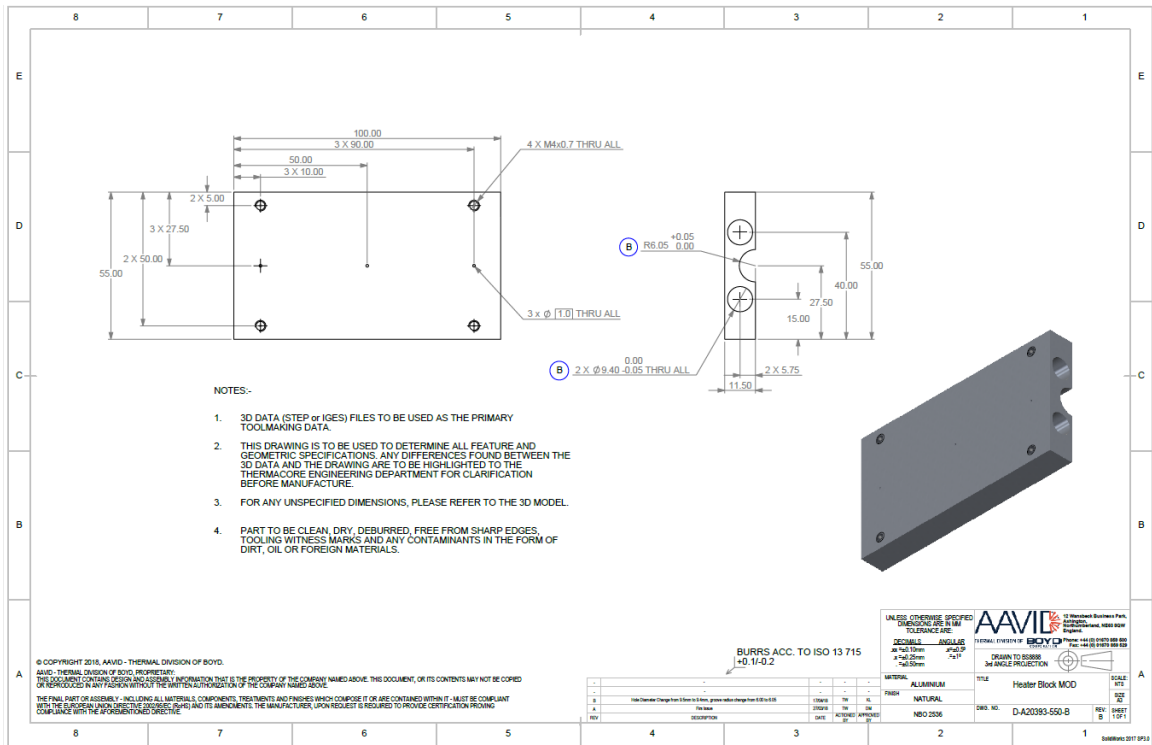
Designed to provide localised heat to a restricted work area requiring close thermal control
Cartridge heaters have low/moderate watt density elements consisting of helical wire coils on ceramic former or high watt density elements with the heating element located close to the sheath, which is swaged to improve heat conduction
All units supplied with instruction leaflet

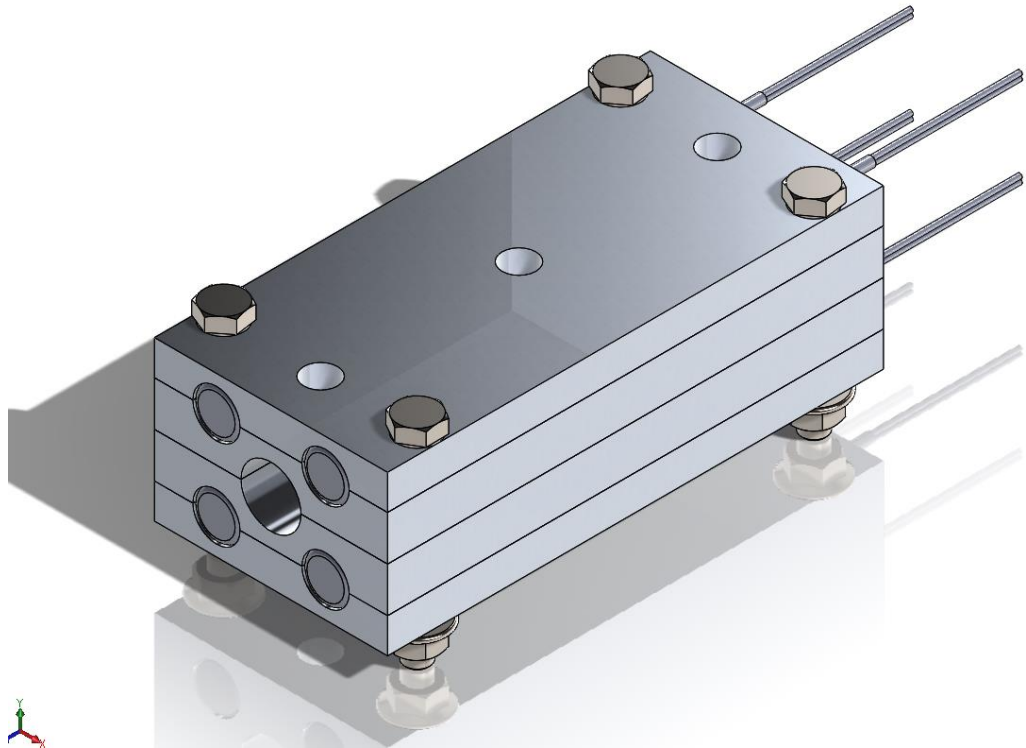
Appendix J Heater block design iterations

Design 1



Design 2





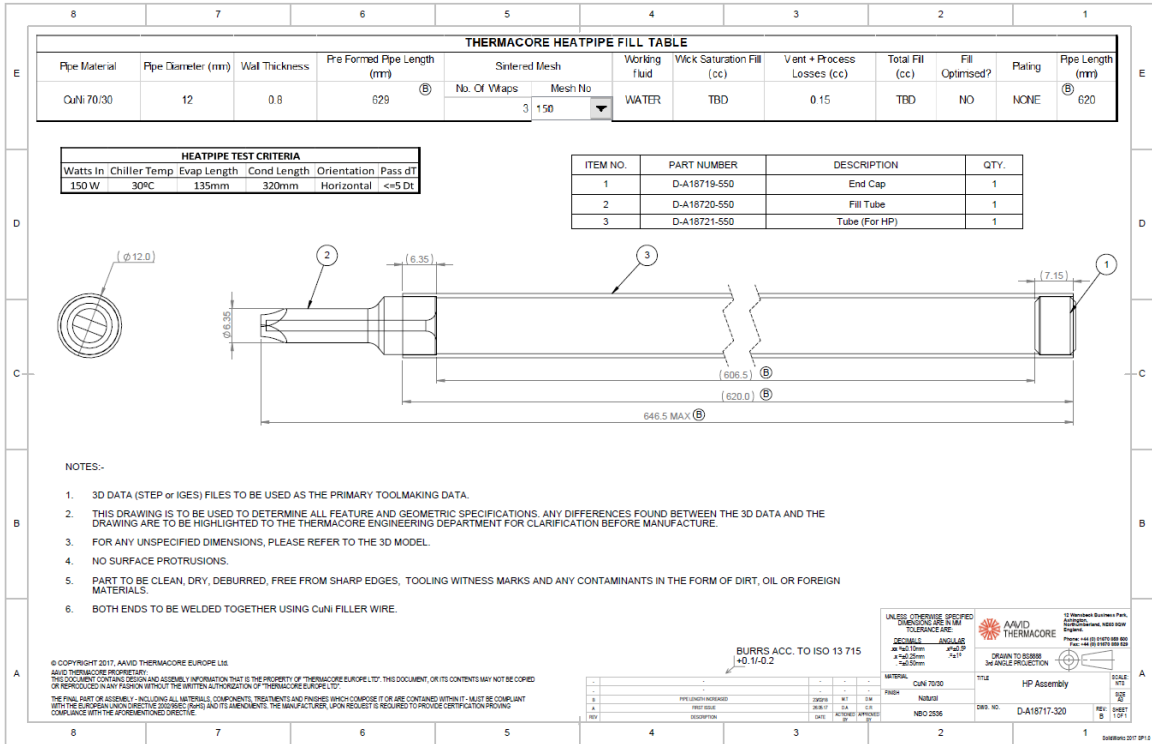
Appendix K Full SEM/EDX imaging data

All images can be found in the share file location below:

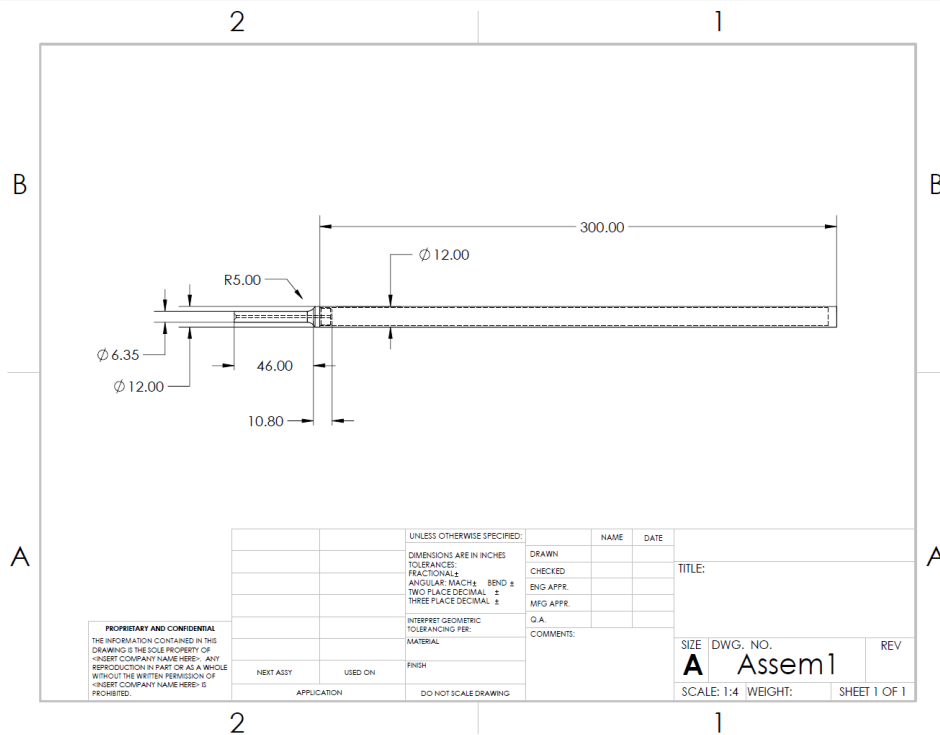
https://uniofnottm-my.sharepoint.com/:f:/g/personal/thomas_werner_nottingham_ac_uk/EhS9aGTswqRJt9cRhsnJ7bYBY8iwuy6rVUww1bDh26J-g?e=BN5XiI

Appendix L Heat pipe design iterations

Design 1

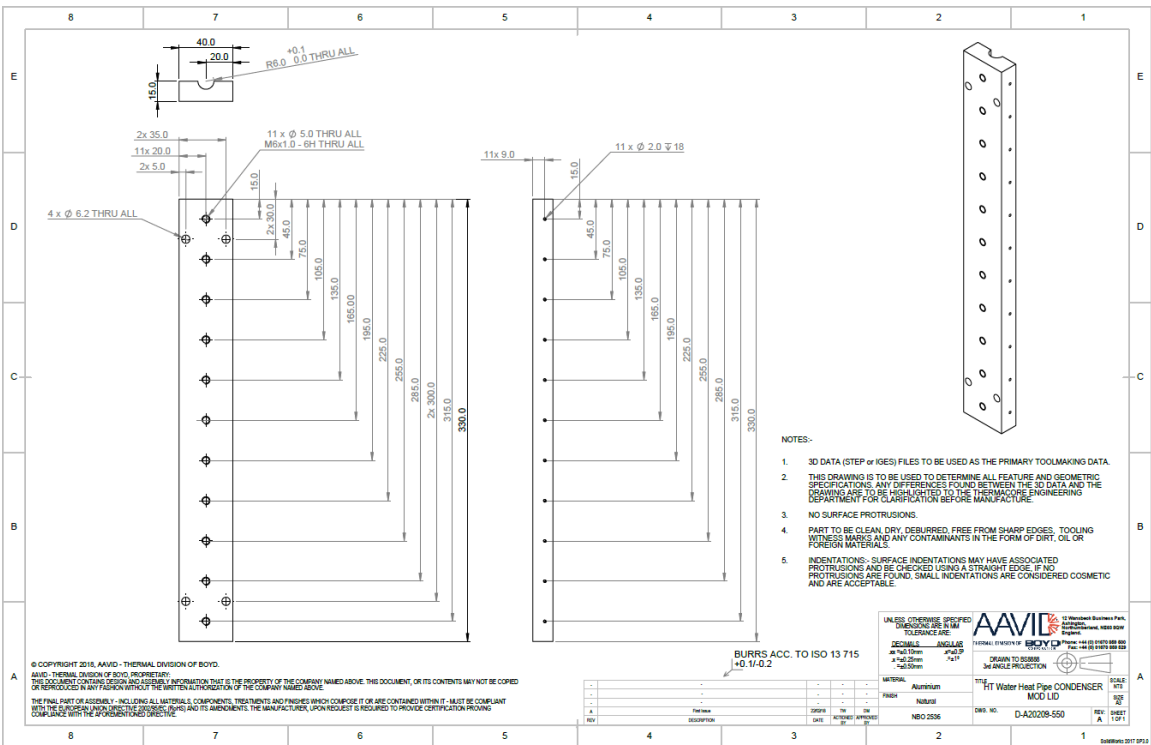
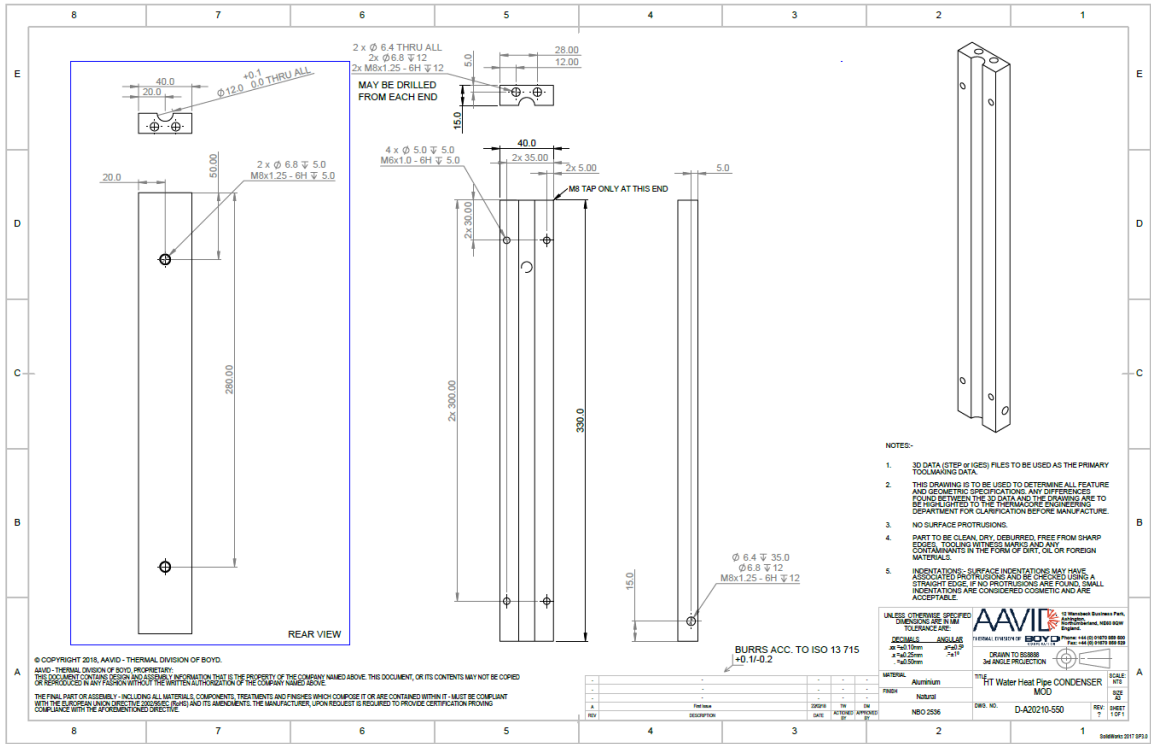


Design 2



Appendix M Calorimeter unit design
iterations

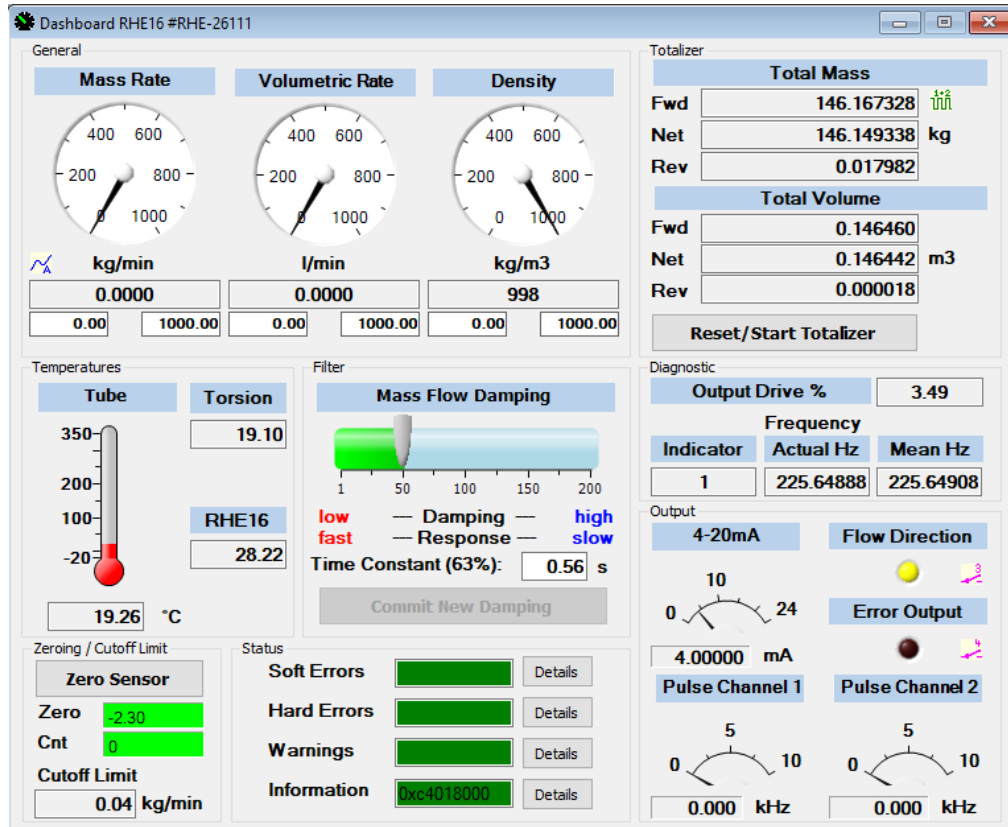
Design 2



Design 5 – Concept



Appendix N RHEONIK Dashboard



RHE16 dashboard